ABSTRACT

MEASUREMENT OF THE $ZZ \to \ell^+\ell^-\ell'^+\ell'^-$ CROSS SECTION AT $\sqrt{S} = 1.96$ TEV WITH THE DØ DETECTOR

Lei Feng, Ph.D.
Department of Physics
Northern Illinois University, 2013
David Hedin, Director

The thesis describes works carried out on the DØ experiment, a particle detector located at the Fermilab Tevatron proton-antiproton ($p\bar{p}$) collider operated at $\sqrt{s} = 1.96$ TeV. This work presents a measurement of Z/γ^* boson pair production decaying in the process $p\bar{p} \to Z/\gamma^* Z/\gamma^* \to \ell^+\ell^-\ell'^+\ell'^-$ with $eeee$, $\mu\mu\mu\mu$ and $ee\mu\mu$ final states and approximately 9.7 fb^{-1} integrated luminosity. After thorough study of the acceptance and efficiencies for each channel, 15.46 $\pm$ 0.05 (stat.) $\pm$ 1.83 (syst.) events are expected in all three channels with a background of 1.47 $\pm$ 0.05 (stat.) $^{+0.15}_{-0.26}$ (syst.) events. 13 candidate events are observed in data. Based on selected data the measured cross section in the mass region ($M_1(Z/\gamma^*) > 30$ GeV, $M_2(Z/\gamma^*) > 30$ GeV) is $\sigma(p\bar{p} \to Z/\gamma^* Z/\gamma^*) = 1.24^{+0.43}_{-0.39}(\text{stat.})^{+0.16}_{-0.15}(\text{syst.}) \pm 0.08(\text{lumi.})$ pb in agreement with the standard model expectation.A correction factor obtained from simulation allows us to convert this into a high mass cross section measurement for pure on-shell ZZ production. The pure ZZ cross section is measured to be $\sigma(p\bar{p} \to ZZ) = 1.10^{+0.38}_{-0.32}(\text{stat.})^{+0.14}_{-0.13}(\text{syst.}) \pm 0.07$ (lumi.) pb.

NORTHERN ILLINOIS UNIVERSITY
DE KALB, ILLINOIS

OCT. 2013

MEASUREMENT OF THE $ZZ \to \ell^+\ell^-\ell'^+\ell'^-$ CROSS SECTION AT $\sqrt{S} = 1.96$ TEV WITH THE DØ DETECTOR

BY

LEI FENG

A DISSERTATION SUBMITTED TO THE GRADUATE SCHOOL

IN PARTIAL FULFILLMENT OF THE REQUIREMENTS

FOR THE DEGREE

DOCTOR OF PHILOSOPHY

DEPARTMENT OF PHYSICS

Dissertation Director:
David Hedin

ACKNOWLEDGEMENTS

During my graduate studies with NIU and DØ, there are too many great people to thank. Without them, it would be impossible to complete this thesis. This section is to acknowledge and thank all the people and friends who have inspired and helped me.

Foremost, I want to express my sincere gratitude to my advisor, Dr. David Hedin. Throughout the years of my PhD life, the greatest influence to me has been far and away due to him. Without your help and wisdom, this wouldn't have been possible at all. I would like to thank him for showing me what kind of physicist I could be and what kind of supervisor I would be. Whenever I had questions, he has always found time to answer me and educate me. I learned a lot from his expertise, enthusiasm and immense knowledge of high energy physics, as well as his insightful way of resolving problems, which have been my most valuable asset. And, I certainly will profit much more from it in the future.

Besides this, Dr. Hedin also gave me a lot of support in my life. Because of some health problems, I took a leave of absence in the middle of my PhD. It was Dr. Hedin who encouraged me to finish my degree, accepted me back, provided me financial support and chose a new thesis topic for me. Whenever I was in any hard circumstance, Dr. Hedin was always the first person I went to for help. And for sure, he always gave me his ultimate support and help without hesitation. His patience, motivation and guidance helped me all the time. I could not have imagined having a better advisor and mentor than him.

I feel extraordinarily lucky to meet Dr. Hedin and have had him as my advisor in these years. I will never forget all he did for me. Even recently, Dr. Hedin has read this thesis many times and corrected a million errors. At this moment, I may only give all my gratefulness. Thanks for all the continuous support of my PhD study. But, there are definitely too much more than that I could not express in words.

Next, I am particularly grateful to Dr. James Kraus, Dr. Ryan Hooper and Dr. Diego Menezes for working on this analysis together. Jim is extremely talented and always has many brilliant ideas to share. He has been guiding me patiently. Thanks for explaining and answering me so numerous questions and leading me to work on this exciting projects. Ryan is super knowledgeable. Thanks for building the original framework and helping me to start. Diego is quite nice. Thanks for discussing many physics questions with me. Without their hard work, I could not go this far and complete this thesis.

I would also like to express my gratitude to Dr. Sergey Uzunyan and Dr. Alexandre Dyshkant. Sergey is smart. Thanks for helping me since my first project at NIU. I must admit that I have learned a lot from him on programing and software ability. Sasha is very warm-hearted. His help goes far beyond any physics in a multitude of ways.

The DØ collaboration is a big family, from which this thesis benefits a lot. I want to thank all members of DØ and the Tevatron staffs. Their jobs made this analysis possible. I would thank all the members and convenors of the DØ Electroweak and EB groups, especially Dr. Hang Yin, Dr. Breese Quinn, Dr. Jadranka Sekaric and Dr. Oleksandr Melnychuk. Thanks for their helpful comments and suggestions.

I am grateful to Dr. Michael Eads and Dr. Philippe Piot for their time and interest to be the members of my dissertation committee. Thank all the friends of Nicadd group and NIU. They made my life here colorful.

In addition to research, I have worked on MuonID and Muon electronics. I thank Muon experts Dr. Penny Kasper and Dr. Albert Ito for their help on my muon detector studies. I thank Dr. Angelo Santos for teaching me how to do muon momentum smearing.

Last but not the least, I want to thank my wife Wenli. Her love, care and patience always encourage me to do what I am interested in, and never give up. It is her who always stands behind me when I am in any hardship of life. I am also very grateful to my parents and parents in law for spiritually supporting me through college and graduate school. Without them, I can never achieve this thesis, which should be dedicated to them.

It is hard to print out all the names. I would like to thank all the people whose efforts have made this thesis come to fruition. I thank them all here.

I also want to acknowledge the National Science Foundation for their financial support.

The work described in this thesis results in the following paper:

Phys. Rev. D 88, 032008 (2013)

arXiv:1304.5422

TABLE OF CONTENTS

Page

LIST OF TABLES xi

LIST OF FIGURES. xvii

LIST OF APPENDICES xxiv

LIST OF SYMBOLS xxv

LIST OF SYMBOLS xxvi

Chapter

1 INTRODUCTION 1

2 THEORY. 2

2.1 Particle Physics 2

2.2 The Standard Model 3

2.2.1 Fermions 3

2.2.2 Bosons. 4

2.2.3 Theoretical Formalism. 5

2.2.4 Z^0 Bosons at the Tevatron. 5

3 EXPERIMENTAL APPARATUS 7

3.1 The Fermilab accelerators 7

3.1.1 The Pre-accelerator. 9

3.1.2 The Linac and Booster 10

3.1.3 The Main Injector. 12

3.1.4 The Antiproton Source 12

Chapter Page

3.1.5 Tevatron 13

3.2 The DØ Coordinate System 15

3.3 DØ Detector 19

3.3.1 The Central Tracking System 19

3.3.1.1 The Silicon Microstrip Tracker 21

3.3.1.2 The Central Fiber Tracker 23

3.3.1.3 Superconducting Solenoid Magnet 24

3.3.1.4 Preshower Detectors 25

3.3.2 The Calorimeter System 26

3.3.2.1 Interaction within Calorimeter 27

3.3.2.2 The Calorimeter 28

3.3.2.3 Calorimeter Resolution 31

3.3.3 The Muon System 32

3.3.4 Luminosity Monitor 40

3.3.5 DØ Trigger System 42

4 EVENT RECONSTRUCTION 47

4.1 Track Reconstruction 48

4.2 Vertex Reconstruction 49

4.3 Electron and Photon Reconstruction 50

4.4 Jet Reconstruction 54

4.5 Missing Transverse Energy ($\not\!\!E_T$) Determination 56

4.6 Muon Reconstruction 56

5 MUON IDENTIFICATION 57

5.1 Muon Reconstruction 57

Chapter Page

5.2 Muon Momentum Measurement 59
5.3 Muon Identification 60
5.3.1 Muon Type 61
5.3.2 Muon Quality 61
5.3.3 Track Quality 63
5.3.4 Muon Isolation 64
5.4 Muon Efficiency 66
5.4.1 Tag and probe method 67
5.4.2 Efficiency of muon system reconstruction 67
5.4.3 Efficiency of muon central track reconstruction 68
5.4.4 Efficiency of isolation requirements 69
6 MUON MOMENTUM OVERSMEARING 72
6.1 Muon Smearing Method 73
6.2 Data and MC Samples and Selections 77
6.3 Computation of the Oversmearing Parameters 80
6.4 Systematic Uncertainties 83
6.5 Results of Muon Oversmearing Parameters 83
7 MEASUREMENT OF THE ZZ CROSS SECTION 88
7.1 Introduction 88
7.1.1 Z Boson Pair Production 88
7.1.2 Signal, Background and Studies 90
7.2 Data Sample 93
7.2.1 Data Set 93
7.2.2 Data Quality 93

Chapter Page

7.2.3 Trigger and Trigger Efficiency Estimation 95

7.2.4 Integrated Luminosity 96

7.3 Identification and Definition 97

7.3.1 Good Muons 97

7.3.2 Muon ID Efficiencies 98

7.3.3 Good Electrons 100

7.3.4 ICD Electrons 101

7.4 Event Selection 102

7.4.1 $\mu\mu\mu\mu$ Channel 102

7.4.1.1 Selections 102

7.4.1.2 Muon Quality and Charge 104

7.4.2 *eeee* Channel 116

7.4.2.1 Selection 116

7.4.3 $ee\mu\mu$ Channel 121

7.4.3.1 Selection 121

7.5 Monte Carlo Simulations 126

7.5.1 Monte Carlo Samples 126

7.5.2 Acceptance in Four Lepton Channels 128

7.6 Backgrounds 136

7.6.0.1 Muon Fakerate 137

7.6.0.2 Electron Fakerate 142

7.6.0.3 QCD background Determination in four lepton channels 144

7.6.1 QCD Background Crosscheck in $\mu\mu\mu\mu$ Channel 148

Chapter Page

7.6.2 $t\bar{t}$ Background 149

7.6.3 Migration 150

7.6.4 Beam Halo and Cosmic Muon Background 150

7.7 Systematic Uncertainties 152

7.8 Results 164

7.8.1 Total Background and Expected Signal 164

7.8.2 Figures of Combined Channel 165

7.8.3 Cross Section 172

8 SUMMARY AND CONCLUSION 174

REFERENCES 176

APPENDICES 185

LIST OF TABLES

Table Page

2.1 The fermions of the standard model. 4

2.2 The bosons of the standard model. 4

3.1 Calorimeter energy resolution parameters for the DØcalorimeter. . . 32

3.2 The depth of the calorimeter layers at normal incidence $\theta = \pi/2$. . . 32

3.3 Summary of drift tubes and scintillator counts in muon detectors. . . 39

5.1 Overview of different muon types. 61

5.2 Definition of isolation working points. 66

6.1 Combinations of data taking epochs and MC versions from which oversmearing parameters have been computed. 73

6.2 Remaining $J/\psi \to \mu^+\mu^-$ and $Z/\gamma^\star \to \mu^+\mu^-$ data events after selection cuts with respect to each Data Epoch. 77

6.3 Remaining $J/\psi \to \mu^+\mu^-$ and $Z/\gamma^\star \to \mu^+\mu^-$ MC events after selection cuts with respect to the MC version. The version numbers refer to different reconstruction releases. 77

6.4 Request IDs correspondent to the J/ψ MC version. 77

6.5 Request IDs correspondent to the $Z/\gamma^\star$ ALPGEN Monte Carlo version. 78

6.6 Summary of all the oversmearing parameters for different track selections, types of tracks, by Double-Gaussian and Single-Gaussian for RunIIb3 + RunIIb4 data versus RunIIb3 MC. 84

Table Page

6.7 χ^2/N_{DoF} values from muon oversmearing parameters using different track quality. Values are compared for Double Gaussian (DG) and Single Gaussian (SG). 85

7.1 Branching Fractions for Z boson decays. 91

7.2 Run IIa and IIb luminosities. 97

7.3 Run IIa and IIb: Cut flow for $\mu\mu\mu\mu$ Data. 103

7.4 Run IIa and IIb: Cut flow for $\mu\mu\mu\mu$ weighted MC signal. 104

7.5 Number of events for different charges for Run II $\mu\mu\mu\mu$ data with cut flow. 105

7.6 Number of events for different charges for Run II $\mu\mu\mu\mu$ MC signal with cut flow. 105

7.7 Number of muons versus nseg types for Run II $\mu\mu\mu\mu$ data with cut flow. 106

7.8 The fraction (%) of each nseg type for Run II $\mu\mu\mu\mu$ MC signal with cut flow. 106

7.9 Run IIa: Cut flow for $eeee$ data for four sub-channels ($= 2$, $= 3$, ≥ 4 central electrons with no ICD electrons, and with 1 ICD electron). . 117

7.10 RunIIb: Cut flow for $eeee$ data for four sub-channels ($= 2$, $= 3$ or ≥ 4 central electrons with no ICD electrons, and with 1 ICD electron). 117

7.11 Run IIa: Cut flow for $ee\mu\mu$ data for three channels ($= 0$, $= 1$ or ≥ 2 central electrons). 122

7.12 RunIIb: Cut flow for $ee\mu\mu$ data for three subchannels ($= 0$, $= 1$ or ≥ 2 central electrons). 122

7.13 Run IIa PYTHIA GEANT p17 MC samples. 127

7.14 Run IIb PYTHIA GEANT p20 MC samples. 127

7.15 Cut flow for Run II $\mu\mu\mu\mu$ MC signal showing cumulative and exclusive $Acc \times \epsilon$. 129

7.16 $Acc \times \epsilon$ values for $\mu\mu\mu\mu$ Channel. 129

Table Page

7.17 Run IIa: Cut flow for *eeee* MC signal showing cumulative and exclusive $Acc \times \epsilon$ for four subchannels (= 2, = 3 or $\geq$ 4 central electrons, = 1 ICD electron). 130

7.18 Run IIb: Cut flow for *eeee* MC signal showing cumulative and exclusive $Acc \times \epsilon$ for three subchannels (= 2, = 3 or $\geq$ 4 central electrons, = 1 ICD electron). 131

7.19 Run IIa: $Acc \times \epsilon$ values for *eeee* channel. 132

7.20 Run IIb: $Acc \times \epsilon$ values for *eeee* channel. 132

7.21 Run IIa: Cut flow for $ee\mu\mu$ MC signal showing cumulative and exclusive $Acc \times \epsilon$ for three subchannels (= 0, = 1 or $\geq$ 2 central electrons). 133

7.22 Run IIb: Cut flow for $ee\mu\mu$ MC signal showing cumulative and exclusive $Acc \times \epsilon$ for three subchannels (= 0, = 1 or $\geq$ 2 central electrons). 134

7.23 Run IIa: $Acc \times \epsilon$ values in $ee\mu\mu$ channel.. 135

7.24 Run IIb: $Acc \times \epsilon$ values in $ee\mu\mu$ channel. 135

7.25 Expected QCD background in the 4e channel for each subchannel. . 145

7.26 Run IIa QCD background in the $ee\mu\mu$ channel for each subchannel. 148

7.27 Run IIb QCD background in the $ee\mu\mu$ channel for each subchannel. 148

7.28 $Acc \times \epsilon$ values for Z+jets MC. 149

7.29 Run IIb: Rejection factors against beam halo and cosmics. 151

7.30 Run IIa: relative uncertainties in the $\mu\mu\mu\mu$ channel for various efficiencies and backgrounds. The top eleven rows are systematic uncertainties, while the next two rows are statistical in nature and the total. 156

7.31 Run IIb: relative uncertainties in the $\mu\mu\mu\mu$ channel for various efficiencies and backgrounds. The top eleven rows are systematic uncertainties, while the next two rows are statistical in nature and the total. 156

Table Page

7.32 Run IIa: relative uncertainties in the *eeee* channel with 2 CC electrons for various efficiencies and backgrounds. The top nine rows are systematic uncertainties, while the next two rows are statistical in nature and the total. 157

7.33 Run IIa: Relative uncertainties in the *eeee* channel with 3 CC electrons for various efficiencies and backgrounds. The top nine rows are systematic uncertainties, while the next two rows are statistical in nature and the total. 157

7.34 Run IIa: Relative uncertainties in the *eeee* channel with 4 CC electrons for various efficiencies and backgrounds. The top nine rows are systematic uncertainties, while the next two rows are statistical in nature and the total. 158

7.35 Run IIa: Relative uncertainties in the *eeee* channel with 1 ICR electron for various efficiencies and backgrounds. The top nine rows are systematic uncertainties, while the next two rows are statistical in nature and the total. 158

7.36 Run IIb: Relative uncertainties in the *eeee* channel with 2 CC electrons for various efficiencies and backgrounds. The top nine rows are systematic uncertainties, while the next two rows are statistical in nature and the total. 159

7.37 Run IIb: Relative uncertainties in the *eeee* channel with 3 CC electrons for various efficiencies and backgrounds. The top nine rows are systematic uncertainties, while the next two rows are statistical in nature and the total. 159

7.38 Run IIb: Relative uncertainties in the *eeee* channel with 4 CC electrons for various efficiencies and backgrounds. The top nine rows are systematic uncertainties, while the next two rows are statistical in nature and the total. 160

7.39 Run IIb: Relative uncertainties in the *eeee* channel with 1 ICR electron for various efficiencies and backgrounds. The top nine rows are systematic uncertainties, while the next two rows are statistical in nature and the total. 160

Table Page

7.40 Run IIa: Relative uncertainties in the $ee\mu\mu$ channel with 0 CC electrons for various efficiencies and backgrounds. The top fourteen rows are systematic uncertainties, while the next two rows are statistical in nature and the total. 161

7.41 Run IIa: Relative uncertainties in the $ee\mu\mu$ channel with 1 CC electrons for various efficiencies and backgrounds. The top fourteen rows are systematic uncertainties, while the next two rows are statistical in nature and the total. 161

7.42 Run IIa: Relative uncertainties in the $ee\mu\mu$ channel with 2 CC electrons for various efficiencies and backgrounds. The top fourteen rows are systematic uncertainties, while the next two rows are statistical in nature and the total. 162

7.43 Run IIb: Relative uncertainties in the $ee\mu\mu$ channel with 0 CC electrons for various efficiencies and backgrounds. The top fourteen rows are systematic uncertainties, while the next two rows are statistical in nature and the total. 162

7.44 Run IIb: Relative uncertainties in the $ee\mu\mu$ channel with 1 CC electrons for various efficiencies and backgrounds. The top fourteen rows are systematic uncertainties, while the next two rows are statistical in nature and the total. 163

7.45 Run IIb: Relative uncertainties in the $ee\mu\mu$ channel with 2 CC electrons for various efficiencies and backgrounds. The top fourteen rows are systematic uncertainties, while the next two rows are statistical in nature and the total. 163

7.46 Contribution from non-negligible backgrounds in the $\mu\mu\mu\mu$ channel, plus expected signal and number of observed events. Errors are statistical followed by systematic. 164

7.47 Contribution from non-negligible backgrounds in the $eeee$ channels, plus expected signal and number of observed events. Errors are statistical followed by systematic. 165

7.48 Contribution from non-negligible backgrounds in the $ee\mu\mu$ channels, plus expected signal and number of observed events. Errors are statistical followed by systematic. 166

Table Page

A.1 Statistical errors associated with oversmearing parameters for different track selections, types of tracks, for Run IIb3 + Run IIb4 data versus Run IIb3 MC. 186

A.2 Systematic errors associated with oversmearing parameters for Medium and Loose track selections, types of tracks, for Run IIb3 + Run IIb4 data versus Run IIb3 MC. 187

A.3 Systematic errors associated with oversmearing parameters for New Medium track selections, types of tracks, for Run IIb3 + Run IIb4 data versus Run IIb3 MC. 188

C.1 Run IIa and IIb: Cut flow for $\mu\mu\mu\mu$ Data with loose DQ. 193

C.2 Run IIa: Cut flow for *eeee* data with loose DQ for four sub-channels ($= 2$, $= 3$, ≥ 4 central electrons with no ICD electrons, and with 1 ICD electron).. 193

C.3 RunIIb: Cut flow for *eeee* data with loose DQ for four sub-channels ($= 2$, $= 3$ or ≥ 4 central electrons with no ICD electrons, and with 1 ICD electron). 194

C.4 Run IIa: Cut flow for $ee\mu\mu$ data with loose DQ for three channels ($= 0$, $= 1$ or ≥ 2 central electrons).. 194

C.5 RunIIb: Cut flow for $ee\mu\mu$ data with loose DQ for three subchannels ($= 0$, $= 1$ or ≥ 2 central electrons).. 195

C.6 Contribution from non-negligible backgrounds in the $\mu\mu\mu\mu$ channel with loose DQ, plus expected signal and number of observed events. Errors are statistical followed by systematic. 195

C.7 Contribution from non-negligible backgrounds in the *eeee* channels with loose DQ, plus expected signal and number of observed events. Errors are statistical followed by systematic. 196

C.8 Contribution from non-negligible backgrounds in the $ee\mu\mu$ channels with loose DQ, plus expected signal and number of observed events. Errors are statistical followed by systematic. 197

LIST OF FIGURES

Figure Page

2.1 Feynman diagram of the tree level Drell-Yan process. 6

3.1 The Fermilab Accelerator complex overview. 8

3.2 The Fermilab Accelerator complex chain. 9

3.3 (a) Cockcroft-Walton pre-accelerator. (b) Power supply and electronic schematic of the Cockcroft-Walton voltage ladder. 10

3.4 Linac RF cavity. 11

3.5 Total Run II integrated luminosity from 2001 to 2011. Run II is the period of time for which the data of this analysis was collected. 15

3.6 The rectangular coordinate system at DØ. 16

3.7 Side view of the DØdetector. 20

3.8 The DØCentral Tracking system. 21

3.9 The DØSilicon Microstrip Tracker. 22

3.10 Cross section of SMT barrel. 23

3.11 a) Overview of CFT. b) Cross section view of axial and stereo layers. 24

3.12 Cross section of Preshower. 25

3.13 Cross section view of the track system. 26

3.14 Overview of the DØcalorimeter. 28

3.15 Unit cell of Calorimeter. 30

3.16 One quarter of the DØdetector with distribution of transverse η and longitudinal segmentation of the calorimeter cells. 31

3.17 Exploded view of the muon wire chambers. 34

Figure Page

3.18 Exploded view of the muon scintillation detectors. 35

3.19 The $y-z$ view of the DØmagnetic field in kG with both the toroidal and solenoidal magnets are at full current.. 36

3.20 Geometry of the PDT deck (top) and cell (bottom) of DØCentral Muon system. 37

3.21 Cross sectional view of a MDT. 37

3.22 Drawing the MDT layout for one layer. 38

3.23 a) Frontal view of one end of the forward pixel layer, and b) photograph of one side of the C layer pixel counters. 39

3.24 The Luminosity Monitor layout: a) $r-z$ view, and b) $r-\phi$ view. . 41

3.25 Overview of the DØtrigger and data acquisition systems. 43

3.26 Block diagram of the DØL1 and L2 trigger systems.. 44

5.1 Efficiencies of the loose, medium and mediumnseg3 muon quality in the muon system as functions of a) η_D and b) ϕ. 68

5.2 Efficiencies of the loose, newmedium, medium and tight muon quality in the tracking system as functions of a) η_{CFT}, b) z_0 and c) $\mathcal{L}$. 69

5.3 Efficiencies of the isolation criteria as functions of η_{CFT}, p_T and $\mathcal{L}$ (from top to bottom). 71

6.1 Comparison of different invariant masses between data and Monte Carlo without oversmearing.. 74

6.2 Data/MC comparison from $Z/\gamma^\star \to \mu^+\mu^-$ with original smearing. . . 75

6.3 χ^2 maps for $Z/\gamma^\star$ and J/ψ events with Type3 and trackmedium quality using II3+II4 Data vs II3 MC. 82

6.4 Data and MC invariant mass in central region ($|\eta_{CFT}| < 1.6$) before (left) and after (right) DG smearing using Run IIb3 MC vs Run IIb3+IIb4 data and trackmedium quality. 86

Figure Page

6.5 Data and MC invariant mass in the tail region before (left) and after (right) DG smearing using Run IIb3 MC vs Run IIb3+IIb4 data and trackmedium quality. 87

7.1 The dominant tree-level Feynman diagram for $q\bar{q} \to ZZ \to \ell^+\ell^-\ell'^+\ell'^-$. 89

7.2 The singly resonant Feynman diagram for $q\bar{q} \to ZZ \to \ell^+\ell^-\ell'^+\ell'^-$. . 90

7.3 The distribution of muon track ΔZ (cm), before and after the $\Delta Z < 3$ cm cut in data. 107

7.4 The muon p_T (GeV) distribution for leading, second, third and fourth muons, in order of p_T before the p_T cut in data. 108

7.5 The muon p_T (GeV) distribution for leading, second, third and fourth muons after the p_T cut in data. 109

7.6 The distribution of dimuon invariant mass (GeV) in data, after passing 4 good muons, ΔZ_{DCA}, isolation, p_T, opposite charge and dimass cuts (from left to right, top to bottom). Red bins show the best dimuon pair while blue shows the second pair. 110

7.7 The scatter plot of dimuon pair invariant mass (GeV) in data, after passing 4 good muons, ΔZ_{DCA}, isolation, p_T, opposite charge and dimass cuts. Red spots are same-sign dimuon pair while black spots are opposite-sign dimuon pair. The best dimuon pair is on x-axis. . . 111

7.8 Above, MC signal dimuon invariant mass (GeV) distribution after passing dimass cut with red indicating the best pair and blue the other pair; Bottom, MC signal dimuon invariant mass (GeV) of the best pair (x-axis) versus the other pair (y-axis) after passing four good muons cut and dimass cut, with black points for opposite-sign events and red points for same-sign events. 112

7.9 The p_T distributions of leading, second, third and fourth muons in $\mu\mu\mu\mu$ channel, with expected signal and backgrounds superimposed. (Based on Sec. 7.8, Z+jets background is too small to see in the 4μ channel comparing to Migration background.) 113

7.10 The η_D distributions of leading, second, third and fourth muons in the $\mu\mu\mu\mu$ channel, with expected signal and backgrounds superimposed. 114

Figure Page

7.11 The p_T distributions of leading Z/γ^* and second Z/γ^* in the $\mu\mu\mu\mu$ channel, with expected signal and backgrounds superimposed.. 115

7.12 The distributions of di-muon invariant mass with both best pair and the other pair included and four muon invariant mass in the $\mu\mu\mu\mu$ channel, with expected signal and backgrounds superimposed.. 115

7.13 The p_T distributions of leading, second, third and fourth muons in $eeee$ channel, with expected signal and backgrounds superimposed. . 118

7.14 The η_D distributions of leading, second, third and fourth muons in the $eeee$ channel, with expected signal and backgrounds superimposed. 119

7.15 The p_T distributions of leading Z/γ^* and second Z/γ^* in the $eeee$ channel, with expected signal and backgrounds superimposed.. 120

7.16 The distributions of di-muon invariant mass with both best pair and the other pair included and four muon invariant mass in the $eeee$ channel, with expected signal and backgrounds superimposed.. 120

7.17 The p_T distributions of leading, second, third and fourth muons in $ee\mu\mu$ channel, with expected signal and backgrounds superimposed.. 123

7.18 The η_D distributions of leading, second, third and fourth muons in the $ee\mu\mu$ channel, with expected signal and backgrounds superimposed. 124

7.19 The p_T distributions of leading Z/γ^* and second Z/γ^* in the $ee\mu\mu$ channel, with expected signal and backgrounds superimposed.. 125

7.20 The distributions of di-muon invariant mass with both best pair and the other pair included and four muon invariant mass in the $ee\mu\mu$ channel, with expected signal and backgrounds superimposed.. 125

7.21 Run IIa: Measured muon fakerates as a function of jet p_T with muons $p_T > 15$ GeV and all muons are isolated for different values of nseg. 138

7.22 Run IIa: Measured muon fakerates as a function of jet η_D with muons $p_T > 15$ GeV and all muons are isolated for different values of nseg. 139

Figure Page

7.23 Run IIb: Measured muon fakerates as a function of jet p_T with muons $p_T > 15$ GeV and all muons are isolated for different values of nseg. 140

7.24 Run IIb: Measured muon fakerates as a function of jet η_D with muons $p_T > 15$ GeV and all muons are isolated for different values of nseg. 141

7.25 Run IIa: Plot of the measured electron fakerates as a function of jet p_T (left) and as a function of jet η_D (right).. 142

7.26 Run IIb: Plot of the measured electron fakerates as a function of jet p_T (left) and as a function of jet η_D (right).. 143

7.27 Run IIa: Plot of the measured ICD electron fakerates as a function of jet p_T (left) and as a function of jet $|\eta_D|$ (right).. 143

7.28 Run IIb: Plot of the measured ICD electron fakerates as a function of jet p_T (left) and as a function of jet $|\eta_D|$ (right).. 144

7.29 Distributions of p_T for the leading, second, third and fourth leptons in data, expected signal and background. 167

7.30 Distributions of η_D for the leading, second, third and fourth leptons in data, expected signal and background. 168

7.31 Distributions of $Z's$ p_T for the lepton pairing with the highest and lowest $Z's$ p_T in data, expected signal and background. 169

7.32 Distribution of $\Delta\phi$ between the two leptons in each Z decay in data, expected signal and background.. 169

7.33 Distribution of dilepton invariant mass (left) and p_T of ZZ system (right) in data, expected signal and background. 170

7.34 Distribution of $\not\!\!E_T$ (left) and ΔR (right) between two leptons in each Z decay in data, expected signal and background. 170

7.35 Distribution of four lepton invariant mass in data, expected signal and background. 171

7.36 Distribution of 2D dilepton invariant mass in data, and expected signal. 171

Figure Page

7.37 $-ln(L)$ versus cross section (in pb) for the combined channels. 173

B.1 Data and reconstructed MC $Z/\gamma^{\star} \to \mu^{+}\mu^{-}$ invariant mass distribution (figures on the top) and (Data - MC)/σ (figures on the bottom) for the 3 type of tracks (from left to right: T1, T2 and T3) in case of *Medium track* selection. Data (dots) is compared with non-smeared MC (blue lines), smeared MC via Double Gaussian (red lines) and via Single Gaussian (green lines). 190

B.2 Data and reconstructed MC $Z/\gamma^{\star} \to \mu^{+}\mu^{-}$ invariant mass distribution (figures on the top) and (Data - MC)/σ (figures on the bottom) for the 3 type of tracks (from left to right: T1, T2 and T3) in case of *Loose track* selection. Data (dots) is compared with non-smeared MC (blue lines), smeared MC via Double Gaussian (red lines) and via Single Gaussian (green lines). 191

B.3 Data and reconstructed MC $Z/\gamma^{\star} \to \mu^{+}\mu^{-}$ invariant mass distribution (figures on the top) and (Data - MC)/σ (figures on the bottom) for the 3 type of tracks (from left to right: T1, T2 and T3) in case of *New Medium track* selection. Data (dots) is compared with non-smeared MC (blue lines), smeared MC via Double Gaussian (red lines) and via Single Gaussian (green lines).. 191

D.1 *eeee* candidate event display for the Run 223736. (Four lepton invariant mass 216.1 GeV) 200

D.2 *eeee* candidate event display for the Run 259028. (Four lepton invariant mass 194.7 GeV) 201

D.3 *eeee* candidate event display for the Run 248547. (Four lepton invariant mass 116.9 GeV) 202

D.4 *eeee* candidate event display for the Run 231347. (Four lepton invariant mass 273.6 GeV) 203

D.5 *eeee* candidate event display for the Run 268798. (Four lepton invariant mass 252.9 GeV) 204

D.6 $\mu\mu\mu\mu$ candidate event display for the Run 232216. (Four lepton invariant mass 347.2 GeV) (This event does not pass normal DQ) . . 205

Figure Page

D.7 $\mu\mu\mu\mu$ candidate event display for the Run 246915. (Four lepton invariant mass 218.6 GeV) 206

D.8 $\mu\mu\mu\mu$ candidate event display for the Run 248990. (Four lepton invariant mass 201.9 GeV) (This event does not pass normal DQ) . . 207

D.9 $\mu\mu\mu\mu$ candidate event display for the Run 248990. (Four lepton invariant mass 339.5 GeV) (This event does not pass normal DQ) . . 208

D.10 $\mu\mu\mu\mu$ candidate event display for the Run 259938. (Four lepton invariant mass 308.8 GeV) 209

D.11 $\mu\mu\mu\mu$ candidate event display for the Run 271330. (Four lepton invariant mass 274.9 GeV) 210

D.12 $\mu\mu\mu\mu$ candidate event display for the Run 222870. (Four lepton invariant mass 270.1 GeV) (This event does not pass normal DQ) . . 211

D.13 $ee\mu\mu$ candidate event display for the Run 208854. (Four lepton invariant mass 151.5 GeV) 212

D.14 $ee\mu\mu$ candidate event display for the Run 208914. (Four lepton invariant mass 359.1 GeV) 213

D.15 $ee\mu\mu$ candidate event display for the Run 243839. (Four lepton invariant mass 277.3 GeV) 214

D.16 $ee\mu\mu$ candidate event display for the Run 244006. (Four lepton invariant mass 235.5 GeV) 215

D.17 $ee\mu\mu$ candidate event display for the Run 244503. (Four lepton invariant mass 237.8 GeV) (This event does not pass normal DQ) . . 216

D.18 $ee\mu\mu$ candidate event display for the Run 260799. (Four lepton invariant mass 136.8 GeV) 217

LIST OF APPENDICES

Appendix Page

A STATISTICAL AND SYSTEMATIC ERRORS WITH OVERSMEARING PARAMETERS 185

B INVARIANT MASS DISTRIBUTIONS OF MUON OVERSMEARING PARAMETERS 189

C RESULTS WITH LOOSE DATA QUALITY 192

D EVENTS DISPLAY 198

LIST OF ABBREVIATIONS

SM	Standard Model
EM	Electromagnetic
EW	Electroweak
MET	Missing Transverse Energy
LM	Luminosity Monitor
SMT	Silicon Microstrip Tracker
CFT	Central Fiber Tracker
VLPC	Visible Light Photon Counter
CPS	Central preshower
FPS	Forward preshower
CC	Central Calorimeter
EC	Endcap Calorimeter
FH	Fine Hadronic
CH	Coarse Hadronic
ICD	Inner cryostat Detector
MIP	Minimum Ionizing Particles
PDT	Proportional Drift Tube
MDT	Mini Drift Tube
L1, L2, L3	Level 1, 2, 3 Trigger
DQ	Data Quality
TFW	The Trigger Framework
DAQ	Data Acquisition System

DCA	Distance of Closet Approach
PV	Primary Vertex
ICR	intercryostat region
JES	Jet Energy Scale
MC	Monte Carlo
BF	Branching Fraction
CL	Confidence Level

CHAPTER 1

INTRODUCTION

The field of high energy physics studies the fundamental particles of our universe and the interactions between them. With new discoveries at the subatomic level, our knowledge has improved as achievable energies have increased. The Tevatron collider, one of the highest energy particle accelerators in the world, collided protons with antiprotons at a center-of-mass energy of 1.96 TeV. Z bosons are produced in many processes when protons and antiprotons collide and can be produced in pairs. This thesis presents measurement of the $p\bar{p} \to Z/\gamma^* \, Z/\gamma^* \to \ell^+\ell^-\ell'^+\ell'^-$ cross section with DØ, a general purpose detector which operated at the Tevatron.

This thesis is set out as follows. Chapter 2 introduces the standard model (SM) and the theoretical description of interactions. Chapter 3 gives a brief introduction of the experimental apparatus, the Tevatron and the DØ detector. Chapter 4 describes the event reconstruction. Chapter 5 and 6 discuss the muon identification and momentum oversmearing procedures. Data samples, Monte Carlo programs, backgrounds, uncertainties and all the analysis procedures are described in Chapter 7. Finally, results are summarized in Chapter 8. Appendices A and B show oversmearing parameters and invariant mass distributions including these parameters. Results with loose DQ are listed in Appendices C. Appendices **??** and D present some studies of the $Z + jets$ channel and event display of all final candidate events.

CHAPTER 2

THEORY

2.1 Particle Physics

It is well known that everyday life is properly described by Newton's laws of classical mechanics. However, the classical rules must be modified by special relativity for objects that travel at speeds comparable to the speed of light c. Furthermore, classical mechanics is superseded by quantum mechanics for objects that are very small (subatomic level). Since elementary particles are both fast and small their description falls under the domain of quantum field theory. Elementary particle physics basically studies the ultimate constituents of matter and the nature of the interactions between them.

Atoms are firstly found to be composed of smaller particles: electrons, protons and neutrons. However, after the discovery of neutrons, muons and pions, particle physics quickly became more complicated as more exotic particles were discovered such as neutrinos and kaons. Neutrons and protons are now known to be composed of more fundamental particles called quarks. The total number of known particles far exceeds the total number of known atoms in the periodic table. A very successful theory has developed which describes all the known particles from a few handfuls of elementary particles and a few particles responsible for their interactions. This theory is called the standard model (SM).

2.2 The Standard Model

The elementary particles can be separated into two classes: fermions and bosons. Fermions make up the matter particles and have half-integer spin. Bosons are the force mediating particles and have integer spin. No more than one fermion can occupy the same quantum state (Pauli exclusion principle). Bosons, however, do not have this restriction.

2.2.1 Fermions

Fermions are subdivided into two types known as leptons and quarks. Each type has three generation of particles. Each generation has the same properties except the mass. Each generation of leptons has a charged lepton and one neutral lepton called neutrino. For example, charged electron and neutral electron-neutrino are the first generation leptons. Each generation of quarks has a quark with +2/3 charge and another with -1/3 charge. For example, up quark and down quark are the first generation quarks. Every charged fermion has an anti-particle with the same mass and opposite charge. Each quark has an additional degree of freedom called color, and labeled red, green or blue. Quarks can only exist in color singlet states and thus can not be isolated. Quarks bound in color singlet states form the hadrons which are found in nature. Table 2.1 is a summary of all the fermions.

	Generation I		Generation II		Generation III		Charge	Interactions
Leptons	Electron	e	Muons	μ	Tau	τ	-1	EM, Weak
	Neutrino	ν_e	Neutrino	ν_μ	Neutrino	ν_τ	0	Weak
Quarks	Up	u	Charm	c	Top	t	2/3	Strong, EM, Weak
	Down	d	Strange	s	Bottom	b	-1/3	Strong, EM, Weak

Table 2.1: The fermions of the standard model.

2.2.2 Bosons

Interactions between the leptons and quarks are mediated by particles called gauge bosons. The known fundamental forces are four: strong, weak, electromagnetic and gravity. The SM does not include gravity. In addition, the SM includes another interaction which gives mass to particles which is usually considered as part of electroweak (EW) interactions. This interaction, the Higgs force, is mediated by the Higgs boson, which has already been observed both at ATLAS and CMS experiments of CERN LHC pp collider with a four lepton resonance at a mass of about 125 GeV [1, 2]. This is consistent with the SM Higgs boson. Tevatron experiments in Fermilab has also confirmed this observation [3]. Table 2.2 is a summary of all the forces and their corresponding gauge bosons.

Force	Particle	Symbol	Spin
Strong	Gluon	g_α	1
Electromagnetic	Photon	γ	1
Weak	W boson	W^+, W^-	1
	Z boson	Z^0	1
Higgs	Higgs boson	H	0

Table 2.2: The bosons of the standard model.

2.2.3 Theoretical Formalism

The SM is a field theory built from quantum mechanics and relativity theory. The Lagrangian of the SM is invariant with respect to local gauge transformations. The SM is based on the symmetry group $SU(3)_C \otimes SU(2)_L \otimes U(1)_Y$. The $SU(3)_C$ group represents the strong interactions and its generators are the eight gluons g_α ($\alpha = 1, 2, 3...8$). The $SU(2)_L \otimes U(1)_Y$ group represents the EW interactions, whose generators are the $W^\pm$ boson, the Z^0 boson and the photon. In the EW interactions, each kind of lepton or quark is represented in the Lagrangian by two fields: left and right. Left handed fermions form doublets of leptons $\binom{\nu_e}{e_L}$, $\binom{\nu_\mu}{\mu_L}$, $\binom{\nu_\tau}{\tau_L}$ and quarks $\binom{u_L}{d_L}$, $\binom{c_L}{s_L}$, $\binom{t_L}{b_L}$. The $SU(2)_L$ group transforms the components of doublets into each other. Right handed fermions $e_R, \mu_R, \tau_R, u_R, c_R, t_R, d_R, s_R, b_R$ are singlets and do not participate in this interaction.

2.2.4 Z^0 Bosons at the Tevatron

At the Tevatron, which collided protons and antiprotons will be described in an upcoming chapter 3.1.5, Z^0 bosons are produced via the leading order annihilation of a quark antiquark pair (Drell-yan process [4]) shown in Figure 2.1. The higher order processes contain an additional gluon or quark in the final state which will appear as a "jet" of hadrons.

While a Z^0 has a mass of about 91 GeV and a width of around 2.5 GeV, corresponding to a lifetime about 10^{-24} s in the rest frame. After that, the Z^0 will decay to a fermion anti-fermion pair. It couples to all the 12 fermions in the SM and branching fractions to quarks and leptons are given by the PDG [5] at Tab. 7.1.

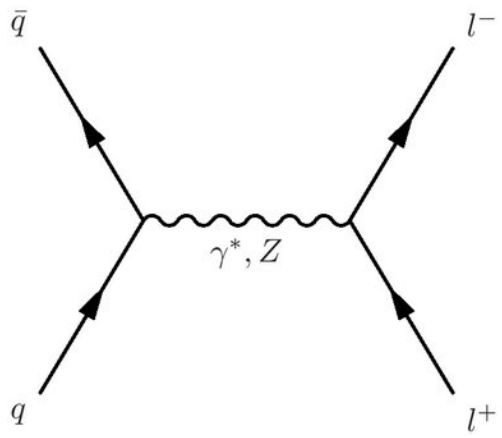

Figure 2.1: Feynman diagram of the tree level Drell-Yan process.

In the hadron collider, the electron and muon channels are experimentally the easiest to identify, with significant background to the quark channels from other (QCD) processes. The muon and electron channels are studied in this thesis. By measuring the 4-momenta of these muons, it is possible to reconstruct the mass of the Z^0 and other properties. More detailed information about Z boson pair production and branching fractions used in this thesis are discussed in Section 7.1.1 and 7.1.2.

CHAPTER 3

EXPERIMENTAL APPARATUS

This chapter will describe the Tevatron collider of Fermi National Accelerator Laboratory (Fermilab) as well as the DØ detector. Before shutting down on Sep. 29, 2011, the Tevatron was the world's highest energy proton-antiproton collider. The detector, called DZero (DØ) [7], contains many detection subsystems that identified the different types of particles emerging form the collisions. This chapter gives an overview of the experimental apparatus.

3.1 The Fermilab accelerators

The Tevatron collider physics program is comprised of two stages: Run I and Run II. From 1992 to 1996, the Run I collider program, operating at a center-of-mass energy level of 1.8 TeV, delivered to DØ and CDF experiments an integrated luminosity in excess of 160 pb^{-1}, which was sufficient to discover the top quark [6]. To continue the discovery of new particles, a series of improvements were made to provide a total energy of 1.96 TeV at the collision points and a higher instantaneous luminosity. The Run II collider program began in 2001 and delivered a total integrated luminosity of 12 fb^{-1}.

The Fermilab accelerator complex is a chain of different accelerators, Figure 3.1 shows an overview of the accelerator complex [8]. The Tevatron is the final stage in a sequence of seven accelerators [9]. A Cockcroft-Walton pre-accelerator, a linear

accelerator (Linac) and a synchrotron (Booster) provide a source of 8 GeV protons. The antiproton De-buncher and Accumulator are two components of the Antiproton Source. The Main Injector serves as the final boosting stage before injecting protons and antiprotons into the Tevatron Ring Synchrotron. It also provides the necessary source of energetic protons which are needed in the Antiproton Source.

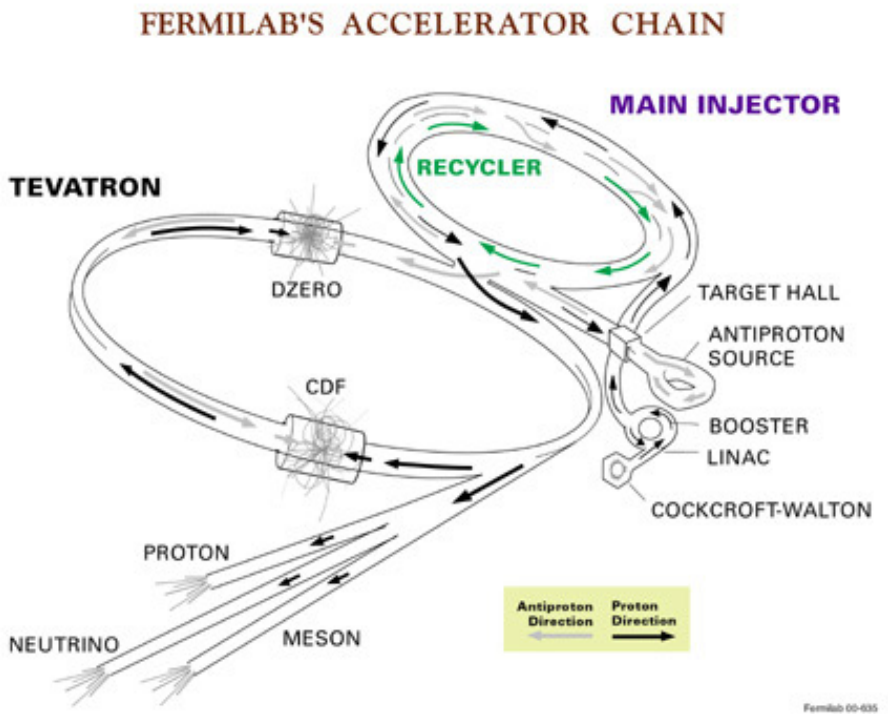

Figure 3.1: The Fermilab Accelerator complex overview.

When enough antiprotons have been accumulated, the Main Injector loads first protons and then antiprotons into the Tevatron. The protons move clockwise around the ring and the antiprotons go counterclockwise. Each beam in the Tevatron moves in a helix around the other. This allows the beams to share the same beam pipe and magnets without colliding into one another. Once the Tevatron is loaded with both beams, beams are accelerated to 980 GeV.

The beam is then subjected to a number of quality controls to improve its properties. Once the beams are stable, low-beta quadrupole magnets are used to focus the beams for collisions at the point B0 where the CDF detector resides and point D0 (Fig. 3.2) where the DØ detector resides.

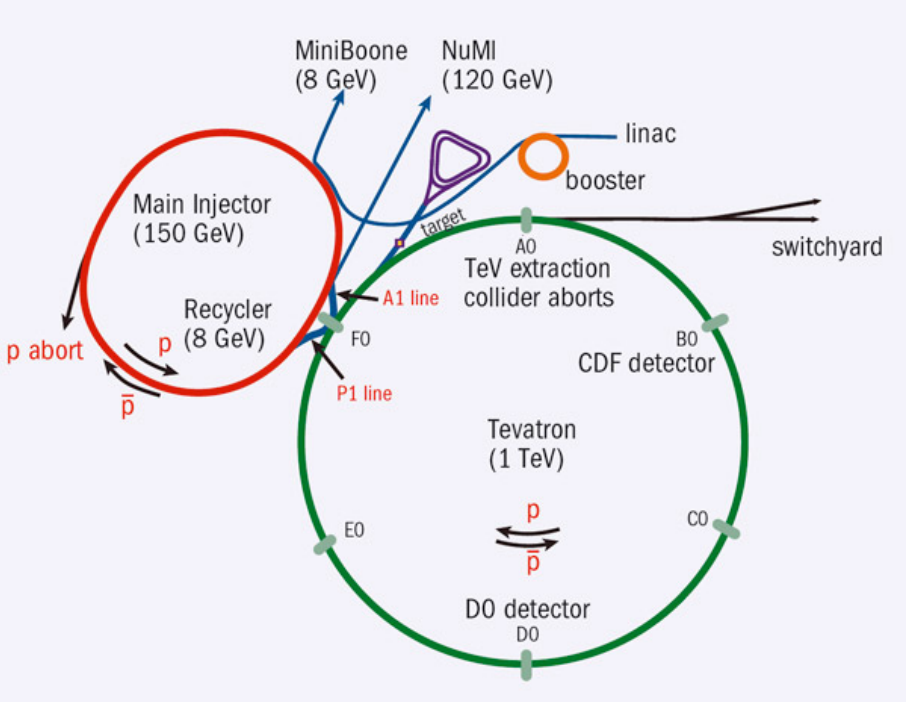

Figure 3.2: The Fermilab Accelerator complex chain.

3.1.1 The Pre-accelerator

The Cockcroft-Walton pre-accelerator [9, 10] shown in Fig. 3.3(a), provides the first stage of acceleration. Inside the device, hydrogen gas (H_2) enters a magnetron surface plasma source. Due to the electric field between anode and cathode, the electrons are stripped away from the hydrogen atoms to create a plasma. The positively charged hydrogen ions then strike the surface of the cathode to collect extra

electrons and thereby form negatively charged hydrogen ions (H^-), each consisting of two electrons and one proton. The ions are accelerated by a positive voltage and reach an energy of 750 KeV. The energy is generated by a combination of capacitors and diodes as show in Fig. 3.3(b). After exiting the Cockcroft-Walton device, the H^- travel through a transfer line. Before entering the Linac the continuous stream of H^- ions passes through a single gap radio frequency (RF) cavity which bunches the beam at the RF frequency of the Linac (201.24 MHz).

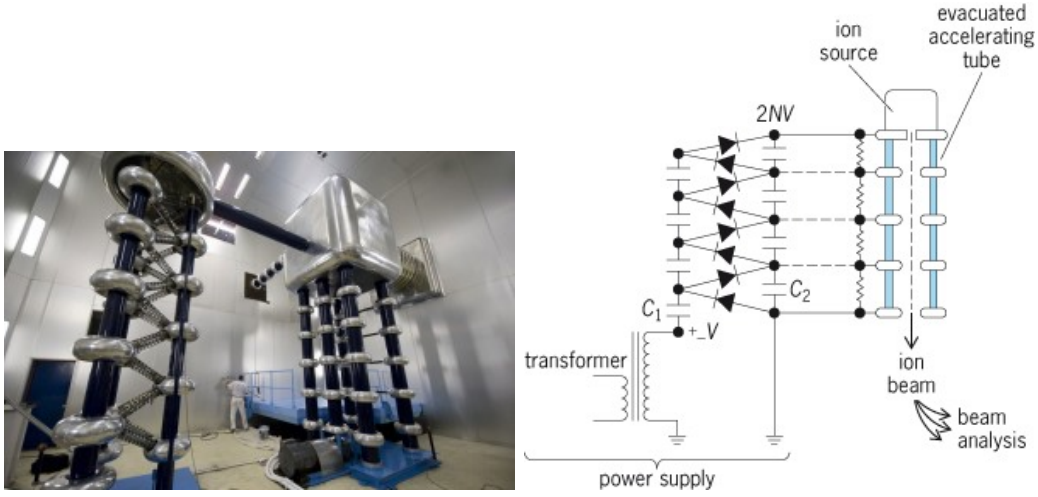

a.) b.)

Figure 3.3: (a) Cockcroft-Walton pre-accelerator. (b) Power supply and electronic schematic of the Cockcroft-Walton voltage ladder.

3.1.2 The Linac and Booster

After being boosted to 750 KeV, the ions are injected into the Linac [10, 12], a linear accelerator which is approximately 150 meter long. Oscillating electric fields accelerate the negative hydrogen ions to 400 MeV.

In this stage, the H^- ions are accelerated with RF cavities (Figure 3.4). The RF cavities [13] are contained within a collection of steel tanks which hold drift tubes separated from each other by gaps. Within the drift tubes, the ions are shielded from the reversed field. So, ions are not accelerated inside the drift tubes. Quadrupole magnets within the tube are used to focus the beam. Once the ions come out of the drift tubes, they experience a positive field gradient, which accelerates ions between the gaps.

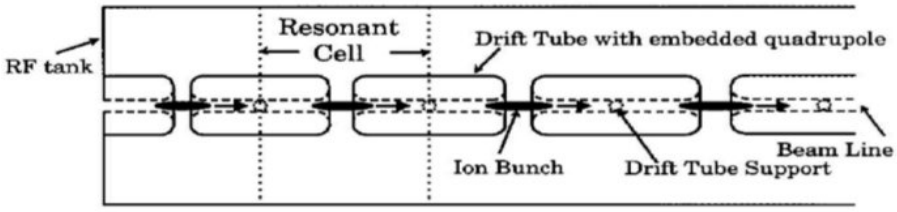

Figure 3.4: Linac RF cavity.

After passing through the Linac, the H^- ions enter the Booster, the first synchrotron in the accelerator chain. The Booster is a circular accelerator with a diameter of 151 meters, that uses magnets to bend the beam of protons in a circular path. The H^- ions pass through a carbon foil, which removes the two electrons, leaving only the positively charged protons. The Linac continuously supplies the H^- ions until approximately 3×10^{12} protons accumulate in the Booster. The protons in the Booster are then accelerated from 400 MeV to 8 GeV in about 0.033 seconds. The velocities of protons are boosted from about half the light speed (c) to $0.99c$. The protons are then transferred into the Main Injector, the next synchrotron in the chain.

3.1.3 The Main Injector

The Main Injector [10], a circular synchrotron with a diameter of 1 km, accelerates particles and transfers beams. It has four main functions:

- Accelerates protons from 8 GeV to 150 GeV
- Produces 120 GeV protons, which are used for antiproton production [Section 3.1.4]
- Receives antiprotons from the Antiproton Source and increases their energy to 150 GeV
- Injects protons and antiprotons into the Tevatron

Inside the Main Injector tunnel is installed another synchrotron, the Antiproton Recycler (green ring in Fig. 3.2). It stores antiprotons from the accumulator, which were then injected into the Tevatron.

3.1.4 The Antiproton Source

The Antiproton Source [10, 15] has three major components: the Target Station for producing antiprotons, the Debuncher for conditioning the antiprotons from the target and the Accumulator for storage of the antiprotons.

The Main Injector delivers 120 GeV protons to the Target Station made with nickel. This produces a shower of secondary particles, including many antiprotons, at many different angles and with a large spread in particle momentum. A lithium

lens is used to focus the beam in one direction. The particles then pass through a bending magnet to remove positively charged particles and be sent to the Debuncher.

Both the Debuncher and Accumulator are located in a rounded-triangle shaped tunnel with a circumference of about 500 m. The particles coming from the Target Station have widely varying momentum. However, their velocities are all essentially relativistic. Therefore, lower energy antiprotons will complete an orbit around the Debuncher in a shorter time than the high energy antiprotons. By adjusting the phase of the RF cavities, the momentum spread of the particles is reduced. Debunching takes about 100 milliseconds after which the beam can be transferred to the Accumulator.

On average, for every 1 million protons that hit the nickel target, only about 20 antiprotons can be gathered. Therefore, it is necessary to store antiprotons until a sufficient amount has been generated to be transferred into the Main Injector. The purpose of the Accumulator is to mainly stack 8 GeV antiprotons over many hours from the Debuncher. A process called stochastic cooling is used in both the Debuncher and Accumulator to reduce the spread in momentum and position of the antiprotons. Cooling the antiproton beam reduces its size and makes it very bright. When a sufficient number of antiprotons has been accumulated (order of 10^{12}), they are transported to the Recycler for additional cooling and accumulation before injecting into the Tevatron.

3.1.5 Tevatron

The Tevatron [10, 16] is the final stage in the accelerator complex, which has a circumference of 6.28 km (radius of 1 km). It is made of over 1000 superconducting

quadrupoles and dipole magnets, which can provide a magnetic filed of 4.2 Tesla (T). Each superconducting magnet contains over 42,000 miles of wire. These wires are made of NbTi (Niobium Titanium) and must be cooled to 4.6 Kelvin by liquid helium. Protons and antiprotons are accelerated to 980 GeV, leading to a center-of-mass collision energy of 1.96 TeV.

Protons and antiprotons travel in bunches in opposite directions while sharing the same beam pipe. A full revolution takes about 21 μs. The Tevatron injects 36 bunches of both protons and antiprotons for each store. The 36 bunches are not uniformly distributed in the Tevatron, instead they are grouped into three super-bunches, with 12 bunches in each super-bunch. Overall, this leads to a time structure where bunches of protons and antiprotons collide at 1.7 MHz or 0.59 μs spacing between bunches [17].The beams cross each other at the centers of the CDF and DØ detectors located inside the Tevatron tunnel, creating bursts of new particles.

The period of time from the first collisions until collisions are stopped is called the store. As the store progresses the beam becomes less focused and the luminosity diminishes. During a store, more antiprotons are being stacked in the Accumulator and Recycler for the next store.

The rate at which interactions happen is measured with a quantity called the instantaneous luminosity. This quantity is given in $\mathrm{cm}^{-2}\mathrm{s}^{-1}$. After the upgrade, the accelerator is able to deliver a luminosity up to 4×10^{32} $\mathrm{cm}^{-2}\mathrm{s}^{-1}$. Actually, we will use integrated luminosity more in the analysis, which means we are adding up the instantaneous luminosity to cumulate total of particle collisions over the entire collider run. It is usually measured in inverse picobarns (pb^{-1}). Before shutting down, the Run II collider program delivered more than 12 fb^{-1} of data [18]. Figure 3.5 shows the integrated luminosity per week and the total integrated luminosity for Run II as a function of time from March 2001.

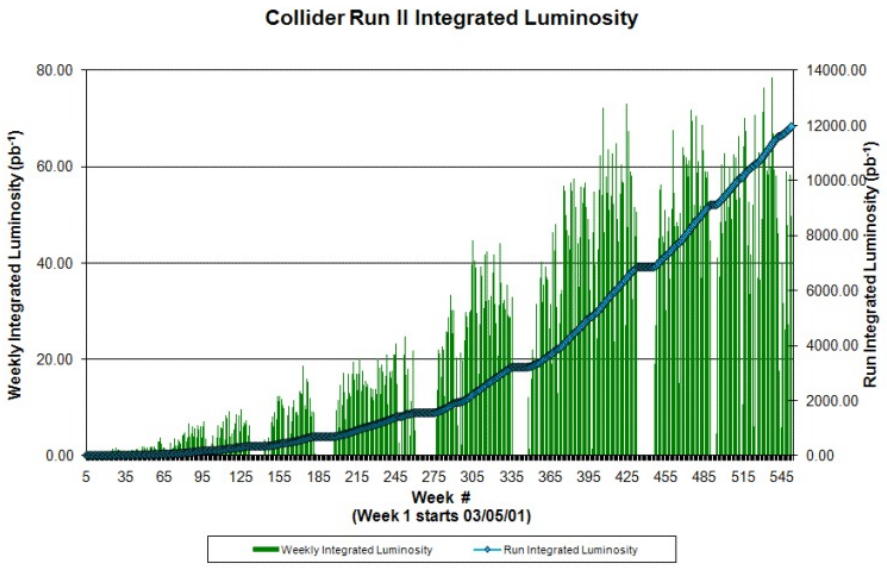

Figure 3.5: Total Run II integrated luminosity from 2001 to 2011. Run II is the period of time for which the data of this analysis was collected.

3.2 The DØ Coordinate System

In this section, we discuss some common conventions and useful definitions. Unless otherwise stated, the following conventions and notations will be assumed through the rest of the thesis. All quantities which involve the speed of light c are normalized that $c = 1$ [14].

The DØ Cartesian coordinate system (Fig. 3.6) is defined such that the z axis points along the proton beam direction, the y axis points vertically upwards, and the x axis lies in the horizontal plane, pointing to the center of the accelerator ring, to correspond to a right-handed system. The origin is defined as $(x, y, z) = (0, 0, 0)$.

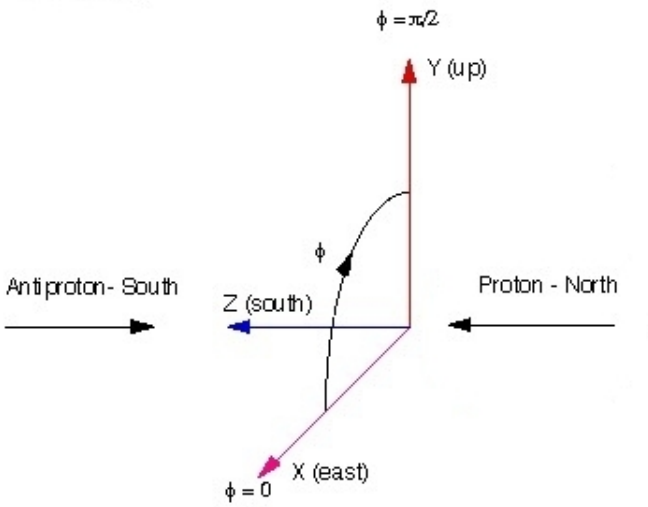

Figure 3.6: The rectangular coordinate system at DØ.

However, it is more useful to work in a spherical coordinates (r, ϕ, θ). Here, r denotes the magnitude of a point with respect to the origin,

$$r = \sqrt{x^2 + y^2 + z^2} \tag{3.1}$$

The azimuthal angle ϕ,

$$\phi = \arctan \frac{y}{x} \tag{3.2}$$

spans 0 to 2π. The polar angle θ,

$$\theta = \arccos(\frac{z}{\sqrt{x^2 + y^2 + z^2}}) \tag{3.3}$$

is measured from the z axis as usual.

The Lorentz transformation from the lab frame to the frame moving along the z-direction can be written as

$$p'_z = p_z \cosh y - E \sinh y \tag{3.4}$$

$$E' = -p_z \sinh y + E \cosh y \tag{3.5}$$

where y is rapidity. An advantage of rapidity is that the boost along the z-direction just adds a constant. It can be expressed as

$$y = \frac{1}{2} \ln \frac{1 + \beta \cos \eta}{1 - \beta \cos \eta} \tag{3.6}$$

where $\beta = p/E$. In the limit $\beta \to 1$, we can define pseudo-rapidity as

$$\eta = \frac{1}{2} \ln \frac{1 + \cos \theta}{1 - \cos \theta} = -\ln \tan(\frac{\theta}{2}) \tag{3.7}$$

which is a good approximation for Tevatron energies and is widely used.

The momentum of particles undergoing elastic scattering which go down the beam pipe is not measured, and therefore it is difficult to determine the total longitudinal component of momentum summed over all particles after a collision. The total transverse component of momentum before $p\bar{p}$ collision is negligibly small. We can require that the total transverse component of the momentum of the system be zero before and after a collision. We therefore define the following quantity, transverse momentum,

$$p_T = p \sin \theta = p_x^2 + p_y^2 \tag{3.8}$$

We determine p_z from p_T using the relation $p_T/p_z = \tan\theta$, solving for p_z in terms of θ we get

$$p_z = p_T \sinh\eta \tag{3.9}$$

$$p_x = p_T \cos\phi \tag{3.10}$$

$$p_y = p_T \sin\phi \tag{3.11}$$

And the total momentum can be written as,

$$p^2 = p_x^2 + p_y^2 + p_z^2 = p_T^2 + p_z^2 = p_T^2(1 + \sinh^2\eta) \tag{3.12}$$

Sometimes it is useful to use the transverse component of energy E_T defined as,

$$E_T^2 = p_x^2 + p_y^2 + m^2 = p_T^2 + m^2 = E^2 - p_z^2 \tag{3.13}$$

and will be equal to $E\sin\theta$ in the limit $\beta \to 1$.

An angular distance between two objects is often expressed in terms of

$$\Delta R = \sqrt{(\Delta\phi)^2 + (\Delta\eta)^2} \tag{3.14}$$

where $|\Delta\phi| < \pi$. The variable ΔR is Lorentz invariant,

Proton and antiproton bunches have length. For this reason the interaction point has a spread in z of roughly 25 cm. Therefore, there are two different η. "Physics η" represents the η of a particle from its production point and "detector η" is from the origin point. We will use η to denote the physics η and η_D to denote detector η. The interaction point in r has a small width of order of 0.1 cm and therefore detector and physics ϕ are essentially identical.

3.3 DØ Detector

The DØ detector [19] is a large multi-purpose detector designed to identify and precisely measure the four momenta of particles. After successful operation in Run I, the detector was significantly upgraded before the start of the Run II physics program. A 2T solenoidal magnet was added and the central tracking detectors were upgraded with a new fiber tracker and silicon microstrip tracker. The forward muon system was also substantially upgraded, providing more robust detectors and enhanced triggering capability, while additional scintillation counters were added to the central muon system. Below, we will describe the detector based on Run II. Figure 3.7 shows an overview of the detector.

The DØ detector is quite large; the entire assembly is about 13 m high $\times$ 11 m wide $\times$ 17 m long with a total weight of about 5500 tons. It has a nested structure, which is typical for most collider detectors. The three major subsystems of the DØ detector, from inner to outer radius, are:

- The Central Tracking System - Records angles and p_T of charged particles
- The Calorimeter - Identifies and measures the energy of EM and hadronic showers
- The Muon System - Identifies and measures the momenta of muons

3.3.1 The Central Tracking System

In the inner layer, the beam crossing point is covered by the central detector [19] (Fig. 3.8), which is embedded in a superconducting solenoid with a mag-

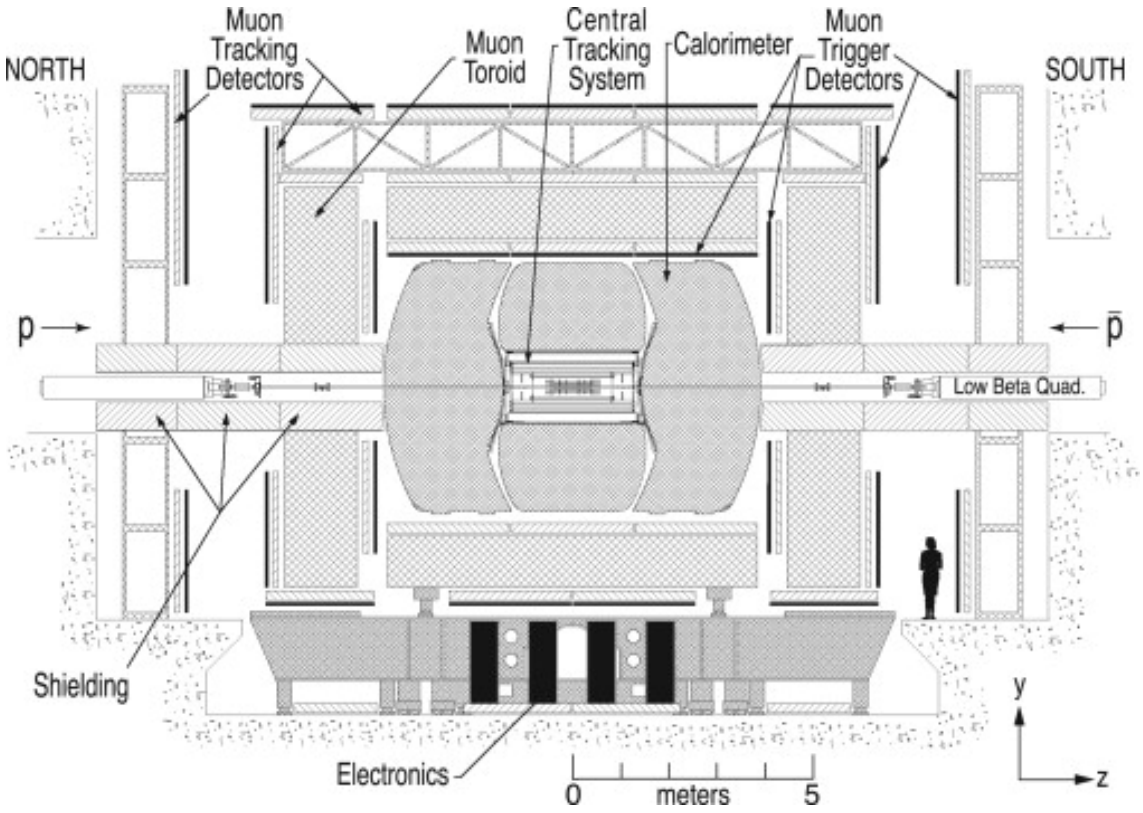

Figure 3.7: Side view of the DØ detector.

netic field of 2 T. The central detector is mainly comprised of two independent subsystems:

- The Silicon Microstrip Tracker (SMT)
- The Central Fiber Tracker (CFT)

The tracking system helps with particle identification. For example, a charged particle such as a muon or an electron should leave a track in the tracking system. Additionally, jets made mostly of many pions will be associated with many tracks. Another important use of the tracking system is to measure the momentum of a

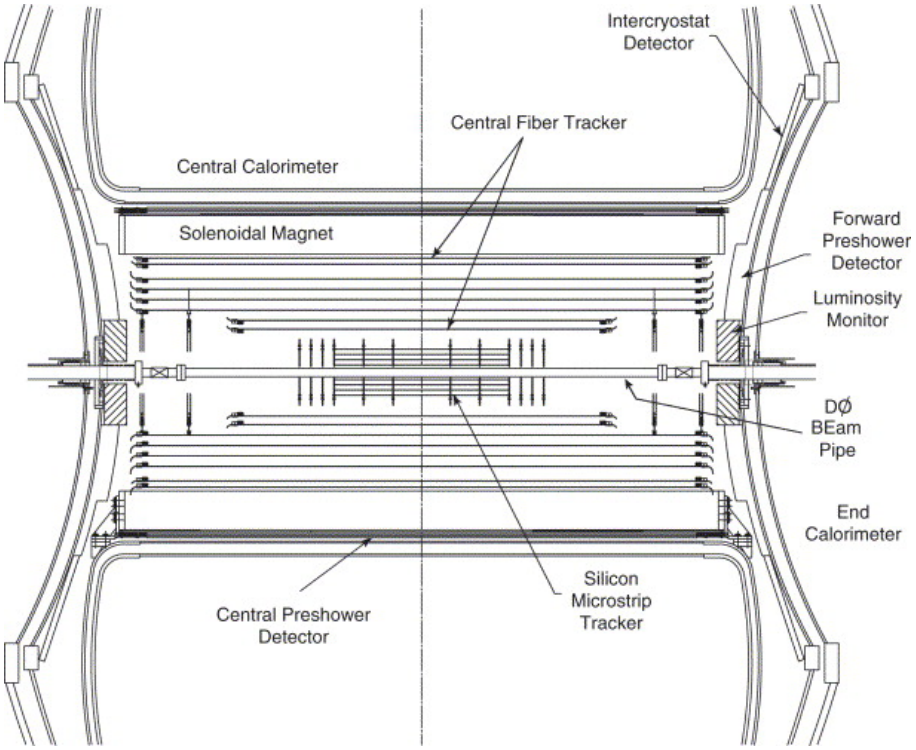

Figure 3.8: The DØ Central Tracking system.

charged particle. The curvature R of charged particle with charge q and a component of momentum p_T perpendicular to a magnet field is given as

$$R = \frac{p_T}{qB} \tag{3.15}$$

and so the p_T/q of a particle can be inferred from its curvature.

3.3.1.1 The Silicon Microstrip Tracker

The Silicon Microstrip Tracker [19, 20] (Fig. 3.9) is the first detector encountered by particles from collisions. It consists of 6 barrel detectors surrounding the beam line and 12 "F-disks" in the plane transverse to the beam direction. It uses both

single and double sided silicon microstrip detectors with expected hit resolution in $r\phi$ in of μm.

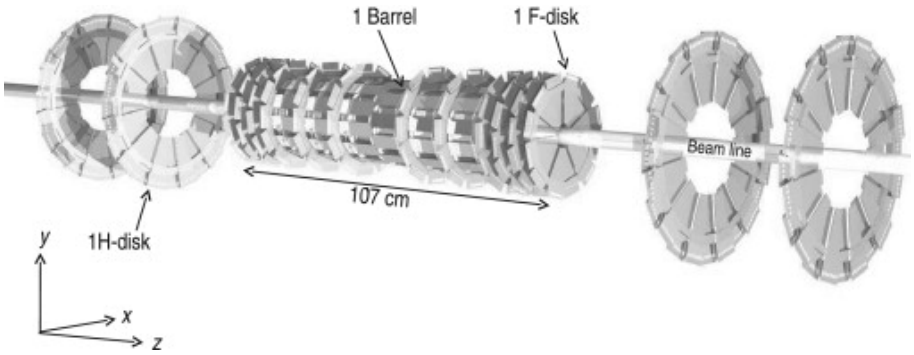

Figure 3.9: The DØ Silicon Microstrip Tracker.

A barrel is 6 cm long and measures the $r-\phi$ coordinates. In general, the barrels are used to identify particles with small η. Each barrel has four readout layers, which are divided into two sublayers. Figure 3.10 shows the cross section of barrel layers. F-disks measure $r-z$ and $r-\phi$ coordinates. It contains 12 double sided silicon microstrip detectors. To provide coverage in pseudo-rapidity up to $|\eta| \leq 3$, the SMT has in the forward and backward regions two large diameter "H-disks". The F-disks are located at $|z| = 12.5$, 25.3, 38.2, 43.1, 48.1 and 53.1 cm. The barrels end at $|z| = 38.1$ cm and are capped of by an F-disk. The H-disks are located at $|z| = 100.4$ and 121.0 cm. Note that, two H-disks were removed when "layer 0" was added during Run IIb.

The SMT strip pitch of 50 to 80 μm provides a high spatial resolution to allow a precise reconstruction of the primary vertex and an accurate measurement of the distance of closest approach of the tracks.

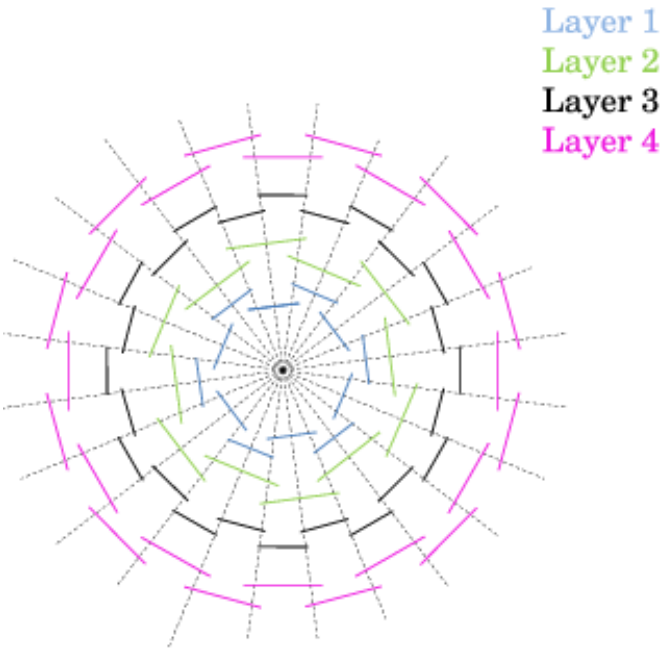

Figure 3.10: Cross section of SMT barrel.

3.3.1.2 The Central Fiber Tracker

The Central Fiber Tracker (CFT) [14, 19, 21] (Fig. 3.11) surrounds the SMT. It consists of layers of 835 μm diameter scintillating fibers mounted on eight concentric support cylinders and occupies the radial space from 20 to 52 cm from the center of the beam pipe. The two innermost cylinders are 1.66 m long, and the outer six cylinders are 2.52 m long. The layers form doublets. Each cylinder supports one doublet layer of fibers oriented along the beam direction (axial layers) and a second doublet layer at a stereo angle of alternating $\pm 3^{\circ}$ with respect to the beam direction (stereo layers).

The two layers of fibers are offset by half fiber width to provide improved coverage. The small fiber diameter gives the CFT a cluster resolution of about 100

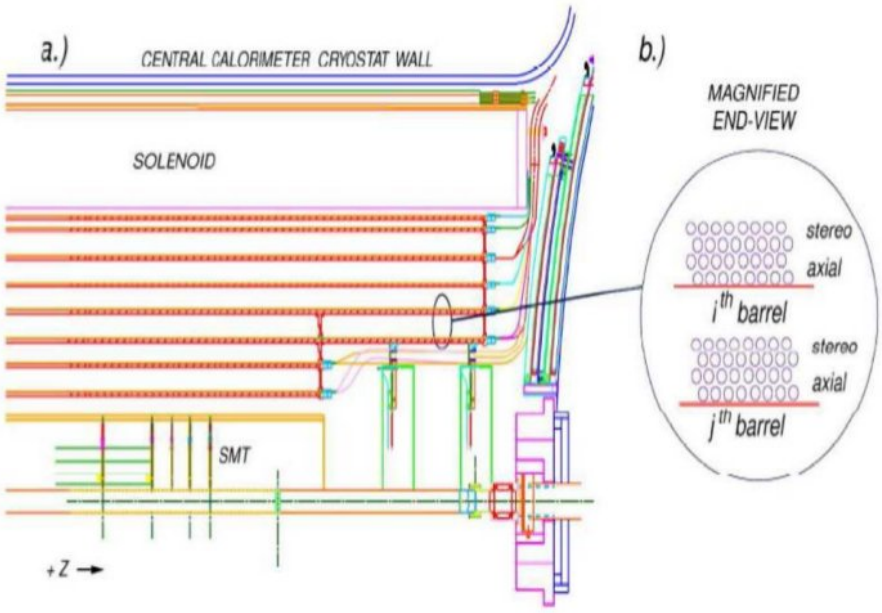

Figure 3.11: a) Overview of CFT. b) Cross section view of axial and stereo layers.

μm per doublet layer. The CFT data combined with the SMT measurements make possible track reconstruction and momentum measurement up to $|\eta| \leq 2.0$. The Scintillating fiber are attached to transport fibers that carry light to photodetectors. Ionizing particles that pass through a fiber produce on average of 10 photons. The photons are then detected with a Visible Light Photon Counter (VLPC) which converts the light into an electronic signal.

3.3.1.3 Superconducting Solenoid Magnet

The CFT is surrounded by the Solenoid Magnet [19] (Fig. 3.8), which is 2.8 m in length, 1.42 m in diameter, with a mean thickness of 60 cm. The momenta of charged particles are determined from their curvature in the 2 T magnetic field. The magnet windings are made of niobium-titanium superconducting wire and are

encased in an aluminum cylinder. The magnet is cooled to 4.2 Kelvin with liquid helium.

3.3.1.4 Preshower Detectors

The last detectors before the calorimeters are the preshower detectors [19]. They are designed to assist the tracker by providing precise position measurements and to assist the calorimeter by early energy sampling of the shower. Additionally, the preshower detectors provide discriminating power to help distinguish electrons and photons from muons and pions.

The preshower scintillators are triangular shaped (Fig. 3.12). This arranges scintillator layers without creating any dead space and thereby improves the accuracy of position measurements. The center of each scintillator carries a wavelength shifting fiber which collects the light created by passing charged particles. The light is transmitted via clear fibers to VLPCs for readout.

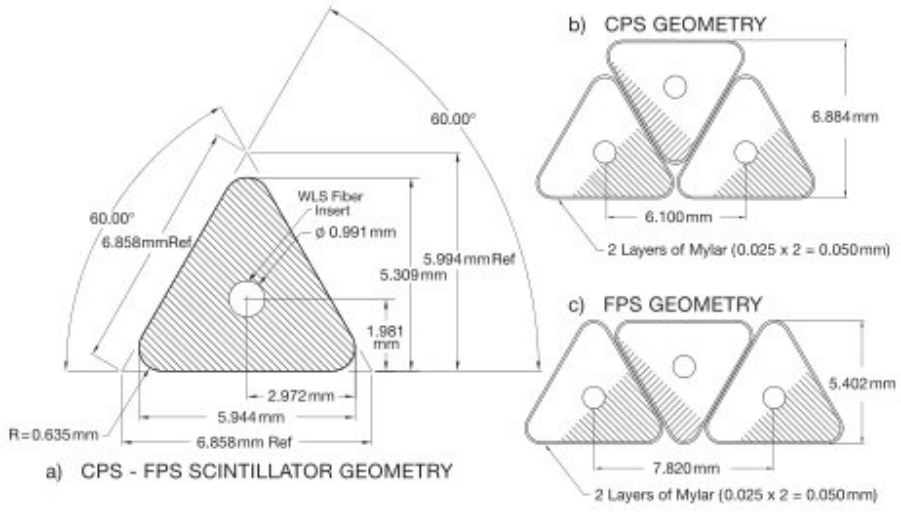

Figure 3.12: Cross section of Preshower.

The CPS is located in the 5 cm gap between the solenoid and the central calorimeter, covering the region $|\eta| < 1.3$ (Fig. 3.13). The scintillating layers are arranged in an axial $u - v$ geometry, with a u stereo angle of 23.8° and a v stereo angle of 24°. Each layer has a total number of 2560 readout channels.

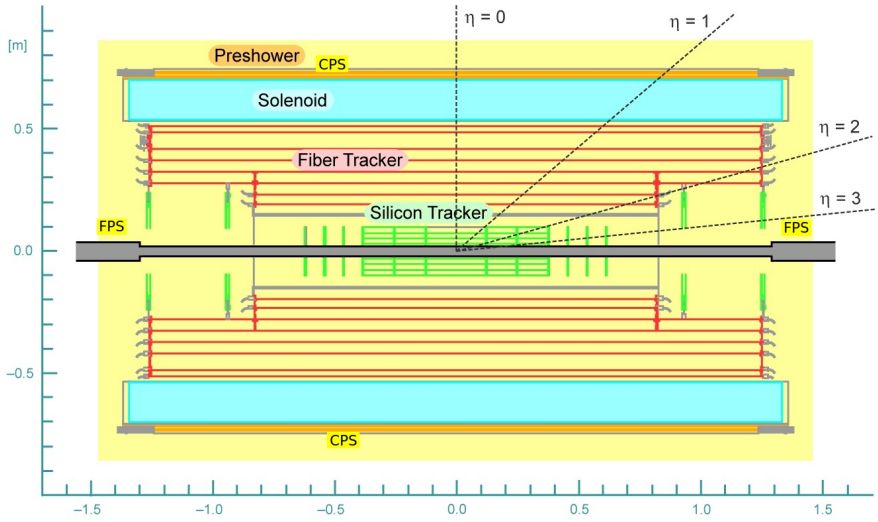

Figure 3.13: Cross section view of the track system.

The two FPS are attached to the faces and end of calorimeters and covering a region $1.1 < |\eta| < 2.5$ (Fig. 3.13). Each detector consists of an upstream double layer of scintillator strips, following by a lead-stainless-steel absorber layer and another double layer of scintillator strips behind it.

3.3.2 The Calorimeter System

The calorimeter system [19] was designed to measure the energy of electrons, photons and jets by inducing them to produce electromagnetic and hadronic showers. It also is used to help identify electrons and photons. The calorimeter sys-

tem is segmented longitudinally into electromagnetic (measure energy of electrons and photons) and hadronic (measure energy of hadrons) calorimeters. Energies are measured, while particles are absorbed after interactions with the material of the calorimeter. Muons only deposit a small amount of energy due to ionization. Neutrinos deposit no energy in the detector, but the absence of energy deposition results in a momentum imbalance in the transverse plane, which is called the missing transverse energy ($\not\!\!E_T$).

3.3.2.1 Interaction within Calorimeter

Electrons and photons interact with matter by pair production $\gamma \rightarrow e^+e^-$ and bremsstrahlung $e \rightarrow e\gamma$. Each new electron or photon interacts in the same way, creating a cascade of particles called a shower until the total mean energy per particle falls below a threshold. The effective energy loss of an electron or photon, as a function of depth x, moving through matter is:

$$E(x) = E_0 e^{-x/X_0} \tag{3.16}$$

where E_0 is the originating particles starting energy and X_0 is the radiation length of the material in which the shower develops.

Hadronic particles such as pions and kaons interact with matter primarily through the strong nuclear force. These interactions produce pions, both charged $\pi^{\pm}$ and neutral π^0. The neutral pions decay promptly to photons which produce an EM shower. The charged pions continue producing more pions. A hadronic shower is a combination of a hadronic cascade and a EM cascade and develops over longer and

wider distance than a purely EM shower. The effective energy loss of a hadronic particle moving through matter is characterized by absorption length λ_0.

3.3.2.2 The Calorimeter

The calorimeter [19] consists of a central calorimeter (CC) covering roughly $|\eta_D| < 1.1$, two end calorimeters (EC) extending the coverage to $1.4 < |\eta_D| < 4.2$ and inter-cryostat detector (ICD) covering $1.1 < |\eta_D| < 1.4$. The CC and ECs are contained inside cryostats and maintained at temperature of 90 Kelvin. Figure 3.14 gives a overview of the whole calorimeter.

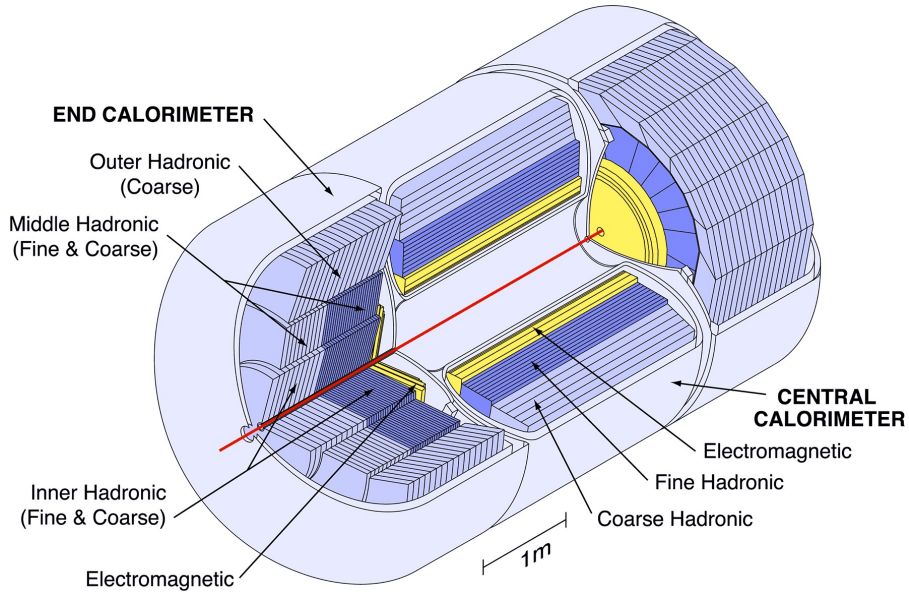

Figure 3.14: Overview of the DØ calorimeter.

The central and end calorimeters are subdivided into three layers: the electromagnetic (EM) layer which is designed to measure electrons, positrons and photons. The electromagnetic section has 4 layers. The fine (FH) layer and coarse (CH) layer

measure hadronic showers of the particles. FH has 2 to 4 layers and the CH has 1 to 3 layers.

Each layer is divided into small units called cells. The readout cells are arranged and sized such that each covers roughly an area of $\Delta\eta \times \Delta\phi = 0.1 \times 0.1$, comparable to the transverse size of showers: 1-2 cm for EM showers and 10 cm for hadronic showers.

A typical calorimeter cell is shown in Figure 3.15, with liquid argon (LAr) as the ionization medium. The primary absorber material is depleted uranium, with cooper and stainless steel used in the outer regions. Since uranium is very dense, the calorimeter is relatively compact. The absorber plates are separated from the signal boards by a LAr-filled gap of 2.3 mm. The signal boards consist of a copper pad sandwiched between two 0.5 mm thick pieces of G10.

During operation, the charged particles from the shower create electron-ion pairs via ionization of the liquid argon in the 2.3 mm gap between the absorber plate and a G10 board. The electron-ion pairs are collected by the electrodes in the presence of an applied electric field. Drift time is approximately 450 ns. Metal absorbers serve as cathodes and the readout boards are used as the anodes. The readout board consists of two sheets made of G10 material. A surface of each sheet is coated with an epoxy. The resistivity of the coated area is about 40 MΩ. Several unit cells are combined into one readout cell. The electrical signal from a readout cell is proportional to the energy deposited by the shower developed in the absorber plates of the unit cells.

All the layers in one 0.1×0.1 projection are called a tower. In total, there are on the order of 50,000 cells and 5,000 towers. The geometry, with towers of cells radiating from the center of the detector, is known as pseudo-projective, because

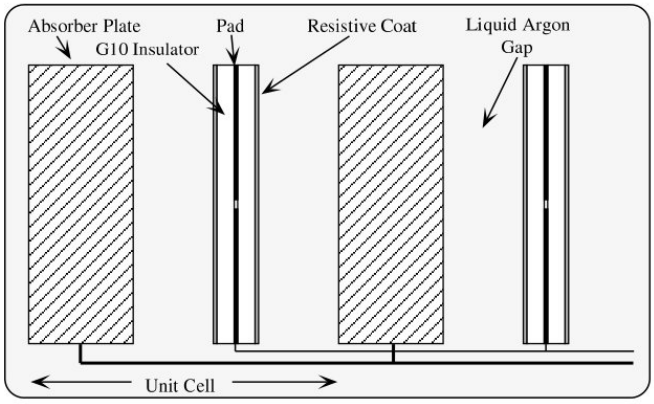

Figure 3.15: Unit cell of Calorimeter.

the cells lie along lines of pseudo-rapidity, but their boundaries do not. Figure 3.16 shows the η distribution in the calorimeter.

There are four separate depth layers for the EM modules in the CC and EC. In the CC, the layers are approximately 1.4, 2.0, 6.8 and $9.8X_0$ thick. In the EC, they are approximately 1.6, 2.6, 7.9 and $9.3X_0$ thick. The values given for the first layers include all material in the calorimeters themselves from the outer warm wall to the first active liquid argon gap. The detector components between the interaction region and the first active gap in the CC at $\eta = 0$ provide about $4.0X_0$ of material; those between the interaction region and the first active gaps of the ECs at $\eta = 2$ are $4.4X_0$ thick [19].

In the CC, the FH modules have three longitudinal gangings of approximately 1.3, 1.0 and 0.76 λ_A. The CH modules has a thickness of about 3.2 λ_A. Summarization of the depth of all the calorimeter layers is shown in Table 3.2.

Given that the calorimeter system is contained in three separate cryostats, it provides incomplete coverage in the region $0.8 < |\eta_D| < 1.4$ (Fig. 3.16). To reduce the loss of performance, additional layers of sampling detectors are added in the

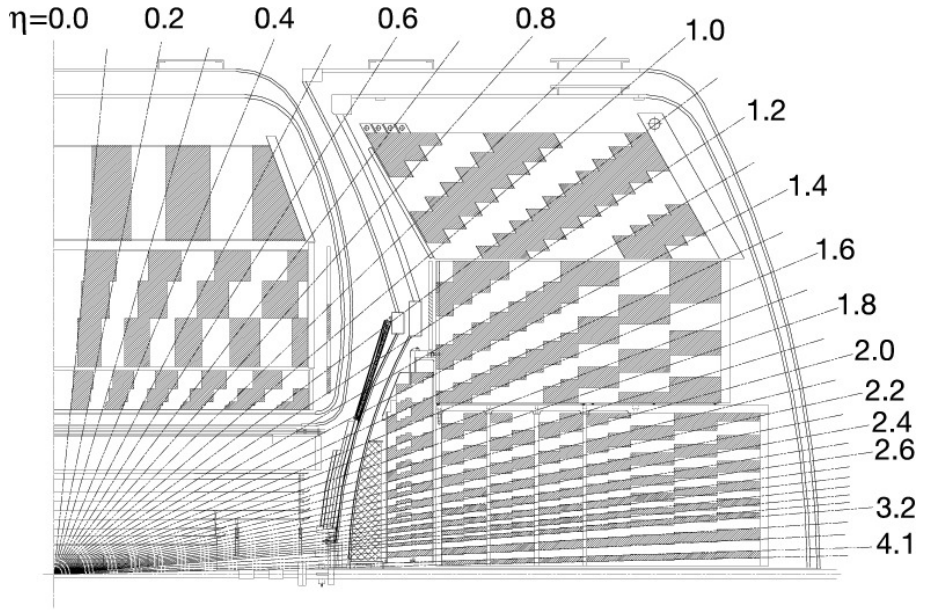

Figure 3.16: One quarter of the DØ detector with distribution of transverse η and longitudinal segmentation of the calorimeter cells.

form of scintillating counters between the CC and EC. These counters are called the Inter Cryostat Detector (ICD). They have exactly the same segmentation as CC and EC. In addition, separate single cell scintillator structures, called massless gaps, are installed inside the cryostat. The ICD allows sampling of the region between CC and EC to improve the energy resolution.

3.3.2.3 Calorimeter Resolution

The energy resolution of the electromagnetic and hadronic calorimeter modules were studied in Run I using pions and electrons from a test beam [22] with energies

between 10 and 150 GeV, typical energies for production in Tevatron collisions. The relative energy resolution can be parametrize as,

$$\frac{\sigma(E)}{E} = \sqrt{C^2 + (\frac{S}{\sqrt{E}})^2 + (\frac{N}{E})^2} \tag{3.17}$$

where S is statistical in its origin and corresponds to sampling fluctuations, N corresponds to the noise contribution and C is a constant due to calibration errors. The parameters for the DØ calorimeter are listed in Table 3.1.

Particle	S	N	C
e	0.135 ± 0.005 GeV$^{1/2}$	0.43 GeV	$0.012^{+0.0027}_{-0.0036}$
$\pi^{\pm}$	0.45 ± 0.04 GeV$^{1/2}$	0.98 GeV	0.032 ± 0.004

Table 3.1: Calorimeter energy resolution parameters for the DØ calorimeter.

The depth of each layer of the three calorimeter sections is shown in Table 3.2 in the units of *radiation length* X_0 and *absorption length* λ_0.

	EM	FH	CH
CC Depth	1.4,2.0,6.8,9.8 X_0	1.3,1.0,0.76 λ_0	3.2 λ_0
EC Depth	1.6,2.6,7.9,9.3 X_0	1.2,1.2,1.2 λ_0	3.6 λ_0

Table 3.2: The depth of the calorimeter layers at normal incidence $\theta = \pi/2$.

3.3.3 The Muon System

Muons originating from a $p\bar{p}$ collision penetrate the tracking system and the calorimeter essentially unperturbed, because they are close to being minimum ionizing particles (MIPs). The lifetime of muons is large enough to appear as stable particles to the detector. As a result, they will leave energy in the calorimeter, but

they will (mostly) make it through the calorimeter. The same is true for muons from cosmic rays. Thus, deflection in a magnetic field is the only way to measure muon energy.

The DØ muon detector is the outermost part of the DØ detector. It is placed around the calorimeter as shown in Fig. 3.7. It serves to identify and trigger on these muons and to provide a measurement of their momenta and charge which is independent of the central tracker but with poorer resolution. The muon detector is a cube and has rectangular symmetry. The calorimeter is contained within the cube. The four sides of the box parallel to the beam line are called WAMUS and the two sides perpendicular to the beam line are called FAMUS.To a rough approximation, the boundary is at $|\eta| = 1$.

The DØ muon detector consists of magnetic toroids and three layers of detectors of three different types: a system of proportional drift tubes (PDTs), mini drift tubes (MDTs) and scintillation counters. The PDTs measure z as well as both x and y, while MDTs measure z and either x or y (not both). The scintillators determine ϕ. Toroidal magnets and special shielding complete the muon system. Each subsystem has three layer called A, B and C, from the inner to the outer part of the detector. The magnetic system is divided into the central and two forward parts. The A layer is innermost and located between the calorimeter and the iron of the toroid magnet. B and C layers are located outside the iron. Each layer consists of a plane of scintillators and 4 plane of drift tubes in the A layer (3 in the bottom part) or 3 plane of drift tubes in both B and C layers. Figure 3.17 shows an expanded view of the drift chamber location for each layer while Figure 3.18 shows a similar view of the scintillator tiles.

The central part of the system uses PDTs covering $|\eta_D| < 1.0$ while the forward parts use MDTs extending the muon detection to $|\eta_D| = 2.0$. In the region directly

below the calorimeter, only partial coverage by muon detectors is possible as the support structure for the DØ detector is located in this region.

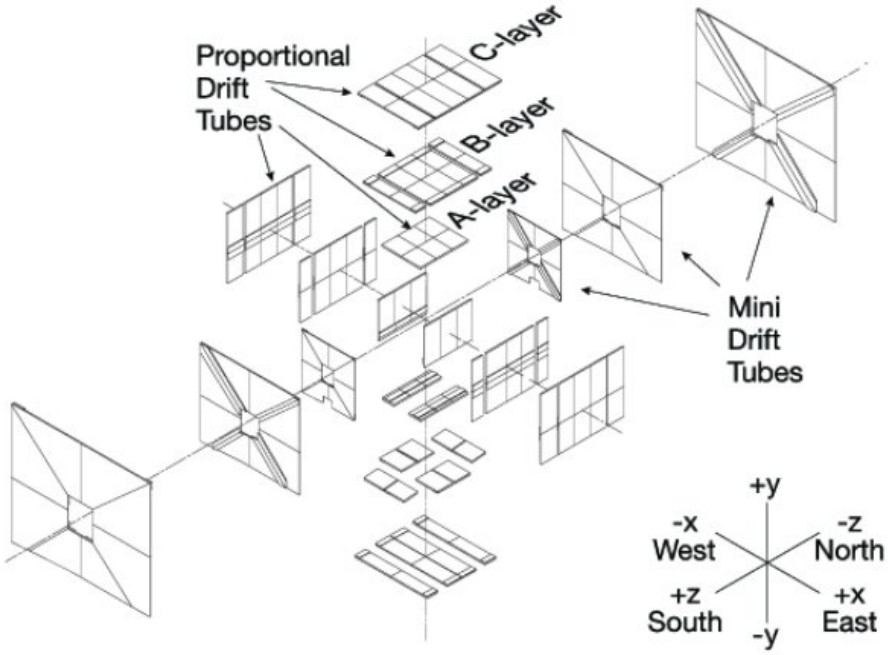

Figure 3.17: Exploded view of the muon wire chambers.

The average energy loss of a muon in the calorimeter is 1.6 GeV, and about 1.7 GeV in the iron. The momentum measurement made by the muon system is corrected for this energy loss. In the following sections, we will describe the subsystems of the muon spectrometer.

The Toroid Magnets. The toroids located between the A layer and B layer consists of three independent solid-iron toroid magnets with a magnetic field of about 1.8 T. The toroid magnets are built in four parts: two central pieces parallel to the beam pipe, and two end caps perpendicular to the beam pipe. The central toroid is a square annulus with 109 cm in thickness while the end toroids are 150 cm thick. In order to give access to the inner portions of the DØ detector, the central toroid

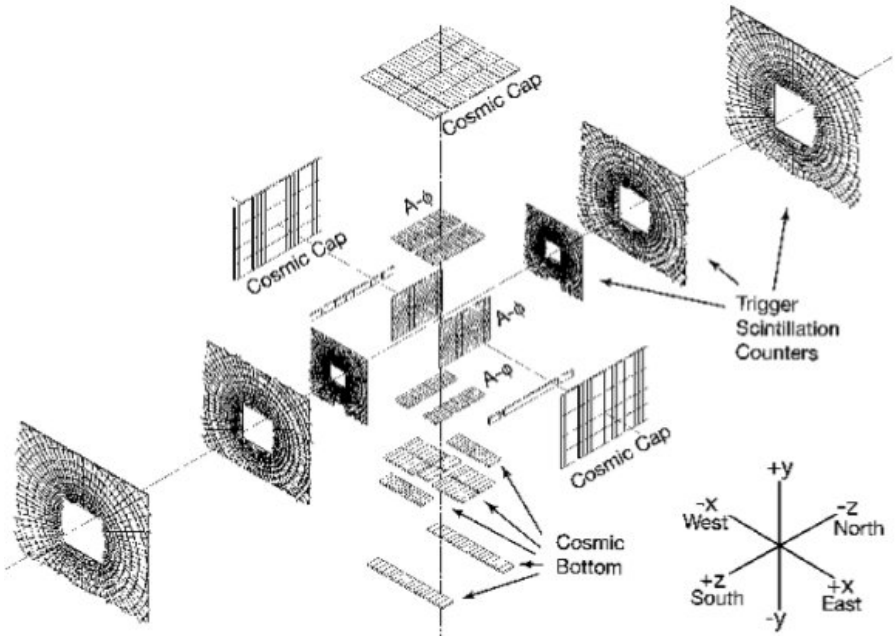

Figure 3.18: Exploded view of the muon scintillation detectors.

is split in 3 parts, a bottom section, east and west sections. The magnets cause the trajectories of the muon to bend in the $r - z$ plane. Due to the shape of the toroid, the magnetic field requires careful mapping to perform a proper measurement of the muon momentum. The magnetic field lines of the central solenoid are returned by the muon toroid magnets as shown in Fig. 3.19.

The Proportional Drift Tubes. The PDTs consist of an aluminum box 10 cm wide and 6.3 cm high, filled with gas. The ionization created by a passing charged particle is collected and amplified by a 50 μm gold-plated tungsten sense wire which runs through the center of the box. Vernier cathode pads are located above and below the wires to provide information on the hit position along the wire. The anodes operate at 4.7 kV and the cathodes at 2.3 kV. A measurement of the arrival time of the pulse from the sense wire and a calibration of the drift time of the gas allows for calculation of the drift distance from the sense wire with a 1 mm

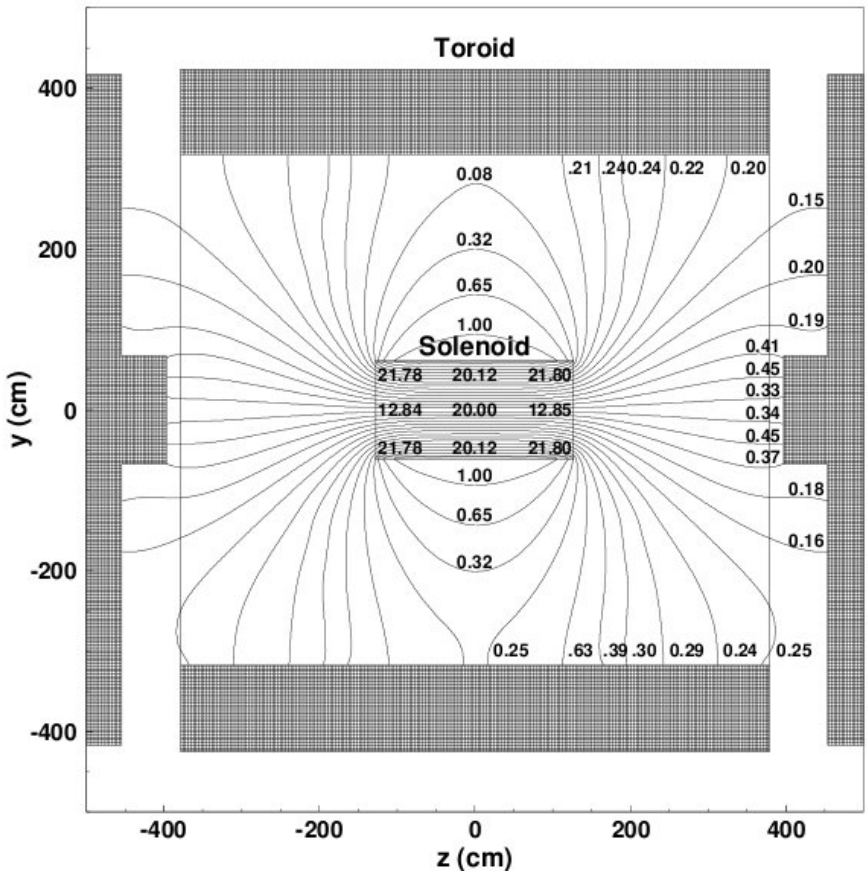

Figure 3.19: The $y - z$ view of the DØ magnetic field in kG with both the toroidal and solenoidal magnets are at full current.

resolution. A comparison of arrival time from adjacent wires provides a measurement of the position of the ionization along the wire with a 10-15 cm resolution.

PDTs are constructed of extruded aluminum coated with steel foil and filled with a mixture of 84% Argon, 8% CH_4 and 8% CF_4. The gas flow rate is 500 liters per hour. The drift velocity is about 10 cm/μs, for a maximum drift time of about 450 ns. Figure 3.20 shows the geometry of deck and drift cells of PDTs. There are 6624 PDTs cells installed in the central (WAMUS) detector.

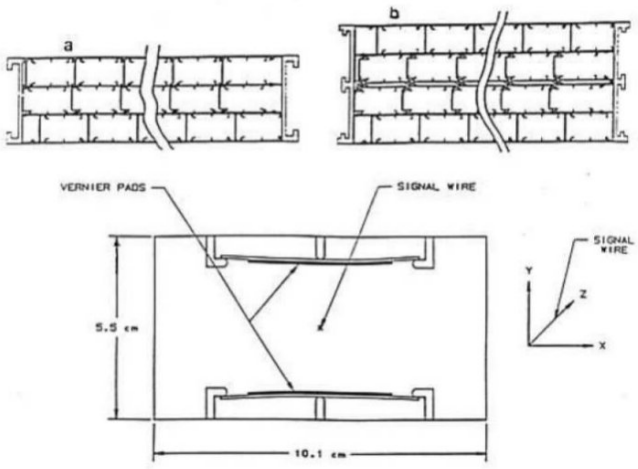

Figure 3.20: Geometry of the PDT deck (top) and cell (bottom) of DØ Central Muon system.

The Mini Drift Tubes. The MDTs cells are significantly smaller than the PDTs with dimensions approximately 1×1 cm^2. Therefore, the MDTs have a shorter electron drift time compared to the PDTs (40-60 ns) and a better coordinate resolution ($\approx$ 0.7 mm). The MDTs are arranged in three layers, each of which is divided into eight octants, as illustrated in Fig. 3.17, 3.22. There are 8 tubes per MDT module. The length of the MDTs varies from 1 to 6 m. They are filled with a mixture of 90% CF_4 and 10% CH_4. Figure 3.21 shows the cross sectional view of a MDT cell.

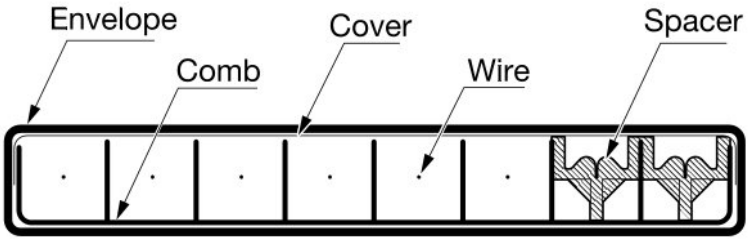

Figure 3.21: Cross sectional view of a MDT.

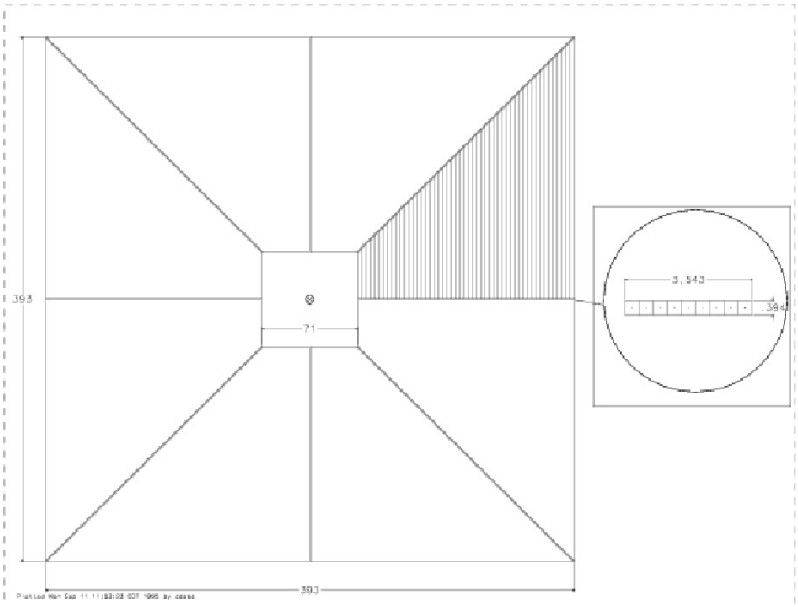

Figure 3.22: Drawing the MDT layout for one layer.

The Scintillation Counters. The muon detector scintillators provide crucial timing information for triggering plus rejection of out of time backgrounds. Scintillation counters accompany each layer of drift tubes, with the exception of most of the B layer (some on bottom) in the central system. Designed to cover 4.5° in ϕ, they are used for triggering, for cosmic or beam related muon rejection, and for track reconstruction. The counters consist of a slab of scintillator in which light collecting fibers are set in grooves and provides an analog voltage pulse to the digitizing electronics. A set of 630 scintillation counters called A_ψ counters are located inside the central toroid, 372 in the central B and C layers, and another 4214 counters called "pixel" counters are installed in the forward region ($1.0 < |\eta| < 2.3$) [23]. Figure 3.23 shows the scintillator forward pixel counters and Figure 3.18 shows all scintillator counters.

The pixel counters vary in size from 9×14 cm^2 to 60×110 cm^2. Table 3.3 shows a summary of the number of drift tubes and scintillators for the muon detectors.

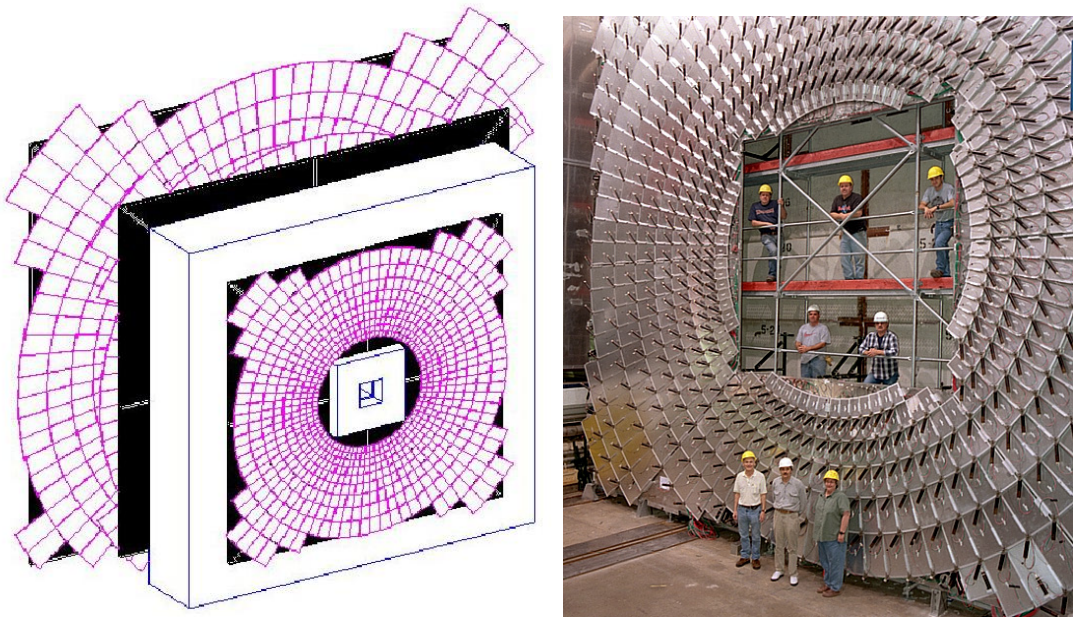

a.) b.)

Figure 3.23: a) Frontal view of one end of the forward pixel layer, and b) photograph of one side of the C layer pixel counters.

Shielding. The shielding consists of layers of iron, polyethylene and lead in a steel structure surrounding the beam pipe and low beta quadrupole magnets. Three different sources contribute to background in the central and forward muon system:

- Scattered proton and antiproton fragments that interact with the end of the calorimeter or beam pipe produce background in the central and forward A layer

	A layer	B layer	C layer	Total
PDT	1584	2424	2616	6624
MDT	16,384	15,552	16,704	48,640
Central scintillator counters	630	96	276	1002
Forward scintillator counters	1518	1420	1276	4214

Table 3.3: Summary of drift tubes and scintillator counts in muon detectors.

- Proton and antiproton fragments, mostly muons from pion decays created by proton and antiproton interactions upstream of the detector, interacting with the low beta quadrupole magnets produce hits in the B and C layers of the forward system

- Beam halo interactions affect both the central and the forward muon system. Iron is used as the hadronic and electromagnetic absorber, polyethylene is a good absorber for neutrons due to its high hydrogen content, and lead is used to absorb gamma rays.

3.3.4 Luminosity Monitor

The purpose of the Luminosity Monitor (LM) [24] is to make an accurate determination of the Tevatron collider luminosity at the DØ interaction region. It consists of two arrays of 24 plastic scintillation counters with photomultiplier readout. A schematic drawing of the system is show in Fig. 3.24.

The arrays are located in front of the end calorimeters at $z = \pm 140$ cm, and in the region between the beam pipe and Forward Preshower Detector. The counters are 15 cm long and cover the pseudo-rapidity range $2.7 < |\eta_D| < 4.4$. The luminosity is measured by detecting inelastic $p\bar{p}$ collisions in the LM, and determined as

$$\mathcal{L} = \frac{R}{\epsilon \cdot A \cdot \sigma_{inelastic}} \tag{3.18}$$

where R is the event rate, and $\sigma_{inelastic}$ is the total inelastic cross section [24].

Typical inelastic collisions produce low p_T events. The collection of final state pions carry most of the longitudinal momentum of the proton or antiproton, and

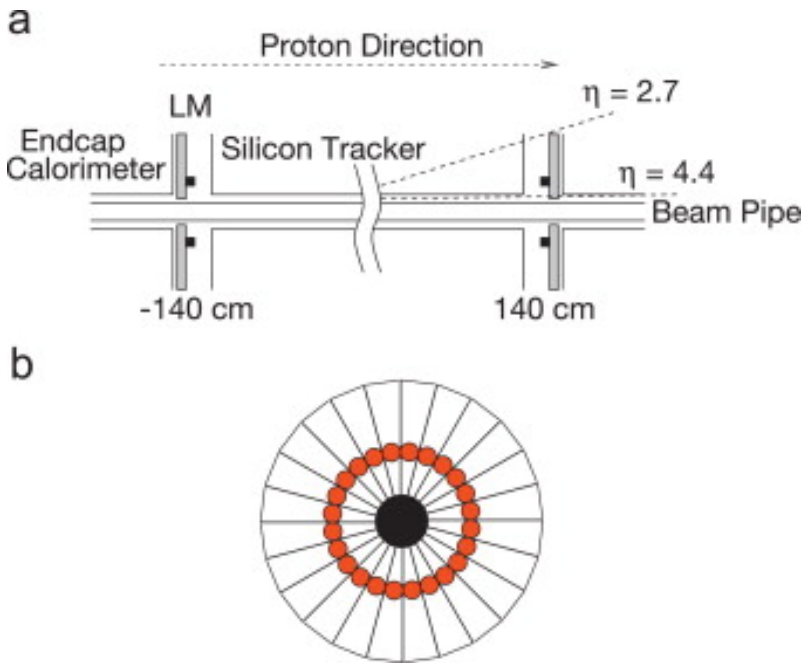

Figure 3.24: The Luminosity Monitor layout: a) $r - z$ view, and b) $r - \phi$ view.

therefore the scattering angle is small ($p_T/p_z = \tan\theta$). Small angle corresponds to large $|\eta|$. By counting interactions at high $|\eta|$ the inelastic cross section can be determined. The event rate has to be corrected for the efficiency ϵ and the acceptance A of the LM detector for inelastic $p\bar{p}$ collisions. Multiple $p\bar{p}$ collisions can occur in a single beam crossing. The number of interactions per bunch crossing is described by Poisson statistics. Collision products arrive at each set of scintillators roughly in coincidence, while beam halo products passing through the detector appear distinctly separated in time.

3.3.5 DØ Trigger System

The $p\bar{p}$ beams overlap every 396 ns, which is called a bunch crossing; the corresponding rate is 2.5 MHz. It is not possible to record and store events at this rate. Since most of the interactions are inelastic collisions and are not of interest, we must apply a selection process which keeps certain events and rejects other. This selection process is done as the Trigger system [19].

The DØ trigger system has a three level hierarchy called the Level 1 (L1), Level 2 (L2), and Level 3 (L3) trigger. L1 comprises a collection of hardware trigger elements that reduces the event rate by a factor of 1000 to a trigger accept rate of about 2 kHz. In L2, hardware engines and embedded microprocessors associated with specific subdetectors provide information to a global processor to construct a trigger decision based on individual objects as well as object correlations. The L2 reduces the event by a factor of 2-5 and has an accept rate of approximately 1 kHz. L3 microprocessors take candidates passing L1 and L2. Sophisticated algorithms reduce the rate by 20 to about 50 Hz and these events are recorded for offline reconstruction. The final result of the trigger is a selection rate of 40 to 80 events per second out of 1.7 million events per second. Fig. 3.25 shows an overview of the trigger and data acquisition system. A block diagram of the L1 and L2 trigger systems is shown in Fig. 3.26.

The triggers often rely on information from more than one system at a time. This makes it important that each system takes into consideration the other system. As a consequence it is necessary that systems have matching segmentation. The overall coordination and control of DØ triggering is handled by the COOR package running

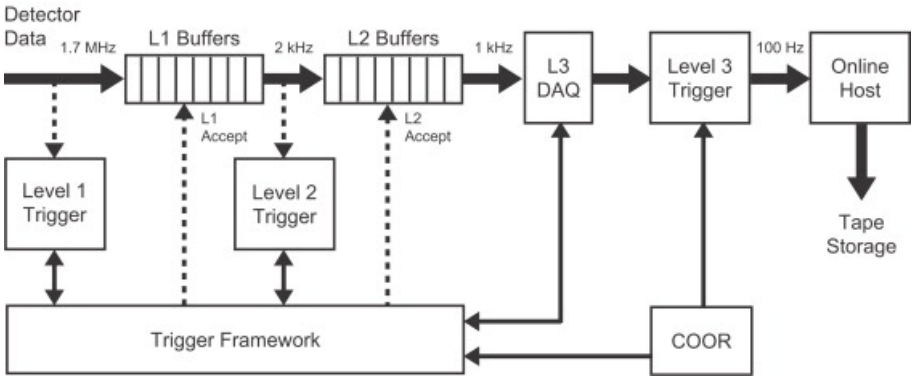

Figure 3.25: Overview of the DØ trigger and data acquisition systems.

on the online host, which manages the trigger system and interacts with the three different trigger levels.

L1 Trigger. L1 is implemented in specialized hardware and examines each event for interesting features [19]. The calorimeter trigger (L1Cal) looks for energy deposition patterns exceeding programmed limits on transverse energy deposits. The central track trigger (L1CTT) and the muon system trigger (L1Muon) compare tracks to see if they exceed preset thresholds in transverse momentum. The L1 forward proton detector trigger (L1FPD) is used to select diffractively-produced events by triggering on protons or antiprotons scattered at very small angles.

All events awaiting L1 trigger decisions are pipelined and thus make minimal contributions to the deadtime. In order to participate in the trigger decision, the L1 trigger decision must arrive at the trigger framework in 3.5 μs or less. The L1 trigger makes a decision in 4.2 μs, resulting in a trigger accept rate of 2 kHz.

The trigger framework (TFW) collects digital information from each of the specific L1 trigger devices and decides whether a particular event is to be accepted for further examination. In addition, it coordinates various vetoes that can inhibit

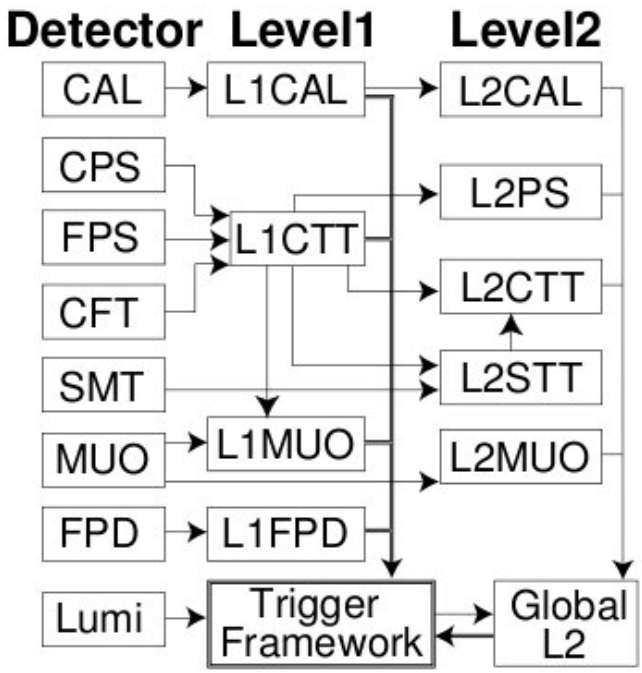

Figure 3.26: Block diagram of the DØ L1 and L2 trigger systems.

triggers, provides the prescaling of triggers too copious to pass on without rate reduction, correlates the trigger and readout functions.

Below we talk some more regarding the muon trigger, because it is very pertinent to this analysis. L1Muon looks for patterns consistent with muons using hits from muon wire chambers, muon scintillation counters, and tracks from the L1CTT. The L1Muon system is divided into central, north, and south regions. Each region is further divided into octants. Front-end data from each octant are processed by a L1Muon Process. Central tracks are matched to muon scintillator hits while scintillator-confirmed track stubs in wire chambers between the two or three layers of the muon system are also matched by the other process. The octant decisions from each process pair are formed and sent to the TFW. Specific triggers are then downloaded to handle them. The total latency of the L1Muon trigger is about 3.2

μs, driven by the central wire chambers (PDTs) and tracks from L1CTT. In short, muon trigger correlates hit in the scintillator, MDT and PDT systems with tracks found by a fast tracking microprocessor.

L2 Trigger. The L2 trigger is the first which makes trigger decisions based on physics objects from all detector subsystems. It combines hardware decisions with fast software algorithms. At the preprocessor state, a list of trigger objects is built using correlation algorithms and L1 detector information. The global processor get this list and compiles the correlations between the various detectors to form the trigger decision, for example, matching tracks and leptons. Events which are passed by L2 are partially reconstructed to look for lepton and jet like objects. L2 has an accept rate of 1 kHz.

The L2 muon track finding [25] is done independently of the L1 results. Due to the large number of front end inputs, the L2 muon subsystem implements one extra level of preprocessing compared to all other L2 subsystems. The muon detectors send specially preformatted data to the "Level 1.5" system of 80 200-MHz processors (DSPs) in a parallel processing scheme.

Each DSP is responsible for finding track segments in a small region of the detector so that the total execution time of the algorithms is independent of the number of hits. The DSPs run on special VME boards (second level input computers or SLICs). Each SLIC carries five DSP chips; four worker DSPs and one administrator DSP. Eleven SLICs process data from the central muon system and five from the forward muon system.

Five different algorithms were developed to run on worker DSPs: four to construct muon segments in the A and BC layers of the central or forward muon systems and one to process the L1 data. At the second stage the segments found by the SLICs

are received by the L2beta processor. The L2beta board uses the track segments to construct integrated muon candidates with an associated p_T and sends them to the global L2 for event selection. The SLICs algorithms for the forward and central muon system are described in [26, 27, 28].

L3 Trigger. The L3 and the data acquisition system (DAQ) are software based and reconstructes the electrons and muons. After that, L3 runs special filters corresponding to the list of triggers. L3 reduces the rate of events to be stored on tape to 50 Hz for offline analysis. The list of filters and their criteria is known as a trigger list and is assigned a version number.

CHAPTER 4

EVENT RECONSTRUCTION

The events recorded by the data acquisition are in a raw data format which contains information such as hits in the central tracking system, digitized counts in the calorimeter cells, timing information in the muon system and so on. The raw data has to be converted into physics objects such as photons, electrons, jets and muons, before they can be used for physics analysis. The tasks are performed offline by a process called Event Reconstruction [29].

Event reconstruction occurs in several hierarchical steps [19]:

- Use detector raw data information to reconstruct cluster (e.g., from the calorimeter and preshower) or hit (from the tracking detectors) objects
- Reconstruct global tracks form the hits in the SMT and CFT with different tracking algorithms
- Primary Vertex (PV) candidates are found. These vertices indicate the location of $p\bar{p}$ interaction and are used in the calculation of various kinematic quantities (e.g., $\not\!\!E_T$)
- Displaced secondary vertex candidates are identified, which are associated with the decays of long-live particles
- Reconstruct local tracks in the muon system
- Using a wide variety of algorithms, information from each of the preceding reconstruction steps is combined and physics object candidates are created

(first finds electrons, photons, muons, neutrinos ($\not\!\!E_T$), and jets. Afterwards, identifies candidates for heavy-quark and τ decays).

4.1 Track Reconstruction

A charged particle curving through the tracking system, leaves traces (hits) in the SMT and CFT. These hits are reconstructed into tracks in three steps:

- Hit Finding: locations in space are reconstructed from hits in the SMT or CFT
- Tracking and clustering: finds lists of clusters in the tracking detectors which are combined to form tracks
- Filtering and refitting: remove duplicate track candidates and find track properties like p_T

The track segments in the first few layers are used to create a seed track, then the seed track is extrapolated to the other layers, and the propagation takes into account the effects of magnetic fields, multiple scattering and energy loss in materials [30].

The final list of reconstructed tracks contains multiple parameters such as ρ, the curvature of the track, and the distance of closet approach (DCA) of the track with respect to the beamspot. Z boson decays promptly so the DCA of a track match to a lepton from Z boson decay should be very small.

4.2 Vertex Reconstruction

The vertex position is needed to reconstructed jets, EM objects and $\not\!\!E_T$ and must be reconstructed with high precision. At DØ, the vertices are determined from reconstructed tracks and the algorithm is similar to tracks. The process begins with the reconstructed tracks. The selected tracks are fitted to a single vertex and the track with the maximum χ^2 is rejected. This procedure is repeated until the resulting χ^2 is smaller than a given value, giving both the vertex and a list of tracks originating from that vertex.

The primary vertex (PV) is defined as the interaction point of the $p\bar{p}$ collision for the physics signal of any analysis. The PV is used to calculate many quantities such as transverse momenta of tracks and transverse energies of jets. PV finding starts from a set of good quality tracks. The reconstruction of the PV consists of three major steps [31]:

- The algorithm locates the position of the beamspot center, and calculates the DCA with respect to the origin point (0,0) in the transverse plane. DCA significance S are fitted to a list of possible PV.

- Track DCA significances are re-calculated with respect to the position of these first pass vertices. Only tracks with at least two SMT hits are fitted to the final PV lists.

- Select the hard scatter vertex from the final PV lists [32]. The method is based on the fact that tracks from minimum bias interactions have smalled transverse momenta than tracks from hard scatter interactions. For each vertex, the product of probabilities of each track divided by the total number of tracks

is calculated, thus forming the probability for a vertex to originate from a minimum bias interaction. The PV with the lowest minimum bias probability is chosen as the hard scatter PV.

A similar procedure is used to determine if a secondary vertex is present in the event. The secondary vertices are the displaced vertices that arise from the decay of long-lived particles (e.g., B and D mesons). The search for secondary vertices uses displaced tracks with respect to the primary vertex. It can be use to tag a b-decay. Details can be found in Ref. [33], but this feature is not used in this analysis.

4.3 Electron and Photon Reconstruction

Electromagnetic candidate objects are initially identified on calorimeter information. As photons do not leave signals in the tracking system, this provides a tool of using a track matched to the energy deposited in the calorimeter to distinguish electrons from photons.

EM objects such as electrons, positrons and photons have similar shower shape in the calorimeter and deposit the majority of their energy in the electromagnetic layers of the calorimeter.

A cluster is a list of cells with significant energy deposits. The standard EM cluster algorithm at DØ is the simple cone algorithm based on towers. The cell energies are then converted to the transverse energies by using the position of the interaction primary vertex. Cells with the same η and ϕ are grouped to form EM towers which will be used for electron, photon and jet identification. An initial EM cluster should pass the crude selection criteria as follows:

- **Transverse Energy** $E_T > 1.5$ GeV

- **Isolation Fraction** (f_{iso}) < 0.2: The isolation of an EM object is defined as

$$f_{iso} = \frac{E_{tot}(R < 0.4) - E_{EM}(R < 0.2)}{E_{tot}(R < 0.2)} \tag{4.1}$$

  where $E_{tot}(R < 0.4)$ is the total calorimeter energy deposited in the cone of 0.4 in $\eta - \phi$ space around the EM object and $E_{EM}(R < 0.2)$ is the energy deposited in the cone of 0.2 in the electromagnetic layers only. Small values of isolation correspond to the situation that most of the energy is deposited in a narrow region of the EM layers in the calorimeter, which is a characteristic of an electron or a photon

- **EM Fraction** (f_{EM}) > 0.9: The fraction of the total energy deposited in the electromagnetic calorimeter layers to the total energy deposited in all calorimeter layers, defined as:

$$f_{EM} = \frac{E_{EM}}{E_{tot}} \tag{4.2}$$

The variables f_{EM} and f_{iso} are useful to discriminate against hadronic jets. But the above criteria for initial cluster finding are very loose. At the final stage of Reconstruction, another variables describing EM cluster properties are stored. They are:

- **HMatrix** ($HMx8$): The discriminator H-matrix has eight inputs with only the first seven designated as $HMx7$ and is based on the shape of the EM shower. The inputs are f_{EM} for each of the four EM layers, PV, E, size of the cluster in $\eta \times \phi$ at the third EM layer and transverse width of the shower. This measures how similar the shower is to an electron shower.

The standard EM identification at DØ requires: $f_{iso} < 0.15$, $f_{EM} > 0.9$ and $Hmax8 < 20$. An electron is expected to have an associated track in the central tracking system. To measure the spatial distance between a cluster and a track, a track matching significance, χ^2, is defined for

- χ^2: This variable is to quantify how consistent the shower shape is with that of electrons or photons. Only clusters with $f_{iso} < 0.2$, $f_{EM} > 0.9$, and $E_T > 1.5$ GeV are stored in a list and a search is done for a track match to the cluster. For each reconstructed track a fit quality variable χ^2 defined as:

$$\chi^2 = (\frac{\Delta\phi}{\sigma_{\Delta\phi}})^2 + (\frac{\Delta z}{\sigma_{\Delta z}})^2 + (\frac{E_T/p_T - 1}{\sigma_{E_T/p_T}})^2 \tag{4.3}$$

  Here, $\Delta\phi$ and Δz are the spatial difference from the track and EM cluster. E is the cluster energy and p is the track momentum. Then we calculate the probability of getting a χ^2 value for a specific track. If a track has the χ^2 probability of $P(\chi^2) > 0.01$, the EM cluster is considered to have a track match, which is a good track.

There are some other EM variables which we also used in this analysis:

- **ID**: The EM cluster can be matched to a track reconstructed from the central tracking system. If such track is found the cluster is assigned an ID of ± 11, sign is the charge of the track. If no track is matched, the cluster is assigned an ID of 10.

- **Coarse Hadronic Fraction** (f_{CH}): Similar to f_{EM}, using energy deposited in the coarse hadronic layers.

- **Hot Fraction**: Ratio of the transverse energies of the calorimeter tower with the highest energy, to the tower with the second highest energy. This cut,

along with following two variables n90 and f90 are used to determine hot cells in the calorimeter that have been misidentified as EM objects

- **n90**: Total number of towers that make up 90% of the EM shower energy
- **f90**: Total number of cells comprising 90% of the EM object energy
- **NNout** ($NNout7$): Seven input variables neural-networks include the energy deposited and number of hit cells in the first EM layer, the track isolation and energy deposited in the central preshower detector.
- **Shower width**: The width of the EM cluster at the third layer of the EM calorimeter is used to identify clusters produced by EM particles. σ_ϕ is for the clusters in central calorimeter only the width in $r-\phi$ plane. σ_z is for the width in z direction.
- **Likelihood**: Electron likelihood is used to efficiently select high p_T, isolated electrons by combining several preselected electron identification variables. Several variables are selected to construct the electron likelihood LHood. They are
  - $0.9 < f_{EM} < 1.0$
  - $0 < HMx7 < 50$
  - $E_T/P_T < 3.1$
  - Spatial track match probability, P(χ^2)> 0
  - Distance of DCA from the PV < 0.05 for tracks with SMT hits
  - Number of tracks in cone of R $= 0.05 < 5$, around and including the candidate track

– Total track p_T in cone of R = 0.04 < 3.5 GeV, but excluding the candidate track

Any EM cluster which does not match any of the bounds above is assigned to be likelihood = -1.

We will discuss the EM ID information more in Sec. 7.3.3.

4.4 Jet Reconstruction

In a $p\bar{p}$ collision, when an energetic parton is produced and moves away from others, the potential of the strong force field between the partons grows as the distance increases until the energy is large enough to create a parton-antiparton pair out of the vacuum. More and more particles are produced with such processes until the energy is too low. This is called the *hadronization process*, and creates a group of hadrons moving about the same direction as the original parton and depositing a cluster of energy in the calorimeter to form a jet.

The momentum of a jet is the sum of momenta of one-tower jets pertaining to the group. The components of jet momentum are connected with transverse energy deposited in the i^{th} tower E_{Ti} as following:

$$p_x = \sum_{i=1}^{n} E_{Ti} \cos\phi_i \tag{4.4}$$

$$p_y = \sum_{i=1}^{n} E_{Ti} \sin\phi_i \tag{4.5}$$

$$p_z = \sum_{i=1}^{n} E_{Ti} \sinh\eta_i \tag{4.6}$$

The energy of a jet is the sum of the energies of all its towers:

$$E = \sum_{i=1}^{n} E_i \tag{4.7}$$

Jets at DØ are reconstructed based on the energies deposited in the calorimeter cell. To select calorimeter towers for the reconstruction of a given jet the DØ Run II jet cone algorithm [34] is used. The major steps are:

- Calculates momentum four vector for each calorimeter cell i and forms the list of all jet towers momentum four vectors.
- Select seed towers with transverse energy over some threshold. A cone cluster of cells in space (η, ϕ) is created starting from each seed.
- Cluster with the highest E_T is considered as the preliminary jet. Cells within a cone R will be added to the jet list. (η, ϕ) of the jet is recalculated using an interactive algorithm after adding each cell.
- Cones are merged or split according to how the clusters are shared to avoid double counting of energy.
- A jet is considered reconstructed if the transverse energy of the jet exceeds a threshold of 8 GeV.

The momentum of jets is adjusted using the *Jet Energy Scale corrections* (JES) for pileup, out of cone shower, and neutrino emission in semileptonic decay.

4.5 Missing Transverse Energy ($\not\!\!E_T$) Determination

The missing transverse energy can be the signature of particles escaping from the detector without interacting in it. They can be either neutrinoes, particles emitted at very low angles along the beam pipe or new non-interacting neutral particles.

The calorimeter missing energy is reconstructed similar to jets. Considering each calorimeter cell as a massless particle emerging from the PV, $\not\!\!E_T$ is the negative magnitude of the vector sum of the calorimeter tower transverse energies and is defined as

$$\not\!\!E_T{}^2 = \not\!\!E_{Tx}{}^2 + \not\!\!E_{Ty}{}^2 = (-\sum_{i=1}^{n} E_{Ti}\cos\phi_i)^2 + (-\sum_{i=1}^{n} E_{Ti}\sin\phi_i)^2 \tag{4.8}$$

4.6 Muon Reconstruction

Muons are primarily reconstructed using information from the tracking and muon systems. Calorimeter information is then used to see if the muon is isolated or part of a jet.

After the individual hits in the muon detector are found, track segments in each muon layer are formed by fitting groups of hits to a straight line. The muon system only momentum is determined from the bend of the track while it passes through the magnetized iron. Tracks in the muon system are then associated with tracks in the central track based on matching in η and ϕ. The momentum determinated by the central tracking system is used in this analysis. Information about muon reconstruction and muon identification will be further described in Chapter 5.

CHAPTER 5

MUON IDENTIFICATION

This Chapter will describe the muon reconstruction as well as identification and standard muon ID variables which are cornerstones for the DØ Run II physics program at the Fermilab Tevatron $p\bar{p}$ collider. Muon reconstruction begins from these electronic signal information in the muon detector. Then, muon hits, segments and local muon tracks are reconstructed. To improve the momentum resolution a muon track is matched with tracks of the central detector. Information from these stages is used for muon identification and quality classification for a muon candidate.

5.1 Muon Reconstruction

Figure 3.7 shows a cross sectional view of the Run II DØ detector. As described in section 3.3.3, the detectors surrounding the interaction region are the SMT for precision tracking of charged particles and determination of the PV, the CFT for precise track reconstruction and determination of momentum, preshower detectors to assist tracker for precise position measurements, and calorimeters. The muon system resides outside the calorimeters consists of two systems: the central angle muon system ($|\eta| < 1.0$) includes PDTs and an iron toroidal magnets (CF), and the forward system ($1.0 < |\eta| < 2.0$) includes a set of mini drift tube planes and two forward iron toroids (EF).

The Run II muon system [35] consists of one layer (A layer) of muon detectors before the toroidal magnet and two similar layers (B and C layers) of detectors after the magnet as indicated on Fig. 3.7 for the purpose of triggering and muon track reconstruction. A set of fast scintillation counters are used in the A and C layers in the central muon system ($|\eta| < 1.0$) and in the A, B and C layers in the forward region ($1.0 < |\eta| < 2.0$, referred to as pixel counters) to provide three independent coordinates and time measurements along muon tracks. The muon system tracking detectors consist of PDTs in the central region and MDTs in the forward region. Both PDTs and MDTs are installed in all three layers. Actually, B and C layers are treated together in segment finding.

To reconstruct muon trajectories, the same algorithm [35] is used in the forward and central regions. First, a list of hits from the muon detectors is built. For the forward system, the ϕ coordinate is determined by the scintillation counter. In the same way, ϕ in the central A layer are measured. In all three layers, PDTs are ganged together in pairs at one end of each chamber. The PDTs measures the ϕ coordinate using the time difference of the signal arrival at each end of paired wires. For both central and forward systems, the drift times of the wires chambers are used to measure the passage point of the muons.

Secondly, these hits are associated to form muon track segments. 2D segments in the deviation plane, i.e. the plane orthogonal to the magnetic field and the wires, are found in each layer using the drift times from the MDT and PDT systems. All possible pairs of wire hits form the first segments. Then, scintillator hits are associated with each segment if they agree with the η position for the forward system and both the η and ϕ for the central system. A single muon can produce multiple segments. To reduce the combinatorics, only the three highest quality segments

arising from a given cluster of hits are kept for the A layer and only the two highest quality segments for the BC layer.

Thirdly, muon track segments form muon tracks in the muon system (called local muon tracks). Segment in the BC layer outside the magnet are combined into a single segment if they lie on a straight line. A and BC layer segments are then combined to form local muon tracks.

Once local muon segment and tracks have been found, they are matched to the precisely measured reconstructed tracks of the central tracking system in order to improve the resolution of the muon momentum. The transverse momentum p_T of the muon is determined from the central track by the relation:

$$p_T = qRB \tag{5.1}$$

where R is the radius of curvature of the track, B is the magnetic field and q is the charge of the muon. The η and ϕ are determined from the track match. The momentum resolution, $\sigma(p_T)/p_T$, achieved is equal to the momentum resolution of the central tracker. The local muon momentum is use as part of the matching algorithm and provide a measurement of the momentum, though this is not used in this analysis.

5.2 Muon Momentum Measurement

Since the local muon momentum resolution is worse than the resolution from the central tracking system, the momentum of a muon matched to a central track is taken to be the momentum measured in the central tracker. For muon objects

defined by non-paired A and BC layer segments, the momenta is also taken from the matched tracks.

For muons without a SMT hit matched to the central track, the additional constraint that the track arises from the beam axis located at (x_b, y_b) is used. This constraint yields a correction for the track curvature C, which is given at first order by

$$C \to C + (x_b \sin\phi_0 - y_b \cos\phi_0 - d_0)\frac{E_{Cd}}{E_{dd}} \tag{5.2}$$

where d_0 is the distance of closest approach to the central axis (x, y) = (0, 0), ϕ_0 is the track azimuthal angle at the point of closest approach, and E_{Cd} and E_{dd} are elements of the covariance matrix resulting from the central track reconstruction fit. E_{Cd} is the covariance between C and d_0. E_{dd} is the squared uncertainty on d_0. The correction is propagated to the track transverse momentum which is proportional to $\frac{1}{C}$. Central tracks without hits in the SMT have a relative resolution on transverse momentum $\frac{\sigma(p_T)}{p_T} = \frac{\sigma(C)}{C}$ of typically 25% for $p_T = 45$ GeV. The correction improves the relative resolution to typically 15% [35].

5.3 Muon Identification

A reconstructed isolated (that is not associated with a jet) muon candidate is defined by the combination of three criteria [35]: (i) the presence of a muon object in the muon system; (ii) the presence of a track in the central tracker which is matched to the muon object; and (iii) the absence of significant activity around the muon trajectory, both in the calorimeter and in the central tracker. For each of these

three criteria, different operating points are defined, which are briefly discussed in the following.

5.3.1 Muon Type

The type of muon is give by the parameter *nseg*. A positive value of *nseg* indicates that the muon reconstructed in the muon system was matched to a track in the central tracking. Table 5.1 shows the requirement for different muon types with their respective values of *nseg*. Additional information about the muon type information can be found in [36, 37].

nseg	Muon Type
3	Central track + local muon track (A and BC layer)
2	Central track + BC layer only
1	Central track + A layer only
0	Central track + muon hit or Central track + MTC

Table 5.1: Overview of different muon types.

nseg is also possibly negative. This means muon segments only that are not matched to a central track. Most muons in this analysis from Z boson decays have nseg=3.

5.3.2 Muon Quality

The second parameter used to classify muons is the quality, which is based on the quality of the information reconstructed in the muon system. The muon quality can be **loose**, **medium** and **mediumnseg3** (These are only defined names for DØ.

Note that **tight** was already dropped since p17). The resulting definitions are given below [35, 36].

- A muon is **loose** if
  - nseg=1, at least one scintillator hit and at least two wire hits in the A layer of the muon system.
  - nseg=2, at least one BC layer scintillator hit and at least two wire hits in the BC layer of the muon system
- A muon is **medium** if
  - nseg=1, fulfills the above nseg=1 loose muon requirements, and if it is located in the bottom part of the detector with $|\eta_D| < 1.6$ or if it is qualified as low momentum muon with its probability to reach the BC layer is less than 70%.
  - nseg=2, fulfills the above nseg=2 loose muon requirements, and if it is located in the bottom part of the detector with $|\eta_D| < 1.6$.
  - nseg=3, (1) at least two A layer wire hits, (2) at least one A layer scintillator hit, (3) at least two BC layer wire hits, and (4) at least one BC scintillator hit (except for central muons where this requirement is dropped).
- nseg=3, **loose** muon is defined as a **mediumnseg3** muon but allowing one of the above tests to fail, with the A wire and scintillator requirement treated as one test and requiring always at least one scintillator hit.

Each of the two operating points requires the hits in the muon system to be matched to a track in the central tracker. Furthermore, the number of operating

points is doubled depending on whether or not a veto against cosmic muons is required. This veto consists in rejecting cosmic muons using the scintillator hit times (when information is available) in A, B and C layer are between -10 ns and 10 ns of the expected time for a $\beta = 1$ particle produced at the $p\bar{p}$ collision point.

The efficiency of this is about 98.3%. It is know that the trackloose, trackmedium and tracktight tracking criteria (described in the next section) have ΔZ_{DCA} cuts which also suppress cosmic muons. The inefficiency associated with this timing cus is included in the efficiencies for the muon criteria loose, medium and mediumnseg3. The efficiencies without the timing cuts are giving in looseNCV, mediumNCV and mediumnseg3NCV[36]. In this analysis, we use NCV muon criteria.

5.3.3 Track Quality

To control the purity of muons matched to central track, four track qualities have been defined. They rely on the following track characteristics:

- Number of hits in the SMT or CFT system.
- χ^2/N_{DoF}: χ^2 is the result of the fit in the central tracking system and N_{DoF} is the number of degrees of freedom.
- ΔZ_{DCA}: Transverse impact parameter, track distance of closest approach to the beamline.

The track quality definitions are the following. We use the definations from the MuonID paper [36] in this analysis, but these name were changed in the Muon NIM paper [35].

- **loose** (loose in NIM)
  - $|\Delta Z_{DCA}| < 0.2$ cm, if the track has no SMT hit
  - or $|\Delta Z_{DCA}| < 0.04$ cm, if the track has SMT hit

  The loose operating point is good choice for analyses that do not need the most accurate muon momentum measurement.

- **medium** (mediumSMT in NIM)
  - fulfills the loose requirements
  - $\chi^2/N_{DoF} < 4$

- **newmedium** (medium in NIM)
  - fulfills the loose requirements
  - $\chi^2/N_{DoF} < 9.5$
  - at least 2 CFT hits on the track

- **tight** (tight in NIM)
  - fulfills the newmedium requirements
  - requires SMT hits

5.3.4 Muon Isolation

The isolation cuts are designed to separate prompt muons from electroweak processes like $Z \to \mu^+\mu^-$, $W \to \mu\nu$ from secondary muons produced in heavy flavor quark decays $b, c \to \mu + X$. Five basic discrimination variables are used related to this analysis:

- $\Delta R \equiv \Delta R(\mu, jet)$

  Closest distance in the (η, ϕ) space ($\Delta R = \sqrt{\Delta\eta^2 + \Delta\phi^2}$) of the muon to any jet with $p_T > 15$ GeV, where the jets are reconstructed from energy deposits in the calorimeter using an iterative midpoint cone algorithm [38] with a cone radius R = 0.5.

- $T^{trk}_{\Delta R<0.5} \equiv \sum_{tracks \in \Delta R<0.5} p_T^{track}$

  The scalar sum of transverse momenta of all tracks inside a $\Delta R(track, \mu) < 0.5$ cone around the muon with the exception of the muon track itself. For all the tracks considered in the sum, $\Delta z_0(\mu, track) < 2$ cm is required to reject tracks arising from secondary $p\bar{p}$ interactions, where z_0 is the z-coordinate of the track at the point of closest approach to the beam axis.

- $T^{trk}_{\Delta R<0.5}/p_T^{\mu}$

  Same quantity as above, but divided by the muon transverse momentum.

- $T^{cal}_{0.1<\Delta R<0.4} \equiv \sum_{clusters \in 0.1<\Delta R<0.4} E_T^{cluster}$

  The scalar sum of transverse energies of all calorimeter clusters inside a hollow cone $0.1 < \Delta(cluster, \mu) < 0.4$ cone around the muon. Only the energy deposits in the electromagnetic calorimeter and the first fine sampling layers of the hadron calorimeter are considered in order to reduce the impact of noise and secondary $p\bar{p}$ interactions.

- $T^{cal}_{0.1<\Delta R<0.4}/p_T^{\mu}$

  Same quantity as above, but divided by the muon transverse momentum.

Based on the variables, several isolation working points are defined as shown in Table 5.2. In this analysis, only variations on "TopScaledTight" and "TrkLooseScaled" are used for muon isolation. We added a luminosity correction to the iso-

lation points, which makes T^{trk}/p_T^{μ} to $\frac{T^{trk}-0.005\mathcal{L}}{p_T^{\mu}}$ and makes T^{cal}/p_T^{μ} to $\frac{T^{cal}-0.005\mathcal{L}}{p_T^{\mu}}$, where $\mathcal{L}$ represents the instantaneous luminosity in units of 10^{30} cm^{-2}s^{-1}.

This selection are similar to the "TrkLooseScaled" and "TopScaleTight" points certified by the muID. The $0.005\mathcal{L}$ term is an attempt to model the luminosity dependence of the halo isolation. Adding this term increases the isolation efficiency by about 1% for TrkLooseScale which is already >98%. Any systematic error on modeling this is very tiny as the efficiency is so close to 100%. More details about related isolation operating points will be discussed in Sec. 7.3.

Operating point	$T^{trk}_{\Delta R<0.5}$	$T^{cal}_{0.1<\Delta R<0.4}$	$T^{trk}_{\Delta R<0.5}/p_T$	$T^{cal}_{0.1<\Delta R<0.4}/p_T$	ΔR
TopScaledLoose			< 0.2	< 0.2	> 0.5
TopScaledMedium			< 0.15	< 0.15	> 0.5
TopScaledTight			< 0.1	< 0.1	> 0.5
TopP14			< 0.06	< 0.08	> 0.5
NPLoose	< 4.0GeV				> 0.5
NPTight	< 2.5GeV	< 2.5GeV			> 0.5
TrkLoose	< 4.0GeV	< 10GeV			> 0.5
TrkTight	< 2.5GeV	< 10GeV			> 0.5
TrkLooseScaled	-	-	< 0.25	< 0.4	> 0.5
TrkTightScaled	-	-	< 0.12	< 0.4	> 0.5
deltaR	-	-			> 0.5

Table 5.2: Definition of isolation working points.

5.4 Muon Efficiency

In this section, the efficiencies for various muon quality criteria, muon central track reconstruction and muon isolation are presented. These efficiencies are uncorrelated, so they can be measured independently. More details can also be found in [37, 39].

5.4.1 Tag and probe method

To measure the identification and reconstruction efficiency for high p_T muons in data, we apply the "tag and probe" method based on $Z/\gamma^\star \to \mu^+\mu^-$ events. One muon candidate with tight selection requirements serves as a tag, whereas the other candidate serves as a probe and is used for the efficiency measurement. Additional requirements for consistency with the decay of a Z boson are imposed on both muon candidates, e.g. a cut on the dimuon invariant mass. Each of the muon candidates in a given event can serve as a tag or as a probe.

5.4.2 Efficiency of muon system reconstruction

The tag and probe selection for the measurement of the efficiency of the DØ muon system to identify and reconstruct muon is summarized as follows. The tag object is required to be a local loose muon matched to a central track of quality tight with $p_T > 30$ GeV and isolated using cuts $T^{trk}_{\Delta R<0.5} < 3.5$ GeV and $T^{cal}_{0.1<\Delta R<0.4} < 2.5$ GeV. It must have fired a single muon trigger and the A or B layer scintillator time has to be less then 7 ns. The probe object is required to be a central track of quality tight with $p_T > 20$ GeV and isolated using cuts $T^{trk}_{\Delta R<0.5} < 3.5$ GeV and $T^{cal}_{0.1<\Delta R<0.4} < 2.5$ GeV, matched within $\Delta R < 0.5$ to the local muon track. The tag and probe tracks have to be of opposite charge and have to fulfill $|\Delta z_0| < 2$ cm and $\Delta R > 2$. Cosmic rays are suppressed by requiring the acollinearity between tag and probe tracks be greater than 0.05.

The probe muon is then matched (either using the reconstruction central matching algorithm or the muon crude $\Delta R < 0.5$) to muon identification objects to es-

timate the muon reconstruction efficiency. The measured efficiencies [35] for loose, medium and mediumnseg3 muons ares shown in Fig. 5.1 as functions of η_D and ϕ, where η_D is the angular coordinate of the position where the muon trajectory traverses the A layer of the muon system. The average reconstruction efficiencies are 89.2%, 80.8% and 72.0% for the loose, medium and mediumnseg3 operating points, while the efficiencies without cosmic veto are 91.2%, 82.5% and 73.2% for looseNCV, mediumNCV and mediumnseg3NCV operating points.

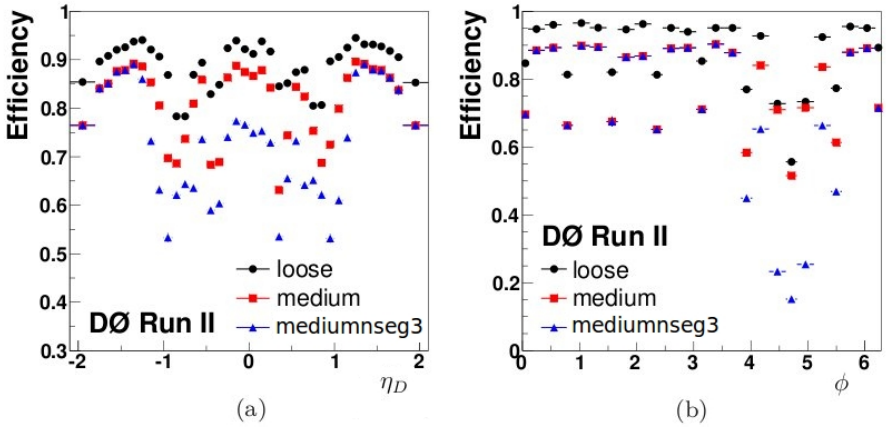

Figure 5.1: Efficiencies of the loose, medium and mediumnseg3 muon quality in the muon system as functions of a) η_D and b) ϕ.

5.4.3 Efficiency of muon central track reconstruction

The tag and probe selection for the measurement of the efficiency of the DØ central tracker to reconstruct muon tracks is summarized as follows. The tag object is required to be a local loose muon matched to a central track of quality tight with $p_T > 30$ GeV and $|\Delta Z_{DCA}| < 0.2$ mm, and isolated using cuts $T^{trk}_{\Delta R<0.5} < 3.5$ GeV and $T^{cal}_{0.1<\Delta R<0.4} < 2.5$ GeV. The probe is a local muon track of quality loose, with

$p_T > 15$ GeV and isolated with $T^{cal}_{0.1<\Delta R<0.4} < 2.5$ GeV. The tag and probe must fulfill $\Delta R > 2$ and scintillator hit times at either the A or B layer have to match within a 6 ns window.

The measured efficiencies are shown in Fig. 5.2 as a function of η_{CFT}, z_0 and $\mathcal{L}$, where η_{CFT} is the angular coordinate of the outermost intercept between the muon trajectory and the CFT detector volume. The average efficiencies are 91.6%, 90.5%, 84.6% and 86.2%, for the loose, newmedium, medium and tight operating points.

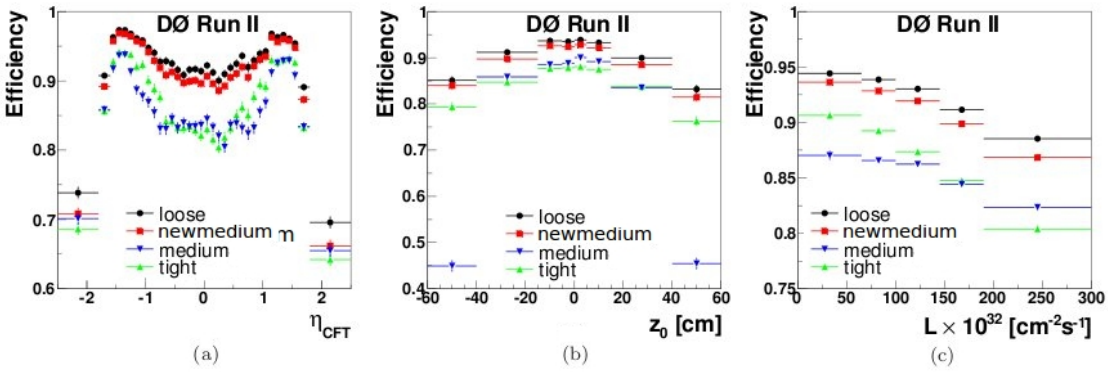

Figure 5.2: Efficiencies of the loose, newmedium, medium and tight muon quality in the tracking system as functions of a) η_{CFT}, b) z_0 and c) $\mathcal{L}$.

5.4.4 Efficiency of isolation requirements

The tag and probe selection for the measurement of the isolation efficiency is summarized as follows. Both the tag and probe objects are required to be local muons of loose quality, with $p_T > 8$ GeV, matched to central tracks of quality loose, with $p_T > 15$ GeV and $|\Delta Z_{DCA}| < 0.4$ (2) mm if matched (not matched) to hits in the SMT. In addition, the tag muon has to be isolated according to $T^{trk}_{\Delta R<0.5} < 2.5$ GeV and $T^{cal}_{0.1<\Delta R<0.4} < 10$ GeV and a dimuon trigger with no explicit isolation

requirement has to have fired. The tag and the probe tracks have to be of opposite charge and must fulfill $|\Delta z_0| < 2$ cm, $\Delta R > 2$, acollinearity greater than 0.05 and 70 GeV $< m_{\mu\mu} <$ 120 GeV.

The measured efficiencies for the operating points are shown in Fig. 5.3 as functions of η_{CFT}, p_T and luminosity [37]. The average efficiencies are 98.4%, 87.3% and 98.6% for the TopScaledTight, NPloose and TrkLooseScaled operating points. Note that, we add in impact of "-0.005$\mathcal{L}$" term to the certified isolation operation points. More details about how it was estimated using the Efficiencies versus $\mathcal{L}$ plots in Fig. 5.3 is given in Sec. 7.3.1.

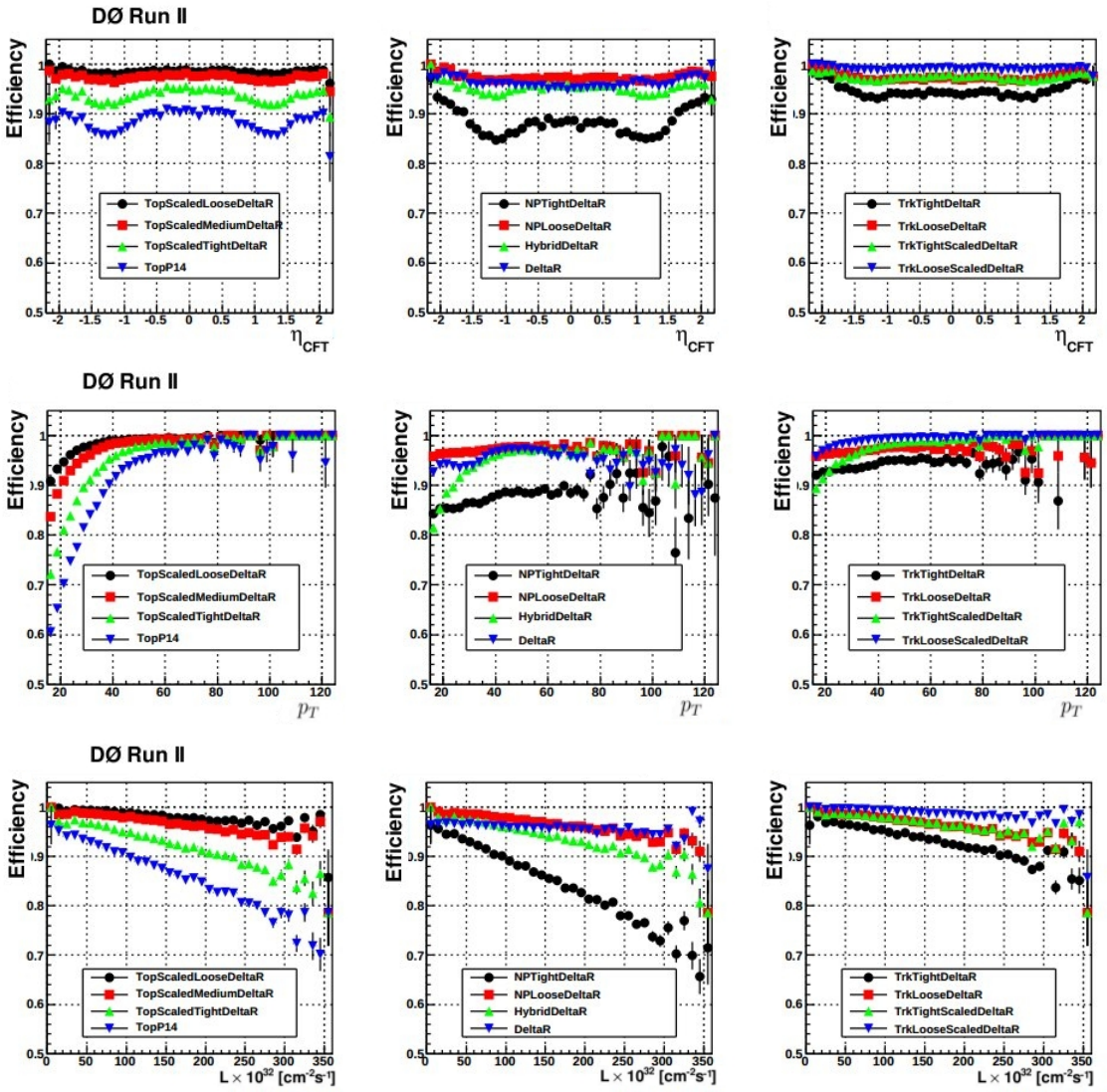

Figure 5.3: Efficiencies of the isolation criteria as functions of η_{CFT}, p_T and $\mathcal{L}$ (from top to bottom).

CHAPTER 6

MUON MOMENTUM OVERSMEARING

A mismodeling in the MC simulation of the muon momentum resolution of the central tracking system compared to the resolution in data has been observed in previous muon-smearing studies [40, 41, 42]. The resolution is worse by typically 30% for a p_T of 40 GeV. This discrepancy is mainly due to the simulation of hit efficiencies with smaller contributions coming from the simulation of hit resolution, the magnetic field mapping, the alignments of detector elements and some matter effects.

The modeling of the muon momentum by MC can be improved by adding in an additional error, called oversmearing, to the muon track curvature. In the following, we discuss the oversmearing method and compute its parameters with $J/\psi \to \mu^+\mu^-$ and $Z/\gamma^\star \to \mu^+\mu^-$ events. Note that the data taking epochs and the generation version of MC are particularly important as different data and MC sets exhibit different momentum resolutions. The muon oversmearing studies described here yield a set of oversmearing and resolution parameters according to the different correspondent data taking epochs and MC version. Such parameters are computed concerning the following combinations shown in Table 6.1.

Figure 6.1 shows the invariant mass distribution of $J/\psi \to \mu^+\mu^-$ data and $Z/\gamma^\star \to \mu^+\mu^-$ data with MC after default DØ reconstruction without oversmearing. The resolution discrepancy between data and MC is quite clear in both cases. In order to recover a good agreement, the MC muon momentum is usually oversmeared.

Run II Data	Run II MC	Result
IIb1	IIb1 (p20.09)	DØ Note 6031
IIb2	IIb1 (p20.09)	
IIb1+IIb2	IIb1 (p20.09)	
IIa	IIa (p18.13)	DØ Note 6190
IIb2	IIb2 (p20.15)	
IIb3	IIb2 (p20.15)	
IIb2+IIb3	IIb1 (p20.09)	
IIb2+IIb3	IIb2 (p20.15)	
IIb3	IIb3 (p20.17)	DØ Note 6312
IIb3+IIb4	IIb3 (p20.17)	
IIb1+IIb2	IIb2 (p20.15)	DØ Note 6314

Table 6.1: Combinations of data taking epochs and MC versions from which oversmearing parameters have been computed.

Based on previous studies [40], many discrepancies have been observed with the original oversmearing methods which used a single Gaussian. For example, the momentum resolution has changed for different periods at DØ; a resolution tail exists in data; with old oversmearing technique, the difference between data and MC exhibited a wave-like shape that produced a momentum scale mismatch as seen in Fig. 6.2.

6.1 Muon Smearing Method

The old way to describe momentum resolution is by the formula

$$\sigma(\frac{q}{p_T}) = A \oplus \frac{B\sqrt{\cosh\eta}}{p_T} \tag{6.1}$$

where A is the resolution term, related to the detector hit resolution (alignment) and B is the effect of multiple scattering term. Sign $\oplus$ means sum in quadrature. As the resolution is different in data and in MC, it is easy to conclude that

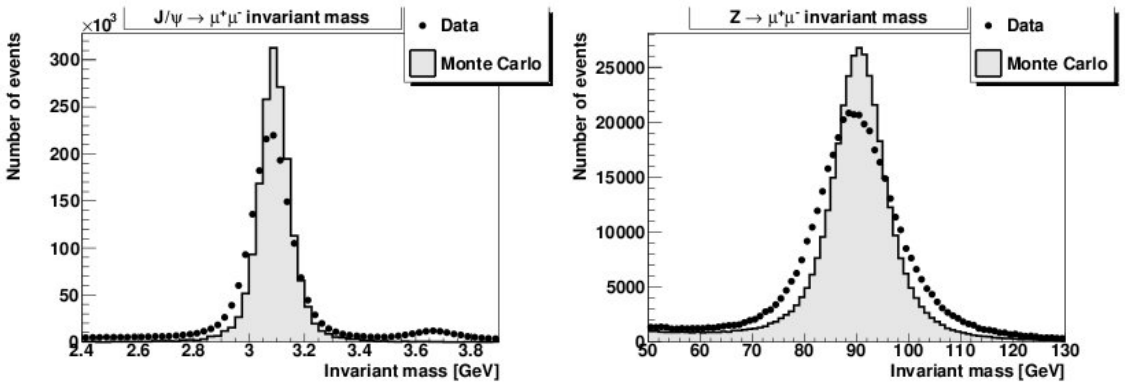

a) $J/\psi \to \mu^+\mu^-$ b) $Z/\gamma^\star \to \mu^+\mu^-$

Figure 6.1: Comparison of different invariant masses between data and Monte Carlo without oversmearing.

$$A_{MC} \neq A_{data},\ B_{MC} \neq B_{data} \tag{6.2}$$

We then define A_{smear} and B_{smear} by the equations

$$A^2_{smear} = A^2_{data} - A^2_{MC},\ B^2_{smear} = B^2_{data} - B^2_{MC} \tag{6.3}$$

As a result, the data resolution can be recovered by modifying the momentum of MC reconstructed track according to

$$\frac{q}{p_T} \to \frac{q}{p_T} + G_1(A_{smear} \oplus \frac{B_{smear}\sqrt{\cosh\eta}}{p_T}) \tag{6.4}$$

where G_1 is a random Gaussian number [41, 42]. The charge q over muon momentum p_T distributions were well described by Gaussian functions.

In tracking systems, the momentum resolution usually goes like $1/L^2$, where L is the actual length of the measured trajectory. Thus, tracks at the edge of the

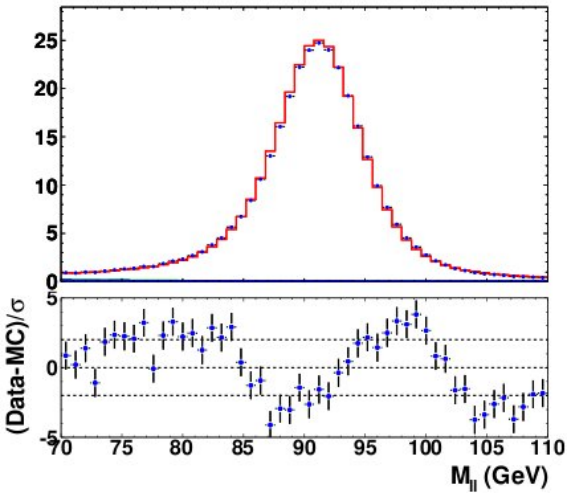

Figure 6.2: Data/MC comparison from $Z/\gamma^{\star} \rightarrow \mu^{+}\mu^{-}$ with original smearing.

detector have a poorer resolution (know as "Lever arm effect"). To have a more accurate description of the resolution, we therefore modify equation 6.1 with

$$\sigma(\frac{q}{p_T}) = \frac{R_{CFT}^2}{L^2}(A \oplus \frac{B\sqrt{\cosh\eta}}{p_T}) \tag{6.5}$$

where R_{CFT} is the radius corresponding to the outermost CFT layer at a average value of 51.69 cm, and L is the radius corresponding to the outermost CFT layer where a hit along its track is found, while the A and B terms are taken at an average value of R_{CFT}. Further studies [40] demonstrate that the η dependence of the resolution is much better described once accounting for the term $\frac{R_{CFT}^2}{L^2}$. As a result, the oversmearing formula 6.6 is modified to

$$\frac{q}{p_T} \rightarrow \frac{q}{p_T} + G_1\frac{R_{CFT}^2}{L^2}(A_{smear} \oplus \frac{B_{smear}\sqrt{\cosh\eta}}{p_T}) \tag{6.6}$$

to account for the lever arm effect. The function could improve the agreement between data and MC and an alternate formula ("Single Gaussian") was still used.

To account for the difference in momentum scale between data and MC, the muon curvature in MC has to be multiplied by a scale factor S, as

$$\frac{q}{p_T} \to (1+S)\frac{q}{p_T} \tag{6.7}$$

The scale factor S multiplies the momentum curvature in MC in order to correct the momentum scale between data and MC.

The most simple way to yield a tail in the resolution consists in having a certain fraction C of track with a much larger resolution. To model the tail observed in the data, we choose randomly in MC the fraction C of muon belonging to the tail. This fraction will be oversmeared according to a new resolution parameter D_{smear}, significantly bigger than A_{smear}, is used to better model the tail instead, leading to the "Double Gaussian" formula.

Based on the discussion of the previous paragraphs, a new scheme is proposed. Two random numbers G_1 and G_2 are drawn with Gaussians. This leads to the new MC reconstructed momentum

$$\frac{q}{p_T} \to (1+S)\frac{q}{p_T} + G_1\frac{R_{CFT}^2}{L^2}(A_{smear} \oplus \frac{B_{smear}\sqrt{\cosh\eta}}{p_T}) \tag{6.8}$$

for fraction C of tracks, and

$$\frac{q}{p_T} \to (1+S)\frac{q}{p_T} + G_2\frac{R_{CFT}^2}{L^2}(D_{smear} \oplus \frac{B_{smear}\sqrt{\cosh\eta}}{p_T}) \tag{6.9}$$

for fraction $1-C$ of tracks. The new expression not only takes care to correct the muon momentum MC curvature related to the Z peak (core region) but also corrects the resolution far from the Z peak (tail region). The method employed to determine the parameters S, A_{smear}, B_{smear}, C and D_{smear} is described in the following.

6.2 Data and MC Samples and Selections

To measure the oversmearing parameters, different data taking epochs and MC events generated by the ALPGEN [49] and PYTHIA [50] are used. We use the methods described above and described also in DØ note [44] to measure the oversmearing parameters for Run IIb3 MC (p20.17) versus Run IIb3 as well as Run IIb3 plus Run IIb4 data taking epochs. Data run number and number of remaining events after selection cuts for $J/\psi \to \mu^+\mu^-$ and $Z/\gamma^\star \to \mu^+\mu^-$ events are shown in Tab. 6.2. For MC, Tab. 6.3 presents the remaining MC events after cuts, while Tab. 6.4 and 6.5 illustrate the corresponding request IDs (a DØ notation) for J/ψ and $Z/\gamma^\star$ samples respectively.

Data Epoch	Run Number	Remaining Events	
		$J/\psi \to \mu^+\mu^-$	$Z/\gamma^\star \to \mu^+\mu^-$
Run IIb3	255,329 - 262,856	1,737,127	125,922
Run IIb4	264,071 - 275,727	1,937,918	140,405

Table 6.2: Remaining $J/\psi \to \mu^+\mu^-$ and $Z/\gamma^\star \to \mu^+\mu^-$ data events after selection cuts with respect to each Data Epoch.

	$J/\psi \to \mu^+\mu^-$	$Z/\gamma^\star \to \mu^+\mu^-$
DØ release for Run II MC	p20.17.02	p20.17.02
CAF version	p21.24.00	p21.24.00
Version of CSG dataset definition	3	3
Remaining Events	47,502	1,396,887

Table 6.3: Remaining $J/\psi \to \mu^+\mu^-$ and $Z/\gamma^\star \to \mu^+\mu^-$ MC events after selection cuts with respect to the MC version. The version numbers refer to different reconstruction releases.

MC version	J/ψ Monte Carlo Request IDs
Run IIb 3	140772, 151212, 151213, 151214, 151215

Table 6.4: Request IDs correspondent to the J/ψ MC version.

$Z/\gamma^\star$ Monte Carlo Request IDs			
MC Version	Subprocess	Mass range GeV	Request IDs
Run IIb3	$Z/\gamma^\star + 0\text{lp} \rightarrow \mu^+\mu^- + 0\text{lp}$	15 — 75	136569,136570,136571,136572,136573,136574,136575,136576,136577,136578 136579,136580,147990,147991,147992,147993,147994,147995,147996,147997 147998,147999,148000,148001,148002,148003,148004,148005,148006,148007 148008,148009,148010,148011,148012,148013
		75 — 130	136607,136608,136609,136610,136611,136612,136613,136614,136615,136616 136617,136618,148066,148067,148068,148069,148071,148072,148073,148074 148075,148076,148077,148078,148079,148080,148081,148082,148083,148084 148085,148086,148087,148088,148089
		130 — 250	136645,136646,148142,148143,148144,148145
		250 — 1960	136656,148156
	$Z/\gamma^\star + 1\text{lp} \rightarrow \mu^+\mu^- + 1\text{lp}$	15 — 75	136581,136582,136583,136584,136585,136586,148014,148015,148016,148017 148018,148019,148020,148021,148022,148023,148024,148025
		75 — 130	136619,136620,136621,136622,136623,136624,148090,148091,148092,148093 148094,148095,148096,148097,148098,148099,148100,148101
		130 — 250	136647,148146,148147
		250 — 1960	136657,148157
	$Z/\gamma^\star + 2\text{lp} \rightarrow \mu^+\mu^- + 2\text{lp}$	15 — 75	136587,136588,136589,148026,148027,148028,148029,148030,148031
		75 — 130	136625,136626,136627,148102,148103,148104,148105,148106,148107
		130 — 250	136648,148148
		250 — 1960	136658,148158
	$Z/\gamma^\star + 3\text{lp} \rightarrow \mu^+\mu^- + 3\text{lp}$	15 — 75	136590,136591,148032,148033,148034,148035,148036,148037
		75 — 130	136628,136629,136630,148108,148109,148110,148111,148112,148113
		130 — 250	136649,148149
		250 — 1960	136659,148159

Table 6.5: Request IDs correspondent to the $Z/\gamma^\star$ ALPGEN Monte Carlo version.

Since muon events with higher number of hits in the SMT and CFT reproduce more accurate track curvatures, the oversmearing should depend on the number of SMT and CFT hits on the reconstructed track. The muon oversmearing parameters may present different values depending on these hits, including having fewer CFT hits if $|\eta| > 1.6$. Thus we define three different types of tracks in the dimuon events for oversmearing parameters determination:

- **Type 1**: both muons have hits in the SMT and are in the central region ($|\eta_{CFT}| < 1.6$)
- **Type 2**: both muons have hits in the SMT and only one muon in the central region ($|\eta_{CFT}| < 1.6$)
- **Type 3**: only one muon has hits in the SMT

The muon oversmearing parameters are also computed considering three different types of muon track qualities: medium, loose and newmedium.

Below is the event selection lists for $J/\psi \to \mu^+\mu^-$ and $Z/\gamma^\star \to \mu^+\mu^-$ events. First of all, we initially select both J/ψ and $Z/\gamma^\star$ events by requiring common selections:

- at least two matched muons of medium quality and opposite charge with $|\eta| < 2.5$
- both muons loosely isolated with $T^{cal}_{0.1<\Delta R<0.4} < 4$ GeV and $T^{trk}_{\Delta R<0.5} < 4$ GeV
- at least one tight isolated muon with $T^{cal}_{0.1<\Delta R<0.4} < 2.5$ GeV and $T^{trk}_{\Delta R<0.5} < 2.5$ GeV
- z vertex cut $|\Delta z(\mu_1, \mu_2)| < 3$ cm
- acolinearity cut $A = |\Delta\phi(\mu_1, \mu_2) + \theta_{\mu_1} + \theta_{\mu_2} - 2\pi| > 0.05$

For J/ψ events, we then require:

- $p^\mu_T > 3$ GeV
- dimuon invariant mass between 2.9 and 3.3 GeV
- only the pair with invariant mass closest to the J/ψ mass of 3 GeV is kept in events containing more than 2 muons
- a pre-scale factor of 50% is applied through an additional random cut due to very high statistics.

For $Z/\gamma^\star$ events, we require:

- $p^\mu_T > 20$ GeV

- dimuon invariant mass close to Z mass
- only the pair with invariant mass closest to the Z mass is kept in events containing more than 2 muons

6.3 Computation of the Oversmearing Parameters

The oversmearing parameters are determined by a χ^2 minimization procedure in which the data and MC invariant mass spectrums are compared. The steps are presented in the following.

As mentioned, the mean value of the invariant mass Z peak is different in the data and MC distribution. To better compare these two distribution, this shift is needed to be taken into account. We fit the distribution of invariant mass around the Z peak of data and MC with a Gaussian function. Then the shift is obtained as the difference of the mean values of the two fitted Gaussian functions.

The next step is χ^2. Before computing a χ^2 between the two invariant mass distributions, the MC distribution is normalized to the data. This is done by counting the number of events in the range on which the χ^2 is computed bin by bin by comparing data and oversmeared MC invariant masses following the formula

$$\chi^2 = \sum_{i=0}^{nbins} \frac{(n_{idata} - \sum_k w_{ikMC})^2}{n_{idata} + \sum_k w_{ikMC}^2} \tag{6.10}$$

where w_{ikMC} is the weight associated to the event. For the $Z/\gamma^\star$ MC, this weight arises not only from the normalization procedure, but also from ALPGEN cross section, Z_{PT} reweighting, muon reconstruction efficiency scale factor, z vertex reweighting and luminosity reweighting.

In order to find the best combination of oversmearing parameters, MC events are smeared while varying the parameters and a χ^2 is computed. The resulted χ^2 map has a minimum for the oversmearing parameters which leads to the best agreement between data and MC invariant mass distributions for $Z/\gamma^\star$ and J/ψ.

Such χ^2 maps we produced in Ref [44] are illustrated on figures 6.3. From left to right and top to bottom, Fig. 1 is the χ^2 map obtained by varying the A and B oversmearing parameters used to oversmear the J/ψ MC distribution. Fig. 2 is the χ^2 map obtained by varying the A and B oversmearing parameters used to oversmear the $Z/\gamma^\star$ MC distribution. Fig. 4 is the χ^2 map obtained by varying the C and D oversmearing parameters used to oversmear the $Z/\gamma^\star$ MC distribution. Fig. 3 is the χ^2 maps summed of the J/ψ and $Z/\gamma^\star$ from Fig. 1 and Fig. 2 respectively. It is clear to see that, χ^2 map has a minimum which leads to the best oversmearing parameters. We see that the J/ψ region mostly determines the parameter B (related to multiple scattering) while the Z region mostly determines the parameter A (related to position resolution).

In order to take into account the shift between the data and MC invariant mass distributions the curvature of the muon track is multiplied by a scale factor S

$$\frac{q}{p_T} \rightarrow (1+S)\frac{q}{p_T} \tag{6.11}$$

Thus the scale factor can be calculated, if both muons have no scale factor applied yet

$$S = \frac{m_{MC} - m_{data}}{m_{data}} \tag{6.12}$$

Or if one muon already has a scale factor

$$S = \frac{m_{MC}^2 - m_{data}^2}{m_{data}^2} \tag{6.13}$$

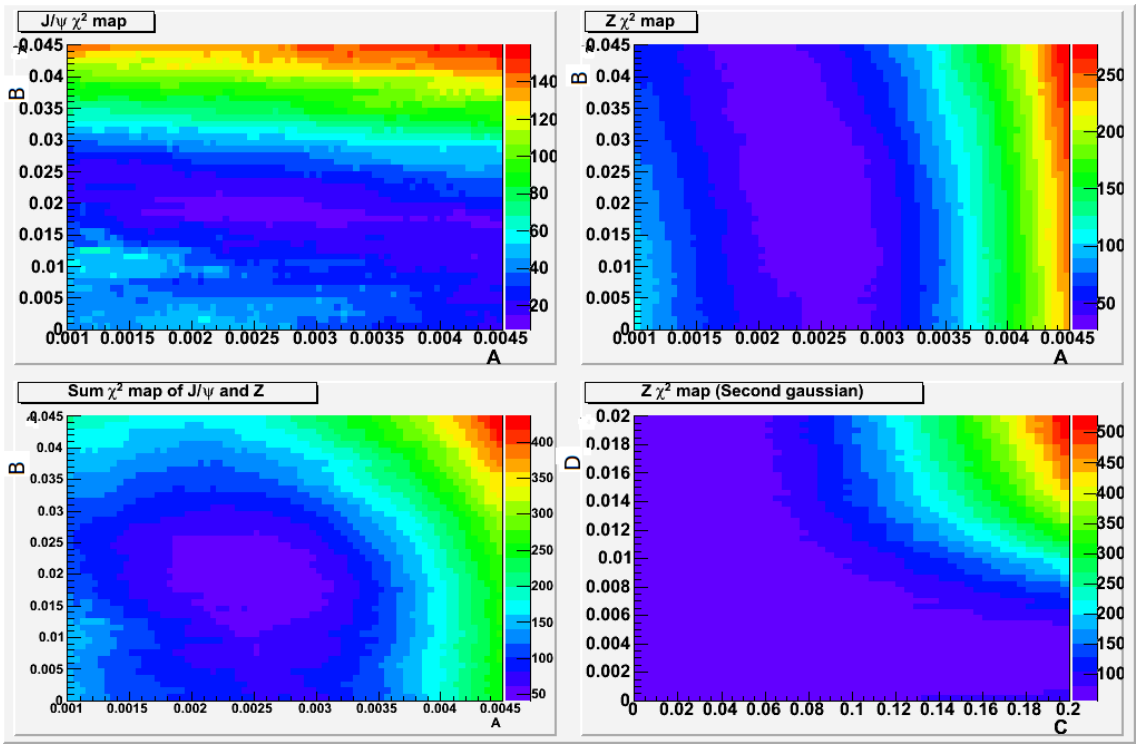

Figure 6.3: χ^2 maps for $Z/\gamma^\star$ and J/ψ events with Type3 and trackmedium quality using II3+II4 Data vs II3 MC.

The double Gaussian model proposed in equation [6.8, 6.9] implies the determination of four parameters. First of all the $Z/\gamma^\star$ and J/ψ data are extracted and the corresponding invariant mass distributions are generated. Then the $Z/\gamma^\star$ and J/ψ MC invariant mass distributions are oversmeared with C and D values fixed and corresponding χ^2 maps are computed. The best (A, B) couple is extracted and the $Z/\gamma^\star$ and J/ψ data distributions are shifted again according to the new found shift parameters A and B. The process is redone until the same couple is found twice. Then, the A and B values are fixed and the $Z/\gamma^\star$ MC are oversmeared, the corresponding χ^2 map is performed and the best (C, D) couple is found. Finally the shift to be applied to the Z peak is converted into a momentum scale factor and the (A, B) and (C, D) parameters are determined a last time.

6.4 Systematic Uncertainties

The muon smearing method uses several techniques to compute systematic uncertainties. To determine the systematic uncertainties, the oversmearing parameters are rederived after modifying either the event selection, the muon selection, the ranges on which χ^2 are computed or how the momentum scale factor is determined. Configuration settings are changed to get new A, B, C, D and S terms. The difference between these last ones and the corresponding central values are summed in quadrature, yielding the total systematic errors for each parameter. For example:

- medium track quality is replaced by loose and newmedium track ones
- medium muon quality is replaced by loose
- 3.5 GeV is using instead of 3.0 GeV in J/ψ p_T cut
- 25 GeV is using instead of 20 GeV in $Z/\gamma^\star$ p_T cut
- Changing the range used to extract the oversmearing parameters via χ^2 minimization from 72 GeV $< m_{\mu\mu} <$ 108.5 GeV to 67 GeV $< m_{\mu\mu} <$ 113.5 GeV

6.5 Results of Muon Oversmearing Parameters

All the results of Run II3 + II4 data versus Run IIb3 MC with different track qualities and types of track, is summarized in Tab. 6.6. Parameters with the modeling of the momentum tail turned off have also been computed as they are supposed to be more suitable for some new physics search, which is also called "Single Gaussian".

	Track	Type	$A(\times 10^{-3})$	$B(\times 10^{-2})$	$C(\times 10^{-2})$	$D(\times 10^{-3})$	Scale $(\times 10^{-2})$	χ^2/N_{DoF}
Double Gaussian	medium	T1	1.5200 ± .0447	1.275 ± .1897	3.10 ± 1.3413	6.1 ±.5656	0.2216 ± .1705	1.1776
		T2	1.5600 ± .5544	0.725 ± .9919	0.90 ± 3.8662	5.1 ± 6.5115	0.2170 ± .2302	1.13766
		T3	1.9750 ± .5512	1.150 ± 1.2875	5.40 ± 7.2050	9.0 ± 5.3823	0.7032 ± .6153	0.677087
	loose	T1	1.4800 ± .0469	1.175 ± .3818	4.50 ± 1.4866	5.6 ± .8944	0.2276 ± .1918	1.10616
		T2	1.5600 ± .2666	0.775 ± .7871	4.90 ± 4.1125	0.3 ± 2.8160	0.1468 ± .1655	1.02155
		T3	2.2250 ± 1.1592	0.550 ± 1.1237	6.60 ± 6.2148	9.4 ± 8.1271	0.6170 ± .5200	0.82921
	newmedium	T1	1.4800 ± .0574	1.225 ± .2179	4.50 ± .8766	6.6 ± 1.1401	0.2152 ± .1910	1.06765
		T2	1.5200 ± .1676	0.575 ± .7021	2.90 ± 2.6300	6.8 ± 6.0835	0.1730 ± .1892	1.10824
		T3	2.5250 ± .7966	1.950 ± .9759	2.60 ± 3.1679	17.8 ± 18.4100	0.4164 ± .3436	0.818105
Single Gaussian	medium	T1	1.6000 ± .0583	1.275 ± .2824	0	0	0.2562 ± .1378	3.01126
		T2	1.6800 ± .2655	0.125 ± .6216	0	0	0.0868 ± .1166	1.25491
		T3	2.1750 ± .5268	1.650 ± .9620	0	0	0.6874 ± .5246	0.905568
	loose	T1	1.6000 ± .0591	1.225 ± .2983	0	0	0.2568 ± .1630	3.02397
		T2	1.5600 ± .1979	0.725 ± .7353	0	0	0.1310 ± .1516	1.10388
		T3	2.4750 ± .3315	1.650 ± 1.3688	0	0	0.6722 ± .6869	1.11885
	newmedium	T1	1.6400 ± .0787	1.275 ± .2410	0	0	0.2752 ± .1385	4.4772
		T2	1.6400 ± .3439	0.575 ± .6555	0	0	0.1595 ± .1769	1.40254
		T3	2.8750 ± 1.4322	1.650 ± 1.1147	0	0	0.5340 ± .4667	1.02376

Table 6.6: Summary of all the oversmearing parameters for different track selections, types of tracks, by Double-Gaussian and Single-Gaussian for RunIIb3 + RunIIb4 data versus RunIIb3 MC.

Errors are already combined by statistics and systematics. Due to the instability of the method in cases with a lack of statistics, the errors on the second Gaussian terms can be very high. They are forced to 100% if they are greater than this number. More specifically, the statistical and systematic errors for different types of track and different track qualities are presented in Tables A.1, A.2 and A.3 for Run IIb3 + Run IIb4 data versus Run IIb3 MC in Appendices A. A careful analysis of the $Z/\gamma^\star \to \mu^+\mu^-$ invariant mass distributions are shown in Appendices B which allows us to better determine the MC oversmearing. One can compare data with non-smeared MC and with smeared MC using either double or single Gaussian, as well as verifying those distribution taking into account different track quality. It also provides $\frac{Data-MC}{\sigma}$ for a better visualization of discrepancies between those distributions.

Muon oversmearing parameters for different Data taking epochs versus Monte Carlo version were produced and the oversmearing parameters are computed for both double and single Gaussian smearing formulations. The difference is small be-

tween them. However, there are substantial difference when comparing the χ^2/N_{DoF}. Table 6.7 shows χ^2/N_{DoF} values of double and single Gaussian from Run II3+II4 Data versus Run II3 MC oversmearing with different track qualities.

Track quality	Type	χ^2/N_{DoF} of DG	χ^2/N_{DoF} of SG
trackmedium	T1	1.1776	3.01126
	T2	1.13766	1.25491
	T3	0.677087	0.905568
trackloose	T1	1.10616	3.02397
	T2	1.02155	1.10388
	T3	0.82921	1.11885
tracknewmedium	T1	1.06765	4.4772
	T2	1.10824	1.40254
	T3	0.818105	1.02376

Table 6.7: χ^2/N_{DoF} values from muon oversmearing parameters using different track quality. Values are compared for Double Gaussian (DG) and Single Gaussian (SG).

Some versions of the MC included track inefficiency which were in agreement with data. So, it is not true that all combination of data with MC needs smearing, and the $Z/\gamma^\star \to \mu^+\mu^-$ invariant mass distributions allow a determination which one of these pairs really need a MC oversmearing. One can compare data with non-smeared MC and with smeared MC using either Double or Single Gaussian, as well as verifying those distributions taking into account different track qualities of muon selections.

Figure 6.4 and 6.5 illustrates the $Z/\gamma^\star \to \mu^+\mu^-$ invariant mass before and after applying the smearing parameters in MC events. As one can see, We have better agreement in the central and tail region between data and MC events after including the muon oversmearing parameters.

The parameter results of all different data taking epochs (Run IIa, IIb1-IIb4) and MC version can be found in DØ notes [40, 43, 44, 45]. Information is summarized

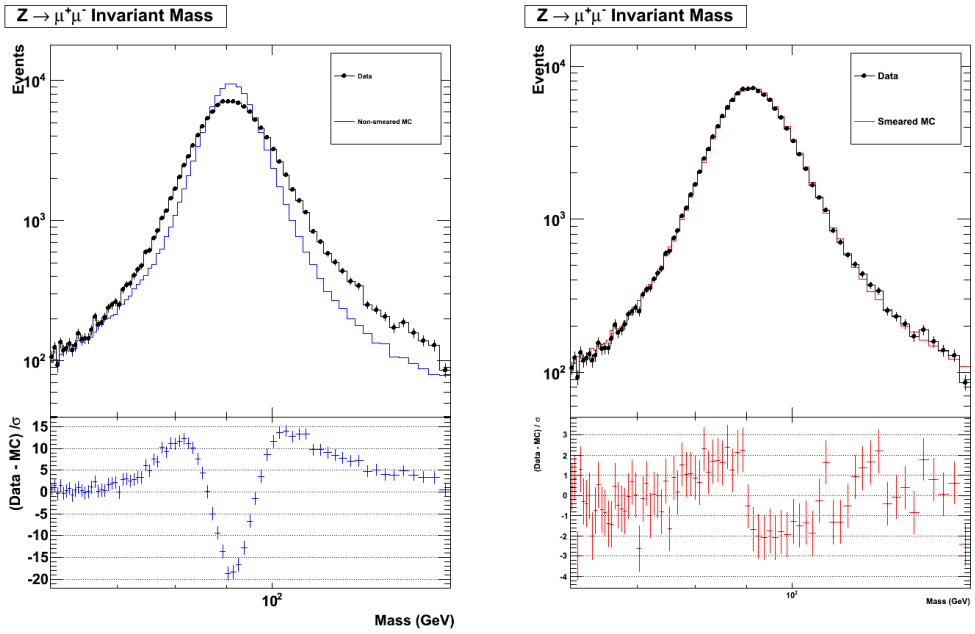

Figure 6.4: Data and MC invariant mass in central region ($|\eta_{CFT}| < 1.6$) before (left) and after (right) DG smearing using Run IIb3 MC vs Run IIb3+IIb4 data and trackmedium quality.

in Tab. 6.1. The analysis below will include all the muon oversmearing results as appropriate for the data period and MC version.

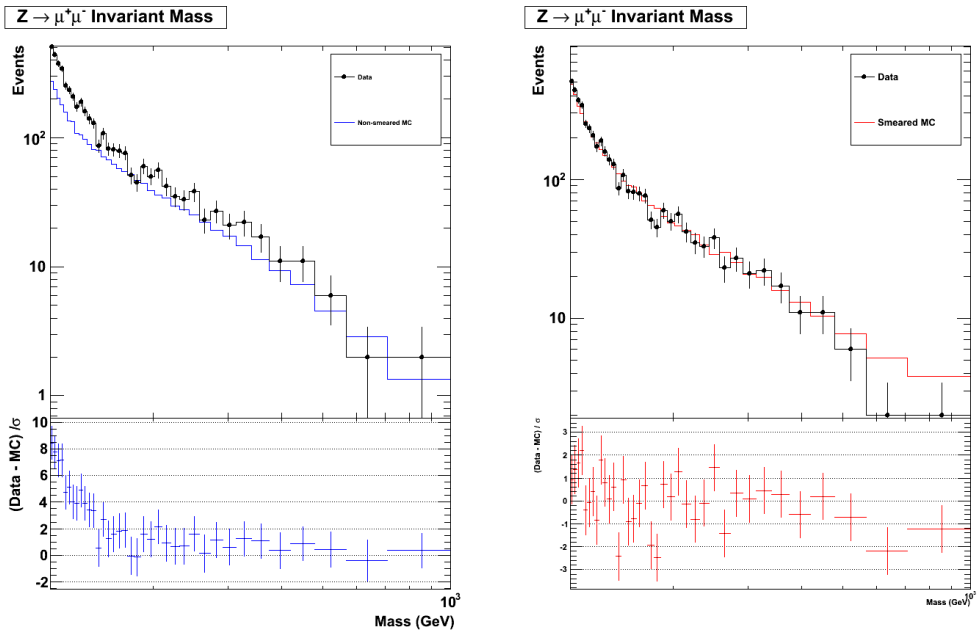

Figure 6.5: Data and MC invariant mass in the tail region before (left) and after (right) DG smearing using Run IIb3 MC vs Run IIb3+IIb4 data and trackmedium quality.

CHAPTER 7

MEASUREMENT OF THE ZZ CROSS SECTION

7.1 Introduction

7.1.1 Z Boson Pair Production

Based on the Drell-yan process we mentioned in Sec. 2.2.4, the dominate tree-level diagram in the Standard Model for $q\bar{q} \to Z/\gamma^* Z/\gamma^* \to \ell^+\ell^-\ell'^+\ell'^-$ at high mass is shown in Fig. 7.1, where ℓ represents electrons or muons. Below in the analysis, Z will be used as a short hand notation for Z/γ^* and this analysis will use Z/γ^* with masses > 30 GeV. Another SM diagram, which contributes at low mass is shown in the diagram in Fig. 7.2.

Another possible Standard Model diagram that has four leptons in the final state is heavy Higgs decaying to ZZ or ZZ^*, $H \to ZZ \to \ell^+\ell^-\ell'^+\ell'^-$ [64, 65]. There is also the possibility of anomalous trilinear Z couplings. Additionally, there are non-Standard Model processes that have four leptons in the final state. These will not be discussed further in this thesis.

The Z bosons decay essentially instantaneously (life time on order of 10^{-25} s) into same flavor fermion anti-fermion pairs. For this analysis, we only study the final states where both Z bosons decay to charged leptons, excluding τ leptons. Therefore, the three charged leptonic decay channels studied are:

- $ZZ \to eeee$

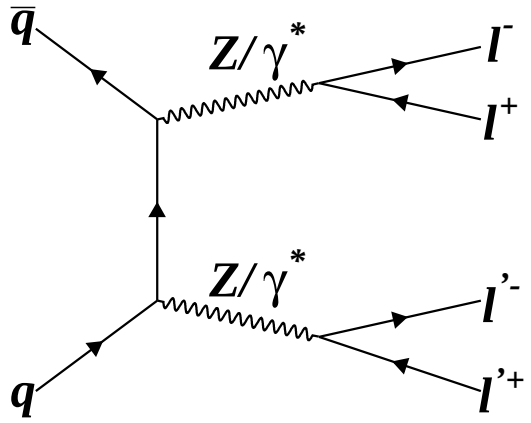

Figure 7.1: The dominant tree-level Feynman diagram for $q\bar{q} \to ZZ \to \ell^+\ell^-\ell'^+\ell'^-$.

- $ZZ \to \mu\mu\mu\mu$
- $ZZ \to ee\mu\mu$ ($\mu\mu ee$)

At the Tevatron collider, protons collide with anti-protons moving in the opposite direction at $\sqrt{s} = 1.96$ TeV (Sec. 3). The proton is made up of three quarks (u, u, d) and a sea of gluons. Z bosons do not couple to gluons directly and Z bosons are produced primarily from quark anti-quark pairs from the colliding of protons and anti-protons at the Tevatron. The t-channel diagram for Z boson pair production is already shown in Fig. 7.1. There is no s-channel diagram for Z boson pair production, because there are no neutral trilinear gauge boson couplings in the SM.

At $\sqrt{s} = 1.96$ TeV, the $p\bar{p} \to Z/\gamma^*Z/\gamma^*$ predicted cross-section with one loop corrections (NLO) is 1.43 ± 0.1 pb.This prediction is made using version 6.2 of the `MCFM` MC [46] with the CTEQ61M PDF set [47] and was made with the same generator level high mass selections as used in this analysis ($M_1(Z/\gamma^*) > 30$ GeV,

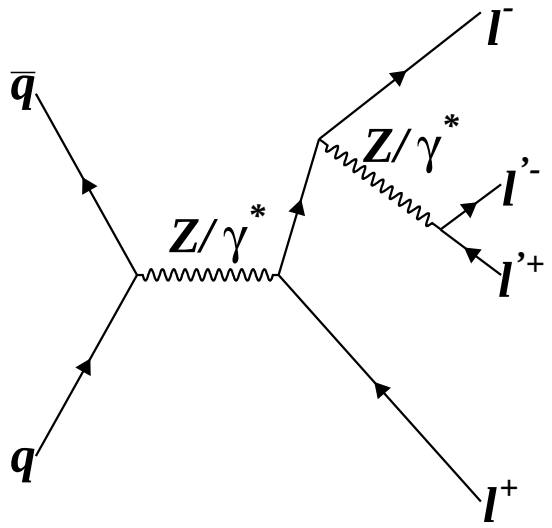

Figure 7.2: The singly resonant Feynman diagram for $q\bar{q} \to ZZ \to \ell^+\ell^-\ell'^+\ell'^-$.

$M_2(Z/\gamma^*) > 30$ GeV). The Born cross-section is 1.2 pb and therefore the K factor [48] K(NLO) $= \sigma^{NLO}/\sigma^{LO} = 1.6/1.2 = 1.33$. It should be noted that version 6.2 of `MCFM` does contain both diagrams from Fig. 7.1 and Fig. 7.2. It is also known that the MC used to generate our signal samples, `PYTHIA` [50], does not contain the diagrams associated with Fig. 7.2. By "turning of" the diagrams associated with Fig. 7.2 within `MCFM`, we determine it only has about 1.5% effect on the cross section in the mass region under study for this analysis ($M_1(Z/\gamma^*) > 30$ GeV,$M_2(Z/\gamma^*) > 30$ GeV). We therefore conclude the event though `PYTHIA` does not contain the diagrams associated with Fig. 7.2 the effect is negligible.

7.1.2 Signal, Background and Studies

The branching fractions (BF) for Z boson decay [5] are shown in Table 7.1. The branching fraction for $Z \to \ell\ell$ is approximately 0.034 per channel, so the predicted

Decay channel	Branching fraction (%)
e^+e^-	3.343 ± 0.004
$\mu^+\mu^-$	3.346 ± 0.007
$\tau^+\tau^-$	3.350 ± 0.008
invisible	20.00 ± 0.06
hadrons	69.91 ± 0.06

Table 7.1: Branching Fractions for Z boson decays.

cross section times branching fraction for $p\bar{p} \to ZZ \to \ell^+\ell^-\ell'^+\ell'^-$ is about 1.8 fb for the $eeee$ and $\mu\mu\mu\mu$ channels, and 3.6 fb for the $ee\mu\mu$ channel. That is a total of 7.2 fb for all three channels, so approximately 70 events in total are expected to be produced with an integrated luminosity of 10.4 fb^{-1}. However, because of limited detector geometric and kinematic acceptance, as well as lepton selection cuts, far fewer events are expected.

There are not many other Standard Model processes which can lead to four high p_T isolated leptons in the final state. Thus, expected background contamination is small. We have considered the following sources of background (Sec. 7.6). The largest fraction of the background results from $Z(\to \ell\ell)$ + jets / $Z(\to \ell\ell) + \gamma$ + jets production (referred to as QCD background), in which a jet has been misidentified as a lepton. Other backgrounds come from $t\bar{t} \to W^+bW^-\bar{b}$ production with subsequent leptonic W and semileptonic $b/\bar{b}$ decays.

Z boson pair production was studied at the CERN LEP2 collider by the L3 [51], OPAL [52], ALEPH [53] and DELPHI [54] collaborations in multiple final states, including $e^+e^- \to \ell\ell\ell\ell$. The LEP experiments have also set limits on anomalous ZZZ and $ZZ\gamma$ couplings [55].

The Tevatron experiments have also looked for the pair production of Z bosons. The DØ analysis of $ZZ \to \ell^+\ell^-\ell'^+\ell'^-$ lepton production with 1.1 fb^{-1} Run IIa data yielded an upper limit of 4.4 pb on the ZZ production cross section at 95% C.L.

Additionally, limits on anomalous ZZZ and $ZZ\gamma^*$ couplings were also derived [56]. DØ has also looked for ZZ production in the $ZZ \to \ell^+\ell^-\nu\nu$ decay mode with 2.2 fb^{-1} of data. The search yielded a 2.33σ observation with a measured cross section of $\sigma(ZZ) = 1.9 \pm 1.0$ (stat.) ± 0.4 (syst.) pb [57]. The CDF experiment has used 1.9 fb^{-1} of data to look for Z pair production. The observed significance in the combined $\ell^+\ell^-\ell'^+\ell'^-$ and $\ell^+\ell^-\nu\nu$ channels is 4.4σ, and the measured cross section is $\sigma(ZZ) = 1.4^{+0.7}_{-0.6}$ (stat. + sys.) pb [58]. The ATLAS Collaboration has observed $pp \to ZZ$ production in the four charged lepton final state in 1.0 fb^{-1} data at $\sqrt{s} = 7.0$ TeV [59]. The CMS Collaboration has measured $\sigma(pp \to ZZ)$ in 5.0 fb^{-1} data at $\sqrt{s} = 7.0$ TeV [60], and has observed the rare decay $Z \to \ell^+\ell^-\ell'^+\ell'^-$ with a branching fraction in agreement with the SM prediction [61].

This thesis is based on our ZZ to four charged lepton analysis with DØ Collaboration [62, 63], which was already published in Physical Review D [64].

This chapter mainly discusses the methods used to search for the four charged leptons final state from ZZ boson pairs decaying, and to measure the corresponding cross section (σ). The number of events N_{exp} expected to be observed in a channel is:

$$N_{exp} = \sigma \cdot BF \cdot L \cdot Acc + Bkg \tag{7.1}$$

where σ is cross section, BF is branching fraction, L is the luminosity, Acc is the acceptance and Bkg is the background.The quantities Acc, Bkg and N_{exp} are measured or calculated for each channel to extract the final production cross section for the four lepton channel.

7.2 Data Sample

7.2.1 Data Set

The data sample used for this analysis corresponds to the full Run IIa and Run IIb (Run IIb1, IIb2, IIb3 and IIb4) datasets collected with the DØ detector from the period of 2001 through September 30, 2011 consisting of runs number in the range from 151817 up to 275727. The number of events collected are about 10 billion.

We use a subsample of data that was preselected to be used by many analyses. The *eeee* channel uses a preselection with two electrons with high transverse momentum ($p_T > 15$ GeV), named as 2EMhighpt in DØ. The $ee\mu\mu$ and $\mu\mu\mu\mu$ channels use the subset with two muons with high transverse momentum, named as 2MUhighpt [66], which requires at least 2 loose muons with $p_T > 15$ GeV measured by the central tracking system.

7.2.2 Data Quality

Only a small fraction is recorded by the DØ detector out of all the data delivered by the Tevatron. A fraction of data in which all detector system are functioning well and reconstructed well by the event reconstruction is then used for the data analysis presented. The quality of the detector is monitored throughout the data taking period and assigned data quality (DQ) levels.

The data quality monitoring is performed both online and offline. Online monitoring guarantees immediate reaction. It catches the malfunction of detector com-

ponents including readout as well as triggering electronics. The remaining deficient data is eliminated by offline checks by comparing basic distribution of physics objects. When noticed, either while data taking or during reconstruction, that part of the DØ detector was malfunctioning, data events are classified as "bad". There are separate bad flags for the calorimeter, SMT, CFT, muon systems and triggers. In addition to keeping quality information for each run, the data taking is broken down into intervals of approximately constant integrated luminosity, called luminosity blocks. Each luminosity block is indexed by a luminosity block number (LBN) to build the basic unit of time for luminosity measurement. The LBN monotonically increases after each run or store transition.

There are two different DQ considered in this analysis. One is normal DQ requirement, events with "bad" run and LBN quality for SMT, CFT, calorimeter and muon subsystems are removed. This DQ is used the most in DØ. In order to obtain better signal efficiencies, no run or LBN based data quality requirement are used. However, events flagged "bad" for the following common calorimeter problems are rejected: calorimeter noise, `cal_empty_crate`, `cal_ring_of_fire`, `cal_noon_noise`, `cal_sca_failure`, `cal_coherent_noise` or `cal_spanish_fan` criteria [67] . The `cal_coherent_noise` means "hot" cells in a tower at the same readout time of the calorimeter, which is due to the hardware failure or a pedestal drift and may produces fake jets and electrons. These data criteria represents the same data quality requirements used in the Z p_T precision measurement [68].

7.2.3 Trigger and Trigger Efficiency Estimation

Because this analysis looks for one of the smallest cross section process in the SM, which also has very little background, we try to apply very loose selections. With that in mind we do not make any explicit trigger requirements. This means that events which pass any trigger are considered as long as they pass preselection cuts. There are many triggers which fire on the presence of one or more high momentum muons or electrons with looser requirements than are made at the preselection level. Trigger efficiency is considered the fraction of events which pass all final selection cuts to the events which also pass the trigger. Since our final state is four high p_T leptons, we assume an almost 100% trigger efficiency. We also estimate that the trigger efficiency for our signal is 99% with an error of 1% below.

To maximize the signal acceptance, we do not apply any trigger requirements on the leptons beyond those used to get into the official preselection defined in Sec. 7.2.1. To study the trigger efficiency, we use the 4μ channel, as muons have a lower trigger efficiency than electrons. Using 2MUhighpt skimmed data, we compare the total number of events reconstructed to the number of events gathered by a single muon OR trigger. The result is an average efficiency of 99%. We do not repeat the study for 2EMhighpt skimmed data, but as the single electron trigger is more efficient than the single muon, we will expect it to be higher. We do not apply the trigger efficiency to the MC samples, but we correct for any deviations by a 1% systematic uncertainty to the signal and background samples (Sec. 7.7). It should be noted that four nseg0 muons can not pass any triggers. To cross check the trigger efficiencies values, we did a simple estimation. Based on the MuonID certification analysis, we can know $Acc \times eff$ for looseNCV plus nseg0 muon is 0.96 for both data and

MC, $Acc \times eff$ for mediumnseg3NCV muon is 0.73 for data and 0.75 for MC. The muon trigger requirements, that is the hits in the wire chambers and scintillators, are mostly that for mediumnseg3, and so the trigger efficiency is the ratio of these plus a 5% inefficiency for the tracker part of the trigger which is p_T dependent. But our muons are high p_T final state, which makes the average single muon trigger efficiency for data equal to $0.95 \times 0.73/0.96 = 0.72$. The reality is that for most data, the efficiency has a $\eta - \phi$ bias due to failed A layer PDTs and the efficiency becomes 0 when there is a failure and 0.75 if there is no failure. So the number 0.73 is "low" but conservative. For those muons with an A layer PDT failure, the trigger will fail for that muon but it is still reconstructed as looseNCV. There will be two conditions: (i) four muons without A layer PDT failure, the efficiency for none to pass the trigger is $0.28^4 = 0.006$; (ii) four muons with one in A layer PDT failure region, efficiency for none of the other three to pass the trigger is $0.28^3 = 0.022$. If we assume 97% muons are in the condition (i) and the remaining 3% are in (ii), the overall trigger efficiency is $0.97 \times 0.994 + 0.03 \times 0.978 = 0.993$. In short, this rough estimation quite agrees with our value of 99%.

7.2.4 Integrated Luminosity

The integrated luminosity for each channel is determined via an unprescaled trigger from the trigger list that covers the full data range after applying data quality corrections as listed in Table 7.2. A luminosity uncertainty of 4.3% is assigned and determined by the DØ luminosity group [69]. With the "no bad" very loose DQ described in previous section, the integrated luminosity for the whole 2EM and 2MU dataset is $\int \mathcal{L}\ dt$= 10.4 fb^{-1}. It drops to 9.7 fb^{-1} if normal DQ is used.

Run Epoch	Integrated Luminosity (pb^{-1})	
	Loose DQ	Normal DQ
Run IIa	1244 ± 53	1079 ± 46
RunIIb	9200 ± 396	8670 ± 373
Total	10444 ± 449	9749 ± 419

Table 7.2: Run IIa and IIb luminosities.

7.3 Identification and Definition

In this section, we describe the selection criteria for all muons and electrons used in this analysis. Jets are not used in identifying signal, but are used in estimating the background.

7.3.1 Good Muons

The definition of "good muons" in the $\mu\mu\mu\mu$ and $ee\mu\mu$ channels is:

- $|\eta| < 2.5$
- looseNCV or nseg=0 muon quality
- Muons matched to a central track
- trackloose track quality: $|\Delta Z_{DCA}| < 0.04$ cm with SMT hits, or $|\Delta Z_{DCA}| < 0.2$ cm without SMT hits
- Muon Isolation:

  nseg > 0 muons: **TrkLooseScaled** isolation

  $\frac{T^{trk}-0.005\mathcal{L}}{p_T^{\mu}} < 0.25$, $\frac{T^{cal}-0.005\mathcal{L}}{p_T^{\mu}} < 0.4$. As mentioned in Sec. 5.3.4, we did not use

the exact MuonID certification isolation working point. Instead, a luminosity correction $-0.005\mathcal{L}$ is added to better model the luminosity dependence of the halo isolation and make the isolation variables distribution flatter [70], where $\mathcal{L}$ represents the instantaneous luminosity. Adding this term increases the isolation efficiency by about 1% to TrkLooseScale which is already >98%. Any systematic error on modeling this is very small as the efficiency is so close to 100%.

nseg=0 muons: **TopScaledTight** isolation

$\frac{T^{trk}-0.005\mathcal{L}}{p_T^{\mu}} < 0.1$, $\frac{T^{cal}-0.005\mathcal{L}}{p_T^{\mu}} < 0.1$. This definition is also modified which will increase the isolation efficiencies.

The isolation requirements are applied in order to suppress QCD and $t\bar{t}$ background contamination, where muons may be generated by quark decays into jets and therefore are expected to be accompanied by significant activity around the subject muon. Tag and probe measurements [36] give an isolation efficiency > 99% for nseg>0 muons and > 95% for nseg=0 muons. As the efficiency is so high, all muons in both the $\mu\mu\mu\mu$ and $ee\mu\mu$ channels are required to be isolated.

7.3.2 Muon ID Efficiencies

The following discussion of muon efficiencies is continued after Sec. 5.4. The data/MC scale factors applied to the MC muons for the looseNCV requirement are measured using $Z \rightarrow \mu^+\mu^-$ events and parametrized as a function of $\mathcal{L}$, ϕ and η_D [69, 35]. The data/MC scale factors applied to the MC muons for the central track requirement are parametrized as a function of z_{vtx} versus η_{CFT} and $|\eta_{CFT}|$ versus $\mathcal{L}$. Isolation is parametrized in η_{CFT} versus p_T versus ΔR(μ,closest jet) and

$|\eta_{CFT}|$ versus $\mathcal{L}$. The isolation corrections are parametrized as a function of $|\eta_{CFT}|$, p_T and ΔR between the muon and the closest 15 GeV jet. These scale factors are applied to all the relevant distributions and numbers. The RunIIb efficiencies for looseNCV vary from 90.6% to 91.4%. Of this, about 82% are nseg=3, 8% are nseg=2, and 2% are nseg=1 for muons from Z, while nseg=0 adds about an additional 5% per muon, and about an additional 24% for the 4-muon acceptance (from 0.69 to 0.85). Note, from studies shown at the 2012 Lancaster workshop [71], the muon certification process appears to underestimate the loose efficiency by 1-2%, which increase the nseg=3 value to about 83-84% while lowering the nseg=0 to about 3-4%. The trackloose efficiency varies from 90.7% to 92.4%. The TopScaledTight efficiency varies from 93.3% to 95.1% while the TrkLooseScaled efficiency varies from 98.3% to 99.0%. The isolation efficiencies are $99.5 \pm 0.3\%$ for nseg>0 muons and $97.0 \pm 1.0\%$ for nseg=0 muons. Note that, the real efficiencies were increased, because of our luminosity correction.

We require the muon to be matched to a track as to get the best possible momentum measurement. The ΔZ_{DCA} requirements helps to reduce poorly reconstructed or faked tracks. About 90% of the tracks which pass trackloose quality have SMT hits; those who do not have their momentum corrected for the z_{vtx}. Chapter 6 already studied the muon momentum resolution, and the amount of "oversmearing" that is needed for the MC to produce the same resolution as seen in the date. From these studies, the difference in resolution between different tracking categories was seen to be small, and a momentum resolution of $0.02 \oplus 0.0025 p_T$ was determined. From this, it is about a 6σ (4σ) effect for a $p_T = 60$ GeV (100 GeV) for a muon to have its charge flipped. As those events will also have their muon momentum badly measured, we will require that dimuon pairs have opposite charge. The acceptance loss is less than 0.3% and modelled by smeared MC.

7.3.3 Good Electrons

The definition of "good electrons" in $eeee$ and $ee\mu\mu$ channels is:

- We use the electron ID so called "Point0" [72], which is illustrated below:
  - |EMID| = 11 or 10 (Variable is assigned to EM cluster which is matched (or not matched) to a track reconstructed from the central tracking system. Sec. 4.3)
  - $f_{EM} \geq 0.90$.
  - $|\eta_D| < 1.1$ (CC) or $1.5 < |\eta_D| < 3.2$ (EC)
  - Further CC specific selections:

    $isolation \leq 0.09$

    $IsoHC4 < 4.0$ GeV (Track isolation variable)

    Track Match $\chi^2 > 0.0$ or Hit-on-Road Discriminant > 0.6

    $NNout7 > 0.4$ (Outputs of 7 variable neural-networks)
  - Further EC specific selections)

    $isolation \leq 0.10$

    $HMx8 \leq 40$ (Eight variables H-Matrix used to discriminate between EM and hadronic showers)

    $IsoHC4 < 2.5$ GeV $\times |\eta_D| + 7.0$ GeV

    $NNout3 > 0.05$

    $\sigma_\phi < 100$ (The width of the EM cluster at the 3rd layer of the EM calorimeter)

More detailed definition of these variables can be found in EM reconstruction Section 4.3. The Data/MC scale factors are applied to MC electrons for the "Point0" requirement and are parametrized as a function of $\mathcal{L}$, η_D and ϕ_D. These scale factors are applied to all the relevant distributions and numbers.

7.3.4 ICD Electrons

In the calorimeter Section 3.3.2.2, we talked about the three separate cryostats. To reduce the loss of performance, additional layers of sampling detectors are added in the form of scintillating counters between the CC ($|\eta| < 1.1$) and EC ($1.5 < |\eta| < 2.5$). These counters are called the Inter Cryostat Detector (ICD, $1.1 < |\eta| < 1.5$). They have exactly the same segmentation as CC and EC. In addition, separate single cell scintillator structures, called massless gaps, are installed inside the cryostat. The ICD allows sampling of the region between CC and EC to improve the energy resolution.

For the *eeee* analysis, we expand our electron acceptance into the intercryostat region of the detector by allowing in ICD electrons. These electrons are initially reconstructed as τ objects. The details of ICD. electron reconstruction can be found in [73, 74, 75, 76], and are illustrated below:

Within the ICD, there is incomplete EM calorimeter coverage. ICD electrons are initially reconstructed as tau objects and must satisfy $1.1 < |\eta| < 1.5$. The candidate must be matched to a central track with $p_T > 15$ GeV, and track momentum is used to estimate ICD electron p_T whose E_T in the calorimeter must be greater than 10 GeV. Additionally, the electron must pass a minimum EM + ICD energy fraction

cut that varies with $|\eta_D|$, pass a cut on a neural network output to distinguish hadronic taus from jets, and pass a cut to distinguish ICD electrons from jets.

The Data/MC scale factors are applied to ICD electrons in the MC and are parametrized as a function of η_D and ϕ_D. These scale factors are applied to all the relevant distributions and numbers.

7.4 Event Selection

Events in all three channels must pass data quality cuts which are described in previous sections. This section will summarize the different selection criteria for each topology.

7.4.1 $\mu\mu\mu\mu$ Channel

7.4.1.1 Selections

After passing data quality, muons are selected with muon quality looseNCV or nseg=0 and track quality trackloose. Additional selections for acquiring $\mu\mu\mu\mu$ events are:

- At least 4 "good" muons
- $\Delta z_{DCA} < 3.0$ cm between all muon pair tracks
- All muons are required to be isolated
  - nseg=0 muons are TopScaledTight isolated with luminosity correction

  - nseg>0 muons are TrkLooseScaled isolated with luminosity correction

- Muon charges should have opposite sign (that is $\sum_{i=1}^{4} q_i = 0$)

- All muon $p_T > 15.0$ GeV

- Both pairing of oppositely charged leptons are considered and we require the dimuon invariant mass [1] $M_{\mu\mu} > 30$ GeV for both pairs

We define the "best" dimuon pair is the set of oppositely charged muon pair whose invariant mass is closest to the Z mass (91.2 GeV). The second muon pair is called the other dimuon pair.

The cut flow for $ZZ \to \mu\mu\mu\mu$ data for both Run IIa and Run IIb is shown in Tab. 7.3. As a reference, weighted MC cut flow for $ZZ \to \mu\mu\mu\mu$ is also shown in Tab. 7.4. The weights for luminosity, ZZ p_T, and vertex z are applied at the initial stage. The corrections for the difference between data and MC muon efficiencies are applied after the four good muon selection, and labeled as "MuonCorr weighting" in this table. For Run IIb, this correction is 0.948 for four muons, or 0.987 per muon.

Cut	Run IIa Events	Run IIb Events
Initial	9776282	139915578
Data Quality	7956763	127068539
Trigger	7956763	127068539
4 good muons	664	801
Track $\Delta z_{DCA} < 3$ cm	3	13
Muon Isolation	3	13
Muon opposite charges	0	5
Muon $p_T > 15$ GeV	0	3
Dimass $M_{\mu\mu} > 30$ GeV	0	3

Table 7.3: Run IIa and IIb: Cut flow for $\mu\mu\mu\mu$ Data.

[1] $M_{\mu_1\mu_2} = \sqrt{(E_1+E_2)^2 - (p_{1x}+p_{2x})^2 - (p_{1y}+p_{2y})^2 - (p_{1z}+p_{2z})^2}$

Cut	Run IIa Events	Run IIb Events
Initial	194731	1114754
Data Quality	188157	1069667
Z Mass generated > 30 GeV	17983.1	103545
Trigger	17983.1	103545
4 good muons	8097.53	36575.7
MuonCorr weighted	6944.67	34752.1
Track $\Delta z_{DCA} < 3$ cm	6932.75	33686.5
Muon isolation	5918.75	28363.3
Muon opposite charges	5013.21	23949
Muon $p_T > 15$ GeV	4915.26	23438.5
Dimass $M_{\mu\mu} > 30$ GeV	4852.39	23109.3

Table 7.4: Run IIa and IIb: Cut flow for $\mu\mu\mu\mu$ weighted MC signal.

Note that, this cut flow tables are associated with normal DQ. We studied the data and MC based on the loose DQ, that is including the "bad" run and LBN quality events, which are presented in Tab. C.1 of the Appendix C. All the results below come from normal DQ. However, to get better statistics, figures below are coming from loose DQ, as it has more candidate events.

7.4.1.2 Muon Quality and Charge

The muon nseg and charge information with the cut flow is shown in Tables 7.5-7.8 for data and MC. In this section, we use the full 4μ samples with loose DQ in order to have better statistics. As a result, 7 events are observed after all selection cuts with loose DQ in 4μ channel compared to 3 events observed with normal DQ in the previous section.

We can see all final muons are required to have opposite signs $2\mu^+2\mu^-$. Muon charge takes the place of the previous acoplanarity cut as well as space angle cut to exclude backgrounds such as from Z+jets events. Finally, all the candidate

muons are actually nseg=2 and nseg=3, consistent with the relative acceptance of the various muon topologies (for 28 muons, one expects about 24-25 to be nseg=3, 2-3 to be nseg=2, 0.5 to be nseg=1, and 0.9-1.5 to be nseg=0).

Type	Cut	All events	$2\mu^+2\mu^-$	$3\mu^+\mu^-$ or $3\mu^-\mu^+$	$4\mu^+$ or $4\mu^-$
Run IIa	4 good muons	1943	964	851	128
	Track $\Delta z_{DCA} < 3$ cm	815	475	327	13
	Isolation	3	3	0	0
	Charge and $p_T > 15$ GeV	0	0	0	0
	Dimass $M_{\mu\mu} > 30$ GeV	0	0	0	0
Run IIb	4 good muons	10476	5060	4774	642
	Track $\Delta z_{DCA} < 3$ cm	4048	2343	1623	82
	Isolation	18	14	4	0
	Charge and $p_T > 15$ GeV	7	7	0	0
	Dimass $M_{\mu\mu} > 30$ GeV	7	7	0	0

Table 7.5: Number of events for different charges for Run II $\mu\mu\mu\mu$ data with cut flow.

Type	Cut	$2\mu^+2\mu^-$	$3\mu^+\mu^-$ or $3\mu^-\mu^+$	$4\mu^+$ or $4\mu^-$
Run IIa	4 good muons	13945	126	1
	Track $\Delta z_{DCA} < 3$ cm	13934	124	1
	Isolation	11995	83	0
	Charge and $p_T > 15$ GeV	10169	0	0
	Dimass $M_{\mu\mu} > 30$ GeV	10037	0	0
Run IIb	4 good muons	59852	1378	11
	Track $\Delta Z_{DCA} < 3$ cm	58671	714	3
	Isolation	49897	425	2
	Charge and $p_T > 15$ GeV	42239	0	0
	Dimass $M_{\mu\mu} > 30$ GeV	41647	0	0

Table 7.6: Number of events for different charges for Run II $\mu\mu\mu\mu$ MC signal with cut flow.

Below, we show all the figures associated with the 4μ analysis channel for the full Run II dataset with loose DQ. This includes in Fig. 7.3 the Δz distribution, before and after cutting on it, and in Figs. 7.4 and 7.5 the p_T distributions of the four muons (ordered in p_T) before and after making the $p_T > 15$ GeV selection given

Type	Cut	All events	Nseg0	Nseg1	Nseg2	Nseg3
Run IIa	4 good muons	1943	1511	54	1912	4295
	Track $\Delta z_{DCA} < 3$ cm	815	28	16	409	2807
	Isolation	3	2	0	0	10
	Charge and $p_T > 15$ GeV	0	0	0	0	0
	Dimass $M_{\mu\mu} > 30$ GeV	0	0	0	0	0
Run IIb	4 good muons	10476	9444	505	5671	26284
	Track $\Delta z_{DCA} < 3$ cm	4048	249	68	1806	14069
	Isolation	18	10	1	9	52
	Charge and $p_T > 15$ GeV	7	0	0	3	25
	Dimass $M_{\mu\mu} > 30$ GeV	7	0	0	3	25

Table 7.7: Number of muons versus nseg types for Run II $\mu\mu\mu\mu$ data with cut flow.

Type	Cut	Nseg0	Nseg1	Nseg2	Nseg3
Run IIa	4 good muons	4.2	4.2	6.0	85.6
	Track $\Delta z_{DCA} < 3$ cm	4.1	4.2	6.0	85.6
	Isolation	4.3	4.4	5.9	85.2
	Charge and $p_T > 15$ GeV	4.3	4.4	6.0	85.1
	Dimass $M_{\mu\mu} > 30$ GeV	4.3	4.5	6.0	85.1
Run IIb	4 good muons	5.2	4.0	5.6	85.1
	Track $\Delta z_{DCA} < 3$ cm	4.8	4.0	5.6	85.5
	Isolation	5.1	4.2	5.5	85.0
	Charge and $p_T > 15$ GeV	5.1	4.2	5.6	84.9
	Dimass $M_{\mu\mu} > 30$ GeV	5.1	4.3	5.6	84.8

Table 7.8: The fraction (%) of each nseg type for Run II $\mu\mu\mu\mu$ MC signal with cut flow.

in the earlier section. Fig. 7.6 shows the dimuon invariant mass distributions for the best pair[2] and the second pair at various steps of the analysis. Fig. 7.7 gives a scatter plot of the two dimuon invariant masses, flagged as being either opposite sign or same sign, with the best pair being along the x-axis.

Fig. 7.8 gives the dimuon invariant mass for ZZ MC after passing the dimass cut. The distributions of all dimuon pairs, split by best pair and the other pair, and the scatter plot of the two invariant masses, all agree with what is seen in the previous

[2]Set of oppositely charged muon pair whose invariant mass is closest to the Z mass of 91.2 GeV.

plots for data. In particular, the dimuon invariant mass for the 14 pairs in the final sample have an average mass of 99 ± 8 GeV and a width of 22 GeV, in agreement with the values of 92.7 GeV and 25.6 GeV for MC events.

Fig. 7.9, 7.11, 7.10 and 7.12 give the distribution of some kinematic variables (muon p_T, muon η_D, Z/γ^* p_T, di-muon invariant mass and four muon invariant mass) in the 4μ channel with expected signal and backgrounds superimposed. Our background mostly comes from Z+jets (QCD) and Migration (Due to mismeasurement or by misassigning the lepton pairs). They are discussed in more detail later in Sec. 7.6 of this Chapter. Note that all figures are associated with loose DQ and have 7 events (instead of 3) in final state, so as to have better distribution plots and statistics.

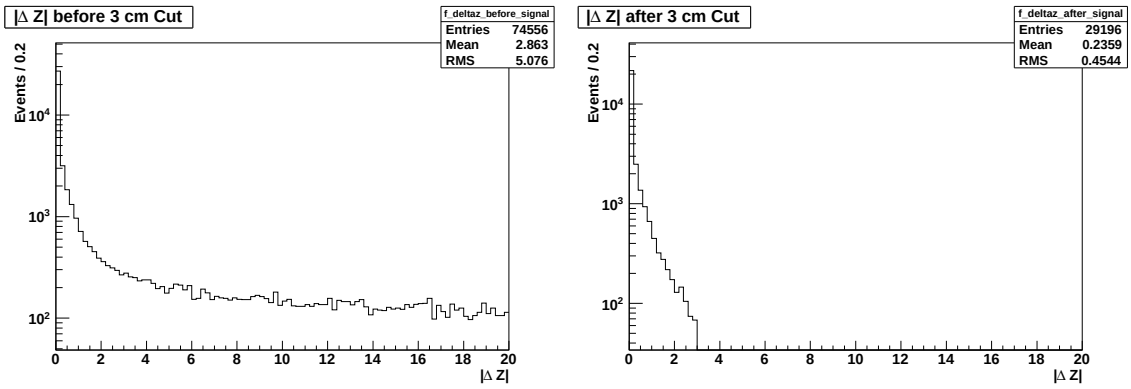

Figure 7.3: The distribution of muon track ΔZ (cm), before and after the $\Delta Z < 3$ cm cut in data.

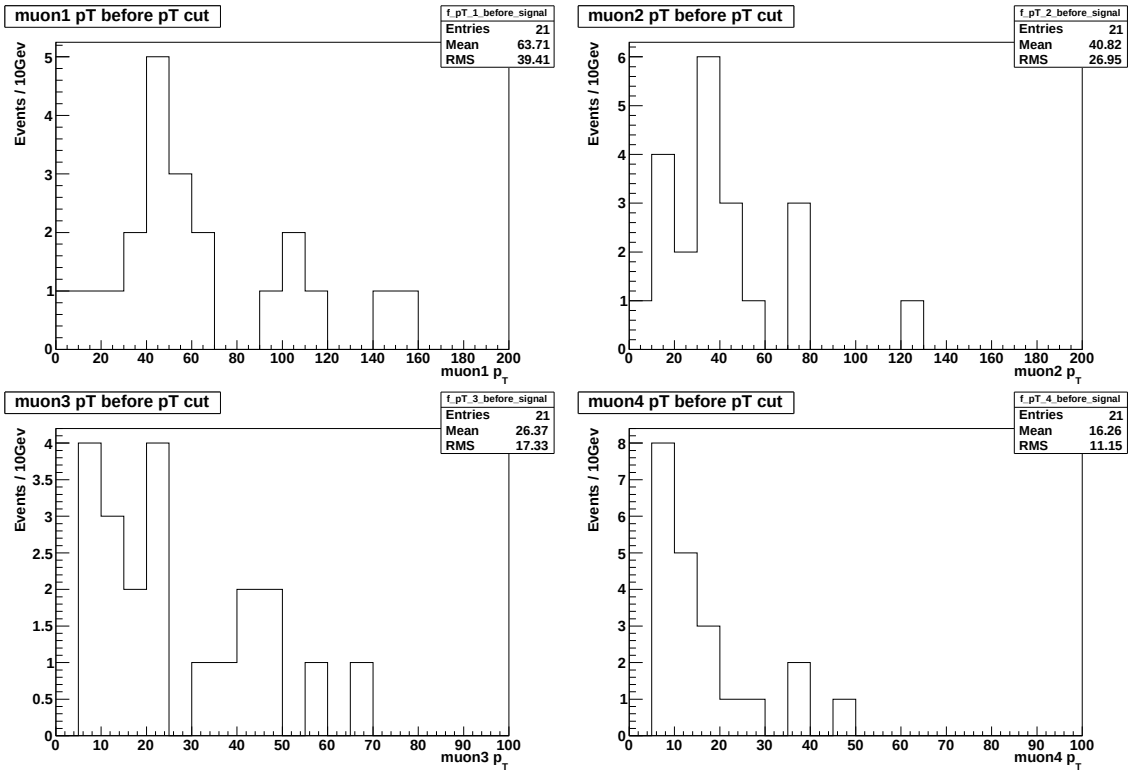

Figure 7.4: The muon p_T (GeV) distribution for leading, second, third and fourth muons, in order of p_T before the p_T cut in data.

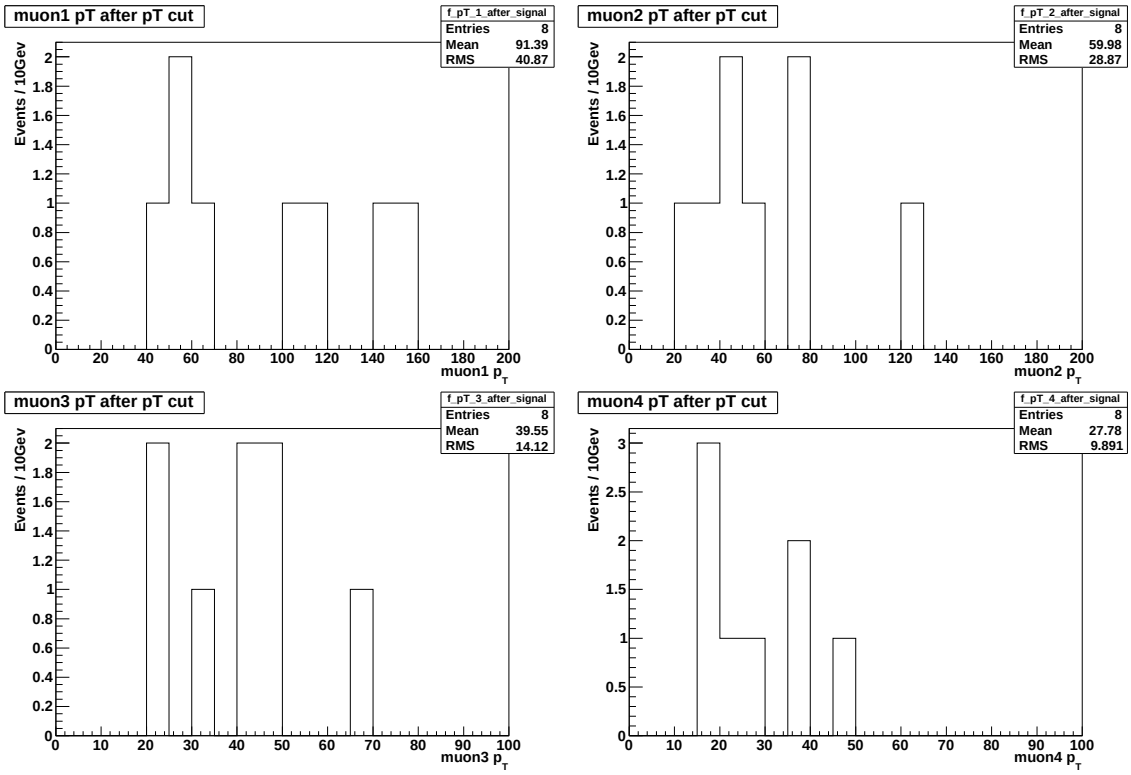

Figure 7.5: The muon p_T (GeV) distribution for leading, second, third and fourth muons after the p_T cut in data.

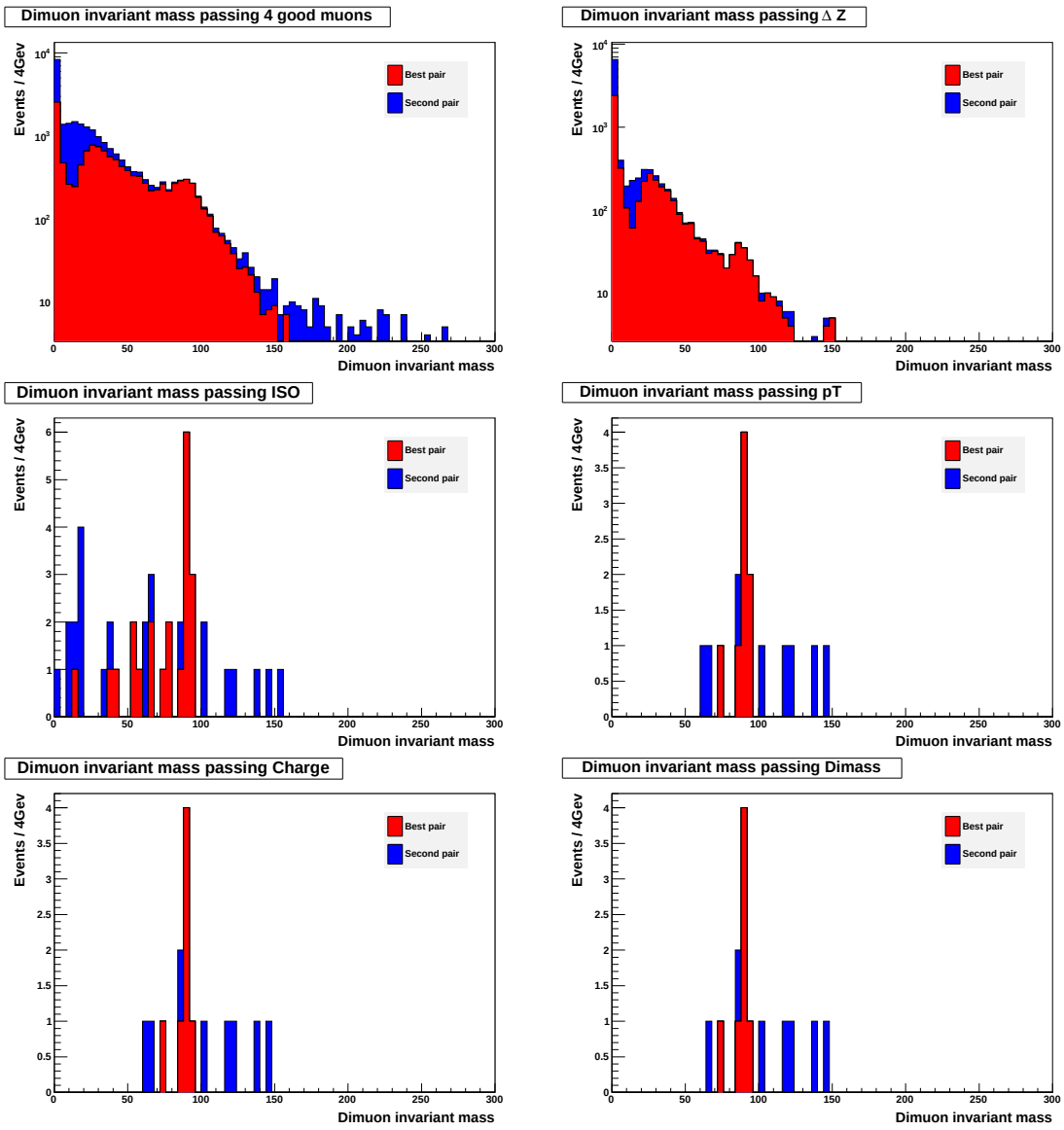

Figure 7.6: The distribution of dimuon invariant mass (GeV) in data, after passing 4 good muons, ΔZ_{DCA}, isolation, p_T, opposite charge and dimass cuts (from left to right, top to bottom). Red bins show the best dimuon pair while blue shows the second pair.

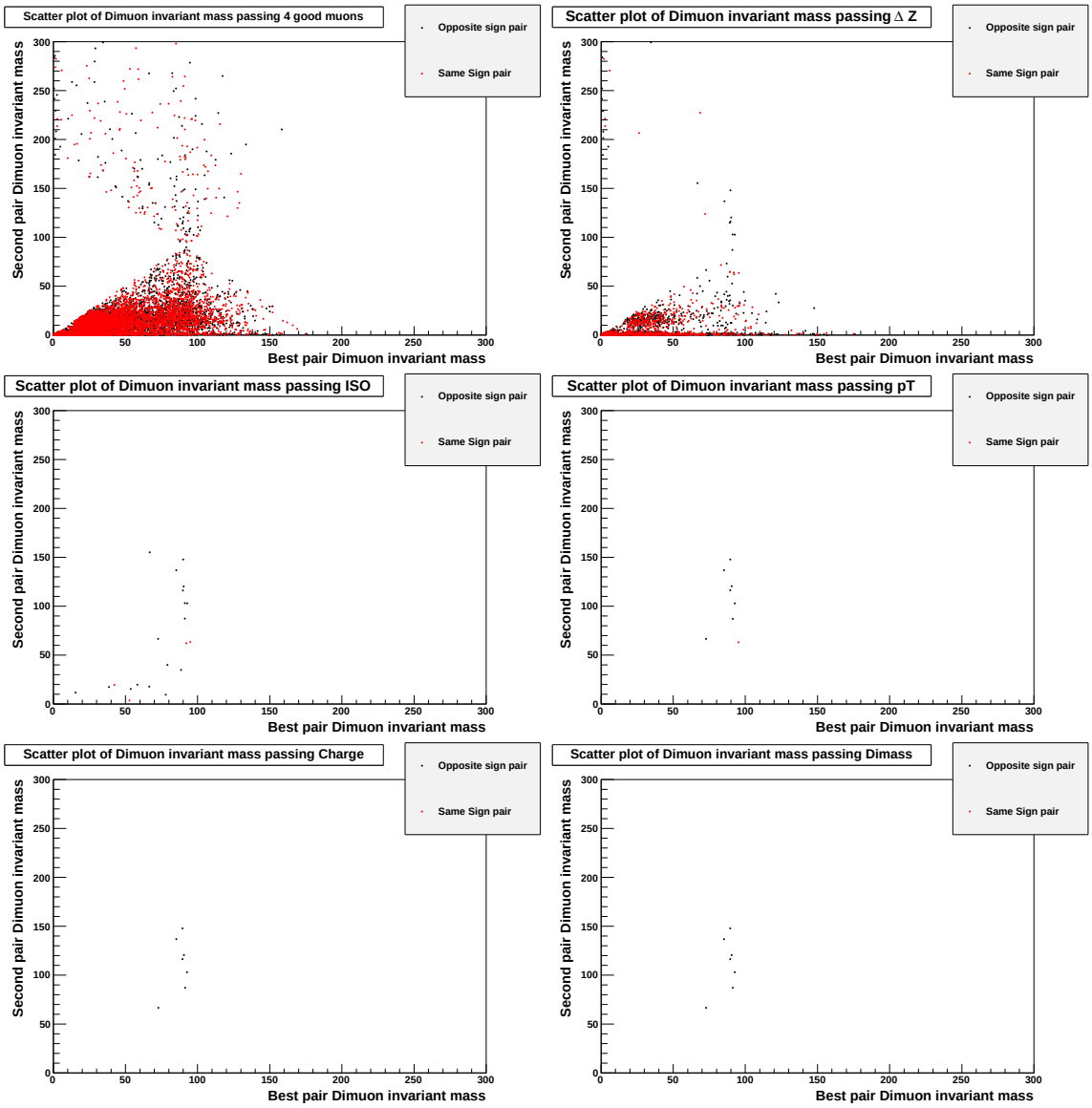

Figure 7.7: The scatter plot of dimuon pair invariant mass (GeV) in data, after passing 4 good muons, ΔZ_{DCA}, isolation, p_T, opposite charge and dimass cuts. Red spots are same-sign dimuon pair while black spots are opposite-sign dimuon pair. The best dimuon pair is on x-axis.

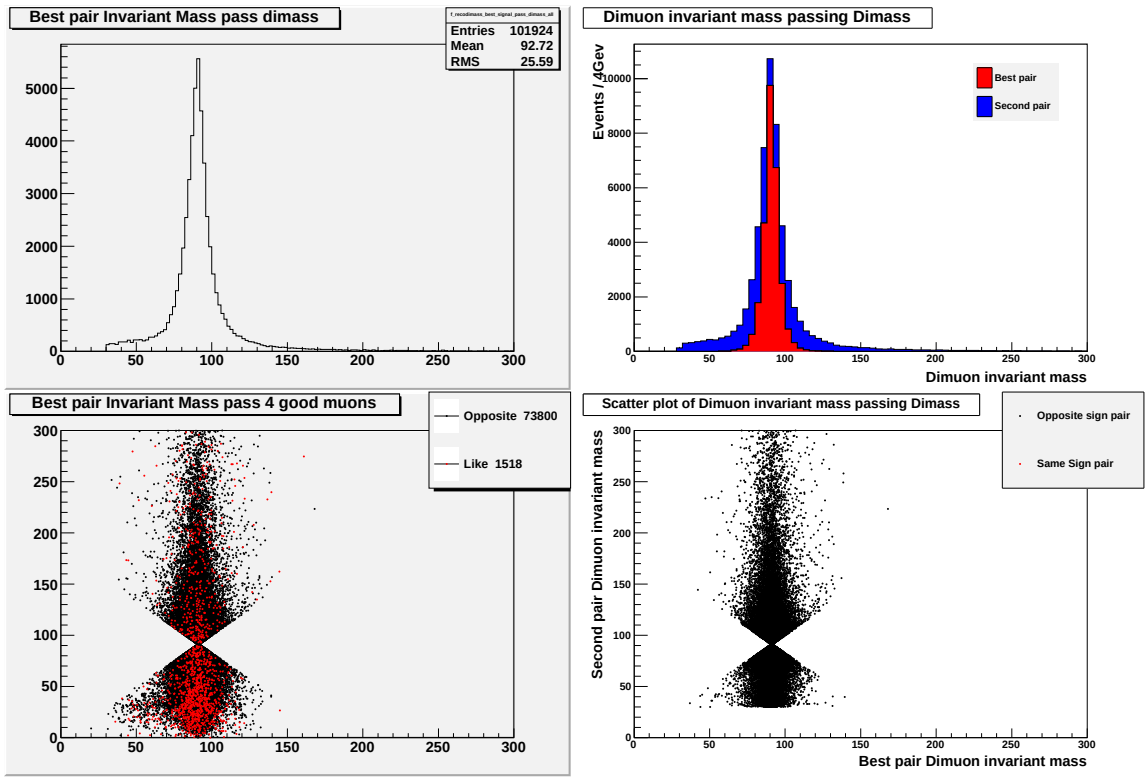

a.) b.)

Figure 7.8: Above, MC signal dimuon invariant mass (GeV) distribution after passing dimass cut with red indicating the best pair and blue the other pair; Bottom, MC signal dimuon invariant mass (GeV) of the best pair (x-axis) versus the other pair (y-axis) after passing four good muons cut and dimass cut, with black points for opposite-sign events and red points for same-sign events.

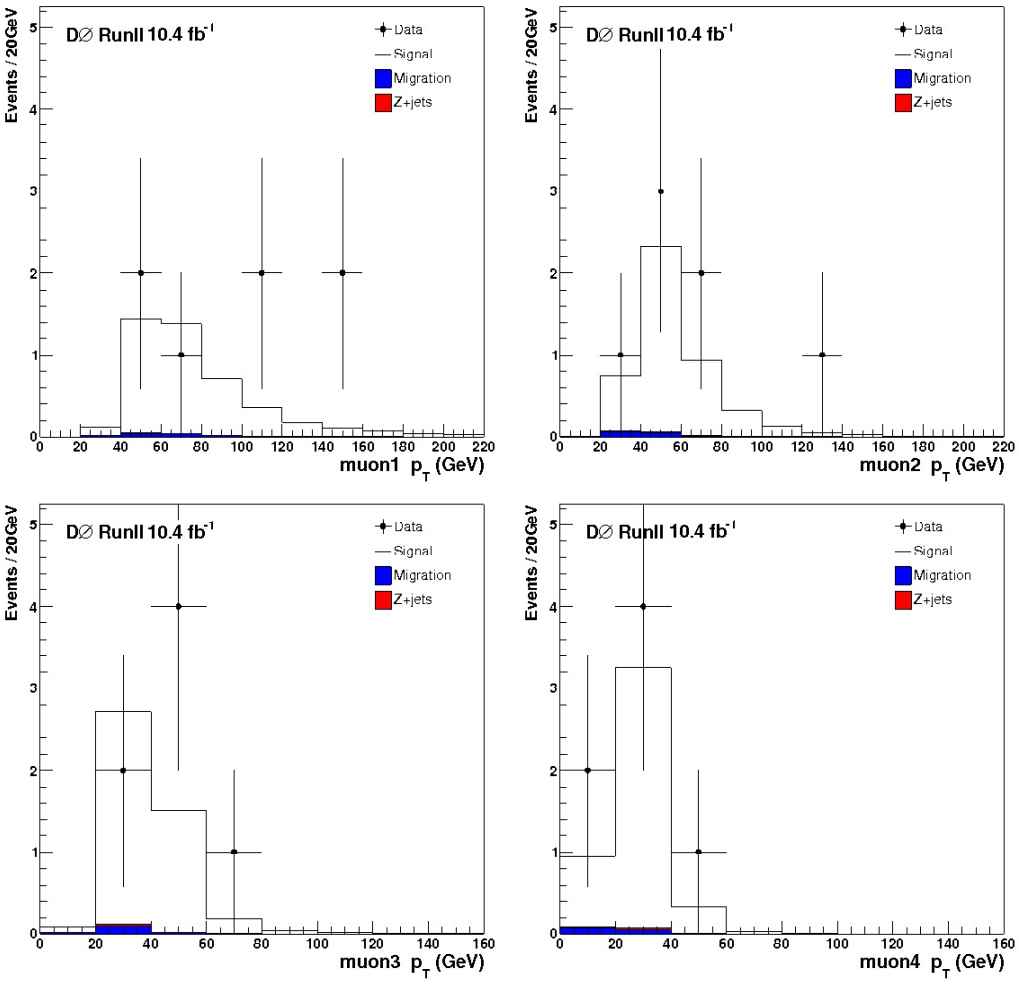

Figure 7.9: The p_T distributions of leading, second, third and fourth muons in $\mu\mu\mu\mu$ channel, with expected signal and backgrounds superimposed. (Based on Sec. 7.8, Z+jets background is too small to see in the 4μ channel comparing to Migration background.)

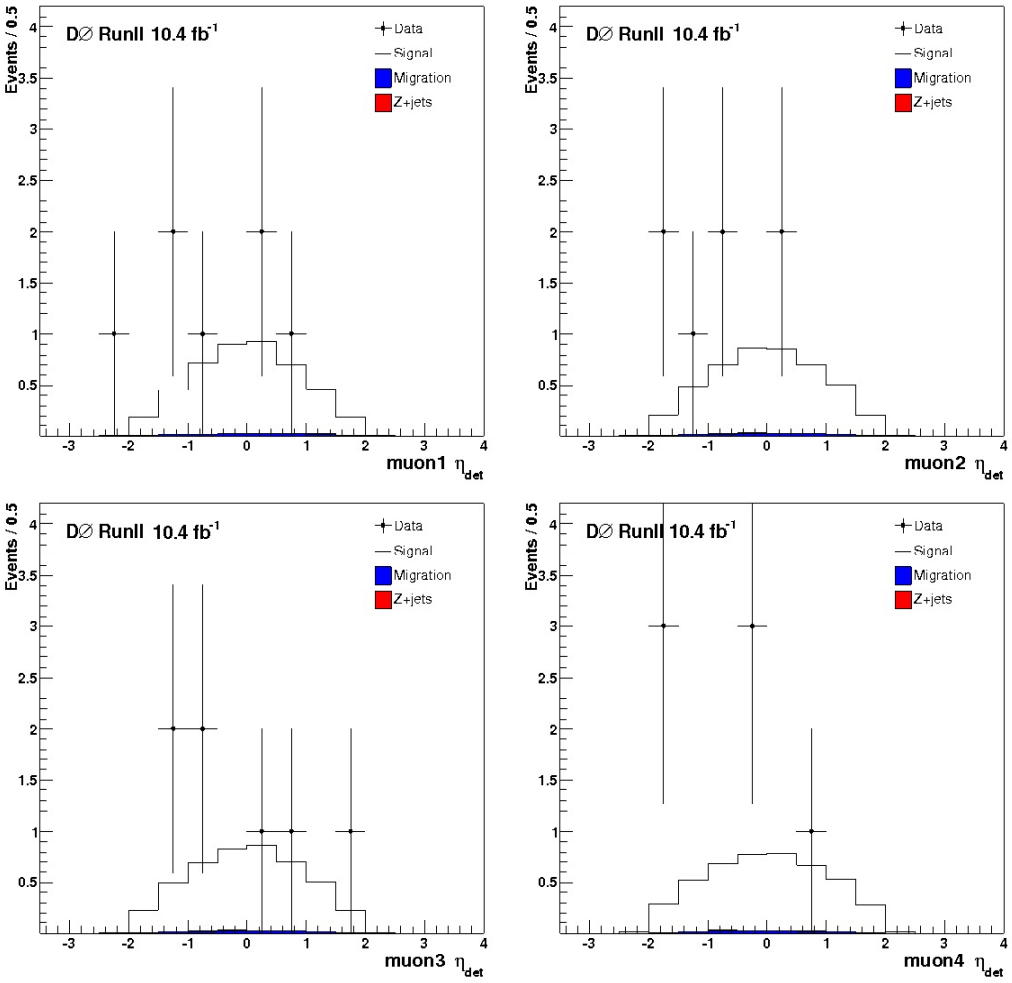

Figure 7.10: The η_D distributions of leading, second, third and fourth muons in the $\mu\mu\mu\mu$ channel, with expected signal and backgrounds superimposed.

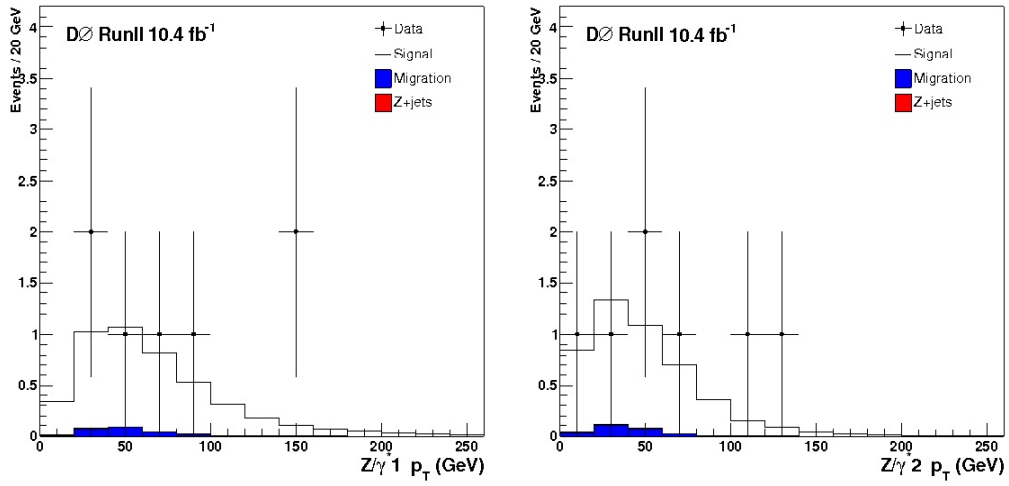

Figure 7.11: The p_T distributions of leading Z/γ^* and second Z/γ^* in the $\mu\mu\mu\mu$ channel, with expected signal and backgrounds superimposed.

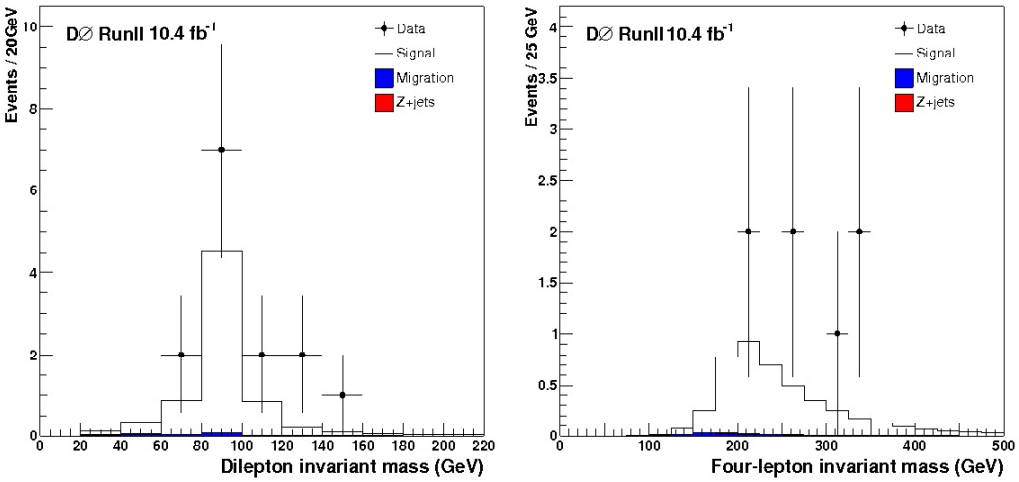

Figure 7.12: The distributions of di-muon invariant mass with both best pair and the other pair included and four muon invariant mass in the $\mu\mu\mu\mu$ channel, with expected signal and backgrounds superimposed.

7.4.2 *eeee* Channel

7.4.2.1 Selection

The event selections utilized for acquiring *eeee* events are:

- At least four "good electrons"
- All four electrons with $p_T > 15.0$ GeV
- The number of CC electrons $N_{CCEM} \geq 2$
- Maximum number of ICD electron is 1
- All possible electron pairing are considered and we require one set of pairing with $M_{ee} > 30$ GeV for both pairs

We break the *eeee* channel into four sub-channels which depend on the number of electrons in the CC and ICD regions: $N_{CCEM} = 2$ and $N_{ICDEM} = 0$, $N_{CCEM} = 3$ and $N_{ICDEM} = 0$, $N_{CCEM} \geq 4$ and $N_{ICDEM} = 0$, and $N_{ICDEM} = 1$. The splitting is applied because QCD background contamination is expected to vary significantly depending on the number of central electrons, which are required to be either track matched or have a significant number of hits in the tracking chamber, and because the jet background in the ICD region is greater than in the CC or EC. We only use ICD electrons within $1.1 < |\eta_D| < 1.5$, as η_D is calculated using different methods for reconstructed taus objects and electromagnetic objects, there are occasionally overlaps. We remove any ICD electron that is found to be within $\Delta R < 0.5$ of a CC/EC electron to avoid double counting. ICD electrons are also required to have a track match. While the CC and EC electrons are not explicitly

required to have a track match, we require those that are track matched to have $\Delta z_{DCA}(e_{CC/EC}, e_{ICD}) < 3.0$ cm to reduce QCD contamination.

The cut flow for $ZZ \rightarrow eeee$ data in both Run IIa and Run IIb is shown in Tables 7.9-7.10. Note that this cut flow are associated with normal DQ. Using loose DQ in 4e channel does not increase the number of candidate events.

Cut	Number of Events			
Initial	36294680			
≥ 3 good electrons	4303			
Data Quality	3753			
≥ 4 good electrons	19			
p_T and ICD overlap removal	1			
≥ 2 CC electrons	0			
CC/ICD topology	2 CC electrons 0 ICD electron	3 CC electrons 0 ICD electron	4 CC electrons 0 ICD electron	1 ICD electron
	0	0	0	0
Dimass	0	0	0	0

Table 7.9: Run IIa: Cut flow for *eeee* data for four sub-channels (= 2, = 3, ≥ 4 central electrons with no ICD electrons, and with 1 ICD electron).

Cut	Number of Events			
Initial	185982072			
≥ 3 good electrons	27238			
Data Quality	25226			
≥ 4 good electrons	117			
p_T and ICD overlap removal	7			
≥ 2 CC electrons	5			
CC/ICD topology	2 CC electrons 0 ICD electron	3 CC electrons 0 ICD electron	4 CC electrons 0 ICD electron	1 ICD electron
	0	1	2	2
Dimass	0	1	2	2

Table 7.10: RunIIb: Cut flow for *eeee* data for four sub-channels (= 2, = 3 or ≥ 4 central electrons with no ICD electrons, and with 1 ICD electron).

Below we show all the figures associated with the 4*e* analysis channel. Fig. 7.13, 7.15, 7.14 and 7.16 give the distribution of some kinematic variables (muon p_T, muon

η_D, Z/γ^* p_T, di-electron invariant mass and four electron invariant mass) in the 4e channel with expected signal and backgrounds superimposed.

In these analysis, we refer to a best set of di-electron pairings. As we have four electrons and do not look at the electron charge, there are three possible sets of electron pairings in each four electron events, e.g. 12,34; 13,24; and 14,23. We examine each pairing and select as the "best pairing" that which has one of the two di-electron masses closest to the Z pole mass of 91.2 GeV.

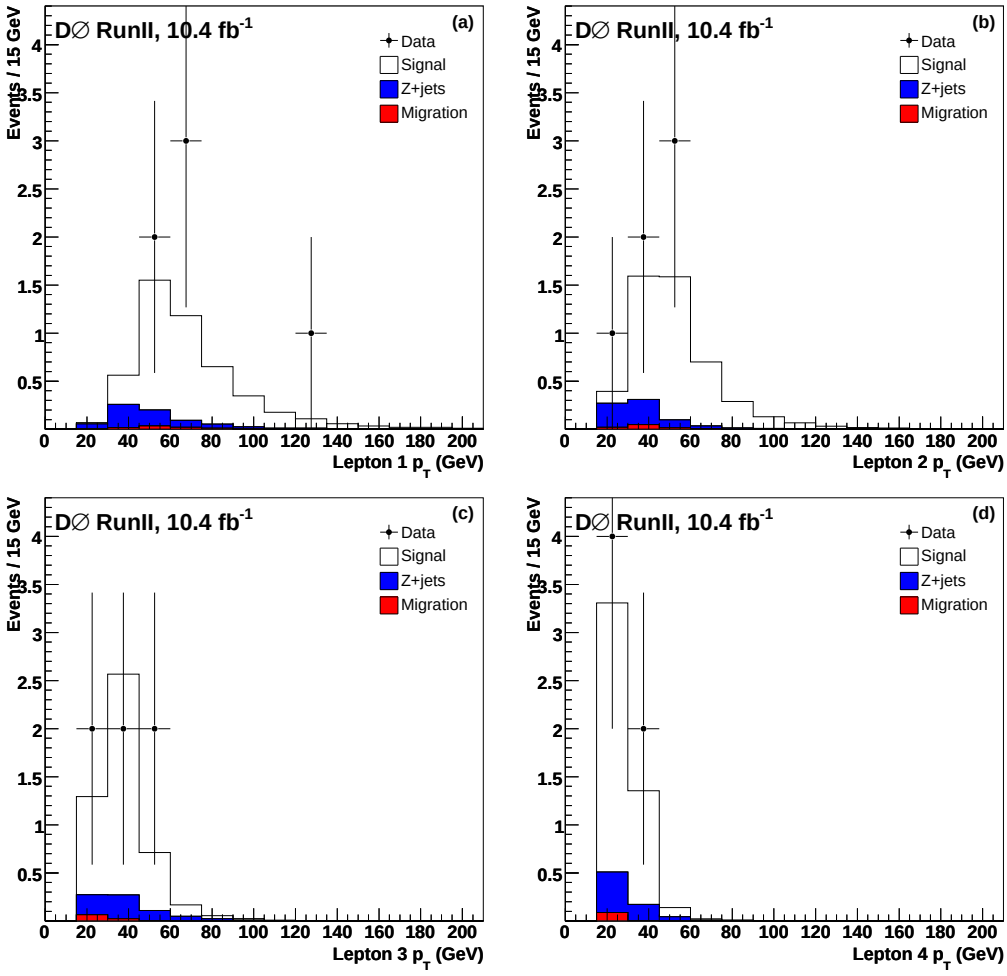

Figure 7.13: The p_T distributions of leading, second, third and fourth muons in *eeee* channel, with expected signal and backgrounds superimposed.

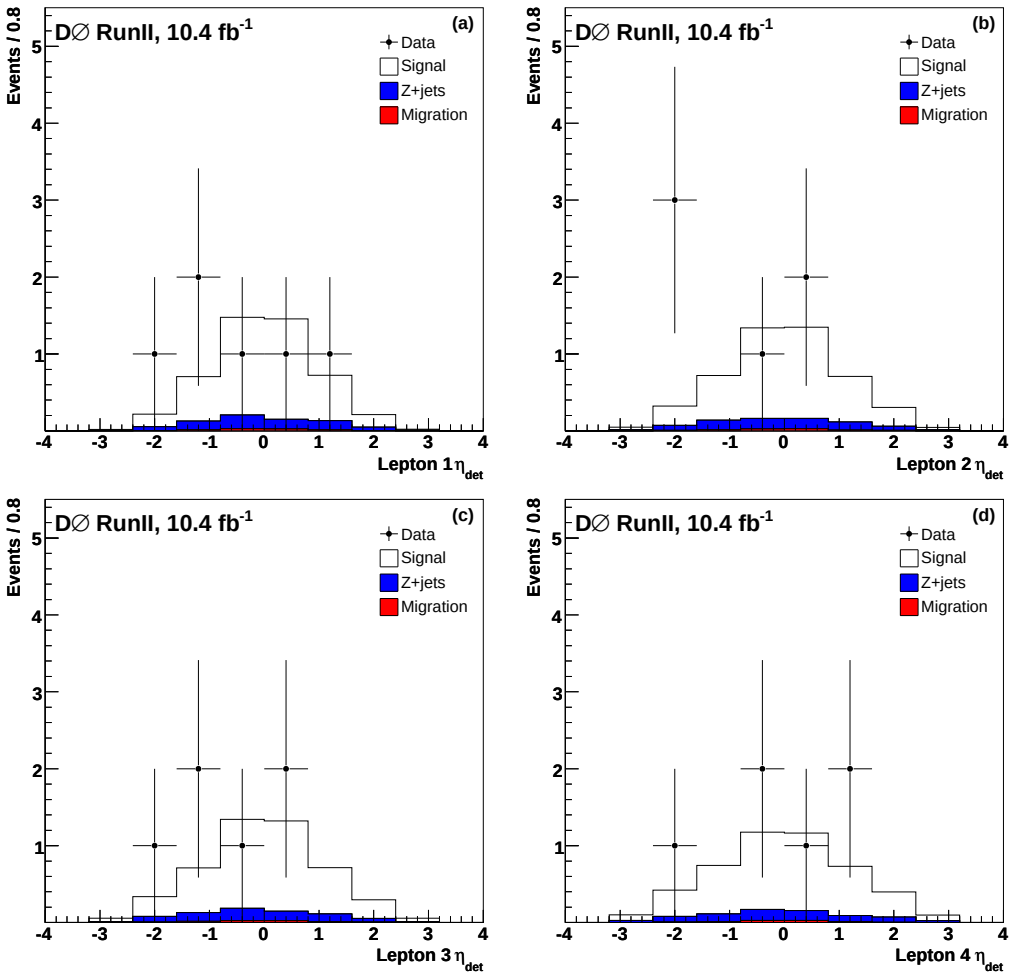

Figure 7.14: The η_D distributions of leading, second, third and fourth muons in the *eeee* channel, with expected signal and backgrounds superimposed.

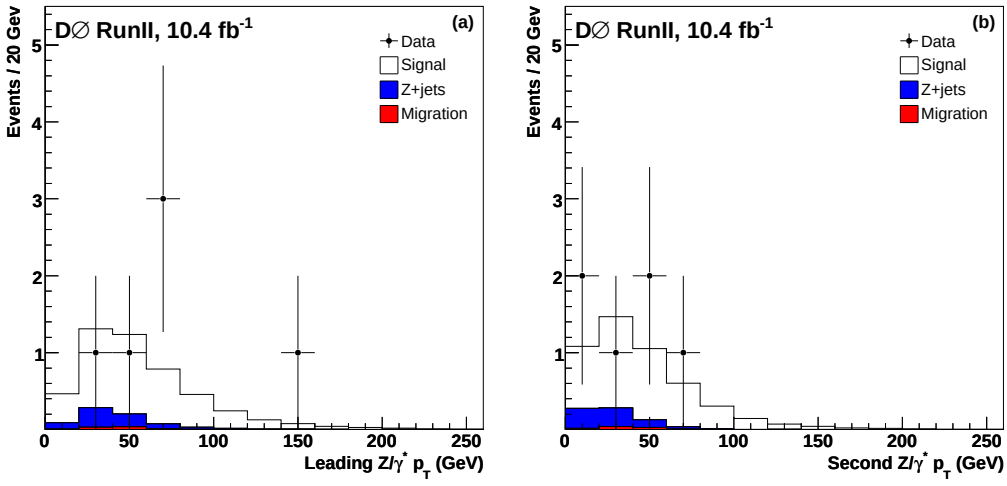

Figure 7.15: The p_T distributions of leading Z/γ^* and second Z/γ^* in the *eeee* channel, with expected signal and backgrounds superimposed.

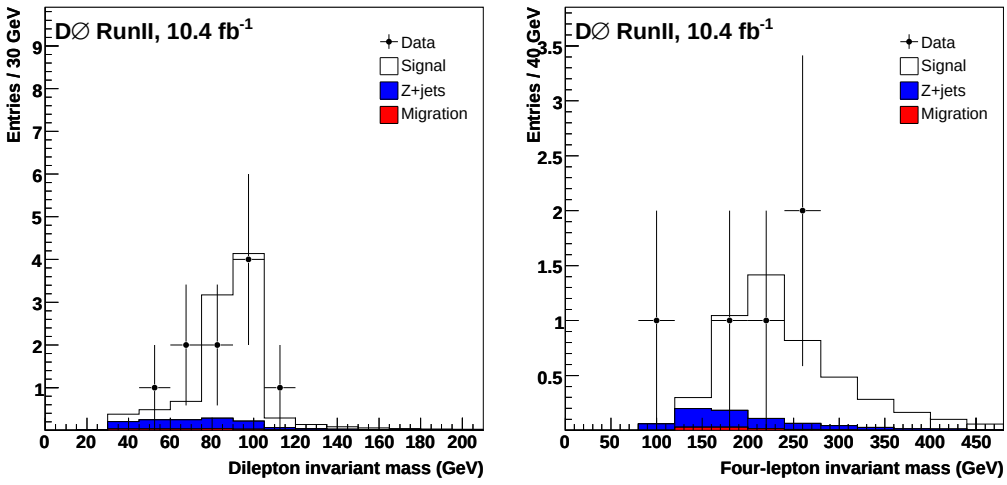

Figure 7.16: The distributions of di-muon invariant mass with both best pair and the other pair included and four muon invariant mass in the *eeee* channel, with expected signal and backgrounds superimposed.

7.4.3 $ee\mu\mu$ Channel

7.4.3.1 Selection

The event selections for acquiring $ee\mu\mu$ events are:

- At least two "good electrons" (not in the ICD region)
- At least two "good muons"
- $p_T > 15.0$ GeV for all electrons and muons
- Both muons are required to be isolated
- Cosine of space angle between muons is $cos(\alpha) < 0.96$. Thus, $\alpha > 16.2°$(0.28 radians)
- Acoplanarity between any two muons must be greater than 0.05 (cosmic ray veto selection)
- $\Delta z_{DCA} < 3.0$ cm between all muon tracks
- $\Delta R > 0.2$ between all electron-muon pairs
- Require di-muon pair invariant mass to be $M_{ll} > 30$ GeV and di-electron pair invariant mass to be $M_{l'l'} > 30$ GeV

Next, we break the $ee\mu\mu$ channel into three sub-channels depending on the number of electrons in the CC region: $N_{CCEM} = 0$, $N_{CCEM} = 1$, and $N_{CCEM} \geq 2$. Same as *eeee* channel, the splitting is applied because QCD background contamination is expected to vary significantly depending on the number of central electrons. The

cut flows for $ZZ \to ee\mu\mu$ data in Run IIa and RunIIb are shown in Tables 7.11-7.12. Note that, this cut flow tables are associated with normal DQ. Results with loose DQ are presented in Appendix C.

Cut	Number of Events		
Initial	36229860		
Data Quality	34513823		
≥ 1 good electron	835304		
≥ 1 good muon	32		
p_T	18		
CC topology	0 CC electrons	1 CC electrons	2 CC electrons
	2	5	11
Space angle and Acop.	2	5	11
μ track Δz	2	4	10
$\Delta R_{e\mu}$	1	1	0
Dimass	1	1	0

Table 7.11: Run IIa: Cut flow for $ee\mu\mu$ data for three channels ($= 0$, $= 1$ or ≥ 2 central electrons).

Cut	Number of Events		
Initial	185982072		
Data Quality	178582022		
≥ 1 good electron	7235058		
≥ 1 good muon	2595		
p_T	368		
CCtopology	0 CC electrons	1 CC electrons	2 CC electrons
	23	97	248
Space angle and Acop.	22	96	245
μ track Δz	3	25	168
$\Delta R_{e\mu}$	1	0	2
Dimass	1	0	2

Table 7.12: RunIIb: Cut flow for $ee\mu\mu$ data for three subchannels ($= 0$, $= 1$ or ≥ 2 central electrons).

The plots of some kinematic variables associated with the $ee\mu\mu$ channel are shown below with expected signal and backgrounds superimposed. Fig. 7.17, 7.19,

7.18 and 7.20 give the distribution of muon p_T, muon η_D, Z/γ^* p_T, di-lepton invariant mass and four lepton invariant mass.

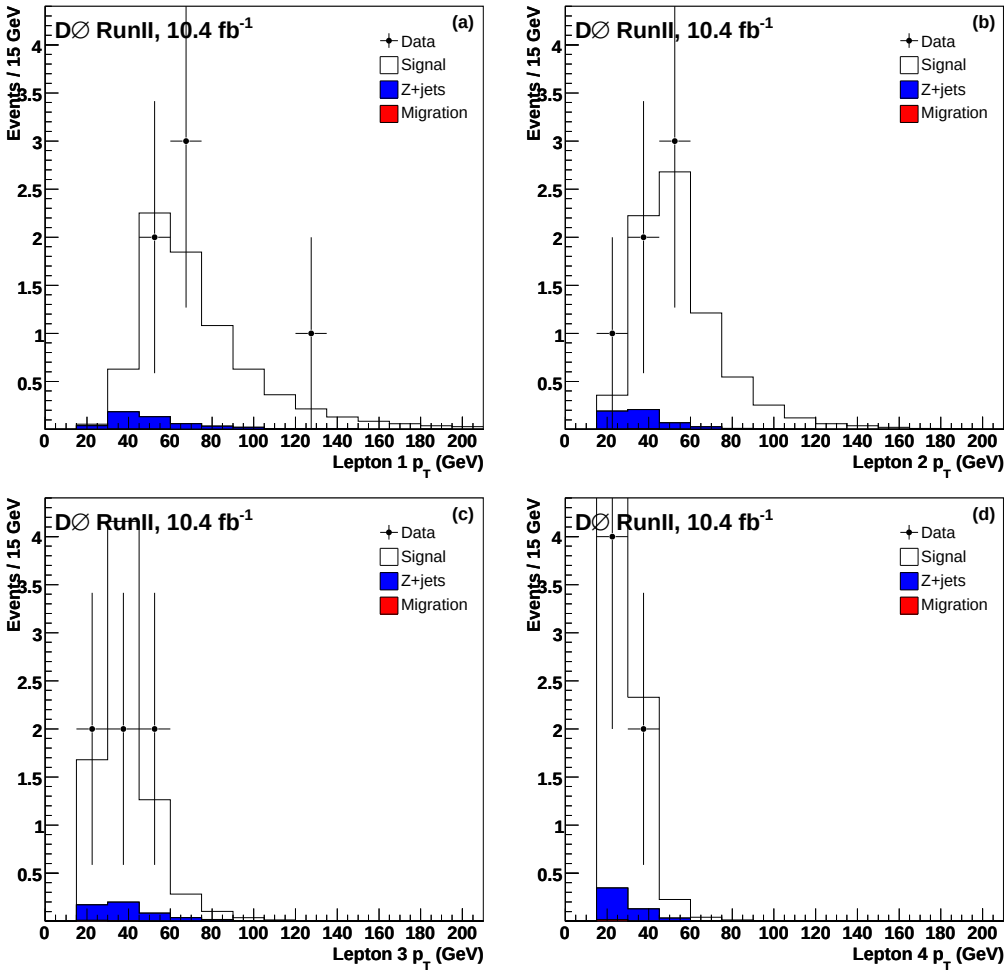

Figure 7.17: The p_T distributions of leading, second, third and fourth muons in $ee\mu\mu$ channel, with expected signal and backgrounds superimposed.

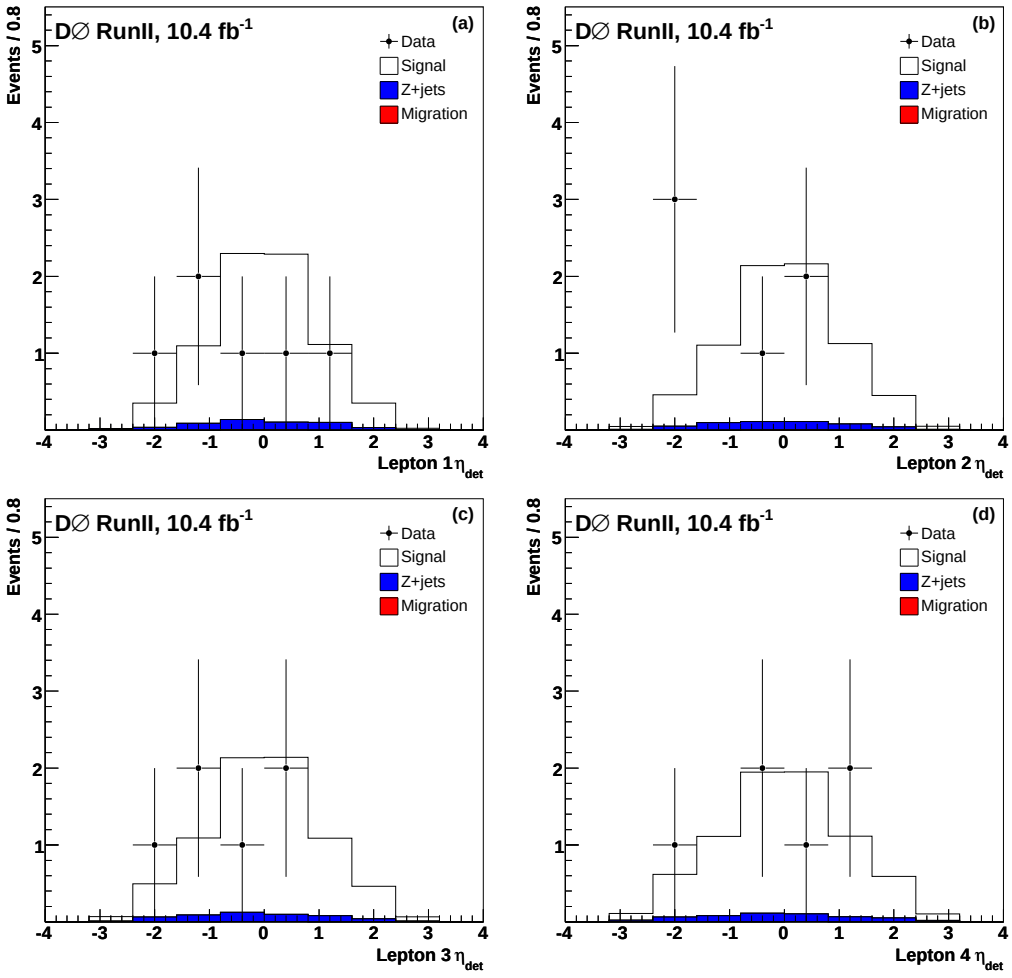

Figure 7.18: The η_D distributions of leading, second, third and fourth muons in the $ee\mu\mu$ channel, with expected signal and backgrounds superimposed.

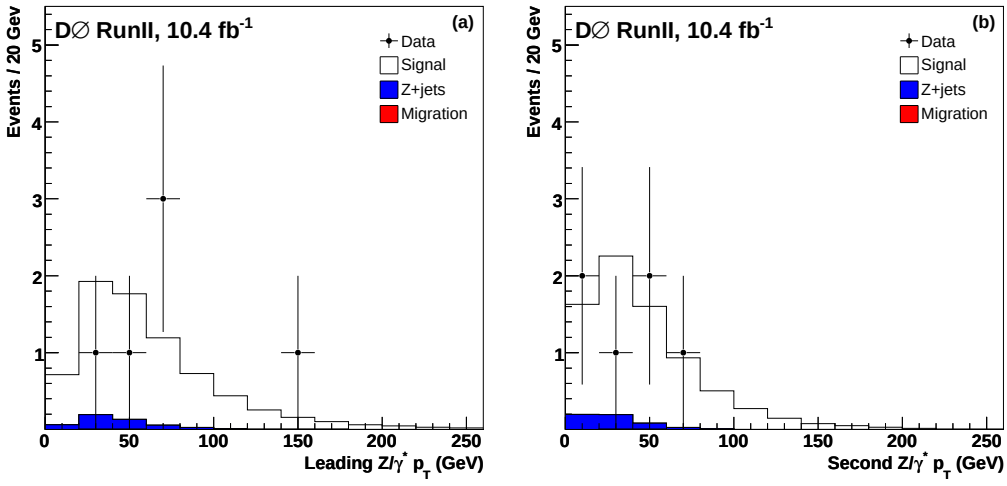

Figure 7.19: The p_T distributions of leading Z/γ^* and second Z/γ^* in the $ee\mu\mu$ channel, with expected signal and backgrounds superimposed.

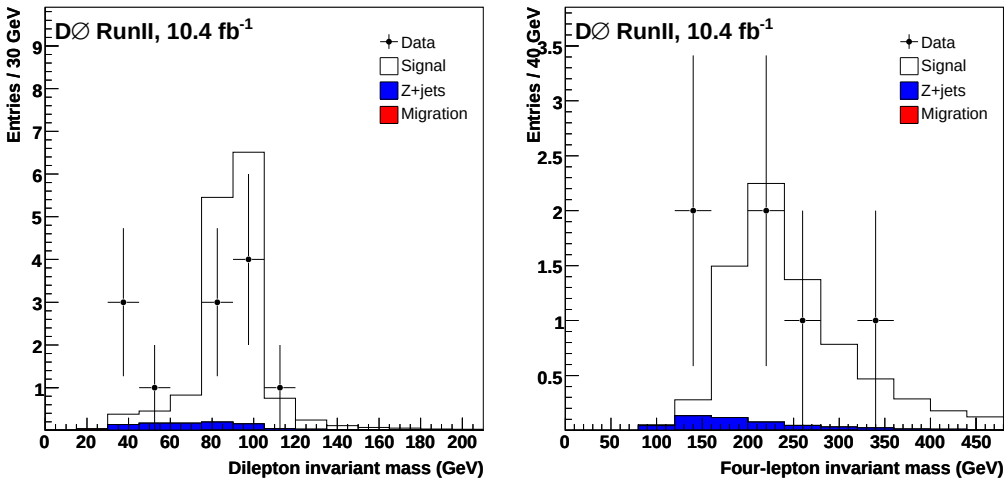

Figure 7.20: The distributions of di-muon invariant mass with both best pair and the other pair included and four muon invariant mass in the $ee\mu\mu$ channel, with expected signal and backgrounds superimposed.

7.5 Monte Carlo Simulations

7.5.1 Monte Carlo Samples

We use PYTHIA [50] MC for simulation of $ZZ \to \ell^+\ell^-\ell^+\ell^-$ signal and $t\bar{t}$ background events. In addition, we look for contributions from $ZZ \to \ell^+\ell^-\tau\tau$ where the taus decay into electrons or muons as appropriate to match our final signal signature. Contributions from $ZZ \to \tau\tau\tau\tau$ and their subsequent decays into muons and electrons were also examined, but found to be insignificant.

The samples were processed through the standard DØ simulation code followed by processing through the full Run IIa and Run IIb geometry detector simulation with zero-suppressed zero-bias data overlaid. These samples are then reconstructed for Run IIa and Run IIb, and then files are produced. The resulting files are available from the database via definitions of the form `CSG_CAF_MCv4-xxxx_pyy.yy.yy` where xxxx is the MC identification of the particular sample and yy.yy.yy is the relevant reconstruction version.

The sample for the $ZZ \to eeee$ and $ZZ \to \mu\mu\mu\mu$ channels have a $\sigma\times$ BR of 1.8 fb. The $ZZ \to ee\mu\mu$ channel has a $\sigma\times$ BR of 3.6 fb. The $t\bar{t} \to 2b + 2\ell + 2\nu$ background is estimated using ALPGEN [49] with a top quark mass of 172 GeV and $\sigma\times$ BR of 814 fb. More details on the MC samples used for both Run IIa and Run IIb are given in Tables 7.13-7.14.

The MC samples are reweighted at an event level by the luminosity profile as determined by comparing the profile from the appropriate data sample described earlier to the profile from the zero-bias overlay in the MC. In addition, the MC has to be reweighted for the z coordinate of the primary vertex which is randomly

Physics Channel	Request IDs (Database Definitions)	$\sigma\times$BR (fb)	Events
$ZZ \to 4\mu$	103593	1.8	194,731
$ZZ \to 4e$	103592	1.8	193,160
$ZZ \to 2e2\mu$	103595	3.6	200,250
$ZZ \to 2\mu2\tau$	103596	3.6	208,500
$ZZ \to 2e2\tau$	103597	3.6	210,000
$t\bar{t} \to 2b + 2\ell + 2\nu$	CSG_alpgenpythia_t+t_2l+2nu+2b_m172_p181400_v12	814	1,550,802

Table 7.13: Run IIa PYTHIA GEANT p17 MC samples.

Physics Channel	Epoch	Request IDs (Database Definitions)	$\sigma\times$BR (fb)	Events
$ZZ \to 4\mu$	Run IIb1	86533,107993	1.8	185,095
	Run IIb2	147675,147676,147677		459,299
	Run IIb3	157357,157358,157359		470,360
$ZZ \to 4e$	Run IIb1	86532,107992	1.8	186,010
	Run IIb2	147672,147673,147674		456,994
	Run IIb3	157353,157354,157355		470,353
$ZZ \to 2e2\mu$	Run IIb1	86534,107995	3.6	192,894
	Run IIb2	147681,147682,147683, 147684,147685,147686		911,864
	Run IIb3	157365,157366 157367, 157369,157370,157371		942,137
$ZZ \to 2\mu2\tau$	Run IIb1	86536,107997	3.6	189,014
	Run IIb2	147689,147688,147687		457,088
	Run IIb3	157373,157374,157375		470,777
$ZZ \to 2e2\tau$	Run IIb1	86535,107996	3.6	185,118
	Run IIb2	157441,157442,157443		456,856
	Run IIb3	157435,157436,157437		470,194
$t\bar{t} \to 2b + 2\ell + 2\nu$	Run IIb1	CSG_alpgenpythia_t+t_2l+2nu+2b_m172_p211100_v13	814	5,067,962
	Run IIb2	CSG_alpgenpythia_t+t_2l+2nu+2b_m172_p211800_Run2b2_v6		
	Run IIb3	CSG_alpgenpythia_t+t_2l+2nu+2b_m172_p212100_Run2b3_v5		

Table 7.14: Run IIb PYTHIA GEANT p20 MC samples.

distributed by a Gaussian centered at 0 with a width of 25 cm in the MC generation, which is quite different from the longitudinal shape of the luminous region in the data. The correction uses a fit to the beamshape region out to 60 cm [77].

The MC samples are additionally reweighted on a lepton by lepton basis as the selection efficiency of a lepton is not the same for data and MC. The data/MC scale factor is determined by dividing data efficiency by MC efficiency as determined by the corresponding EM [72, 78] and Muon [79, 80] ID groups. More details on the specific correction factors have been discussed in sections 4.3 and 5.3 . This is

applied to each lepton, and the product for all leptons gives an event weight which is combined with the previously determined weights.

In addition to reweighing, we apply additional lepton momentum smearing to MC events. This is done to achieve better momentum matching between data and MC. More information about muon oversmearing methods and parameters are illustrated in Chapter 6.

7.5.2 Acceptance in Four Lepton Channels

We use several MC samples to measure the product of the geometric acceptance and the event selection efficiency, $Acc \times \epsilon$, for each topology and for the various physics processes. Recall that, signal represents direct $ZZ \to eeee$, $ZZ \to \mu\mu\mu\mu$, and $ZZ \to ee\mu\mu$ processes. Migration represents low mass ZZ production where final lepton combinations and reconstruction errors can cause these events to appear as signal. For top-antitop ($t\bar{t}$) quark production and decay we only look at $t\bar{t} \to 2b + 2\ell + 2\nu$ samples. The $2\mu 2\tau$ and $2e2\tau$ samples represent the case where pair produced Z decay into a relevant lepton pair (2μ or $2e$), a 2τ pair, and then the τ leptonically decay into a muon or electron, thus resulting in a final state which looks like direct signal.

The Run IIa and IIb $Acc \times \epsilon$ cut flow in $\mu\mu\mu\mu$ channel for our MC signal, migration and $t\bar{t}$ samples are given in Tab. 7.15. The IIa and IIb $Acc \times \epsilon$ values are summarized in Tab. 7.16 for the 4μ channel, where all uncertainties are statistical. These values are normalized to the mass ($M_1(Z/\gamma^*) > 30$ GeV, $M_2(Z/\gamma^*) > 30$ GeV) region.

Cut	Run IIa		Run IIb	
	Cumulative $A \times \epsilon$	Exclusive $A \times \epsilon$	Cumulative$A \times \epsilon$	Exclusive $A \times \epsilon$
MC ZZ Norm.	1.0000 ± 0.0000		1.0000 ± 0.0000	
4 good muons	0.4502 ± 0.0029	0.4502 ± 0.0029	0.3532 ± 0.0011	0.3532 ± 0.0011
Track ΔZ_{DCA}	0.3855 ± 0.0028	0.9982 ± 0.0004	0.3253 ± 0.0011	0.9693 ± 0.0007
Isolation	0.3291 ± 0.0027	0.8537 ± 0.003	0.2739 ± 0.0011	0.8419 ± 0.0015
p_T	0.2787 ± 0.0026	0.8470 ± 0.003	0.2312 ± 0.0010	0.8443 ± 0.0016
Opposite charge	0.2733 ± 0.0026	0.9942 ± 0.0008	0.2263 ± 0.0010	0.9927 ± 0.0004
Dimass	0.2804 ± 0.0026	0.9872 ± 0.0011	0.2311 ± 0.0010	0.9859 ± 0.0006

Table 7.15: Cut flow for Run II $\mu\mu\mu\mu$ MC signal showing cumulative and exclusive $Acc \times \epsilon$.

	Signal	$2\mu 2\tau$	$2e2\tau$	4τ
Run IIa	0.2804 ± 0.0026	$(4.02 \pm 0.35) \times 10^{-3}$	–	$(1.48 \pm 2.09) \times 10^{-5}$
Run IIb	0.2311 ± 0.0010	$(2.90 \pm 0.12) \times 10^{-3}$	–	$(6.81 \pm 1.90) \times 10^{-5}$

	Signal Migration	$2\mu 2\tau$ Migration	4τ Misre.	$t\bar{t}$
Run IIa	$(8.55 \pm 0.73) \times 10^{-4}$	$(1.95 \pm 1.11) \times 10^{-5}$	–	$(3.94 \pm 5.09) \times 10^{-7}$
Run IIb	$(6.78 \pm 0.27) \times 10^{-4}$	$(0.92 \pm 0.32) \times 10^{-5}$	–	$(0.79 \pm 1.26) \times 10^{-7}$

Table 7.16: $Acc \times \epsilon$ values for $\mu\mu\mu\mu$ Channel.

The $Acc \times \epsilon$ cut flow in $eeee$ channel for our MC signal, migration and $t\bar{t}$ samples are given in Tables 7.17 and 7.18. The $Acc \times \epsilon$ values for various topologies in $4e$ channel are summarized in Table 7.19 and 7.20, where all uncertainties are statistical. These values are normalized to the mass ($M_1(Z/\gamma^*) > 30$ GeV, $M_2(Z/\gamma^*) > 30$ GeV) region.

Cut	Cumulative $A \times \epsilon$		Exclusive $A \times \epsilon$	
MC ZZ Norm.	1.0000 ± 0.0000		–	
≥ 4 good elec.	0.3349 ± 0.0035		0.3349 ± 0.0035	
p_T and overlap removal	0.2813 ± 0.0031		0.8400 ± 0.0038	
Number of CC electrons	2 CC electrons		3 CC electrons	
	Cumulative $A \times \epsilon$	Exclusive $A \times \epsilon$	Cumulative $A \times \epsilon$	Exclusive $A \times \epsilon$
	0.0309 ± 0.0011	0.1098 ± 0.0034	0.0702 ± 0.0016	0.2500 ± 0.0048
Dimass	0.0309 ± 0.0011	1.0000 ± 0.0001	0.0702 ± 0.0016	1.0000 ± 0.0001
Number of CC electrons	4 CC electrons		1 ICD electron	
	Cumulative $A \times \epsilon$	Exclusive $A \times \epsilon$	Cumulative $A \times \epsilon$	Exclusive $A \times \epsilon$
	0.0658 ± 0.0015	0.2339 ± 0.0046	0.0901 ± 0.0018	0.3203 ± 0.0051
Dimass	0.0658 ± 0.0015	1.0000 ± 0.0001	0.0901 ± 0.0018	1.0000 ± 0.0001

Table 7.17: Run IIa: Cut flow for *eeee* MC signal showing cumulative and exclusive $Acc \times \epsilon$ for four subchannels ($= 2$, $= 3$ or ≥ 4 central electrons, $= 1$ ICD electron).

Cut	Cumulative $A \times \epsilon$		Exclusive $A \times \epsilon$	
MC ZZ Norm.	1.0000 ± 0.0000		–	
≥ 4 good elec.	0.2728 ± 0.0012		0.2728 ± 0.0012	
p_T and overlap removal	0.2292 ± 0.0011		0.8402 ± 0.0016	
Number of CC electrons	2 CC electrons		3 CC electrons	
	Cumulative $A \times \epsilon$	Exclusive $A \times \epsilon$	Cumulative $A \times \epsilon$	Exclusive $A \times \epsilon$
	0.0242 ± 0.0004	0.1056 ± 0.0015	0.0578 ± 0.0006	0.2522 ± 0.0021
Dimass	0.0242 ± 0.0004	1.0000 ± 0.0001	0.0578 ± 0.0006	1.0000 ± 0.0001
Number of CC electrons	4 CC electrons		1 ICD electron	
	Cumulative $A \times \epsilon$	Exclusive $A \times \epsilon$	Cumulative $A \times \epsilon$	Exclusive $A \times \epsilon$
	0.0514 ± 0.0005	0.2243 ± 0.0020	0.0745 ± 0.0006	0.3250 ± 0.0022
	0.0514 ± 0.0005	0.9998 ± 0.0001	0.0745 ± 0.0006	1.0000 ± 0.0001

Table 7.18: Run IIb: Cut flow for *eeee* MC signal showing cumulative and exclusive $Acc \times \epsilon$ for three subchannels ($= 2$, $= 3$ or ≥ 4 central electrons, $= 1$ ICD electron).

Channel	Signal	Migration	$2e2\tau$
$4e$ (2CC)	0.0309 ± 0.0011	$(4.16 \pm 0.61) \times 10^{-5}$	$(4.41 \pm 1.29) \times 10^{-4}$
$4e$ (3CC)	0.0702 ± 0.0016	$(6.37 \pm 0.71) \times 10^{-5}$	$(7.13 \pm 1.53) \times 10^{-4}$
$4e$ (4CC)	0.0658 ± 0.0015	$(6.69 \pm 0.72) \times 10^{-5}$	$(9.33 \pm 1.84) \times 10^{-4}$
$4e$ (1ICD)	0.0901 ± 0.0018	$(6.51 \pm 0.68) \times 10^{-5}$	$(1.01 \pm 0.19) \times 10^{-3}$

Table 7.19: Run IIa: $Acc \times \epsilon$ values for $eeee$ channel.

Channel	Signal	Migration	$2e2\tau$
$4e$ (2CC)	0.0242 ± 0.0004	$(2.16 \pm 0.27) \times 10^{-4}$	$(2.14 \pm 0.32) \times 10^{-4}$
$4e$ (3CC)	0.0578 ± 0.0006	$(3.73 \pm 0.20) \times 10^{-4}$	$(6.11 \pm 0.57) \times 10^{-4}$
$4e$ (4CC)	0.0514 ± 0.0005	$(3.99 \pm 0.19) \times 10^{-4}$	$(6.78 \pm 0.61) \times 10^{-4}$
$4e$ (1ICD)	0.0745 ± 0.0006	$(3.91 \pm 0.19) \times 10^{-4}$	$(7.34 \pm 0.64) \times 10^{-4}$

Table 7.20: Run IIb: $Acc \times \epsilon$ values for $eeee$ channel.

The $Acc \times \epsilon$ cut flow for our MC signal, migration and $t\bar{t}$ samples are given in Tables 7.21 and 7.22 for the $ee\mu\mu$ channel. The $Acc \times \epsilon$ values for various topologies in $ee\mu\mu$ channel are summarized in Table 7.23 and 7.24, where all uncertainties are statistical. These values are normalized to the mass ($M_1(Z/\gamma^*) > 30$ GeV, $M_2(Z/\gamma^*) > 30$ GeV) region.

Cut	Cumulative $A \times \epsilon$	Exclusive $A \times \epsilon$
MC ZZ Norm.	1.0000 ± 0.0000	–
≥ 1 good electron	0.5507 ± 0.0029	0.5507 ± 0.0029
≥ 1 good muon	0.2819 ± 0.0026	0.5964 ± 0.0039
p_T	0.2443 ± 0.0025	0.8665 ± 0.0034
Number of CC electrons	0 CC electrons	
	Cumulative $A \times \epsilon$	Exclusive $A \times \epsilon$
	0.0152 ± 0.0007	0.0620 ± 0.0026
Space angle and Acoplanarity cut	0.0151 ± 0.0007	1.0000 ± 0.0001
μ track Δz	0.0151 ± 0.0007	0.9935 ± 0.0035
$\Delta R_{e\mu}$	0.0148 ± 0.0007	0.9829 ± 0.0057
Dimass	0.0147 ± 0.0007	0.9939 ± 0.0034
Number of CC electrons	1 CC electrons	
	Cumulative $A \times \epsilon$	Exclusive $A \times \epsilon$
	0.0789 ± 0.0016	0.3229 ± 0.0050
Space angle and Acoplanarity cut	0.0789 ± 0.0016	0.9997 ± 0.0003
μ track Δz	0.0787 ± 0.0015	0.9982 ± 0.0008
$\Delta R_{e\mu}$	0.0756 ± 0.0015	0.9608 ± 0.0036
Dimass	0.0755 ± 0.0015	0.9979 ± 0.0009
Number of CC electrons	2 CC electrons	
	Cumulative $A \times \epsilon$	Exclusive $A \times \epsilon$
	0.1503 ± 0.0021	0.6150 ± 0.0052
Space angle and Acoplanarity cut	0.1502 ± 0.0021	0.9996 ± 0.0002
μ track Δz	0.1502 ± 0.0022	0.9999 ± 0.0001
$\Delta R_{e\mu}$	0.1398 ± 0.0020	0.9310 ± 0.0034
Dimass	0.1395 ± 0.0020	0.9975 ± 0.0007

Table 7.21: Run IIa: Cut flow for $ee\mu\mu$ MC signal showing cumulative and exclusive $Acc \times \epsilon$ for three subchannels ($= 0$, $= 1$ or ≥ 2 central electrons).

Cut	Cumulative $A \times \epsilon$	Exclusive $A \times \epsilon$
MC ZZ Norm.	1.0000 ± 0.0000	–
≥ 1 good elec.	0.4768 ± 0.0012	0.4768 ± 0.0012
≥ 1 good muon	0.2517 ± 0.0011	0.5279 ± 0.0017
p_T	0.1977 ± 0.0010	0.8590 ± 0.0018
Number of CC electrons	0 CC electrons	
	Cumulative $A \times \epsilon$	Exclusive $A \times \epsilon$
	0.0111 ± 0.0003	0.0562 ± 0.0013
Space angle and Acoplanary Cut	0.0111 ± 0.0003	0.9979 ± 0.0011
μ track Δz	0.0109 ± 0.0003	0.9868 ± 0.0026
$\Delta R_{e\mu}$	0.0107 ± 0.0002	0.9840 ± 0.0029
Dimass	0.0107 ± 0.0002	0.9935 ± 0.0019
Number of CC electrons	1 CC electrons	
	Cumulative $A \times \epsilon$	Exclusive $A \times \epsilon$
	0.0660 ± 0.0006	0.3342 ± 0.0026
Space angle and Acoplanary Cut	0.0660 ± 0.0006	0.9997 ± 0.0002
μ track Δz	0.0654 ± 0.0006	0.9901 ± 0.0009
$\Delta R_{e\mu}$	0.0616 ± 0.0006	0.9413 ± 0.0022
Dimass	0.0614 ± 0.0006	0.9981 ± 0.0004
Number of CC electrons	2 CC electrons	
	Cumulative $A \times \epsilon$	Exclusive $A \times \epsilon$
	0.1201 ± 0.0008	0.6084 ± 0.0027
Space angle and Acoplanary Cut	0.1199 ± 0.0008	0.9989 ± 0.0002
μ track Δz	0.1189 ± 0.0008	0.9908 ± 0.0007
$\Delta R_{e\mu}$	0.1059 ± 0.0007	0.8912 ± 0.0022
Dimass	0.1057 ± 0.0007	0.9981 ± 0.0003

Table 7.22: Run IIb: Cut flow for $ee\mu\mu$ MC signal showing cumulative and exclusive $Acc \times \epsilon$ for three subchannels ($= 0$, $= 1$ or ≥ 2 central electrons).

Channel	Signal	Migration	$t\bar{t}$
$2e2\mu$ (0CC)	0.014 ± 0.001	$(4.68^{+6.35}_{-3.27}) \times 10^{-6}$	$(1.00^{+1.00}_{-1.00}) \times 10^{-7}$
$2e2\mu$ (1CC)	0.076 ± 0.002	$(5.69^{+2.43}_{-1.89}) \times 10^{-5}$	$(1.05^{+1.42}_{-0.73}) \times 10^{-6}$
$2e2\mu$ (2CC)	0.140 ± 0.002	$(8.68^{+6.02}_{-4.09}) \times 10^{-6}$	$(5.35^{+7.26}_{-3.73}) \times 10^{-7}$

	$2\mu2\tau$	$2e2\tau$	4τ
$2e2\mu$ (0CC)	$(0.30 \pm 0.10) \times 10^{-3}$	$(0.25 \pm 0.09) \times 10^{-3}$	–
$2e2\mu$ (1CC)	$(0.87 \pm 0.16) \times 10^{-3}$	$(0.66 \pm 0.14) \times 10^{-3}$	–
$2e2\mu$ (2CC)	$(1.45 \pm 0.21) \times 10^{-3}$	$(1.98 \pm 0.24) \times 10^{-3}$	–

Table 7.23: Run IIa: $Acc \times \epsilon$ values in $ee\mu\mu$ channel.

Channel	Signal	Migration	$t\bar{t}$
$2e2\mu$ (0CC)	0.011 ± 0.001	$(2.18 \pm 0.55) \times 10^{-5}$	$(2.95^{+4.00}_{-2.06}) \times 10^{-6}$
$2e2\mu$ (1CC)	0.061 ± 0.001	$(5.10 \pm 0.84) \times 10^{-5}$	$(1.31^{+0.68}_{-0.51}) \times 10^{-6}$
$2e2\mu$ (2CC)	0.106 ± 0.001	$(5.17 \pm 0.86) \times 10^{-5}$	$(3.29^{+2.00}_{-1.26}) \times 10^{-7}$

	$2\mu2\tau$	$2e2\tau$	4τ
$2e2\mu$ (0CC)	$(1.79 \pm 0.31) \times 10^{-4}$	$(9.26 \pm 2.93) \times 10^{-5}$	–
$2e2\mu$ (1CC)	$(6.63 \pm 0.60) \times 10^{-4}$	$(7.72 \pm 0.84) \times 10^{-4}$	–
$2e2\mu$ (2CC)	$(1.85 \pm 0.10) \times 10^{-3}$	$(1.32 \pm 0.11) \times 10^{-3}$	–

Table 7.24: Run IIb: $Acc \times \epsilon$ values in $ee\mu\mu$ channel.

7.6 Backgrounds

There are two primary sources of background for our ZZ to four lepton signal. First is $Z(\rightarrow \ell\ell)$ + jets and $Z(\rightarrow \ell\ell) + \gamma$ + jets production, which we collectively refer to as **QCD** background. Here a jet is falsely reconstructed as an electron, or contains a muon. A second source of background is $t\bar{t} \rightarrow W^+bW^-\bar{b}$ production with subsequent leptonic W and semileptonic $b/\bar{b}$ decays. Here two out of four leptons are expected to be embedded in significant energy activity from the b-jets and therefore be non-isolated. There is also the migration background described earlier coming from low mass Z/γ^* pair production due to mismeasurement or by misassigning the lepton pair. Besides these dominant sources of the background there is also the possibility that beam halo interactions or cosmic ray muons contaminate the $\mu\mu\mu\mu$ final state. We use data to determine the QCD background and MC for the other sources.

QCD background arises in cases where there is a $Z(\rightarrow \ell\ell)$ with ≥ 1 jets in the final state and the jets mimic an electron or contain a muon. In the case of a mimicked electron, a jet is falsely identified as an electron. In the case of a muon, the jet usually contains a real muon from in-flight decays of pions, kaons, or a heavy quark. $Z(\rightarrow \ell\ell) + \gamma$ + jets production where a photon is also mis-identified as an electron primarily contaminates $eeee$ and $ee\mu\mu$ channels.

To calculate QCD background, first the probability for a jet to be mis-identified as a lepton (fakerate) for each type of lepton (electron or muon) is determined. This is found by processing the appropriate QCD skim. For Run IIa, the skim is given by definition `CSG_CAF_QCD_PASS3_p18.14.00` which contains 3,773 files and 98,176,223 events. While for Run IIb we use the merged Run IIb1-IIb4 QCD

skims which contains 9,651 files with 121,792,353 events and is the combination of `CSG_CAF_QCD_PASS[2,4,5,6]_pxx.xx.xx`. Once the fakerates are calculated, the QCD background is determined by running over the signal data skim for each channel and applying an appropriate cut flow. Details of how the fakerates and backgrounds are determined are described below.

7.6.0.1 Muon Fakerate

The muon fakerate is determined using a tag and probe method. First, we find all jets that have a $p_T > 15$ GeV. We require that the event has two such jets. To find the tag jet, we apply the following additional criteria:

- $0.05 < f_{EM} < 0.95$ (fraction of energy deposited in the electromagnetic calorimeter to the total deposited energy)
- $chf < 0.4$ (fraction of transverse momentum of a jet that is deposited in the coarse hadronic layers of the calorimeter)
- $n90 < 20$ (number of towers that make up 90% of the jet energy)
- L1Conf (L1 confirmation was introduced in order to deal with precision readout noise problems)

The remaining jet is the probe jet. We then additionally require that the $\Delta\phi$ between the tag and probe jets be > 3.0 radians. At this point we reject events with $\not\!\!E_T > 20$ GeV. This is to suppress possible W+jet contamination, which would contribute by increasing the fakerate to larger than expected values.

We then find all good muons in the event as defined previously with $p_T > 15$ GeV. We look for cases where the ΔR between the muon and the probe jet is < 0.5

which means the jet is mimicking a muon. The fakerate is then determined as a function of η_D and p_T by dividing the number of probe jets near a muon by the total number of probe jets. The obtained muon fakerate results with the muons required to be isolated are shown in Fig. 7.21-7.24. For reference, the average fakerate for Run IIb muons with $p_T > 15$ GeV, where only nseg = 0 and 1 muons are isolated, is 0.0039 ± 0.003, while the average is 0.0017 ± 0.0001 for the same muon p_T but all the muons are required to be isolated.

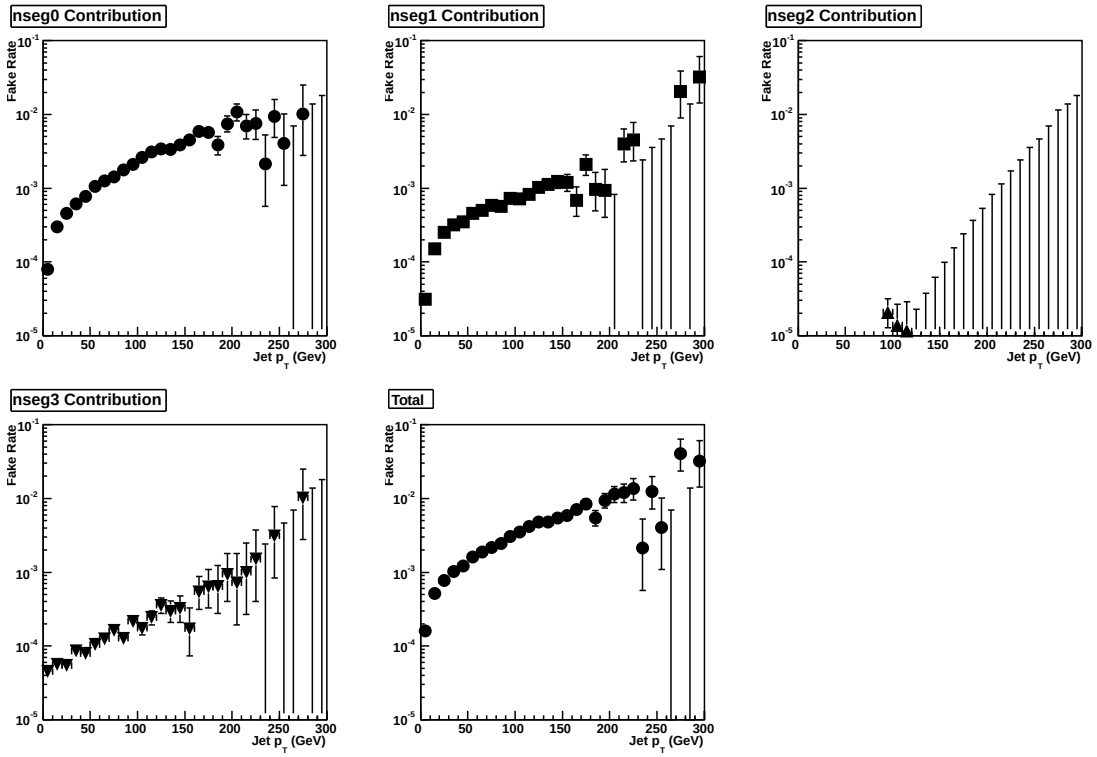

Figure 7.21: Run IIa: Measured muon fakerates as a function of jet p_T with muons $p_T > 15$ GeV and all muons are isolated for different values of nseg.

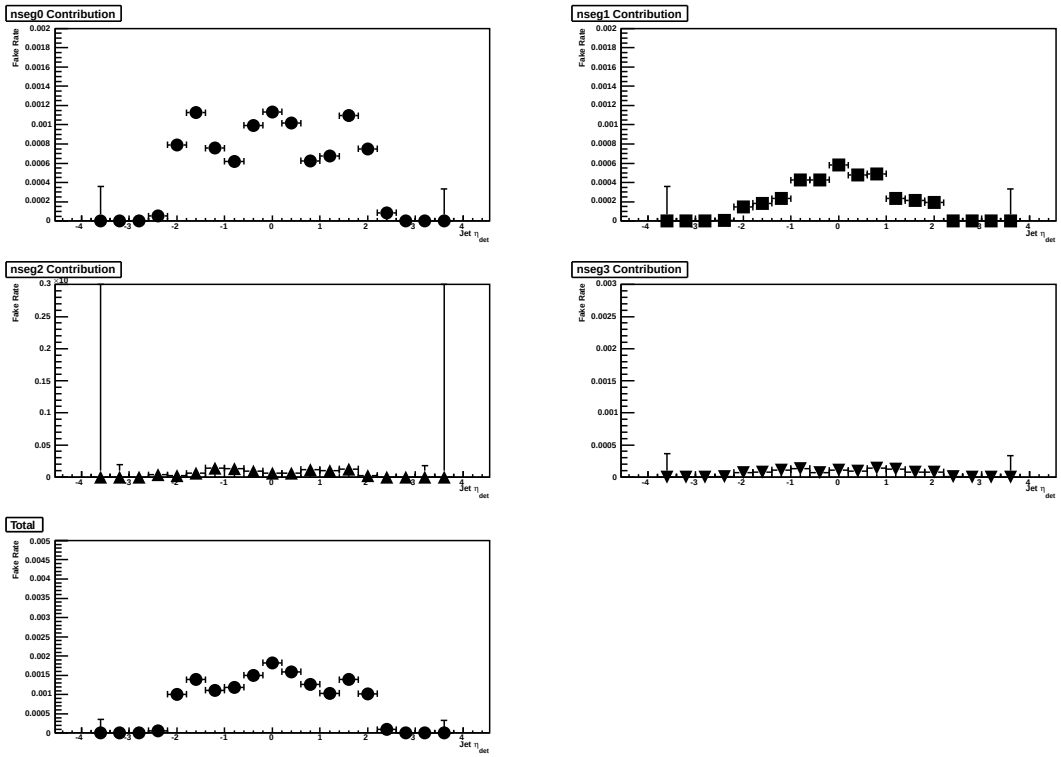

Figure 7.22: Run IIa: Measured muon fakerates as a function of jet η_D with muons $p_T > 15$ GeV and all muons are isolated for different values of nseg.

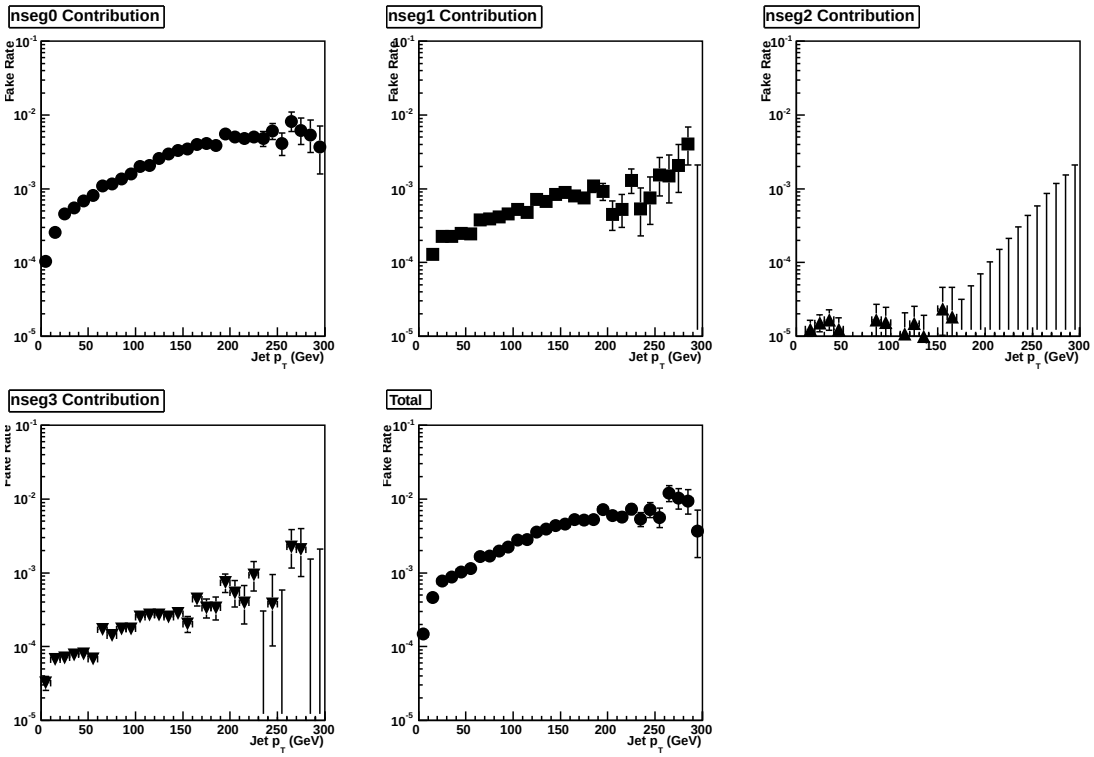

Figure 7.23: Run IIb: Measured muon fakerates as a function of jet p_T with muons $p_T > 15$ GeV and all muons are isolated for different values of nseg.

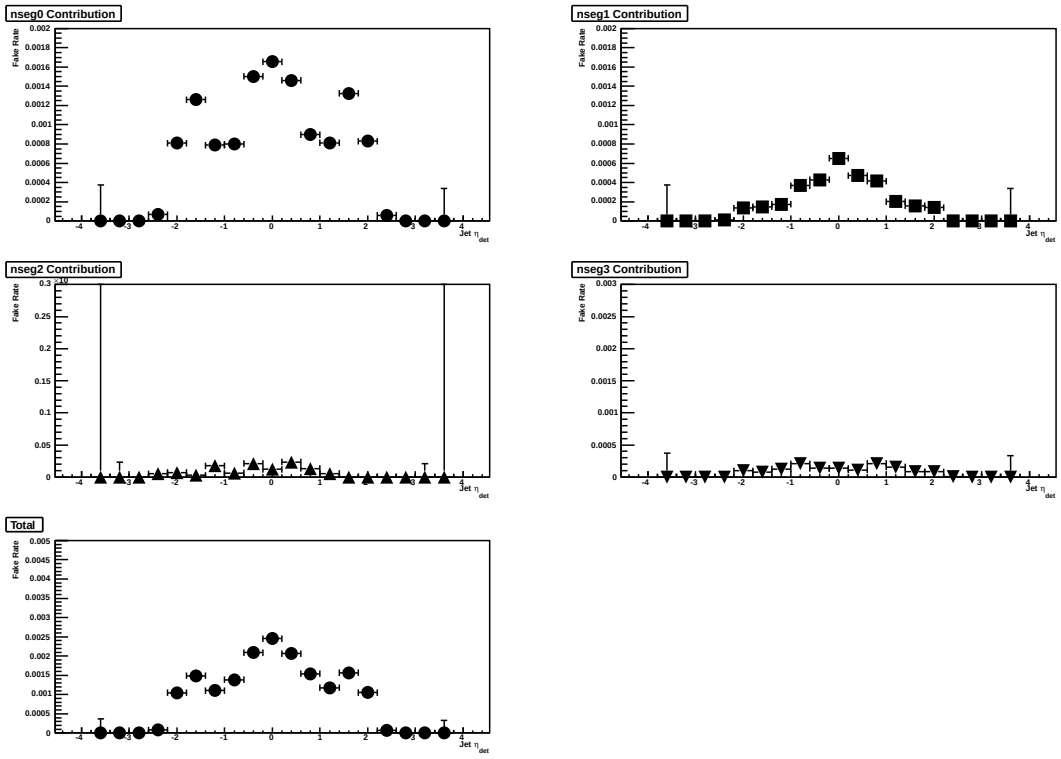

Figure 7.24: Run IIb: Measured muon fakerates as a function of jet η_D with muons $p_T > 15$ GeV and all muons are isolated for different values of nseg.

7.6.0.2 Electron Fakerate

The electron fakerate is determined using the same tag and probe method as described in the previous section for the muon fakerate. We find all good electrons in the event as defined previously with a p_T requirement of 15 GeV. We then look for cases where the ΔR between the electron and the probe jet is < 0.5 which means the jet is mimicking an electron. The fakerate is then the efficiency as a function of η_D and p_T by dividing the number of probe jets which have an associated electron over the number of probe jets. The obtained electron fakerate results are shown in Fig. 7.25-7.26.

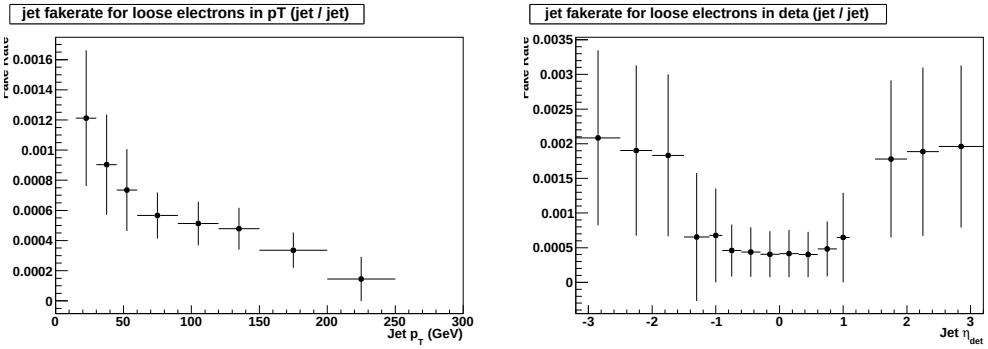

Figure 7.25: Run IIa: Plot of the measured electron fakerates as a function of jet p_T (left) and as a function of jet η_D (right).

In addition to the background from a jet faking an electron in the CC or EC, we also may have events where a jet fakes an electron in the ICD. We model this background using the same method as outline above, except in this case we determine the fakerate using probe jets within the ICD region, and apply the fakerate to events with three good CC/EC electrons and a jet in the ICD region.

In the ICD region, the energy resolution is poorer, so we first examined the fakerate versus $\not\!\!E_T$ to determine where to cut to remove W contamination. We

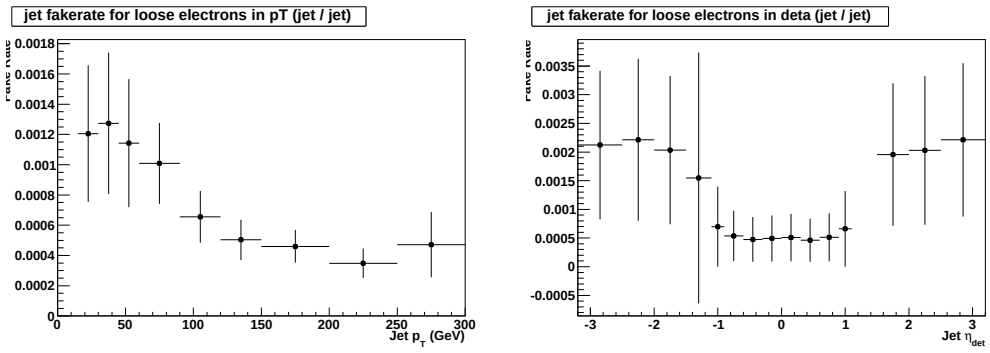

Figure 7.26: Run IIb: Plot of the measured electron fakerates as a function of jet p_T (left) and as a function of jet η_D (right).

apply the standard jet energy scale (JES) correction for the jet in the ICD when determining the $\not\!\!E_T$ for the event, unless the jet passes all of our signal ICD cuts. It has previously been found [81] that the standard JES correction overestimates the energy of ICD electron objects. We instead substitute the p_T of the track for the calorimeter energy of the ICD object in the $\not\!\!E_T$ calculation for these events. All other objects in the event enter the $\not\!\!E_T$ calculation normally. We find that an $\not\!\!E_T$ cut of 20 GeV also works well in the ICD region. The fakerate results are shown in Fig. 7.27 and 7.28.

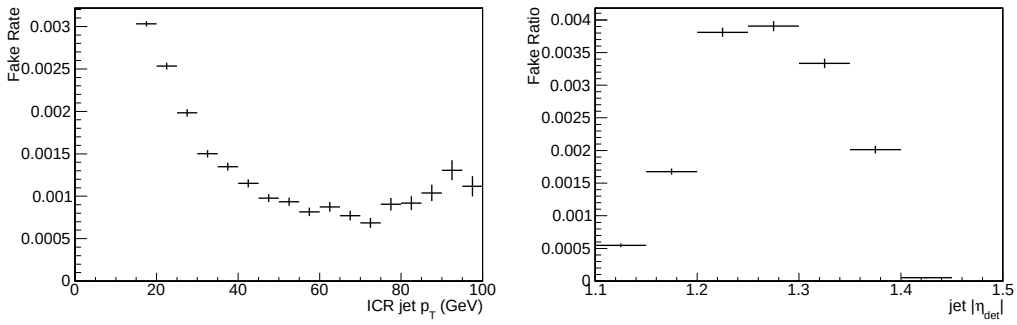

Figure 7.27: Run IIa: Plot of the measured ICD electron fakerates as a function of jet p_T (left) and as a function of jet $|\eta_D|$ (right).

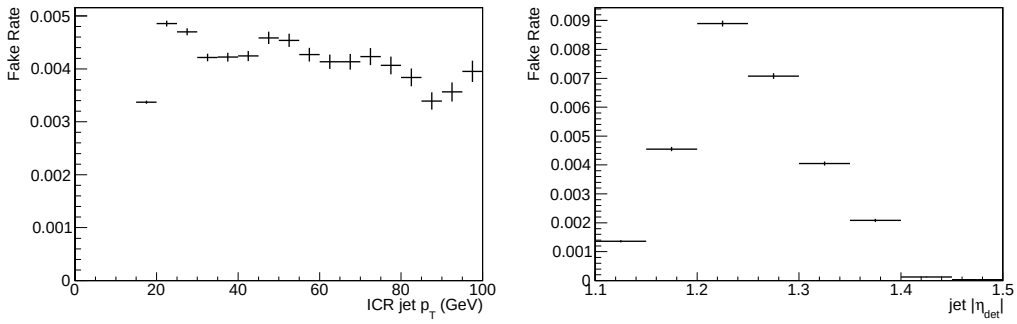

Figure 7.28: Run IIb: Plot of the measured ICD electron fakerates as a function of jet p_T (left) and as a function of jet $|\eta_D|$ (right).

7.6.0.3 QCD background Determination in four lepton channels

To estimate the QCD background of the 4μ channel, we run the muon fakerate over the "two muon high p_T" (2MUhighpt) data sample and select events with good muons and jets. The following selection cuts are applied:

- at least two muons
- muons satisfy $p_T^1 > 15$ GeV, $p_T^2 > 15$ GeV
- both muons must be isolated
- $\cos\alpha < 0.96$ between muon pair
- $\Delta Z_{DCA} < 3.0$ cm between muon tracks
- at least two jets with respect to the two $\Delta R > 0.5$ muons that also pass $p_T > 15.0$ GeV

We loop over all jets in events passing the above selections, and sum up all of the fakerate values for each jet to obtain the total QCD background. Note that no Z mass cut is applied since the jet kinematics are not the same as those for the muon.

The resulting Run IIa QCD background event yield is 0.0028 ± 0.0001, and the resulting Run IIb QCD background event yield is 0.0161 ± 0.0002.

The QCD background of the $4e$ channel is calculated by running over the "two EM objects high p_T" (2EMhighpt) data sample and selecting events with good electrons and jets that are in the CC, ICD or EC region. We apply the following selection cuts:

- at least three electrons (to correctly account for $Z + \gamma$ +jets background)
- electrons must satisfy $p_T^1 > 15.0$ GeV, $p_T^2 > 15.0$ GeV and $p_T^3 > 15.0$ GeV
- at least one jet with respect to the three $\Delta R > 0.5$ electrons that also passes $p_T > 15.0$ GeV
- pass the Z mass requirement of one pair with a dimass > 30 GeV and the other with a dimass > 30 GeV

We split the sample into four subchannels, corresponding to $N_{CCEM} = 2, 3 or 4; N_{ICDEM} = 0$ and $N_{CCEM} \geq 2; N_{ICDEM} = 1$. We then loop over all jets passing the above cuts, requiring that the combination of each jet and the three electrons satisfy the normal p_T cuts of the signal selection, and sum up all of the fakerate values for each jet.

The resulting background for the $4e$ channel is shown in Table 7.25.

CC objects	ICD objects	Run IIa	Run IIb	Total
2	0	0.016 ± 0.003	0.148 ± 0.013	0.164 ± 0.013
3	0	0.009 ± 0.003	0.111 ± 0.011	0.121 ± 0.011
4	0	0.003 ± 0.001	0.053 ± 0.006	0.056 ± 0.006
≥ 2	1	0.022 ± 0.015	0.281 ± 0.039	0.303 ± 0.042

Table 7.25: Expected QCD background in the 4e channel for each subchannel.

The QCD background of the $2e2\mu$ channel is estimated using the fakerates of both electrons and muons. Two different contributions are determined:

1. Two muons plus an electron plus a jet, where we apply the electron fakerate to the jet. This method gives us an estimate of background due to $Z(\rightarrow \mu\mu)$ + jets and $Z(\rightarrow \mu\mu) + \gamma$ + jets where a jet can mimic an electron.

2. Two electrons plus two jets, where we apply the muon fakerate to the jets. This method gives us an estimate of the background due to $Z(\rightarrow ee)$ + jets where jets can contain muons.

In the first case, the background is determined by running over the 2MUhighpt data sample and finding good muons and electrons in the event as defined previously and any jets in the event. We then apply the following cuts:

- at least two muons and one electron
- muons satisfy $p_T^1 > 15.0$ GeV, $p_T^2 > 15.0$ GeV and electron satisfies $p_T > 15.0$ GeV
- both muons must be isolated
- require $\cos\alpha < 0.96$ between muon pair
- require acoplanarity between any two muons must be greater than 0.05
- require $\Delta Z_{DCA} < 3.0$ cm between muon tracks
- require ΔR between electron and muons to be > 0.2
- at least one jet with $\Delta R > 0.5$ with respect to the muons and an electron that also passes $p_T > 15.0$ GeV and is either CC or EC
- perform a cut on the number of CC objects $(= 0, = 1, \geq 2)$ combining the electron with the jets

- pass the Z mass requirement of one pair with a dimass > 30 GeV and the other with a dimass > 30 GeV where one pair is the (μ, μ) and the other is the (e, jet) mass with the leading jet

We then loop over all jets passing the above cuts, requiring that the combination of each jet and the electron satisfy the normal p_T cuts of the signal selection, and sum up all of the fakerate values for each jet.

While this method correctly takes into account the contribution from $Z + \gamma +$ jets production (and other smaller possible contributions such as WZ + jets, WW + jets, W + jets, $\geq$4 jets), it double counts $Z \rightarrow \mu\mu +$ jets background as an event with two muons and two jets enters the two muons + electron + jet sample if either of the jets is misidentified as an electron, but will only enter the $ee\mu\mu$ sample if both jets are misidentified. To correct for this effect, we estimate the $Z \rightarrow \mu\mu +$ jets contribution separately by selecting a two muons plus two jets sample, applying the similar cut flow as described above, and applying the electron fakerate to both jets. We subtract the resulting estimate from the one obtained using the two muons plus electron plus jets sample.

In the second case, the background is determined by running over the 2EMhighpt data sample and finding good electrons in the event as defined previously and any jets in the event. We then apply the following cuts:

- at least two electrons
- electrons satisfy $p_T^1 > 15$ GeV, $p_T^2 > 15$ GeV
- perform a cut on the number of CC electrons $(= 0, = 1, \geq 2)$
- at least two jets with $\Delta R > 0.5$ with respect to the two electrons that also pass $p_T > 15.0$ GeV

- require $M_{ee} > 30$ GeV

We then loop over all jets passing the above cuts and sum up all of the fakerate values for each jet. We have three events for each subchannel and the total fakerate is events of 2μ+e+jet minus 2μ+2jet plus $2e$+2jet.

The resulting background for $2e2\mu$ is shown in Tab. 7.26 and 7.27.

CC objects	2μ+e+jet	2μ+2jet	$2e$+2jet	Total
0	$3.47 \pm 0.51 \times 10^{-3}$	$3.12 \pm 0.10 \times 10^{-4}$	$9.22 \pm 0.51 \times 10^{-4}$	$4.08 \pm 0.57 \times 10^{-3}$
1	$2.25 \pm 0.49 \times 10^{-2}$	$7.40 \pm 0.11 \times 10^{-4}$	$1.33 \pm 0.04 \times 10^{-3}$	$2.31 \pm 0.50 \times 10^{-2}$
≥ 2	$1.61 \pm 0.36 \times 10^{-2}$	$0.99 \pm 0.01 \times 10^{-3}$	$1.09 \pm 0.06 \times 10^{-3}$	$1.63 \pm 0.37 \times 10^{-2}$

Table 7.26: Run IIa QCD background in the $ee\mu\mu$ channel for each subchannel.

CC objects	2μ+e+jet	2μ+2jet	$2e$+2jet	Total
0	$5.97 \pm 0.23 \times 10^{-2}$	$2.30 \pm 0.03 \times 10^{-3}$	$6.50 \pm 0.10 \times 10^{-3}$	$6.39 \pm 0.23 \times 10^{-2}$
1	$1.27 \pm 0.03 \times 10^{-1}$	$7.05 \pm 0.05 \times 10^{-3}$	$9.31 \pm 0.11 \times 10^{-3}$	$1.29 \pm 0.03 \times 10^{-1}$
≥ 2	$2.51 \pm 0.05 \times 10^{-1}$	$2.23 \pm 0.10 \times 10^{-2}$	$7.08 \pm 0.11 \times 10^{-3}$	$2.36 \pm 0.05 \times 10^{-1}$

Table 7.27: Run IIb QCD background in the $ee\mu\mu$ channel for each subchannel.

7.6.1 QCD Background Crosscheck in $\mu\mu\mu\mu$ Channel

In the previous sections, we discussed the jet fakerate from Z+jet events by determining the number of events with a good isolated muon opposite a tag jet divided by the number of events with a probe jet opposite a tag jet. The QCD background of the 4μ channel is estimated by applying the fakerate probability to events with two good muons and two jets.

In order to crosscheck the background results obtained from the jet weighting procedure, we in addition use the Z+jets MC with light and heavy flavors to estimate

the background as heavy quark decay to real muons dominate for this background. $t\bar{t}$ background is too small to consider in the 4μ channel. The samples are full Run IIa and Run IIb Z/γ+jets MC. The only energy range of interest for us is 75-130 GeV. All four lepton channels ($\mu\mu$, $\nu\nu$, $\tau\tau$, ee) are considered in this study.

We apply all the selection used for the 4μ analysis with proper event weighting for the Z+jets samples. Only the $\mu\mu$ channel gives 14 passing events while the other channels have no events passing the selection. Among these events, 6 are light flavor, 3 are b-jet heavy flavor, and 5 are c-jet heavy flavor. The $Acc \times \epsilon$ are shown below in Table 7.28.

$Z/\gamma^* + 2b + lp \rightarrow \mu\mu + 2b + lp$	$Z/\gamma^* + 2c + lp \rightarrow \mu\mu + 2c + lp$	$Z/\gamma^* + lp \rightarrow \mu\mu + lp$
$(2.78 \pm 1.60) \times 10^{-7}$	$(3.84 \pm 1.62) \times 10^{-7}$	$(1.07 \pm 0.41) \times 10^{-7}$

Table 7.28: $Acc \times \epsilon$ values for Z+jets MC.

The background is estimated by Run IIb samples. We use cross section values of $\sigma(Z + lf) = 185.541$ pb, $\sigma(Z + bb) = 0.696$ pb, $\sigma(Z + cc) = 1.728$ pb, and $BR(Z \rightarrow \mu\mu) = 0.034$. The total resulting Run IIb background event yield is 0.0064 ± 0.0023, which is comparable to the fakerate background results 0.0161 ± 0.0002. All the figures associated with these Z+jets MC are listed in Appendix **??**.

7.6.2 $t\bar{t}$ Background

Top pair production can lead to final states with four leptons. This background is estimated using $t\bar{t} \rightarrow 2b{+}2\ell{+}2\nu$ MC events by `ALPGEN` [49]. We use a cross section value of $\sigma^{NNLL}(t\bar{t})$ =7.9 pb [82] assuming a top quark mass of $m_{top} = 172$ GeV, which gives us $\sigma^{NNLL}(t\bar{t})\times$ BR$^2(W \rightarrow \ell)$=7.9×0.321^2=814 fb for the normalization. It is normalized to the approximate next-to-NLO (NNLO) cross section calculation [83].

The $Acc \times \epsilon$ values for $t\bar{t} \to 2b + 2\ell + 2\nu$ can be found in Tables 7.16, 7.23 and 7.24. A small contamination is observed only in the $ee\mu\mu$ channel.

7.6.3 Migration

The migration background arises from the same $Z/\gamma^* Z/\gamma^* \to \ell^+\ell^-\ell'^+\ell'^-$ events as our signal, but from low mass Z/γ^* pair production. This occurs either due to mismeasurement or by misassigning the lepton pairs. In the $eeee$ and $\mu\mu\mu\mu$ channels these events can pass the reconstructed Z mass requirement of > 30 GeV on the dilepton pairs because the final state involves leptons of the same flavor. Since we do not consider the charge of the leptons (except for the 4μ analysis), there are three possible ZZ pairs that can be formed. Wrong pairings (leptons from different Zs wrongly assigned to each other) from low mass $Z/\gamma^* Z/\gamma^*$ events can pass mass requirements and contribute into our signal. Momentum resolution also allows events to be mismeasured in all three channels. This contribution is determined by finding the $Acc \times \epsilon$ from the MC signal sample. We generate Z/γ^* pairs down to 5 GeV and estimate the cross section of these events using Next-to-Lead-Order (NLO) MC [46]. The results for the various subchannels are given in Tables 7.16, 7.19, 7.20, 7.23 and 7.24.

7.6.4 Beam Halo and Cosmic Muon Background

Beam halo interactions and multiple interactions in the same crossing, both combined as "beam halo" background and cosmic ray muons overlaying a physics processes such as $WZ \to \mu\mu\mu$ can produce events containing four muons.

To estimate the contribution due to beam halo and cosmic rays, we select events with four muons applying our normal selection cuts, but removing requirements on muon dca, dimuon pair opposite charges plus space angle cut plus acoplanarity cut (we call it "charge" below), and $\Delta Z_{DCA} < 3$ cm between muon tracks. For Run IIb we can see 117867 candidate events, which we assume to be dominated by beam halo and cosmic ray contributions. We relax the p_T cut on muons to 5 GeV to gain statistics. We apply muon dca, charge and ΔZ_{DCA} cuts to the pre-selected events. Note that cosmic ray muons are a small contribution when cuts are relaxed. Then the rejection factor of each of the three requirements is estimated in a subsample where the two other requirements are reversed. The result for Run IIb is given in Tab. 7.29.

Requirement	$N_{initial}$	N_{pass}	Rejection
dca	55668	39	1427
Charge	290858	235229	1.2
ΔZ_{DCA}	55639	10	5564

Table 7.29: Run IIb: Rejection factors against beam halo and cosmics.

We obtain a total Run IIb rejection factor of $1427 \times 1.2 \times 5564 = 9.8 \times 10^6$. Applying this to the 117867 Run IIb events observed in the sample, we get a conservative estimate of 0.012 events in the four muon channel. For Run IIa, this number is about 0.0033 in the four muon channel.

7.7 Systematic Uncertainties

Numerous factors contribute to systematic uncertainties in this measurement. This section describes these various factors and estimates their uncertainty. The considered systematics include:

- **Data Quality and Trigger**: The systematic uncertainty on the measured data quality flag efficiency was estimated to be 0.5% [84] by comparing the effect of data quality removal with calorimeter quality flag events removed compared to that without calorimeter quality flag events removed. We also include a 1.0% uncertainty here due to possible trigger uncertainty.

- z_{vtx} **Reweighting**: The nominal reweighting used according to the procedure described in note [77] uses a fit from ± 60 cm in the data. An alternate fit from ± 40 cm is also available, and this is used to estimate the uncertainty. This procedure uses the shapes of the p and $\bar{p}$ bunches and the β_x^* and the β_y^* of the interaction point for various instantaneous luminosities and z_{vtx} cut.

- ZZ p_T **Reweighting**: To estimate the effect of higher order corrections on signal acceptance, we apply a ZZ p_T reweighting function, derived by fitting the p_T spectra of WW in `Sherpa` and `Pythia` [85]. We estimate this uncertainty by switching on this correction and measuring its effect on the relevant acceptance times efficiencies.

- **Electron ID**: The systematic errors on Electron ID have been calculated by the EMID group and their results are presented in [72, 78]. They include dependence on the distance to the closest jet, jet multiplicity, fits to efficiency curves and sensitivity to cuts on p_T and calorimeter fiducial region. Since these

issues are in common with our analysis, we use their results and calculate a systematic uncertainty for "Point0" electrons. For electrons between 15 and 20 GeV, the uncertainties are 6.7%, 4.2%, 3.5%, and 2.9% for Run IIa, Run IIb1, Run IIb2, and Run IIb3 respectively (the same uncertainty is used in Run IIb3 and Run IIb4), for a luminosity weighted average of 3.7%. The systematic uncertainty is smaller at higher p_T, but we use this number to be conservative. This gives us an overall uncertainty of 14.8% on the $4e$ channel and 7.4% on the $2e2\mu$ channel. We use a systematic uncertainty of 6% per ICD electron, following [74, 75], leading to a systematic uncertainty of 12.6% on $4e$ events with an ICD electron.

- **Electron energy resolution**: We apply additional smearing to the energies of the electrons. We estimate this uncertainty by switching off this correction and measuring its effect on the relevant acceptance times efficiencies.

- **Electron Fakerate**: The systematic error for the electron QCD fakerate is determined by using a second form of the fakerate where the energy from the electron associated with the probe jet is used rather than the energy from the probe jet itself. The QCD background is recalculated to estimate the uncertainty.

- **Muon ID**: The systematic errors on Muon ID have been calculated by the Muon ID group [79, 80]. The Run IIa systematic uncertainty for loose muons (0.5%) is used here. This includes tag and probe bias, background and cut variations and finite binning uncertainties which are in common with our analysis, hence our use of their results. The Run IIb systematic uncertainty for loose muons is found to be 0.9% per muon. nseg=0 muons are not part of the muon certification and are not as well modeled in MC relative to the other

muon types (they have a higher efficiency in MC). But, as seen above in Table 7.8, nseg=0 muon are about 5% of the MC muon acceptance. If we assign a 10% error to this, and add this in quadrature to the systematic uncertainty of other muon topologies, we obtain a 1% error per muon, which we use as the systematic uncertainty of for all muons in this analysis.

- **Muon track**: The Run IIa systematic errors on muon track reconstruction (0.6%) are also taken from note [79] while that for IIb is 1.0% from note 6326 [80]. This includes tag and probe bias, background and cut variation, luminosity and time bias, time average, finite binning and average over ϕ uncertainties.

- **Muon Isolation**: For both the Run IIa and Run IIb channels we assign a 0.6% systematic uncertainty based on results from the Muon ID group [79, 80] for the isolation criteria used in this analysis. Note combining muon ID, tracking efficiency, and isolation one obtains an overall muon uncertainty of 1.5% with 100% correlation between muons and so the uncertainty on the 4μ channel would be 6%.

- **Muon momentum resolution**: We apply additional smearing to muon momentum. We estimate this uncertainty by switching off this correction and measuring its effect on the relevant acceptance times efficiencies.

- **Muon Fakerate**: The systematic error for the muon QCD fakerate is determined by varying the nominal fakerate by $\pm 20\%$ and the QCD background is recalculated to estimate the uncertainty.

- $t\bar{t}$ **cross section uncertainty**: We assign $\pm 20\%$ uncertainty to the top pair production cross-section. This covers theory uncertainty of 10% at $m_{top} =$

172 GeV [82], plus cross section variation due to top mass uncertainty of ±2 GeV.

- **PDF**: The parton distribution functions (PDF) are optimized with respect to deep inelastic proton data, expressing the uncertainties as a density measure over the functional space of parton distribution functions. For variation in signal acceptance due to PDF uncertainty we add in quadrature PDF errors estimated in the $ZZ \to \ell\ell\nu\nu$ [57] and $Z \to ee$ [86] cross-section analysis. The combination of the two errors is done because the $ZZ \to \ell\ell\nu\nu$ analysis is normalized with respect to the inclusive Z cross section. We obtain an estimate of ±2.5%.

- ZZ **cross section uncertainty**: We assign 7.1% uncertainty on the $\sigma(ZZ)$ as quoted in [46].

- **MC Statistics**: The systematic error due to limited statistics in the Monte Carlo samples is determined from the statistical error over the mean value.

- **QCD Sample Statistics**: The systematic error due to the limited number of events in the normalization sample, used to estimate QCD background is determined from the statistical error over the mean value.

An additional source of systematics in all channels not included in the tables but used in the determination of significance and cross section is the 4.3% uncertainty in the luminosity determination as provided by the luminosity group [69]. The uncertainties for the $\mu\mu\mu\mu$ channel are listed in tables 7.30 and 7.31. The individual uncertainties for the $eeee$ channel are listed in Tables 7.32, 7.33, 7.34, 7.35, 7.36, 7.37, 7.38, and 7.39. The individual uncertainties for the $ee\mu\mu$ channel are listed in Tables 7.40, 7.41, 7.42, 7.43, 7.44 and 7.45.

Systematic	Signal, %		Migration, %		QCD, %	
	up	down	up	down	up	down
Data quality	+0.5	-0.5	+0.5	-0.5	+0.5	-0.5
Trigger	+1.0	-1.0	+1.0	-1.0	+1.0	-1.0
vtx_z reweight	+0.57	-0.57	+0.33	-0.33	–	–
ZZ p_T reweight	–	-0.41	+18.28	–	–	–
Muon ID	+4.0	-4.0	+4.0	-4.0	–	–
Muon momentum res.	+0.31	–	–	-8.70	–	–
Muon Track	+2.4	-2.4	+2.4	-2.4	–	–
Muon Isolation	+2.4	-2.4	+2.4	-2.4	–	–
Muon Fakerate	–	–	–	–	+44.00	-36.00
PDF	+2.5	-2.5	+2.5	-2.5	–	–
$\sigma(ZZ)$	+7.1	-7.1	+7.1	-7.1	–	–
MC Stats	+0.94	-0.94	+8.79	-8.79	–	–
QCD Sample Stats	–	–	–	–	+4.50	-4.50
Total	+9.31	-9.32	+22.29	-15.44	+44.24	-36.30

Table 7.30: Run IIa: relative uncertainties in the $\mu\mu\mu\mu$ channel for various efficiencies and backgrounds. The top eleven rows are systematic uncertainties, while the next two rows are statistical in nature and the total.

Systematic	Signal, %		Migration, %		QCD, %	
	up	down	up	down	up	down
Data quality	+0.5	-0.5	+0.5	-0.5	+0.5	-0.5
Trigger	+1.0	-1.0	+1.0	-1.0	+1.0	-1.0
vtx_z reweight	+0.32	-0.32	+0.41	-0.41	–	–
ZZ p_T reweight	+0.20	–	+17.44	–	–	–
Muon ID	+4.0	-4.0	+4.0	-4.0	–	–
Muon momentum res.	+0.32	–	–	-2.85	–	–
Muon Track	+4.0	-4.0	+4.0	-4.0	–	–
Muon Isolation	+2.4	-2.4	+2.4	-2.4	–	–
Muon Fakerate	–	–	–	–	+44.34	-36.62
PDF	+2.5	-2.5	+2.5	-2.5	–	–
$\sigma(ZZ)$	+7.1	-7.1	+7.1	-7.1	–	–
MC Stats	+0.45	-0.45	+4.14	-4.14	–	–
QCD Sample Stats	–	–	–	–	+1.34	-1.34
Total	+9.80	-9.80	+20.42	-11.01	+44.37	-36.66

Table 7.31: Run IIb: relative uncertainties in the $\mu\mu\mu\mu$ channel for various efficiencies and backgrounds. The top eleven rows are systematic uncertainties, while the next two rows are statistical in nature and the total.

	signal, %		misrec., %		QCD, %	
Systematic	up	down	up	down	up	down
Data quality	+0.50	-0.50	+0.50	-0.50	+0.50	-0.50
Trigger	+1.0	-1.0	+1.0	-1.0	+1.0	-1.0
vtx_z reweight	+0.55	-0.55	+0.36	-0.36	–	–
ZZ p_T reweight	–	-6.04	–	-3.18	–	–
Electron ID	+26.80	-26.80	+26.80	-26.80	–	–
Electron energy res.	+1.22	–	+1.88	–	–	–
EM Fakerate	–	–	–	–	+6.37	-6.37
PDF	+2.50	-2.50	+2.50	-2.50	–	–
$\sigma(ZZ)$	+7.1	-7.1	+7.1	-7.1	–	–
MC Stats	+3.44	-3.44	+14.76	-14.76	–	–
QCD Sample Stats	–	–	–	–	+20.06	-20.06
Total	+28.10	-28.72	+31.59	-31.69	+21.08	-21.08

Table 7.32: Run IIa: relative uncertainties in the *eeee* channel with 2 CC electrons for various efficiencies and backgrounds. The top nine rows are systematic uncertainties, while the next two rows are statistical in nature and the total.

	signal, %		misrec., %		QCD, %	
Systematic	up	down	up	down	up	down
Data quality	+0.50	-0.50	+0.50	-0.50	+0.50	-0.50
Trigger	+1.0	-1.0	+1.0	-1.0	+1.0	-1.0
vtx_z reweight	+0.53	-0.53	+0.62	-0.62	–	–
ZZ p_T reweight	–	-6.84	–	-3.04	–	–
Electron ID	+26.80	-26.80	+26.80	-26.80	–	–
Electron energy res.	+0.58	–	–	-3.32	–	–
EM Fakerate	–	–	–	–	+4.84	-4.84
PDF	+2.50	-2.50	+2.50	-2.50	–	–
$\sigma(ZZ)$	+7.1	-7.1	+7.1	-7.1	–	–
MC Stats	+2.26	-2.26	+11.17	-11.17	–	–
QCD Sample Stats	–	–	–	–	+29.06	-29.06
Total	+27.96	-28.78	+30.02	-30.36	+29.48	-49.48

Table 7.33: Run IIa: Relative uncertainties in the *eeee* channel with 3 CC electrons for various efficiencies and backgrounds. The top nine rows are systematic uncertainties, while the next two rows are statistical in nature and the total.

	signal, %		misrec., %		QCD, %	
Systematic	up	down	up	down	up	down
Data quality	+0.50	-0.50	+0.50	-0.50	+0.50	-0.50
Trigger	+1.0	-1.0	+1.0	-1.0	+1.0	-1.0
vtx_z reweight	+0.57	-0.57	+0.53	-0.53	–	–
ZZ p_T reweight	–	-5.01	–	-4.42	–	–
Electron ID	+26.80	-26.80	+26.80	-26.80	–	–
Electron energy res.	0.09	–	0.07	–	–	–
EM Fakerate	–	–	–	–	+9.05	-9.05
PDF	+2.50	-2.50	+2.50	-2.50	–	–
$\sigma(ZZ)$	+7.1	-7.1	+7.1	-7.1	–	–
MC Stats	+2.27	-2.27	+10.79	-10.79	–	–
QCD Sample Stats	–	–	–	–	+43.28	-43.28
Total	+27.96	-28.40	+28.40	-29.88	+44.23	-44.23

Table 7.34: Run IIa: Relative uncertainties in the *eeee* channel with 4 CC electrons for various efficiencies and backgrounds. The top nine rows are systematic uncertainties, while the next two rows are statistical in nature and the total.

	signal, %		misrec., %		QCD, %	
Systematic	up	down	up	down	up	down
Data quality	+0.50	-0.50	+0.50	-0.50	+0.50	-0.50
Trigger	+1.0	-1.0	+1.0	-1.0	+1.0	-1.0
vtx_z reweight	+0.59	-0.59	+0.57	-0.57	–	–
ZZ p_T reweight	–	-6.12	–	-7.68	–	–
Electron ID	+20.97	-20.97	+20.97	-20.97	–	–
Electron energy res.	0.17	–	–	-0.82	–	–
EM Fakerate	–	–	–	–	+0.61	-63.23
PDF	+2.50	-2.50	+2.50	-2.50	–	–
$\sigma(ZZ)$	+7.1	-7.1	+7.1	-7.1	–	–
MC Stats	+4.06	-4.06	+10.49	-10.49	–	–
QCD Sample Stats	–	–	–	–	+66.69	-66.69
Total	+22.68	-23.49	+24.66	-25.84	+66.70	-91.91

Table 7.35: Run IIa: Relative uncertainties in the *eeee* channel with 1 ICR electron for various efficiencies and backgrounds. The top nine rows are systematic uncertainties, while the next two rows are statistical in nature and the total.

	signal, %		misrec., %		QCD, %	
Systematic	up	down	up	down	up	down
Data quality	+0.5	-0.5	+0.5	-0.5	+0.5	-0.5
Trigger	+1.0	-1.0	+1.0	-1.0	+1.0	-1.0
vtx_z reweight	+0.41	-0.41	+0.44	-0.44	–	–
ZZ p_T reweight	–	-5.11	–	-0.56	–	–
Electron ID	+13.20	-13.20	+13.20	-13.20	–	–
Electron energy res.	+0.96	–	–	-0.26	–	–
EM Fakerate	–	–	–	–	+21.25	-21.25
PDF	+2.5	-2.5	+2.5	-2.5	–	–
$\sigma(ZZ)$	+7.1	-7.1	+7.1	-7.1	–	–
MC Stats	+2.47	-2.47	+6.45	-6.45	–	–
QCD Sample Stats	–	–	–	–	+8.59	-8.59
Total	+15.47	-16.26	+16.55	-16.56	+22.95	-22.95

Table 7.36: Run IIb: Relative uncertainties in the *eeee* channel with 2 CC electrons for various efficiencies and backgrounds. The top nine rows are systematic uncertainties, while the next two rows are statistical in nature and the total.

	signal, %		misrec., %		QCD, %	
Systematic	up	down	up	down	up	down
Data quality	+0.5	-0.5	+0.5	-0.5	+0.5	-0.5
Trigger	+1.0	-1.0	+1.0	-1.0	+1.0	-1.0
vtx_z reweight	+0.43	-0.43	+0.45	-0.45	–	–
ZZ p_T reweight	–	-5.44	–	-4.65	–	–
Electron ID	+13.20	-13.20	+13.20	-13.20	–	–
Electron energy res.	+0.72	–	–	+1.25	–	–
EM Fakerate	–	–	–	–	+16.96	-16.96
PDF	+2.5	-2.5	+2.5	-2.5	–	–
$\sigma(ZZ)$	+7.1	-7.1	+7.1	-7.1	–	–
MC Stats	+2.53	-2.53	+5.08	-5.08	–	–
QCD Sample Stats	–	–	–	–	+9.51	-9.51
Total	+15.47	-16.38	+16.12	-16.73	+19.48	-19.48

Table 7.37: Run IIb: Relative uncertainties in the *eeee* channel with 3 CC electrons for various efficiencies and backgrounds. The top nine rows are systematic uncertainties, while the next two rows are statistical in nature and the total.

	signal, %		misrec., %		QCD, %	
Systematic	up	down	up	down	up	down
Data quality	+0.5	-0.5	+0.5	-0.5	+0.5	-0.5
Trigger	+1.0	-1.0	+1.0	-1.0	+1.0	-1.0
vtx_z reweight	+0.46	-0.46	+0.36	-0.36	–	–
ZZ p_T reweight	–	-5.18	–	-5.72	–	–
Electron ID	+13.20	-13.20	+13.20	-13.20	–	–
Electron energy res.	+0.35	–	+0.30	–	–	–
EM Fakerate	–	–	–	–	+10.49	-10.49
PDF	+2.5	-2.5	+2.5	-2.5	–	–
$\sigma(ZZ)$	+7.1	-7.1	+7.1	-7.1	–	–
MC Stats	+3.08	-3.08	+4.87	-4.87	–	–
QCD Sample Stats	–	–	–	–	+11.96	-11.96
Total	+15.56	-16.39	+16.00	-16.99	+15.95	-15.95

Table 7.38: Run IIb: Relative uncertainties in the *eeee* channel with 4 CC electrons for various efficiencies and backgrounds. The top nine rows are systematic uncertainties, while the next two rows are statistical in nature and the total.

	signal, %		misrec., %		QCD, %	
Systematic	up	down	up	down	up	down
Data quality	+0.5	-0.5	+0.5	-0.5	+0.5	-0.5
Trigger	+1.0	-1.0	+1.0	-1.0	+1.0	-1.0
vtx_z reweight	+0.46	-0.46	+0.46	-0.46	–	–
ZZ p_T reweight	–	-5.08	–	-4.94	–	–
Electron ID	+11.58	-11.58	+11.58	-11.58	–	–
Electron energy res.	+0.58	–	–	-0.75	–	–
EM Fakerate	–	–	–	–	+0.17	-40.71
PDF	+2.5	-2.5	+2.5	-2.5	–	–
$\sigma(ZZ)$	+7.1	-7.1	+7.1	-7.1	–	–
MC Stats	+2.35	-2.35	+4.94	-4.94	–	–
QCD Sample Stats	–	–	–	–	+14.02	-14.02
Total	+14.07	-14.95	+14.72	-15.54	+14.07	-43.07

Table 7.39: Run IIb: Relative uncertainties in the *eeee* channel with 1 ICR electron for various efficiencies and backgrounds. The top nine rows are systematic uncertainties, while the next two rows are statistical in nature and the total.

	signal, %		misrec., %		$t\bar{t}$, %		QCD, %	
Systematic	up	down	up	down	up	down	up	down
Data quality	+0.5	-0.5	+0.5	-0.5	+0.5	-0.5	+0.5	-0.5
Trigger	+1.0	-1.0	+1.0	-1.0	+1.0	-1.0	+1.0	-1.0
vtx_z reweight	+0.09	-0.09	+1.46	-1.46	+100.00	-100.00	–	–
ZZ p_T reweight	–	-0.03	–	-32.65	–	–	–	–
Electron ID	+7.40	-7.40	+7.40	-7.40	+7.40	-7.40	–	–
EM Fakerate	–	–	–	–	–	–	+1.95	-1.95
Muon ID	+2.00	-2.00	+2.00	-2.00	+2.00	-2.00	–	–
Muon Track	+1.20	-1.20	+1.20	-1.20	+1.20	-1.20	–	–
Muon Isolation	+1.20	-1.20	+1.20	-1.20	+1.20	-1.20	–	–
Muon Fakerate	–	–	–	–	–	–	+9.94	-8.13
Lepton momentum res.	+0.53	–	+0.00	–	+100.00	-100.00	–	–
$\sigma(t\bar{t})$	–	–	–	–	+20.00	-20.00	–	–
PDF	+2.5	-2.5	+2.5	-2.5	–	–	–	–
$\sigma(ZZ)$	+7.1	-7.1	+7.1	-7.1	–	–	–	–
MC Stats	+4.71	-4.71	+135.76	-69.82	+100.0	-100.0	–	–
QCD Sample Stats	–	–	–	–	–	–	+75.25	-47.30
Total	+11.92	-11.90	+136.21	-77.86	+174.55	-174.55	+75.94	-48.05

Table 7.40: Run IIa: Relative uncertainties in the $ee\mu\mu$ channel with 0 CC electrons for various efficiencies and backgrounds. The top fourteen rows are systematic uncertainties, while the next two rows are statistical in nature and the total.

	signal, %		misrec., %		$t\bar{t}$, %		QCD, %	
Systematic	up	down	up	down	up	down	up	down
Data quality	+0.5	-0.5	+0.5	-0.5	+0.5	-0.5	+0.5	-0.5
Trigger	+1.0	-1.0	+1.0	-1.0	+1.0	-1.0	+1.0	-1.0
vtx_z reweight	+0.44	-0.44	+0.57	-0.57	+1.35	-1.35	–	–
ZZ p_T reweight	+0.65	–	+9.40	–	-27.91	–	–	–
Electron ID	+7.40	-7.40	+7.40	-7.40	+7.40	-7.40	–	–
EM Fakerate	–	–	–	–	–	–	+6.02	-6.02
Muon ID	+2.00	-2.00	+2.00	-2.00	+2.00	-2.00	–	–
Muon Track	+1.2	-1.2	+1.2	-1.2	+1.2	-1.2	–	–
Muon Isolation	+1.2	-1.2	+1.2	-1.2	+1.2	-1.2	–	–
Muon Fakerate	–	–	–	–	–	–	+8.65	-3.74
Lepton momentum res.	+0.97	–	–	-15.99	+3.05	-3.05	–	–
$\sigma(t\bar{t})$	–	–	–	–	+20.00	-20.00	–	–
PDF	+2.5	-2.5	+2.5	-2.5	–	–	–	–
$\sigma(ZZ)$	+7.1	-7.1	+7.1	-7.1	–	–	–	–
MC Stats	+2.01	-2.01	+51.62	-38.32	+135.76	-69.82	–	–
QCD Sample Stats	–	–	–	–	–	–	+24.68	-21.21
Total	+11.19	-11.13	+52.77	-51.21	+137.52	-73.18	+25.56	-22.17

Table 7.41: Run IIa: Relative uncertainties in the $ee\mu\mu$ channel with 1 CC electrons for various efficiencies and backgrounds. The top fourteen rows are systematic uncertainties, while the next two rows are statistical in nature and the total.

Systematic	signal, %		misrec., %		$t\bar{t}$, %		QCD, %	
	up	down	up	down	up	down	up	down
Data quality	+0.5	-0.5	+0.5	-0.5	+0.5	-0.5	+0.5	-0.5
Trigger	+1.0	-1.0	+1.0	-1.0	+1.0	-1.0	+1.0	-1.0
vtx_z reweight	+0.31	-0.31	+2.08	-2.08	+0.75	-0.75	–	–
ZZ p_T reweight	+0.82	–	–	-11.53	–	–	–	–
Electron ID	+7.40	-7.40	+7.40	-7.40	+7.40	-7.40	–	–
EM Fakerate	–	–	–	–	–	–	+1.95	-1.95
Muon ID	+2.00	-2.00	+2.00	-2.00	+2.00	-2.00	–	–
Muon Track	+1.2	-1.2	+1.2	-1.2	+1.2	-1.2	–	–
Muon Isolation	+1.2	-1.2	+1.2	-1.2	+1.2	-1.2	–	–
Muon Fakerate	–	–	–	–	–	–	+2.92	-2.43
Lepton momentum res.	+1.01	–	–	-32.87	+49.43	-49.43	–	–
$\sigma(t\bar{t})$	–	–	–	–	+20.00	-20.00	–	–
PDF	+2.5	-2.5	+2.5	-2.5	–	–	–	–
$\sigma(ZZ)$	+7.1	-7.1	+7.1	-7.1	–	–	–	–
MC Stats	+1.43	-1.43	+128.77	-76.11	+135.76	-69.81	–	–
QCD Sample Stats	–	–	–	–	–	–	+25.77	-22.09
Total	+11.11	-11.03	+129.25	-84.44	+129.25	-84.44	+26.03	-22.34

Table 7.42: Run IIa: Relative uncertainties in the $ee\mu\mu$ channel with 2 CC electrons for various efficiencies and backgrounds. The top fourteen rows are systematic uncertainties, while the next two rows are statistical in nature and the total.

Systematic	signal, %		misrec., %		$t\bar{t}$, %		QCD, %	
	up	down	up	down	up	down	up	down
Data quality	+0.5	-0.5	+0.5	-0.5	+0.5	-0.5	+0.5	-0.5
Trigger	+1.0	-1.0	+1.0	-1.0	+1.0	-1.0	+1.0	-1.0
vtx_z reweight	+1.00	-1.00	+9.63	-9.63	+0.89	-0.89	–	–
ZZ p_T reweight	+2.11	–	–	-40.84	–	–	–	–
Electron ID	+7.40	-7.40	+7.40	-7.40	+7.40	-7.40	–	–
EM Fakerate	–	–	–	–	–	–	+10.61	-10.61
Muon ID	+2.00	-2.00	+2.00	-2.00	+2.00	-2.00	–	–
Muon Track	+2.00	-2.00	+2.00	-2.00	+2.00	-2.00	–	–
Muon Isolation	+1.20	-1.20	+1.20	-1.20	+1.20	-1.20	–	–
Muon Fakerate	–	–	–	–	–	–	+4.48	-3.71
Lepton momentum res.	+1.41	–	–	-19.61	–	–	–	–
$\sigma(t\bar{t})$	–	–	–	–	+20.00	-20.00	–	–
PDF	+2.5	-2.5	+2.5	-2.5	–	–	–	–
$\sigma(ZZ)$	+7.1	-7.1	+7.1	-7.1	–	–	–	–
MC Stats	+2.32	-2.32	+42.70	-33.19	+135.75	-69.81	–	–
QCD Sample Stats	–	–	–	–	–	–	+3.60	-3.60
Total	+11.42	-11.53	+45.15	-58.04	+137.47	-73.08	+12.12	-11.86

Table 7.43: Run IIb: Relative uncertainties in the $ee\mu\mu$ channel with 0 CC electrons for various efficiencies and backgrounds. The top fourteen rows are systematic uncertainties, while the next two rows are statistical in nature and the total.

	signal, %		misrec., %		$t\bar{t}$, %		QCD, %	
Systematic	up	down	up	down	up	down	up	down
Data quality	+0.5	-0.5	+0.5	-0.5	+0.5	-0.5	+0.5	-0.5
Trigger	+1.0	-1.0	+1.0	-1.0	+1.0	-1.0	+1.0	-1.0
vtx_z reweight	+2.21	-2.21	+1.06	-1.06	+0.01	-0.01	–	–
ZZ p_T reweight	+0.28	–	–	-23.79	–	–	–	–
Electron ID	+7.40	-7.40	+7.40	-7.40	+7.40	-7.40	–	–
EM Fakerate	–	–	–	–	–	–	+14.45	-14.45
Muon ID	+2.00	-2.00	+2.00	-2.00	+2.00	-2.00	–	–
Muon Track	+2.00	-2.00	+2.00	-2.00	+2.00	-2.00	–	–
Muon Isolation	+1.20	-1.20	+1.20	-1.20	+1.20	-1.20	–	–
Muon Fakerate	–	–	–	–	–	–	+3.17	-2.61
Lepton momentum res.	–	-0.46	–	-4.41	–	-0.01	–	–
$\sigma(t\bar{t})$	–	–	–	–	+20.00	-20.00	–	–
PDF	+2.5	-2.5	+2.5	-2.5	–	–	–	–
$\sigma(ZZ)$	+7.1	-7.1	+7.1	-7.1	–	–	–	–
MC Stats	+0.94	-0.94	+16.44	-16.44	+51.62	-38.32	–	–
QCD Sample Stats	–	–	–	–	–	–	+2.33	-2.33
Total	+11.31	-11.32	+19.84	-31.29	+55.95	-43.98	+15.02	-14.91

Table 7.44: Run IIb: Relative uncertainties in the $ee\mu\mu$ channel with 1 CC electrons for various efficiencies and backgrounds. The top fourteen rows are systematic uncertainties, while the next two rows are statistical in nature and the total.

	signal, %		misrec., %		$t\bar{t}$, %		QCD, %	
Systematic	up	down	up	down	up	down	up	down
Data quality	+0.5	-0.5	+0.5	-0.5	+0.5	-0.5	+0.5	-0.5
Trigger	+1.0	-1.0	+1.0	-1.0	+1.0	-1.0	+1.0	-1.0
vtx_z reweight	+1.79	-1.79	+11.82	-11.82	+0.18	-0.18	–	–
ZZ p_T reweight	+1.52	–	–	-17.43	–	–	–	–
Electron ID	+7.40	-7.40	+7.40	-7.40	+7.40	-7.40	–	–
EM Fakerate	–	–	–	–	–	–	+12.24	-12.24
Muon ID	+2.00	-2.00	+2.00	-2.00	+2.00	-2.00	–	–
Muon Track	+2.00	-2.00	+2.00	-2.00	+2.00	-2.00	–	–
Muon Isolation	+1.20	-1.20	+1.20	-1.20	+1.20	-1.20	–	–
Muon Fakerate	–	–	–	–	–	–	+1.32	-1.08
Lepton momentum res.	+1.23	–	+11.59	–	+99.63	–	–	–
$\sigma(t\bar{t})$	–	–	–	–	+20.00	-20.00	–	–
PDF	+2.5	-2.5	+2.5	-2.5	–	–	–	–
$\sigma(ZZ)$	+7.1	-7.1	+7.1	-7.1	–	–	–	–
MC Stats	+0.70	-0.70	+16.67	-16.67	+88.27	-55.12	–	–
QCD Sample Stats	–	–	–	–	–	–	+2.12	-2.12
Total	+11.28	-11.22	+25.96	-29.04	+134.85	-59.19	+12.54	-12.52

Table 7.45: Run IIb: Relative uncertainties in the $ee\mu\mu$ channel with 2 CC electrons for various efficiencies and backgrounds. The top fourteen rows are systematic uncertainties, while the next two rows are statistical in nature and the total.

7.8 Results

7.8.1 Total Background and Expected Signal

We observe 3 events in the 4μ channel with an estimated background of 0.15 events and an expected signal of 3.98 events. A summary of the results is show in Table 7.46.

For the *eeee* channel, we observe 5 events, with an estimated background of 0.71 events, and an expected signal of 3.83 events. Two of them come from the 1 ICD subchannel, two from 4 CC, and one from 3 CC. Details are given in Table 7.47.

For the $ee\mu\mu$ channel, we observe 5 candidate events, with an estimated background of 0.62 events, and an expected signal of 6.45 events. Two of them come from the 2 CC subchannel, one from the 1 CC subchannel, and two from the 0 CC subchannel. Details of these events are given in Table 7.48.

Background	
$Z(\gamma)$+jets	$0.118 \pm 0.002^{+0.065}_{-0.053}$
Migration	$0.349 \pm 0.021^{+0.071}_{-0.039}(\times 10^{-1})$
Cosmics	<0.01
Total Background	$0.153 \pm 0.003^{+0.065}_{-0.053}$
Expected Signal	$3.981 \pm 0.017 \pm 0.394$
Observed Events	3

Table 7.46: Contribution from non-negligible backgrounds in the $\mu\mu\mu\mu$ channel, plus expected signal and number of observed events. Errors are statistical followed by systematic.

Background	2 CC 0 ICD	3 CC 0 ICD
$Z(\gamma)$+jets	$0.154 \pm 0.013 \pm 0.031$	$0.121 \pm 0.011 \pm 0.019$
Migration	$0.0138 \pm 0.0008 \pm 0.0021$	$0.0247 \pm 0.0011 \pm 0.0037$
Total Background	$0.168 \pm 0.013 \pm 0.031$	$0.143 \pm 0.012 \pm 0.019$
Expected Signal	$0.446 \pm 0.006 \pm 0.068$	$1.063 \pm 0.010 \pm 0.165$
Observed Events	0	1

Background	4 CC 0 ICD	$\geq$ 2 CC 1 ICD
$Z(\gamma)$+jets	$0.054 \pm 0.006 \pm 0.006$	$0.294 \pm 0.042^{+0.003}_{-0.128}$
Migration	$0.0249 \pm 0.0012 \pm 0.0039$	$0.0258 \pm 0.0012 \pm 0.0033$
Total Background	$0.079 \pm 0.006 \pm 0.007$	$0.329 \pm 0.042^{+0.004}_{-0.128}$
Expected Signal	$0.957 \pm 0.009 \pm 0.147$	$1.367 \pm 0.011 \pm 0.179$
Observed Events	2	2

Table 7.47: Contribution from non-negligible backgrounds in the *eeee* channels, plus expected signal and number of observed events. Errors are statistical followed by systematic.

7.8.2 Figures of Combined Channel

We combine together the three channels to obtain our final results and show the distributions of various quantities in data, expected signal and background. In Fig. 7.29 and Fig. 7.30 we show the distributions for p_T and η_D of the four leptons. Fig. 7.31 is the p_T distribution of each Z/γ^*. Fig. 7.32 is the $\Delta\phi$ between the two leptons from each Z/γ^* decay. Fig. 7.8.2, 7.8.2, 7.8.2 and 7.8.2 show dilepton mass,

Background	0 CC	1 CC	2 CC
$Z(\gamma)$+jets	$0.114^{+0.004\ +0.008}_{-0.003\ -0.008}$	$0.215^{+0.006\ +0.022}_{-0.006\ -0.021}$	$0.265^{+0.007\ +0.030}_{-0.006\ -0.030}$
$t\bar{t}$	$0.21^{+0.30}_{-0.16} \pm 0.63(\times 10^{-2})$	$1.02^{+0.53}_{-0.38} \pm 0.24(\times 10^{-2})$	$0.27^{+0.23}_{-0.14} \pm 0.28(\times 10^{-2})$
Migration	$2.17^{+0.93\ +0.34}_{-0.72\ -1.06}(\times 10^{-3})$	$5.10^{+0.93\ +0.70}_{-0.89\ -1.64}(\times 10^{-3})$	$4.86^{+0.87\ +1.06}_{-0.86\ -1.29}(\times 10^{-3})$
Cosmics	< 0.001	< 0.003	< 0.006
Total BK	$0.118^{+0.005\ +0.009}_{-0.004\ -0.009}$	$0.230^{+0.008\ +0.025}_{-0.007\ -0.025}$	$0.273^{+0.007\ +0.034}_{-0.006\ -0.032}$
Expected Sg.	$0.40 \pm 0.01 \pm 0.05$	$2.21 \pm 0.02 \pm 0.28$	$3.84 \pm 0.03 \pm 0.49$
Observed Ev.	2	1	2

Table 7.48: Contribution from non-negligible backgrounds in the $ee\mu\mu$ channels, plus expected signal and number of observed events. Errors are statistical followed by systematic.

p_T of the ZZ system, $\not\!\!E_T$ and ΔR between the two leptons. Four lepton mass is in Fig. 7.35 and 2D dilepton mass ($M_{\ell^+\ell^-}$ versus $M_{\ell'^+\ell'^-}$) is in Fig. 7.36.

Note that, these figures use the full sample without date quality cuts and so have 18 events.

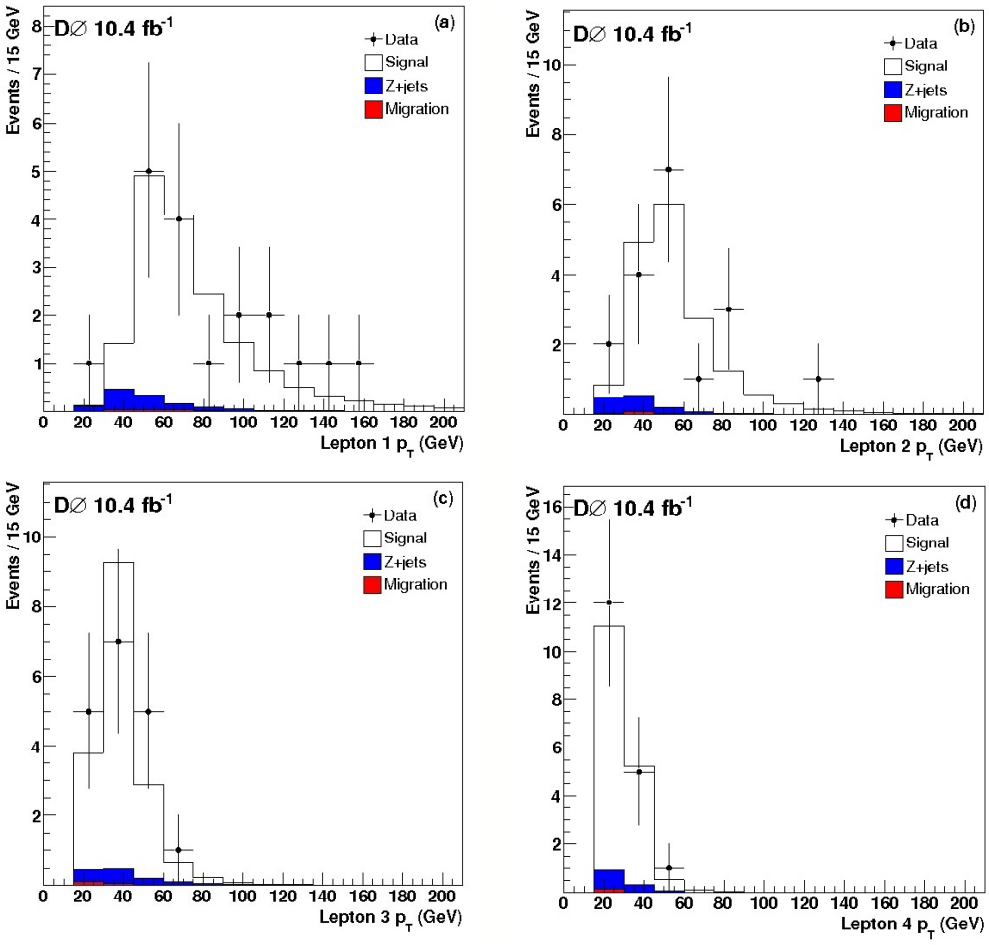

Figure 7.29: Distributions of p_T for the leading, second, third and fourth leptons in data, expected signal and background.

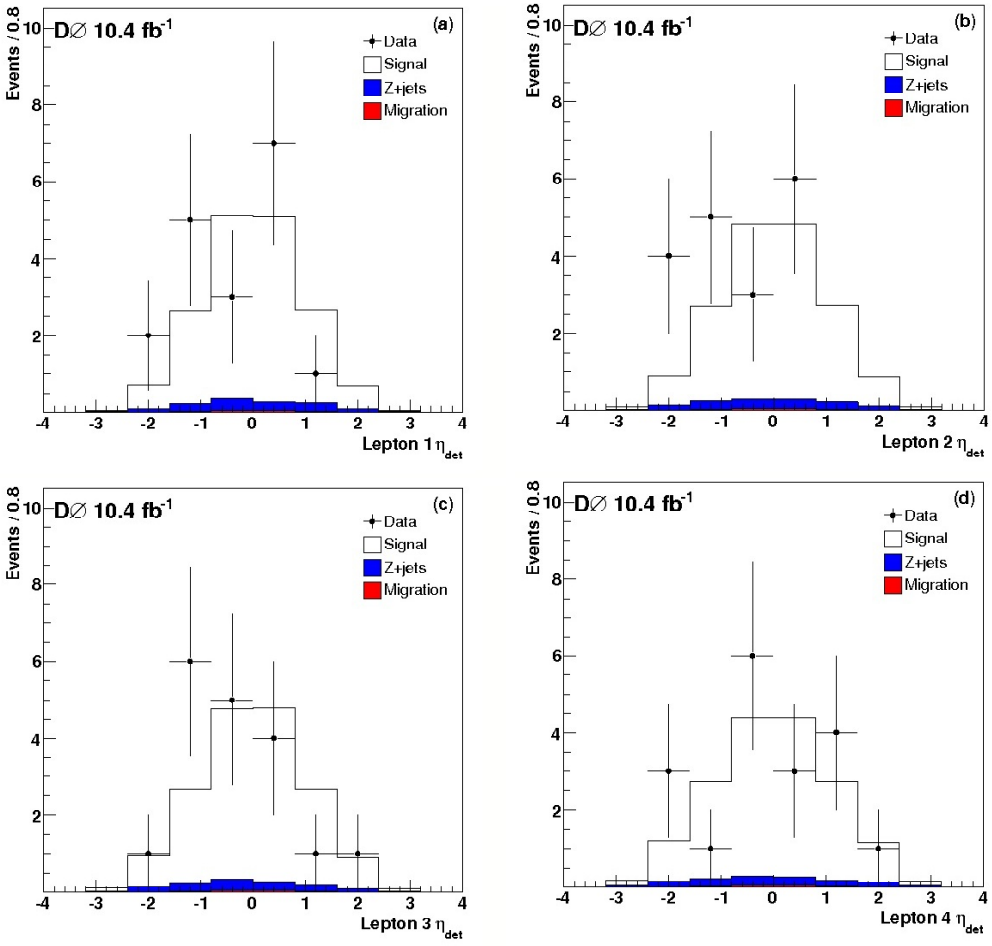

Figure 7.30: Distributions of η_D for the leading, second, third and fourth leptons in data, expected signal and background.

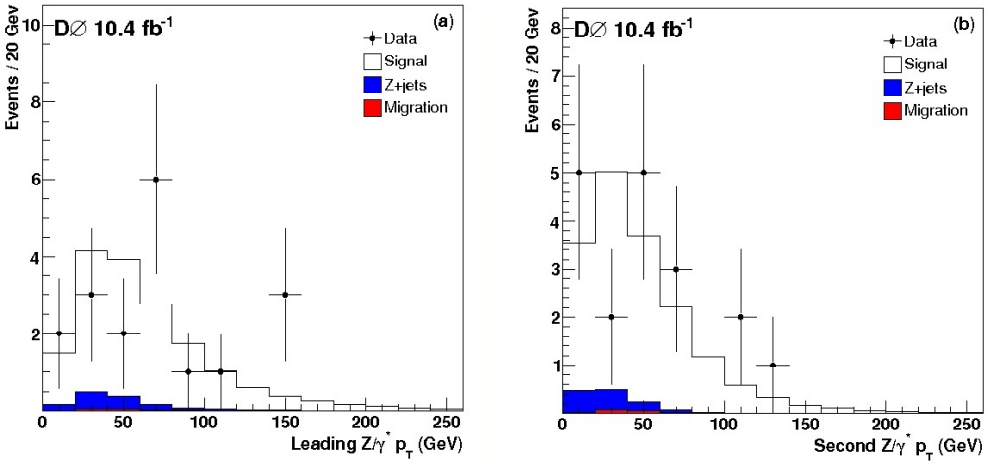

Figure 7.31: Distributions of $Z's$ p_T for the lepton pairing with the highest and lowest $Z's$ p_T in data, expected signal and background.

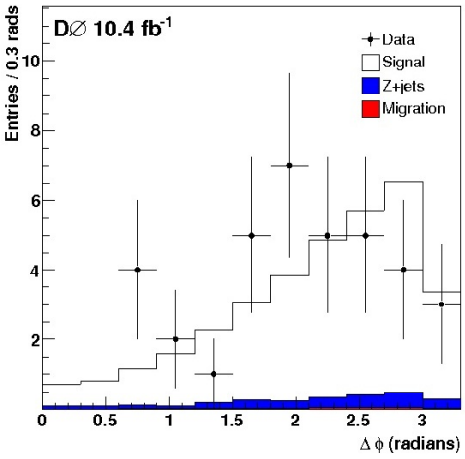

Figure 7.32: Distribution of $\Delta\phi$ between the two leptons in each Z decay in data, expected signal and background.

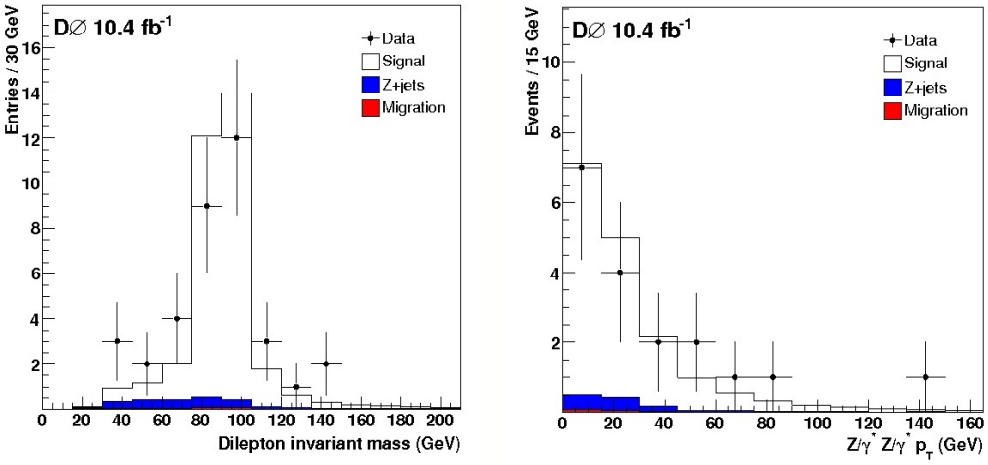

Figure 7.33: Distribution of dilepton invariant mass (left) and p_T of ZZ system (right) in data, expected signal and background.

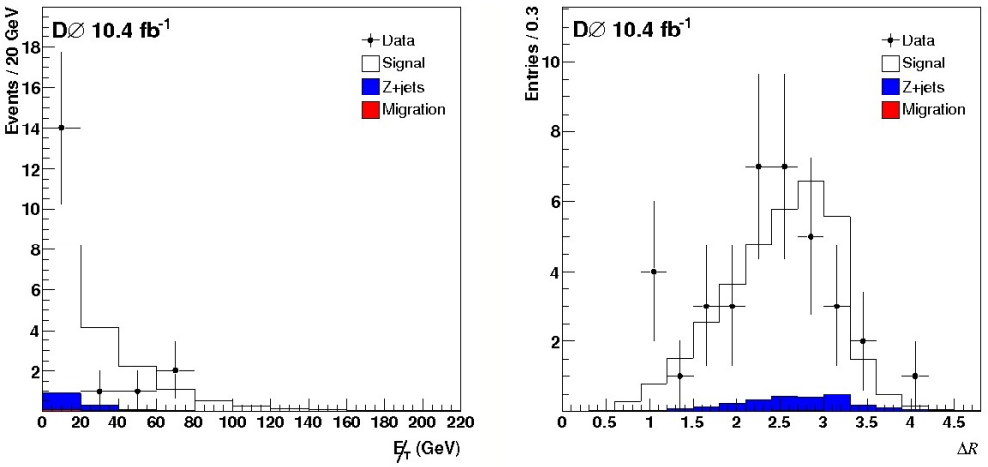

Figure 7.34: Distribution of $\not\!\!E_T$ (left) and ΔR (right) between two leptons in each Z decay in data, expected signal and background.

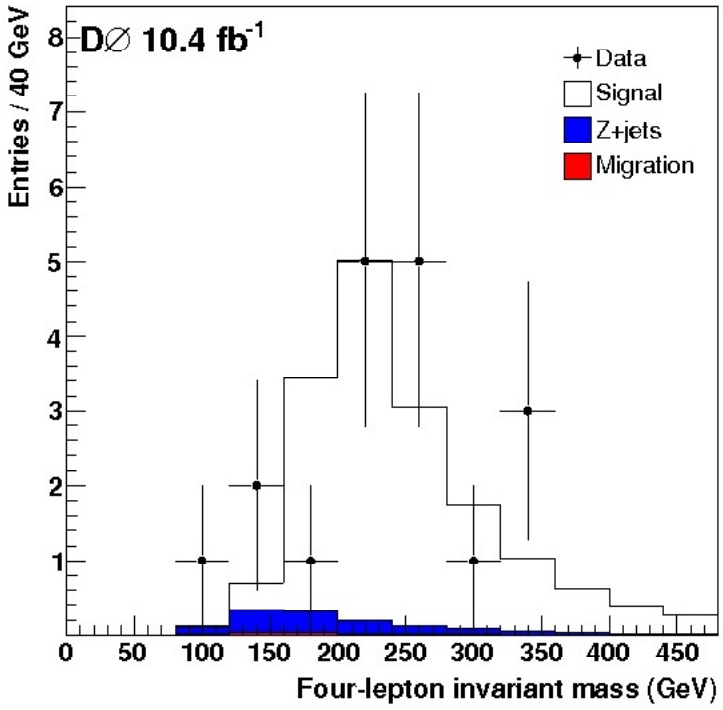

Figure 7.35: Distribution of four lepton invariant mass in data, expected signal and background.

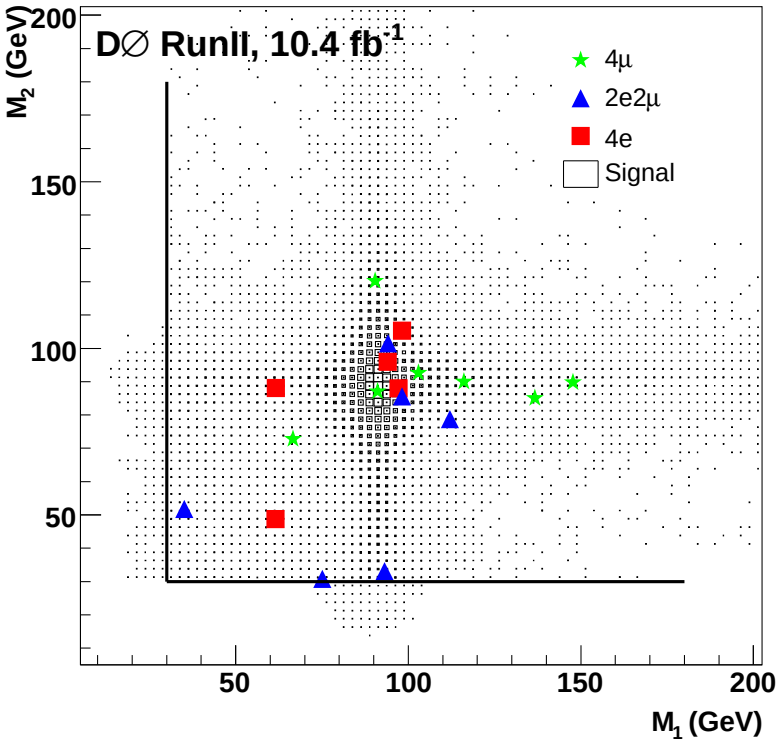

Figure 7.36: Distribution of 2D dilepton invariant mass in data, and expected signal.

7.8.3 Cross Section

When we combine the cross sections obtained above from the three channels, 13 events (all candidate event displays are shown in Appendix D) remaining in the data, with an estimated background of 1.47 events. We combine all final states using the negative log likelihood

$$-ln(L) = \sum_i \sigma \times BF_i \times \alpha_i \times \epsilon_i \times \int \mathcal{L} \cdot dt + N_i^{bkg} - N_i ln\big(\sigma \times BF_i \times \alpha_i \times \epsilon_i \times \int \mathcal{L} \cdot dt\big) \quad (7.2)$$

where i indicates a sum over all final states, BF_i is the branching fraction for the i^{th} final state, $\alpha_i \times \epsilon_i$ is the efficiency times acceptance for the i^{th} final state, $\int \mathcal{L} \cdot dt$ is our total integrated luminosity, N_i^{bkg} is the estimated total background for the i^{th} final state, N_i is the number of events in date for the i^{th} final state. We vary the cross section, σ, to minimize the negative log likelihood and measure the cross section.

The likelihood function yields a cross section of $1.24^{+0.43}_{-0.39}$(stat.) pb as seen in Fig. 7.37, with a statistical error of about 27%. To assess the systematic uncertainties, we vary the uncertainties individually by one standard deviation, recalculate the cross section, and take the difference as our systematic. This gives a final result of $\sigma(p\bar{p} \rightarrow Z/\gamma^* Z/\gamma^*) = 1.24^{+0.43}_{-0.39}(\text{stat.})^{+0.16}_{-0.15}(\text{syst.}) \pm 0.08(\text{lumi.})$ pb, which is comparable to the SM prediction of 1.43 ± 0.10 pb.

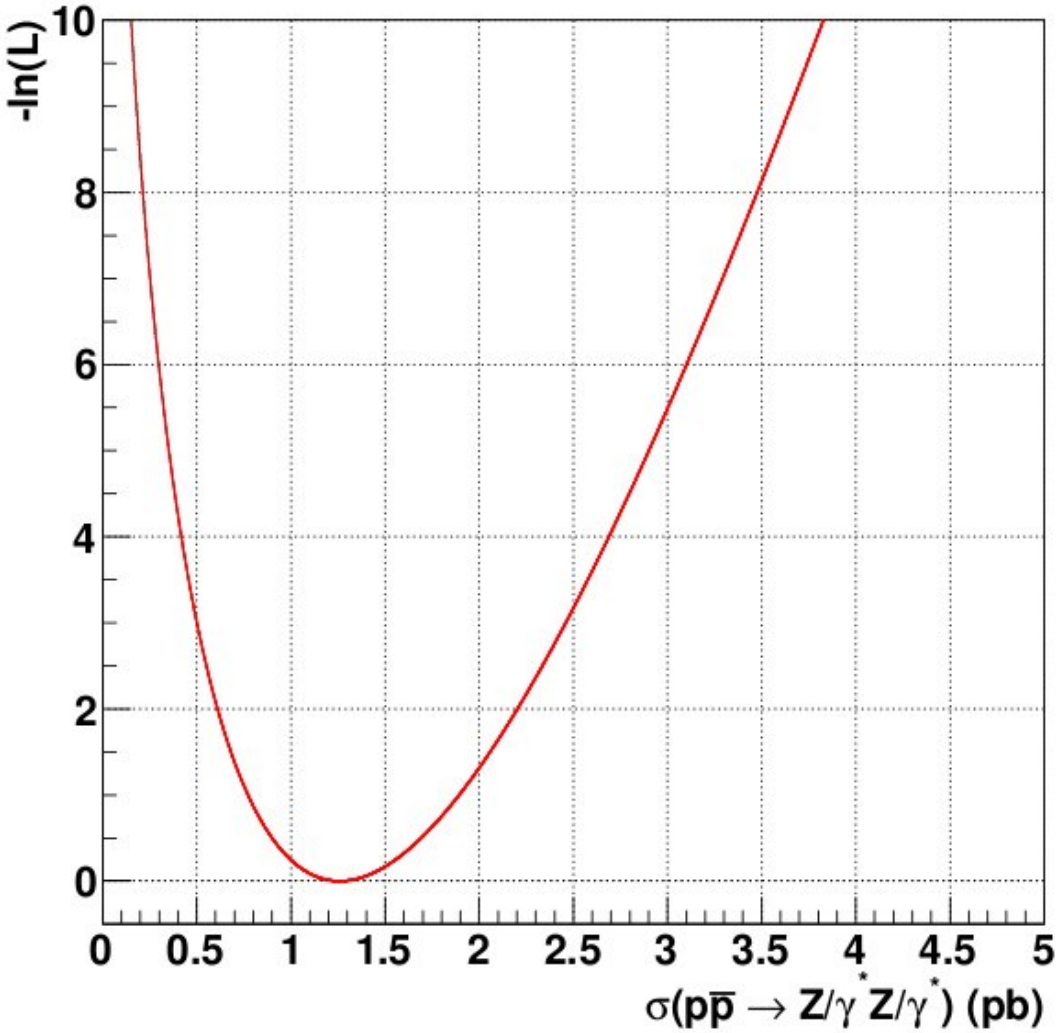

Figure 7.37: $-ln(L)$ versus cross section (in pb) for the combined channels.

CHAPTER 8

SUMMARY AND CONCLUSION

We performed a measurement of the production cross section of $p\bar{p} \to ZZ$ using 9.7 fb^{-1} of data collected by the DØ experiment at a center of mass energy of 1.96 TeV. A summary of the signal and background event expectations are included in Sec. 7.8.1.

From the analysis, we have three $\mu\mu\mu\mu$ candidate events as well as five $eeee$ candidate events, one from 3 CC subchannel, two from 4 CC subchannel and two from 1 ICR subchannel. We also see five $ee\mu\mu$ candidate events, two from 0 CC subchannel, one from 1 CC subchannel and two from 2 CC subchannel.

We observe a signal with greater than 6.1σ Gaussian significance and measure a high mass ($M_1(Z/\gamma^*) > 30$ GeV,$M_2(Z/\gamma^*) > 30$ GeV) cross section of $\sigma(p\bar{p} \to Z/\gamma^* Z/\gamma^*) = 1.24^{+0.43}_{-0.39}(\text{stat.})^{+0.16}_{-0.15}(\text{syst.}) \pm 0.08(\text{lumi.})$ pb. A correction factor of 0.89 obtained from MCFM simulation allows us to convert this cross section into a high mass cross section measurement for pure ZZ production. The result turns out to be $\sigma(p\bar{p} \to ZZ) = 1.10^{+0.38}_{-0.32}(\text{stat.})^{+0.14}_{-0.13}(\text{syst.}) \pm 0.07$ (lumi.) pb after multiplying the scale factors.

We combine the $\sigma(p\bar{p} \to ZZ \to \ell^+\ell^-\ell^+\ell^-)$ result with a previous result from the $ZZ \to \ell^+\ell^-\nu\nu$ channel. As discussed in Sec. 7.8.3, we calculate the negative log likelihood (containing signal, background and data), for both the $ZZ \to \ell^+\ell^-\ell^+\ell^-$ channel and the $ZZ \to \ell^+\ell^-\nu\nu$ channel separately. We then multiply them together to get the total log likelihood. By minimizing this product, we find the result for the combination of the two channels. The $ZZ \to \ell^+\ell^-\nu\nu$ result did not use the

luminosity as it normalized to Z events and so its systematic error does not include that on the luminosity. The combined measurement of the $p\bar{p} \to ZZ$ cross section is $1.37^{+0.28}_{-0.22}(\text{stat.}) \pm 0.12(\text{syst.}) \pm 0.04$ (lumi.) pb. This result is consistent with the standard model prediction at 1.43 ± 0.10 pb.

REFERENCES

[1] G. Aad, et al. (ATLAS Collaboration), *Phys. Lett. B 716, 1* (2012).

[2] S. Chatrchyan, et al. (CMS Collaboration), *Phys. Lett. B 716, 30* (2012).

[3] V. M. Abazov, et al. (DØ Collaboration), "Evidence for a particle produced in association with weak bosons and decaying to a bottom-antibottom quark pair in Higgs boson searches at the Tevatron", *Phys. Rev. Lett. 109, 071804,* (2012)

[4] S. Drell, T. Yan, *Ann. Phys. (N.Y.) 66, 578,* (1971)

[5] `http://pdg.lbl.gov`

[6] S. Abachi, et al. (DØ Collaboration) , "Observation of the Top Quarkr", *hep-ex/9503003,* (1995)

[7] `http://www-d0.fnal.gov`

[8] `http://www.fnal.gov/pub/science/accelerator`

[9] J. Thomason, "Introduction to colliding beams at Fermilab", *Fermilab-TM-1909,* (1994)

[10] `http://www.fnal.gov/faw/future/accelerators.shtml`

[11] `http://www.fnal.gov/pub/today/archive/archive_2010/today10-11-29.html`

[12] C. Johnstone, "Implementation of a Low Energy Proton Line from the Fermilab Linac", *FERMILAB-TM-1788,* (1992)

[13] L. Navas, "Diffractive $Z/\gamma^* \to \mu^+\mu^-$ Boson Production in Proton-antiproton Collisions at $\sqrt{s} = 1.96$ TeV in the DØ Experiment" *PhD Thesis, Universidad de los Andes*

[14] C. Jarvis, "A Search for Z Boson Pair Production at the Fermilab Tevatron Collider", *PhD Thesis, University of Maryland* (2007)

[15] B. Worthel, "Antiproton source rookie book", Version 2.2, (2011)

[16] `http://www.fnal.gov/pub/science/experiments/energy/tevatron/`

[17] D. Edmunds, "RunII a Tevatron beam structure", `http://www.pa.msu.edu/hep/d0/ftp/l1/framework/drawings/runiia_beam_structure.ps`

[18] `http://www-d0.fnal.gov/runcoor/RUN/run2_lumi.html`

[19] V. M. Abazov, et al. (DØ Collaboration), "The upgraded DØ detector", *hep-ph/0507191,* (2005)

[20] V. M. Abazov, et al. (DØ Collaboration), "The DØ silicon microstrip tracker", *Nucl. Instrum. Meth. A634:8-46,* (2011)

[21] V. M. Abazov, et al. (DØ Collaboration), "Upgraded D0 central fiber tracker", *Instrumentation for Colliding Beam Physics,* (2008)

[22] V. M. Abazov, et al. (DØ Collaboration), "Beam tests of the DØ uranium liquid argon end calorimeters " *Nucl. Instrum. Meth. A, 324/53,* (1993)

[23] V. M. Abazov, et al. (DØ Collaboration), "The muon system of the Run II DØ detector" *Fermilab-PUB-05-034-E,* (2005)

[24] V. M. Abazov, et al. (DØ Collaboration), "The DØ Run II luminosity monitor", *Nucl. Phys. Proc. Suppl. 78,* (1999)

[25] S. Uzunyan, "A search for charge 1/3 third generation leptoquarks in muon channels", *PhD Thesis, Northern Illinois University* (2006)

[26] T. Cristiansen, et al., "The DØ L2-Muon trigger performance for P11", *DØ Note 4053*

[27] A. Maciel, et al., "The L2-Muon trigger methods and algorithms", *DØ Note 4756*

[28] M. Fortner, et al., "The L2-muon trigger at DØ", *IEEE Trans. Nucl. Sci. 49 1589.* (2002)

[29] `http://www-d0.fnal.gov/computing/algorithms`

[30] G. Hesketh, "Central Track Extrapolation Through the DØ Detector", *DØ Note 4756*

[31] A. Garcia-Bellido, et al., "Primary Vertex certification in p14", *DØ Note 4320*

[32] `http://www-d0.fnal.gov/Run2Physics/cs/index.html`

[33] M. Roco, "Secondary Vertex B-Tagging in Top Events", *DØ Note 3236*

[34] E. Busato, B. Andrieu, "Jet Algorithms in DØ Run II Software", *DØ Note 4457*

[35] O. Brandt, et al., "Muon reconstruction and identification with the run II DØ detector", *Submitted to Nucl. Inst. A, arXiv:1307.5202*

[36] O. Brandt, S. Cho, M. Cooke, et al., "Muon identification certification for the summer 2009 extended dataset", *DØ Note 6025*

[37] O. Brandt, et al., "The muon certification procedure of the DØ experiment in Run II", *FERMILAB-TM-2541-PPD, July,* 2012.

[38] G. Blazey et al., "Run II jet physics", *FERMILAB-CONF-00-092-E , 47* (2000)

[39] O. Brandt, D. Hedin, et al., "The Muon Momentum Resolution for the DØ Experiment in Run II", *FERMILAB-TM-2540-PPD, July,* 2012

[40] A. Croc, F. Dliot, V. Sharyy, et al., "Muon momentum oversmearing update for p20 Data", *DØ Note 6031*

[41] M. Arthaud, F. Dliot, B. Tuchming, et al., "Muon momentum oversmearing for p20 Data", *DØ Note 5449*

[42] M. Arthaud, F. Dliot, B. Tuchming, et al., "Muon momentum oversmearing for p17 Data", *DØ Note 5444*

[43] O. Brandt, D. Hedin, A.S. Santos, et al., "Muon momentum oversmearing update for Run IIa, Run IIb2 and Run IIb3 Data taking epochs and Monte Carlo p17 and p20", *DØ Note 6190*

[44] O. Brandt, L. Feng, D. Hedin, et al., "Muon momentum oversmearing update for Run IIb3 MC (p20.17) versus Run IIb3 as well as the combined Run IIb3 and Run IIb4 Data taking epochs", *DØ Note 6312*

[45] O. Brandt, L. Feng, D. Hedin, et al., "Muon momentum oversmearing update for Run IIb1 and Run IIb2 Data taking epochs and Run IIb2 Monte Carlo", *DØ Note 6314*

[46] J. M. Campbell, et al., "An update on vector boson pair production at hadron colliders", *Phys. Rev., D60,* (1999); we use version 6.2.

[47] J. Pumplin, et al., *J. High Energy Phys. 07* (2002) 012.

[48] R. Hamberg, et al., *Nucl. Phys. B359, 343* (1991)

[49] M. Mangano, et al., *J. High Energy Phys. 07, 1* (2003) we use version 2.11

[50] T. Sjöstrand, S. Mrenna, and P. Skands, *J. High Energy Phys. 05, 026* (2006), we use version 6.323.

[51] The L3 Collaboration, "Study of Z Boson Pair Production in e^+e^- collisions at LEP at $\sqrt{s} = 189$ GeV", *Phys. Lett., B465,* (1999)

[52] The OPAL Collaboration, "Study of Z pair production and anomalous couplings in e+e- collisions at $\sqrt{s}$ between 190 GeV and 209 GeV", *Eur. Phys. J., C32,* (2003)

[53] The ALEPH Collaboration, "Measurement of the $ZZ \to e^+e^-$ production cross section at center-of-mass energies of 183 GeV and 189 GeV", *Phys. Lett., B469,* (1999)

[54] The DELPHI Collaboration, "ZZ production in e^+e^- interactions at $\sqrt{s} = 183$ to 209 GeV", *Eur. Phys. J., C30,* (2003)

[55] J. Alcaraz, et al. (ALEPH, DELPHI, L3, OPAL, and LEP Electroweak Working Group collaborations), *arXiv:hep-ex/0612034.*

[56] V. M. Abazov, et al. (DØ Collaboration), "Search for ZZ and $Z\gamma^*$ production in $p\bar{p}$ collisions at $\sqrt{s} = 1.96$ TeV and limits on anomalous ZZZ and $ZZ\gamma^*$ couplings", *Phys. Rev. Lett., 100,* (2008)

[57] V. M. Abazov, et al. (DØ Collaboration), "$ZZ \to \ell\ell\nu\nu$ production in $p\bar{p}$ collisions at $\sqrt{s} = 1.96$ TeV", *DØ Note 5620-CONF*

[58] The CDF Collaboration, "First Measurement of ZZ Production in $p\bar{p}$ Collisions at $\sqrt{s}$=1.96 TeV", *hep-ex/0801.4806.*

[59] The ATLAS Collaboration, "Measurement of the ZZ Production Cross Section and Limits on Anomalous Neutral Triple Gauge Couplings in Proton-Proton Collisions at $\sqrt{s} = 7$TeV with the ATLAS Detector", *Phys. Rev. Lett. 108, 041804* (2012)

[60] The CMS Collaboration, "Measurement of the ZZ Production Cross Section and Search for Anomalous Couplings in $2\ell\ell'$ Final States in pp collisions at $\sqrt{s} = 7$ TeV", *J. High Energy Phys. 01* (2013) 063

[61] The CMS Collaboration, "Observation of Z Decays to Four Leptons with the CMS detector at the LHC", *J. High Energy Phys. 12* (2012) 034

[62] R. Hooper, L. Feng, D. Hedin, D. Menezes, J. Kraus, "Updated measurement of the $p\bar{p} \to Z/\gamma^* Z/\gamma^*$ and $p\bar{p} \to ZZ$ cross sections using 10.4 fb^{-1} of Run II Data", *DØ Note 6350*

[63] R. Hooper, L. Feng, D. Hedin, D. Menezes, J. Kraus, "Measurement of the $ZZ \to \ell^+\ell^-\ell'^+\ell'^-$ cross section using the 10.4 fb^{-1} of Run II Data", *DØ Note-CONF*

[64] DØ Collaboration, "Measurement of the ZZ production cross section and search for the standard model Higgs boson in the four lepton final state in $p\bar{p}$ collisions", *Physics Review D 88, 032008* (2013)

[65] D. Menezes, "Search for the standard model Higgs Boson in the four lepton final state", *PhD Thesis, Northern Illinois University* (2013)

[66] `http://www-d0.fnal.gov/Run2Physics/cs/`

[67] S. Park, M. Begel, "Efficiency of the Data Quality Calorimeter Flags", *DØ Note 5324*

[68] M. Vesterinen, T. Wyatt, "Precise study of the $Z/\gamma*$ boson transverse momentum distribution in *pbarp* collisions using a novel technique", *DØ Note 6088*

[69] B.C.K. Casey, et al., "The DØ Run IIb Luminosity Measurement", *Fermilab Technical Memo, FERMILAB-TM-2529-E* (2012)

[70] S. Redford, et. al., "A Measurement of the Forward-Backward Charge Asymmetry at the Z Pole using the Dimuon Channel",

[71] D. Hedin, Private communication

[72] O. Atramentov, et al., "Electron and Photon Identification with p20 data", *DØ Note 5761*

[73] J. Kraus, T. Gadfort, O. Atramentov, "p20 ICR Electron Identification", *DØ Note 5691*

[74] B. Calpas, J. Kraus and T. Yasuda, "ICR Electron Efficiencies for Run IIa", *DØ Note 5939*

[75] B. Calpas, J. Kraus and T. Yasuda, "ICR electron efficiencies for the Run IIb1 and Run IIb2 combined datasets", *DØ Note 6051*

[76] X. Bu, L. Han, P. Jiang, Q. Li, "ICR Electron Identification with BDT/NN Combined Cut", *DØ Note 6271*

[77] H. Schellman, "The longitudinal shape of the luminous region at DØ", *DØ Note 5142*

[78] `https://plone4.fnal.gov/P1/D0Wiki/object-id/emid/emcert/Moriond2009/uncertainty_moriond09` `https://plone4.fnal.gov/P1/D0Wiki/object-id/emid/emcert/eleID_Summer2010/uncertainty_summer10`

[79] P. Calfayan, et al., "Muon Identification Certification for p17", *DØ Note 5157*

[80] O. Brandt, D. Hedin, S. Cho, "Certification of muon identification efficiencies and treatment of systematic uncertainties for the Run IIb dataset", *DØ Note 6326*

[81] A. Askew, et al., "Measurement of the $WZ \to lll\nu$ Cross Section and Limits on Anomalous Triple Gauge Couplings", *DØ Note 6021*

[82] N. Kidonakis, R. Vogt, "Next-to-next-to-leading order soft gluon corrections in top quark hadroproduction", *Phys. Rev., D68*, (2003)

[83] S. Moch and P. Uwer, *Phys. Rev. D 78, 034003*, (2008)

[84] S. Park, M. Begel, "Efficiency of the data quality calorimeter flags", *DØ Note 5324*

[85] T. Gleisberg, S. Hoeche, et. al., *High Energy Phys. 02 (2004) 056; , 02 (2009) 007*; we use version 1.0.11.

[86] H. Fox, et. al., "Measurement of the cross section for $Z/\gamma* \to e^+e^-c$ production at DØ", *DØ Note 5672*

[87] S. Yacoob, J. Hays, H. Schellman, "A Comparison of Monte Carlo Distributions for Z boson production at the Tevatron", *DØ Note 5273*

[88] H. Fox, et al., "Measurement of the cross section for $Z/\gamma^* \to e^+e^-$ production at DØ", *DØ Note 5627*

[89] V. M. Abazov, et al. (DØ Collaboration), "Collie: A Confidence Level Limit Evaluator, Version 4.00", *DØ Note 5595, 4975, 5309, and 5491*

[90] P. Gris, "Electron Smearing Studies with Run IIa Data", *DØ Note 5400*

[91] E. Barberis, et al., "ZZ$\to$ $ll\nu\nu$ production in $p\overline{p}$collisions at $\sqrt{s} = 1.96$ TeV", *DØ Note 5574*

APPENDIX A

STATISTICAL AND SYSTEMATIC ERRORS WITH OVERSMEARING PARAMETERS

Option			Double Gaussian				Single Daussian	
Tk	Tp	Statistical Errors	$A(\times 10^{-3})$	$B(\times 10^{-2})$	$C(\times 10^{-2})$	$D(\times 10^{-3})$	$A(\times 10^{-3})$	$B(\times 10^{-2})$
medium	T1	Data J/ψ	0	0.009	—	—	0	0.014
		Monte Carlo J/ψ	0.0030	0.053	—	—	0.0020	0.038
		Data Z	0.0200	0.025	0.43	0.4	0.0190	0.028
		Monte Carlo Z	0.0040	0.011	0.17	0.1	0.0030	0.012
		Total errors	± 0.0206	± 0.060	± 0.46	± 0.4	± 0.0193	± 0.051
	T2	Data J/ψ	0.0380	0.118	—	—	0.0180	0.140
		Monte Carlo J/ψ	0.1370	0.513	—	—	0.1050	0.504
		Data Z	0.2160	0.372	2.56	3.1	0.1150	0.245
		Monte Carlo Z	0.1230	0.205	2.76	3.1	0.0670	0.189
		Total errors	± 0.2863	± 0.677	± 3.76	± 4.4	± 0.1704	± 0.609
	T3	Data J/ψ	0.0460	0.173	—	—	0.0260	0.058
		Monte Carlo J/ψ	0.1230	0.435	—	—	0.1040	0.344
		Data Z	0.2090	0.278	3.79	2.6	0.2130	0.259
		Monte Carlo Z	0.0750	0.194	2.90	1.7	0.0580	0.085
		Total errors	± 0.2579	± 0.579	± 4.77	± 3.1	± 0.2454	± 0.443
loose	T1	Data J/ψ	0	0.016	—	—	0	0
		Monte Carlo J/ψ	0.0040	0.066	—	—	0.0020	0.041
		Data Z	0.0230	0.034	0.49	0.4	0.0200	0.017
		Monte Carlo Z	0.0100	0.016	0.07	0	0.0080	0.003
		Total errors	± 0.0253	± 0.078	± 0.50	± 0.4	± 0.0216	± 0.045
	T2	Data J/ψ	0.0070	0.027	—	—	0.0030	0
		Monte Carlo J/ψ	0.0350	0.113	—	—	0.0400	0.118
		Data Z	0.0620	0.065	1.81	2.7	0.0580	0.036
		Monte Carlo Z	0.0240	0.037	0.77	0.8	0.0280	0.002
		Total errors	± 0.0754	± 0.138	± 1.97	± 2.8	± 0.0758	± 0.123
	T3	Data J/ψ	0.0290	0.210	—	—	0.0050	0.043
		Monte Carlo J/ψ	0.1330	0.682	—	—	0.0970	0.554
		Data Z	0.2160	0.612	3.20	3.9	0.1600	0.255
		Monte Carlo Z	0.0380	0.278	2.07	2.3	0.0090	0.035
		Total errors	± 0.2581	± 0.980	± 3.81	± 4.6	± 0.1873	± 0.613
newmedium	T1	Data J/ψ	0	0.023	—	—	0	0
		Monte Carlo J/ψ	0	0.031	—	—	0.0130	0.070
		Data Z	0.0160	0.024	0.45	0.3	0.0320	0.022
		Monte Carlo Z	0	0.023	0.12	0.1	0.0180	0.017
		Total errors	± 0.0160	± 0.051	± 0.47	± 0.3	± 0.0389	± 0.076
	T2	Data J/ψ	0	0	—	—	0.0070	0
		Monte Carlo J/ψ	0.0660	0.344	—	—	0.0540	0.300
		Data Z	0.0830	0.210	1.44	2.2	0.0670	0.097
		Monte Carlo Z	0.0320	0.014	1.54	1.4	0.0240	0
		Total errors	± 0.1107	± 0.403	± 2.11	± 2.6	± 0.0896	± 0.315
	T3	Data J/ψ	0.0510	0.062	—	—	0.0110	0.043
		Monte Carlo J/ψ	0.1590	0.288	—	—	0.1320	0.290
		Data Z	0.2800	0.096	1.65	3.7	0.3010	0.128
		Monte Carlo Z	0.1960	0.093	0.73	2.8	0.0780	0.039
		Total errors	± 0.3803	± 0.323	± 1.81	± 4.7	± 0.3379	± 0.323

Table A.1: Statistical errors associated with oversmearing parameters for different track selections, types of tracks, for Run IIb3 + Run IIb4 data versus Run IIb3 MC.

Option			Double Gaussian					Single Daussian		
Tk	Tp	Systematics	$A(\times10^{-3})$	$B(\times10^{-2})$	$C(\times10^{-2})$	$D(\times10^{-3})$	Scale $(\times10^{-2})$	$A(\times10^{-3})$	$B(\times10^{-2})$	Scale $(\times10^{-2})$
medium		Reference	1.5200	1.275	3.10	6.1	0.2216	1.6000	1.275	0.2562
		Loose muon	1.5200	1.425	3.50	5.8	0.2272	1.6000	1.475	0.2628
		Newmedium track	1.5600	1.275	4.30	6.3	0.2565	1.6400	1.375	0.2878
		Tight Z p_T cut	1.5200	1.275	3.10	6.3	0.1943	1.6000	1.325	0.2230
	T1	Tight J/ψ p_T cut	1.5200	1.375	—	—	—	1.6000	1.425	—
		J/ψ scale	—	—	—	—	0.3838	—	—	0.3826
		Larger χ^2 range	1.5200	1.275	3.10	6.1	0.2216	1.6400	1.225	0.2562
		Loose track	1.5200	1.275	3.10	6.1	0.2216	1.6000	1.275	0.2562
		Total errors	± 0.0400	± 0.180	± 1.26	± 0.4	± 0.1682	± 0.0565	± 0.278	± 0.1346
		Reference	1.5600	0.725	0.90	5.1	0.2170	1.6800	0.125	0.0868
		Loose muon	1.3200	1.425	1.70	5.8	0.1211	1.5600	1.075	0.0981
		Newmedium track	1.6400	0.775	4.30	4.6	0.2509	1.7200	0.925	0.1658
		Tight Z p_T cut	1.3200	0.725	6.90	0.3	−0.1421	1.5200	0.675	−0.1947
	T2	Tight J/ψ p_T cut	1.2400	1.575	—	—	—	1.6800	0.975	—
		J/ψ scale	—	—	—	—	1.4816	—	—	1.4040
		Larger χ^2 range	1.5200	0.825	0.90	5.1	0.1844	1.6800	0.475	0.0855
		Loose track	1.5600	0.725	0.90	5.1	0.2170	1.6800	0.125	0.0868
		Total errors	± 0.4749	± 0.725	± 0.90	± 4.8	± 0.2170	± 0.2039	± 0.125	± 0.0868
		Reference	1.9750	1.150	5.40	9.0	0.7032	2.1750	1.650	0.6874
		Loose muon	1.9250	2.250	8.60	5.8	0.5052	2.1750	2.250	0.5751
		Newmedium track	2.4250	1.750	12.60	7.4	0.4417	2.6250	2.050	0.4646
		Tight Z p_T cut	1.9750	1.150	9.00	7.0	0.2577	2.0750	2.050	0.2914
	T3	Tight J/ψ p_T cut	1.8750	1.950	—	—	—	2.2250	1.850	—
		J/ψ scale	—	—	—	—	0.5414	—	—	0.5456
		Larger χ^2 range	2.1250	1.650	5.80	7.4	0.5383	2.2250	1.550	0.5572
		Loose track	1.9750	1.150	5.40	9.0	0.7032	2.1750	1.650	0.6874
		Total errors	± 0.4873	± 1.150	± 5.40	± 4.4	± 0.5995	± 0.4663	± 0.854	± 0.5061
loose		Reference	1.4800	1.175	4.50	5.6	0.2276	1.6000	1.225	0.2568
		Loose muon	1.4800	1.475	4.50	5.3	0.2233	1.6000	1.475	0.2664
		Newmedium track	1.4800	1.325	4.50	5.3	0.2380	1.6000	1.275	0.2813
		Tight Z p_T cut	1.4800	1.225	4.50	5.8	0.1667	1.6400	1.225	0.2040
	T1	Tight J/ψ p_T cut	1.4800	1.325	—	—	—	1.6000	1.375	—
		J/ψ scale	—	—	—	—	0.4070	—	—	0.4064
		Larger χ^2 range	1.5200	1.225	3.10	6.3	0.2284	1.6400	1.225	0.2568
		Medium track	1.4800	1.175	4.50	5.6	0.2276	1.6000	1.225	0.2568
		Total errors	± 0.0400	± 0.374	± 1.40	± 0.8	± 0.1898	± 0.0565	± 0.295	± 0.1608
		Reference	1.5600	0.775	4.90	0.3	0.1468	1.5600	0.725	0.1310
		Loose muon	1.4800	1.175	3.70	3.1	0.1604	1.6800	1.025	0.2176
		Newmedium track	1.4000	1.375	4.90	2.1	0.2638	1.4400	1.375	0.2582
		Tight Z p_T cut	1.4800	0.725	5.10	0.1	−0.1847	1.5200	0.725	−0.1367
	T2	Tight J/ψ p_T cut	1.4000	1.375	—	—	—	1.5200	1.225	—
		J/ψ scale	—	—	—	—	1.2426	—	—	1.2219
		Larger χ^2 range	1.5200	0.725	1.50	6.3	0.1732	1.5200	0.725	0.1248
		Medium track	1.5600	0.775	4.90	0.3	0.1468	1.5600	0.725	0.1310
		Total errors	± 0.2561	± 0.775	± 3.61	± 0.3	± 0.1468	± 0.1833	± 0.725	± 0.1310
		Reference	2.2250	0.550	6.60	9.4	0.6170	2.4750	1.650	0.6722
		Loose muon	1.7250	2.550	2.60	11.8	0.8696	2.2750	2.550	0.7788
		Newmedium track	1.2750	2.150	6.20	5.4	0.5334	2.4750	2.250	0.4445
		Tight Z p_T cut	2.0750	0.550	6.20	12.2	0.1933	2.3250	1.750	0.0335
	T3	Tight J/ψ p_T cut	1.9750	2.050	—	—	—	2.3750	2.050	—
		J/ψ scale	—	—	—	—	0.6177	—	—	0.5966
		Larger χ^2 range	2.4250	1.750	3.80	13.4	0.6097	2.5250	1.250	0.4205
		Medium track	2.2250	0.550	6.60	9.4	0.6170	2.4750	1.650	0.6722
		Total errors	± 1.1302	± 0.550	± 4.91	± 6.7	± 0.5003	± 0.2738	± 1.224	± 0.6722

Table A.2: Systematic errors associated with oversmearing parameters for Medium and Loose track selections, types of tracks, for Run IIb3 + Run IIb4 data versus Run IIb3 MC.

Option			Double Gaussian					Single Daussian		
Tk	Tp	Systematics	$A(\times 10^{-3})$	$B(\times 10^{-2})$	$C(\times 10^{-2})$	$D(\times 10^{-3})$	Scale $(\times 10^{-2})$	$A(\times 10^{-3})$	$B(\times 10^{-2})$	Scale $(\times 10^{-2})$
newmedium		Reference	1.4800	1.225	4.50	6.6	0.2152	1.6400	1.275	0.2752
		Loose muon	1.4400	1.425	3.90	6.1	0.2089	1.6000	1.475	0.2551
		Medium track	1.4400	1.225	4.10	5.6	0.2053	1.6000	1.225	0.2616
		Tight Z p_T cut	1.4800	1.275	4.70	6.3	0.1677	1.6400	1.275	0.2202
	T1	Tight J/ψ p_T cut	1.4800	1.275	—	—	—	1.6400	1.375	—
		J/ψ scale	—	—	—	—	0.3979	—	—	0.3965
		Larger χ^2 range	1.4800	1.225	4.50	6.6	0.2205	1.6800	1.275	0.2662
		Loose track	1.4800	1.225	4.50	6.6	0.2152	1.6400	1.275	0.2752
		Total errors	± 0.0565	± 0.212	± 0.74	± 1.1	± 0.1891	± 0.0692	± 0.229	± 0.1357
		Reference	1.5200	0.575	2.90	6.8	0.1730	1.6400	0.575	0.1595
		Loose muon	1.4800	1.225	3.30	3.3	0.1760	1.5200	1.275	0.2199
		Medium track	1.4400	1.175	4.30	2.6	0.1607	1.5200	1.275	0.2187
		Tight Z p_T cut	1.4400	0.625	2.30	6.6	−0.3312	1.3600	1.175	−0.1913
	T2	Tight J/ψ p_T cut	1.5600	0.825	—	—	—	1.6000	0.675	—
		J/ψ scale	—	—	—	—	1.5961	—	—	1.4220
		Larger χ^2 range	1.5200	0.575	2.90	6.8	0.1658	1.6000	0.575	0.2180
		Loose track	1.5200	0.575	2.90	6.8	0.1730	1.6400	0.575	0.1595
		Total errors	± 0.1264	± 0.575	± 1.57	± 5.5	± 0.1730	± 0.3322	± 0.575	± 0.1595
		Reference	2.5250	1.950	2.60	17.8	0.4164	2.8750	1.650	0.5340
		Loose muon	2.1250	2.250	19.80	0.6	0.4889	2.1250	2.450	0.6183
		Medium track	2.1750	1.450	11.40	1.0	0.6069	2.0750	1.450	0.4710
		Tight Z p_T cut	2.0750	1.850	3.40	12.2	0.1844	2.0250	1.950	0.1655
	T3	Tight J/ψ p_T cut	2.5750	2.650	—	—	—	2.7750	2.250	—
		J/ψ scale	—	—	—	—	0.4708	—	—	0.4335
		Larger χ^2 range	2.4750	2.050	3.40	17.8	0.4120	2.8250	1.750	0.3310
		Loose track	2.5250	1.950	2.60	17.8	0.4164	2.8750	1.650	0.5340
		Total errors	± 0.7000	± 0.921	± 2.60	± 17.8	± 0.3135	± 1.3919	± 1.067	± 0.4452

Table A.3: Systematic errors associated with oversmearing parameters for New Medium track selections, types of tracks, for Run IIb3 + Run IIb4 data versus Run IIb3 MC.

APPENDIX B

INVARIANT MASS DISTRIBUTIONS OF MUON OVERSMEARING PARAMETERS

In this section, figures illustrate $Z/\gamma^{\star} \rightarrow \mu^{+}\mu^{-}$ invariant mass distributions for muon-smearing parameters corresponding to each type of track selections, comparing data with non-smeared MC and smeared MC (both DG and SG) in 3 different types of tracks (T1, T2 and T3), for Run IIb3 + Run IIb4 Data versus Run IIb3 MC:

It is also provided (Data - MC)/σ for a better visualization of discrepancies between those distributions, each data distribution being subtracted by its correspondent MC one. For example, data distribution for *Medium track* is subtracted by MC using the same working point.

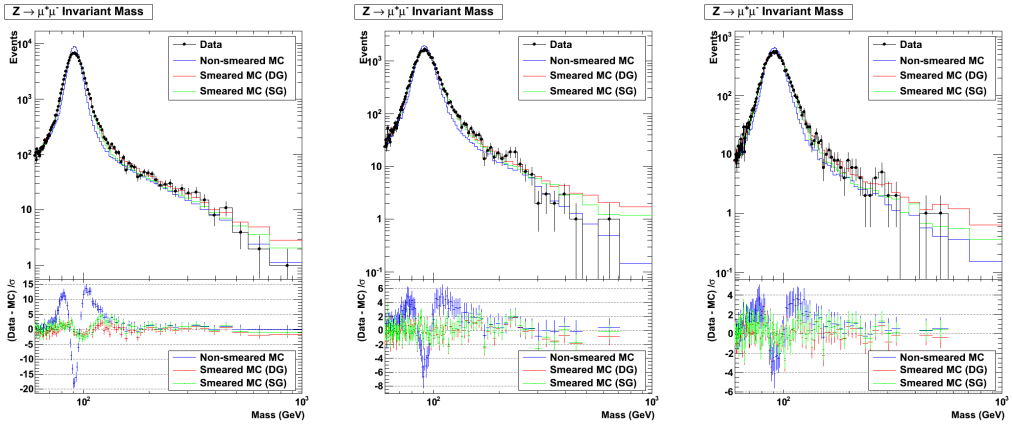

Figure B.1: Data and reconstructed MC $Z/\gamma^{\star} \rightarrow \mu^{+}\mu^{-}$ invariant mass distribution (figures on the top) and (Data - MC)/σ (figures on the bottom) for the 3 type of tracks (from left to right: T1, T2 and T3) in case of *Medium track* selection. Data (dots) is compared with non-smeared MC (blue lines), smeared MC via Double Gaussian (red lines) and via Single Gaussian (green lines).

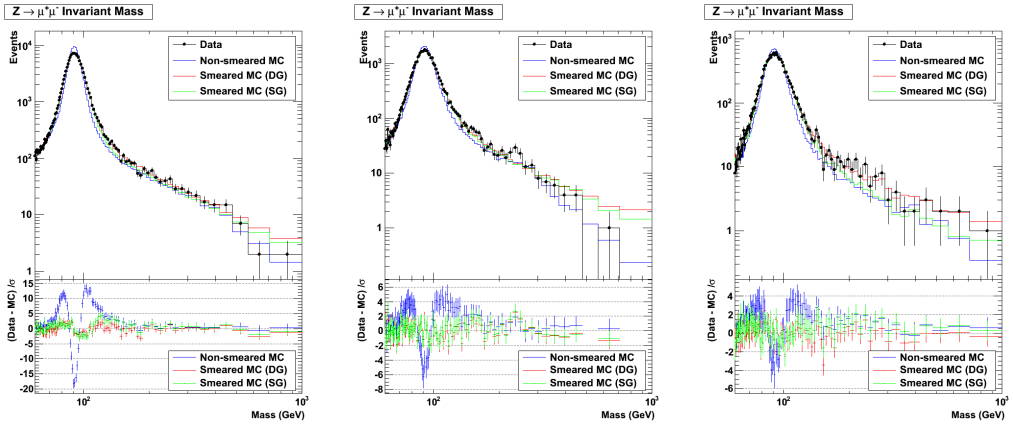

Figure B.2: Data and reconstructed MC $Z/\gamma^{\star} \rightarrow \mu^{+}\mu^{-}$ invariant mass distribution (figures on the top) and (Data - MC)/σ (figures on the bottom) for the 3 type of tracks (from left to right: T1, T2 and T3) in case of *Loose track* selection. Data (dots) is compared with non-smeared MC (blue lines), smeared MC via Double Gaussian (red lines) and via Single Gaussian (green lines).

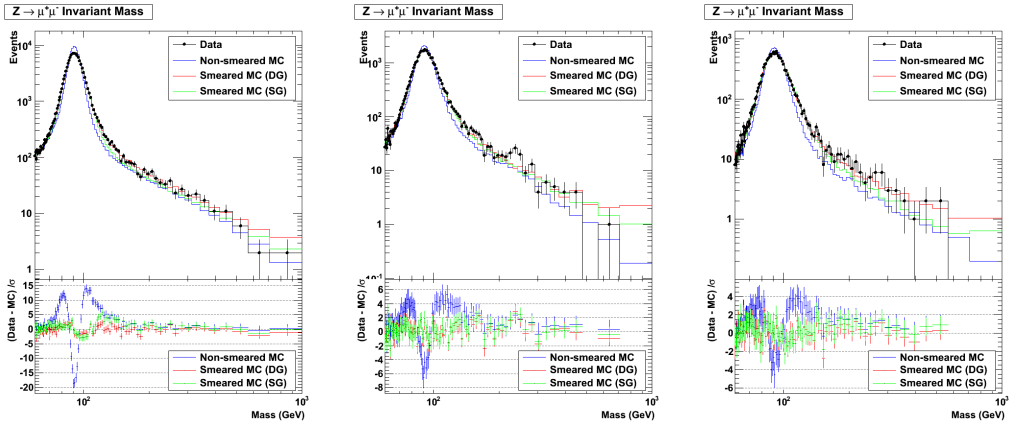

Figure B.3: Data and reconstructed MC $Z/\gamma^{\star} \rightarrow \mu^{+}\mu^{-}$ invariant mass distribution (figures on the top) and (Data - MC)/σ (figures on the bottom) for the 3 type of tracks (from left to right: T1, T2 and T3) in case of *New Medium track* selection. Data (dots) is compared with non-smeared MC (blue lines), smeared MC via Double Gaussian (red lines) and via Single Gaussian (green lines).

APPENDIX C

RESULTS WITH LOOSE DATA QUALITY

To get better statistics, we created figures with loose DQ, which makes more candidate events. As a reference, cut flows with loose DQ for each channel are listed below. Therefore, we gain 4 more events in 4μ channel (was 3) and 1 more events in $2e2\mu$ channel (was 5), while events do not change in 4e channel.

The cut flow of 4μ channel with loose data quality is shown in Table C.1. The cut flows for 4e channel are shown in Tables C.2 and C.3. The cut flows for $2e2\mu$ channel are shown in Tables C.4 and C.5.

Cut	Run IIa Events	Run IIb Events
Initial	9776282	139915578
Loose Data Quality	9069996	133654953
Trigger	9069845	133654953
4 good muons	1943	10476
Track $\Delta z_{DCA} < 3$ cm	815	4048
Muon Isolation	3	18
Muon opposite charges	3	14
Muon $p_T > 15$ GeV	0	7
Dimass $M_{\mu\mu} > 30$ GeV	0	7

Table C.1: Run IIa and IIb: Cut flow for $\mu\mu\mu\mu$ Data with loose DQ.

Cut	Number of Events			
Initial	36294680			
≥ 3 good electrons	4303			
Loose Data Quality	3911			
≥ 4 good electrons	21			
p_T and ICD overlap removal	1			
≥ 2 CC electrons	0			
CC/ICD topology	2 CC electrons 0 ICD electron	3 CC electrons 0 ICD electron	4 CC electrons 0 ICD electron	1 ICD electron
	0	0	0	0
Dimass	0	0	0	0

Table C.2: Run IIa: Cut flow for *eeee* data with loose DQ for four sub-channels ($= 2$, $= 3$, ≥ 4 central electrons with no ICD electrons, and with 1 ICD electron).

Cut	Number of Events			
Initial	185982072			
≥ 3 good electrons	27238			
Loose Data Quality	26059			
≥ 4 good electrons	117			
p_T and ICD overlap removal	7			
≥ 2 CC electrons	5			
CC/ICD topology	2 CC electrons 0 ICD electron	3 CC electrons 0 ICD electron	4 CC electrons 0 ICD electron	1 ICD electron
	0	1	2	2
Dimass	0	1	2	2

Table C.3: RunIIb: Cut flow for *eeee* data with loose DQ for four sub-channels ($= 2$, $= 3$ or ≥ 4 central electrons with no ICD electrons, and with 1 ICD electron).

Cut	Number of Events		
Initial	36229860		
Loose Data Quality	34513823		
≥ 1 good electron	835304		
≥ 1 good muon	32		
p_T	18		
CC topology	0 CC electrons	1 CC electrons	2 CC electrons
	2	5	11
Space angle and Acop.	2	5	11
μ track Δz	2	4	10
$\Delta R_{e\mu}$	1	1	0
Dimass	1	1	0

Table C.4: Run IIa: Cut flow for $ee\mu\mu$ data with loose DQ for three channels ($= 0$, $= 1$ or ≥ 2 central electrons).

With loose DQ, we observe seven events in the 4μ channel with an estimated background of 0.27 events and an expected signal of 4.5 events. A summary of the results are show in Table C.6.

For the *eeee* channel, we observe five events, with an estimated background of 0.74 events, and an expected signal of 4.1 events. Two of them come from the 1 ICD subchannel, two from 4 CC, and one from 3 CC. Details are given in Table C.7.

Cut	Number of Events		
Initial	185982072		
Loose Data Quality	178582022		
≥ 1 good electron	7235058		
≥ 1 good muon	2595		
p_T	368		
CCtopology	0 CC electrons	1 CC electrons	2 CC electrons
	23	97	248
Space angle and Acop.	22	96	245
μ track Δz	3	25	169
$\Delta R_{e\mu}$	1	0	3
Dimass	1	0	3

Table C.5: RunIIb: Cut flow for $ee\mu\mu$ data with loose DQ for three subchannels ($= 0$, $= 1$ or ≥ 2 central electrons).

For the $ee\mu\mu$ channel, we observe six candidate events, with an estimated background of 0.50 events, and an expected signal of 6.9 events. Three of them come from the 2 CC subchannel, one from the 1 CC subchannel, and one from the 0 CC subchannel. Details of these events are given in Table C.8.

Background	
$Z(\gamma)$+jets	$0.211 \pm 0.003^{+0.093}_{-0.077}$
Migration	$0.397 \pm 0.015^{+0.081}_{-0.044}(\times 10^{-1})$
Cosmics	<0.01
Total Background	$0.618 \pm 0.015^{+0.174}_{-0.121}(\times 10^{-1})$
Expected Signal	$4.465 \pm 0.017^{+0.463}_{-0.462}$
Observed Events	7

Table C.6: Contribution from non-negligible backgrounds in the $\mu\mu\mu\mu$ channel with loose DQ, plus expected signal and number of observed events. Errors are statistical followed by systematic.

Background	2 CC 0 ICD	3 CC 0 ICD
$Z(\gamma)$+jets	$0.164 \pm 0.013 \pm 0.031$	$0.121 \pm 0.011 \pm 0.019$
Migration	$0.0145 \pm 0.0008 \pm 0.0021$	$0.0247 \pm 0.0011 \pm 0.0037$
Total Background	$0.165 \pm 0.013 \pm 0.031$	$0.146 \pm 0.012 \pm 0.019$
Expected Signal	$0.473 \pm 0.006 \pm 0.068$	$1.124 \pm 0.010 \pm 0.165$
Observed Events	0	1

Background	4 CC 0 ICD	$\geq$ 2 CC 1 ICD
$Z(\gamma)$+jets	$0.056 \pm 0.006 \pm 0.006$	$0.303 \pm 0.042^{+0.003}_{-0.128}$
Migration	$0.0264 \pm 0.0012 \pm 0.0039$	$0.0258 \pm 0.0012 \pm 0.0033$
Total Background	$0.082 \pm 0.006 \pm 0.007$	$0.329 \pm 0.042^{+0.004}_{-0.128}$
Expected Signal	$1.012 \pm 0.009 \pm 0.147$	$1.446 \pm 0.011 \pm 0.179$
Observed Events	2	2

Table C.7: Contribution from non-negligible backgrounds in the *eeee* channels with loose DQ, plus expected signal and number of observed events. Errors are statistical followed by systematic.

Background	0 CC	1 CC	2 CC
$Z(\gamma)$+jets	$0.068^{+0.004\ +0.008}_{-0.003\ -0.008}$	$0.152^{+0.006\ +0.022}_{-0.006\ -0.021}$	$0.252^{+0.007\ +0.030}_{-0.006\ -0.030}$
$t\bar{t}$	$0.23^{+0.30}_{-0.16} \pm 0.63(\times 10^{-2})$	$1.09^{+0.53}_{-0.38} \pm 0.24(\times 10^{-2})$	$0.30^{+0.23}_{-0.14} \pm 0.28(\times 10^{-2})$
Migration	$2.24^{+0.93\ +0.34}_{-0.72\ -1.06}(\times 10^{-3})$	$5.86^{+0.93\ +0.70}_{-0.89\ -1.64}(\times 10^{-3})$	$5.28^{+0.87\ +1.06}_{-0.86\ -1.29}(\times 10^{-3})$
Cosmics	< 0.001	< 0.003	< 0.006
Total BK	$0.073^{+0.005\ +0.009}_{-0.004\ -0.009}$	$0.169^{+0.008\ +0.025}_{-0.007\ -0.025}$	$0.261^{+0.007\ +0.034}_{-0.006\ -0.032}$
Expected Sg.	$0.42 \pm 0.01 \pm 0.05$	$2.36 \pm 0.02 \pm 0.28$	$4.16 \pm 0.03 \pm 0.49$
Observed Ev.	2	1	3

Table C.8: Contribution from non-negligible backgrounds in the $ee\mu\mu$ channels with loose DQ, plus expected signal and number of observed events. Errors are statistical followed by systematic.

APPENDIX D

EVENTS DISPLAY

This section shows the event display of all our candidate events. Under loose DQ, there are five candidate events in the $eeee$ channel with display figures given in Figures D.1-D.5.

There are seven candidates in the $\mu\mu\mu\mu$ channel. Figures D.6-D.12 give the relevant information for these events.

There are six candidates in the $ee\mu\mu$ channel. Figures D.13-D.18 show give the relevant information for these events.

Five events do not pass the normal DQ (four in 4μ channel and one in $2e2\mu$ channel), which makes total candidate from 18 to 13 events. They have been marked in the event displays below.

Uncertainties on the electron energies are determined from the resolution formula found in reference [90]. Uncertainties on muon p_Ts are found using the muon transfer function described in the appendices of reference [91].

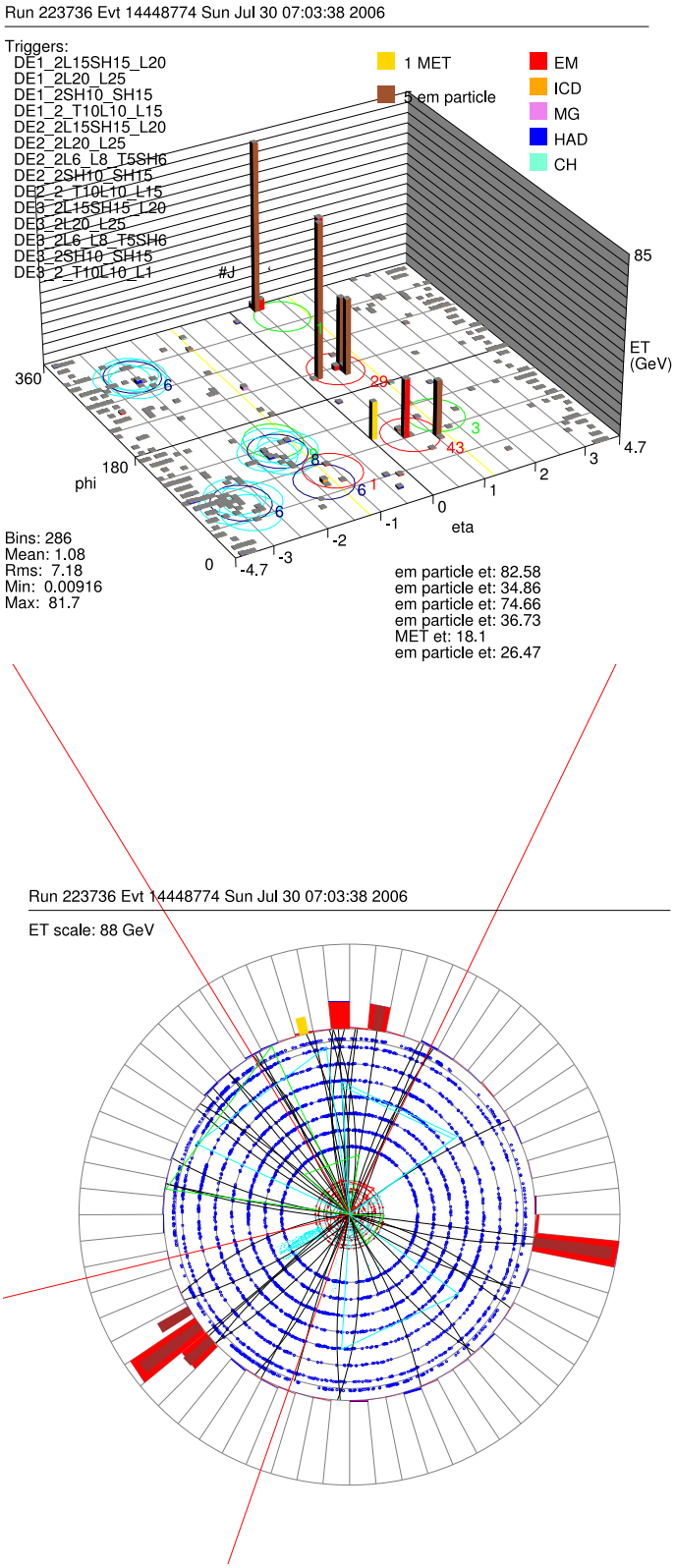

Figure D.1: *eeee* candidate event display for the Run 223736. (Four lepton invariant mass 216.1 GeV)

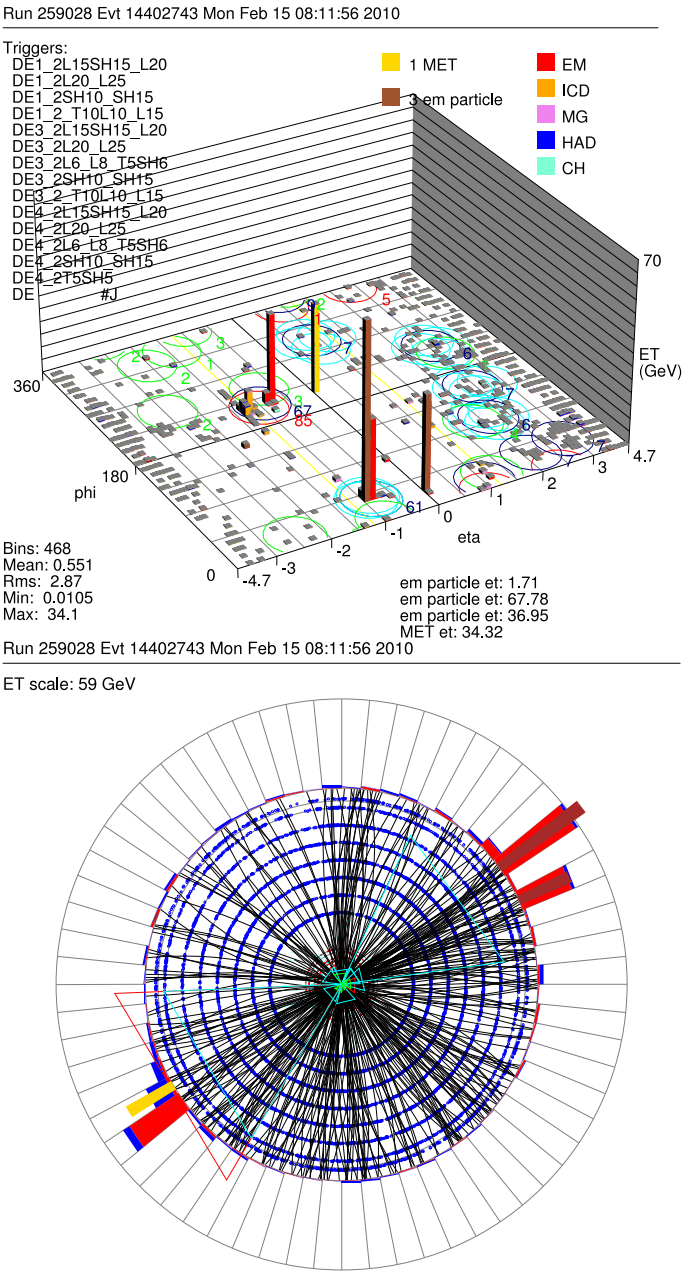

Figure D.2: *eeee* candidate event display for the Run 259028. (Four lepton invariant mass 194.7 GeV)

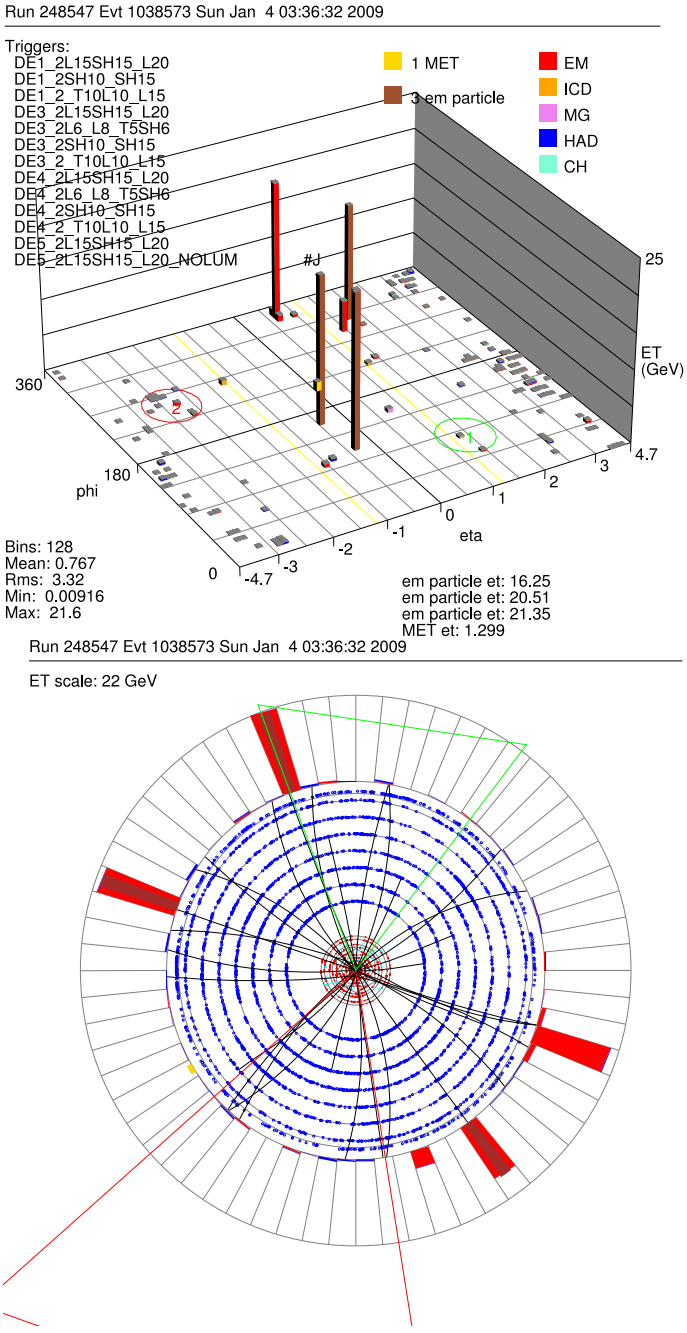

Figure D.3: *eeee* candidate event display for the Run 248547. (Four lepton invariant mass 116.9 GeV)

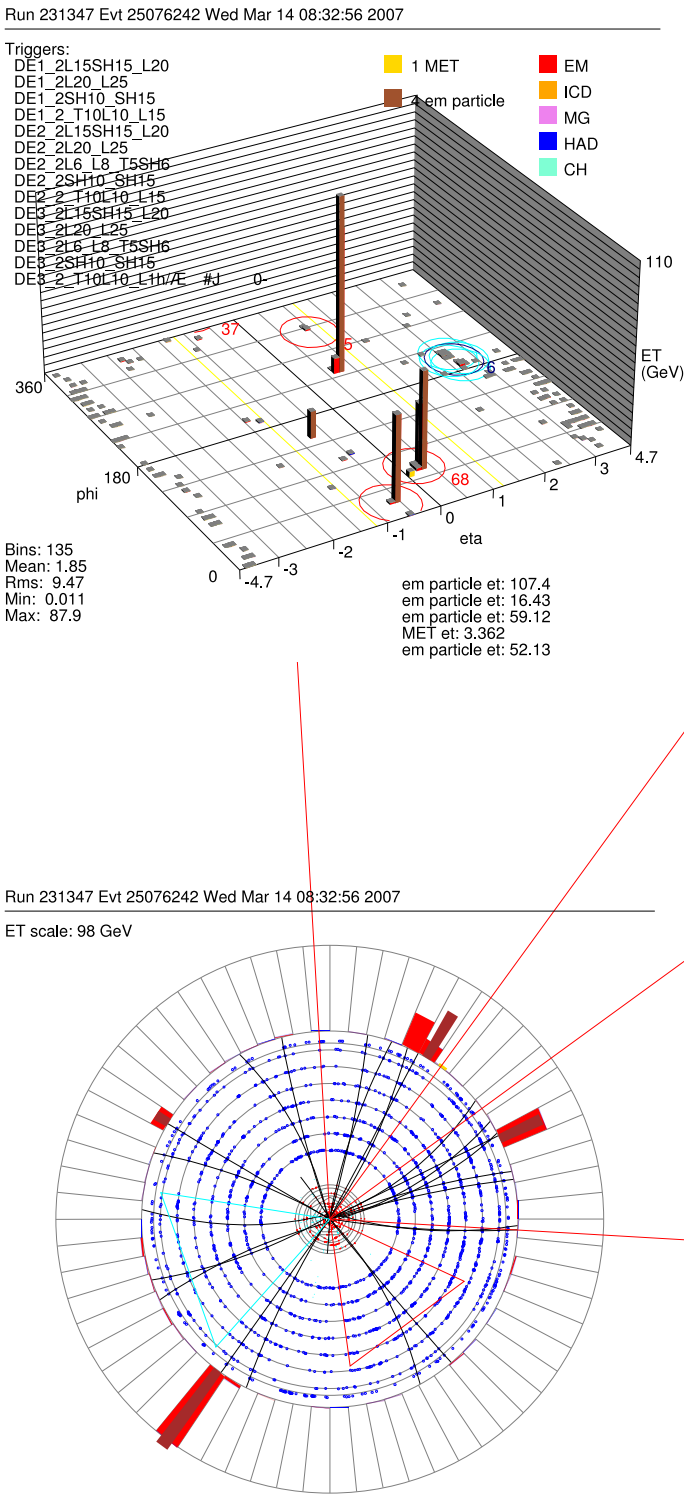

Figure D.4: *eeee* candidate event display for the Run 231347. (Four lepton invariant mass 273.6 GeV)

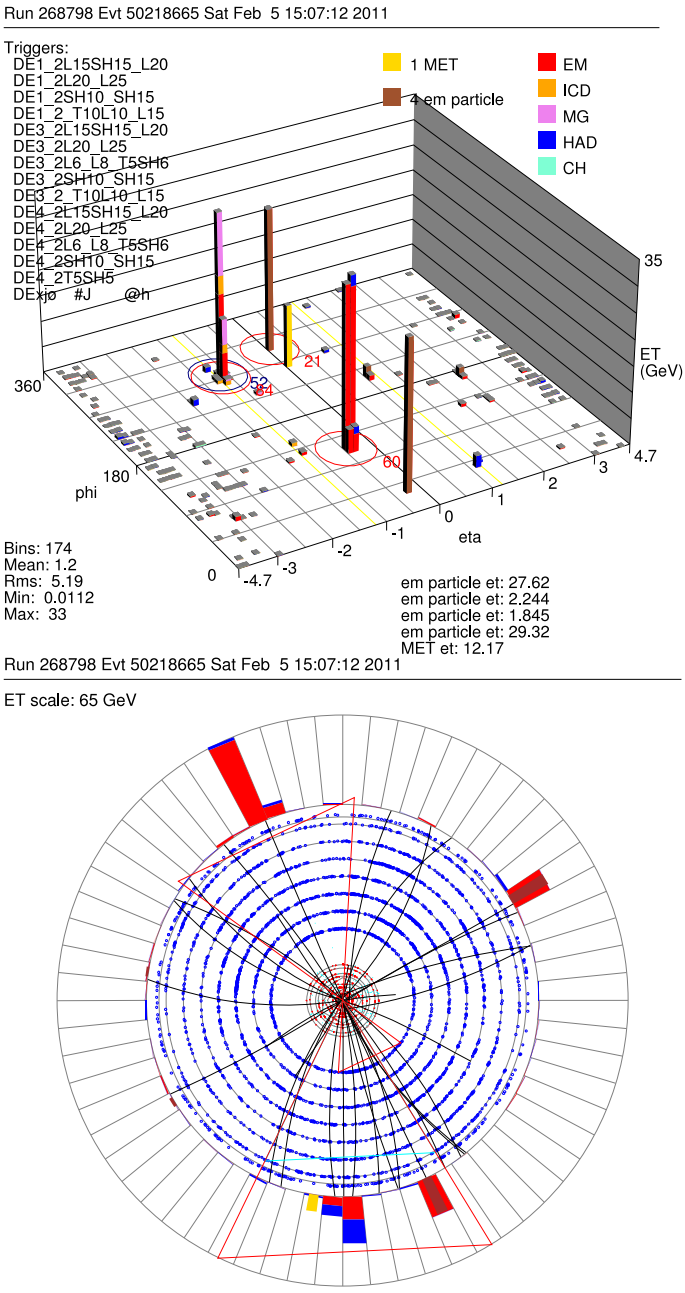

Figure D.5: *eeee* candidate event display for the Run 268798. (Four lepton invariant mass 252.9 GeV)

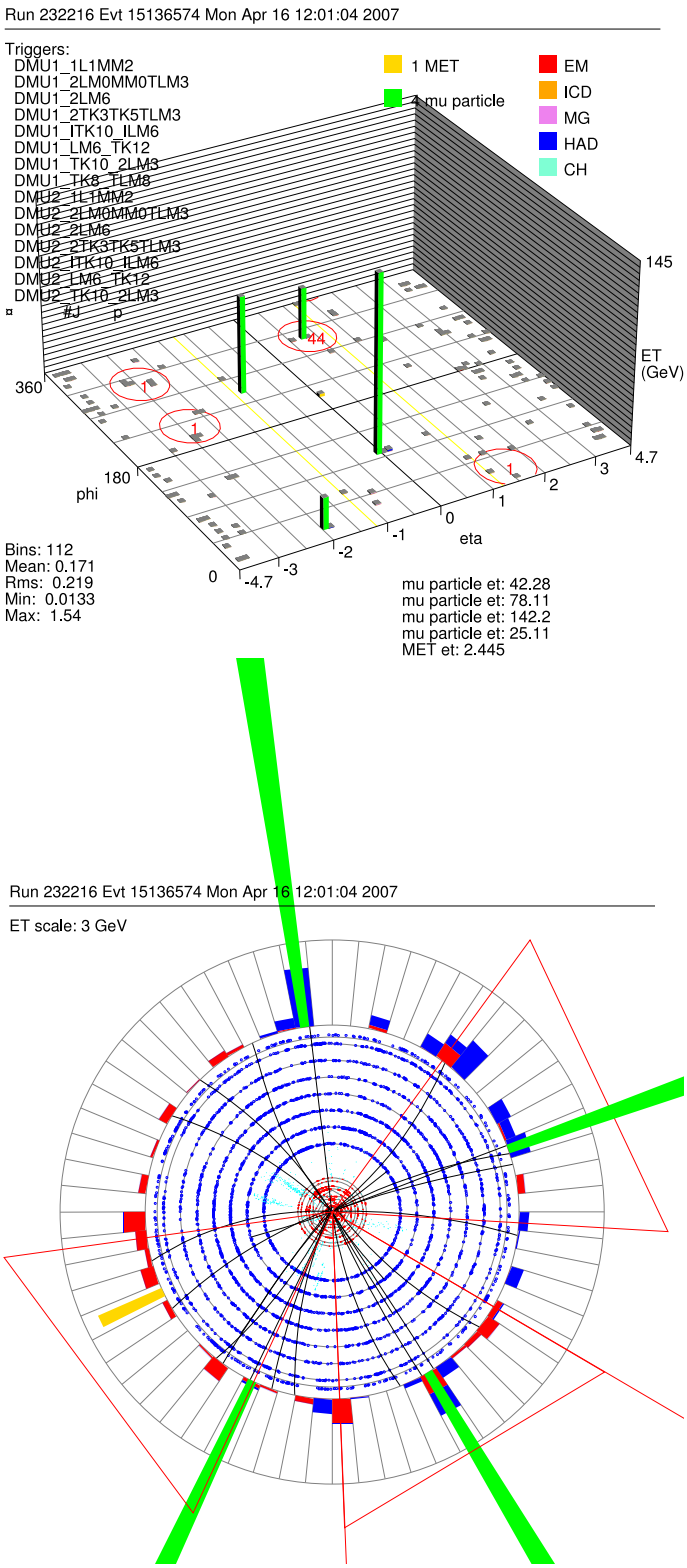

Figure D.6: $\mu\mu\mu\mu$ candidate event display for the Run 232216. (Four lepton invariant mass 347.2 GeV) (This event does not pass normal DQ)

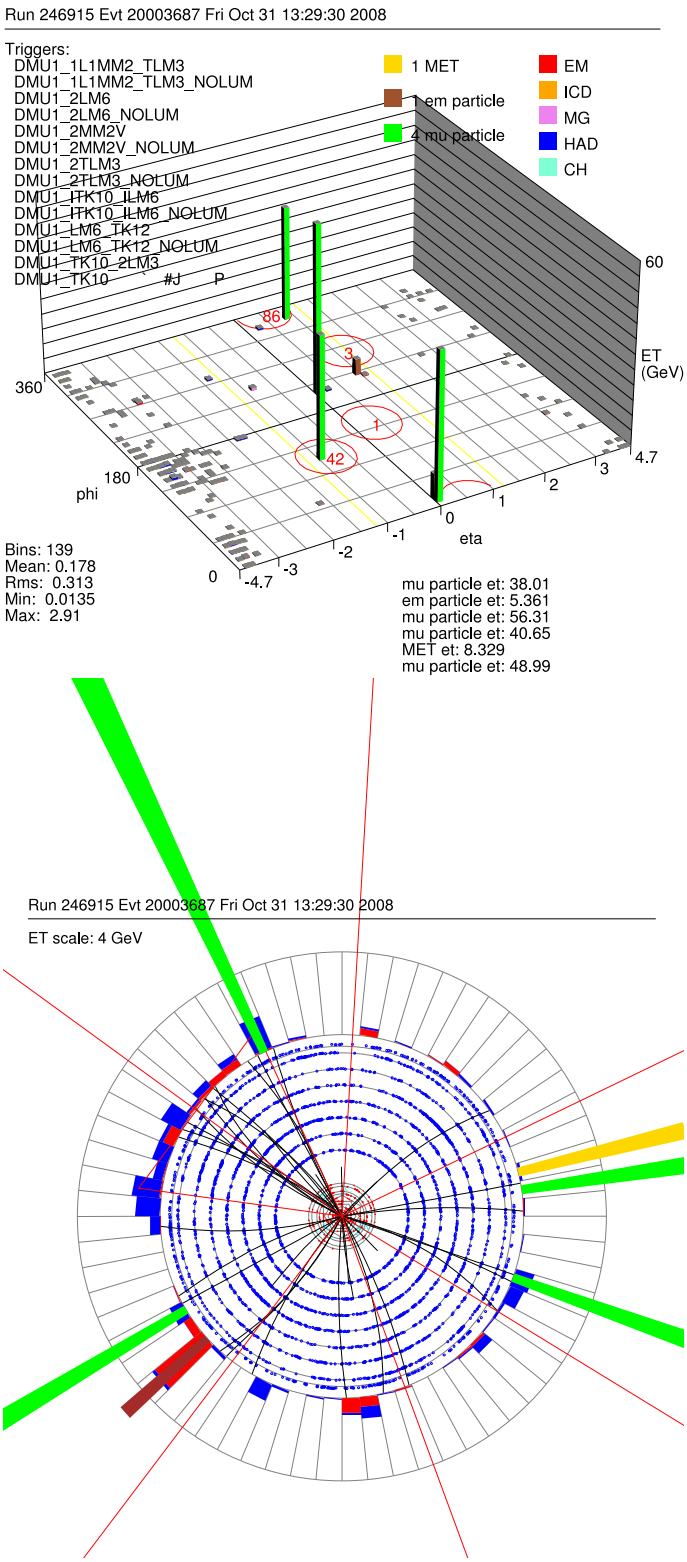

Figure D.7: $\mu\mu\mu\mu$ candidate event display for the Run 246915. (Four lepton invariant mass 218.6 GeV)

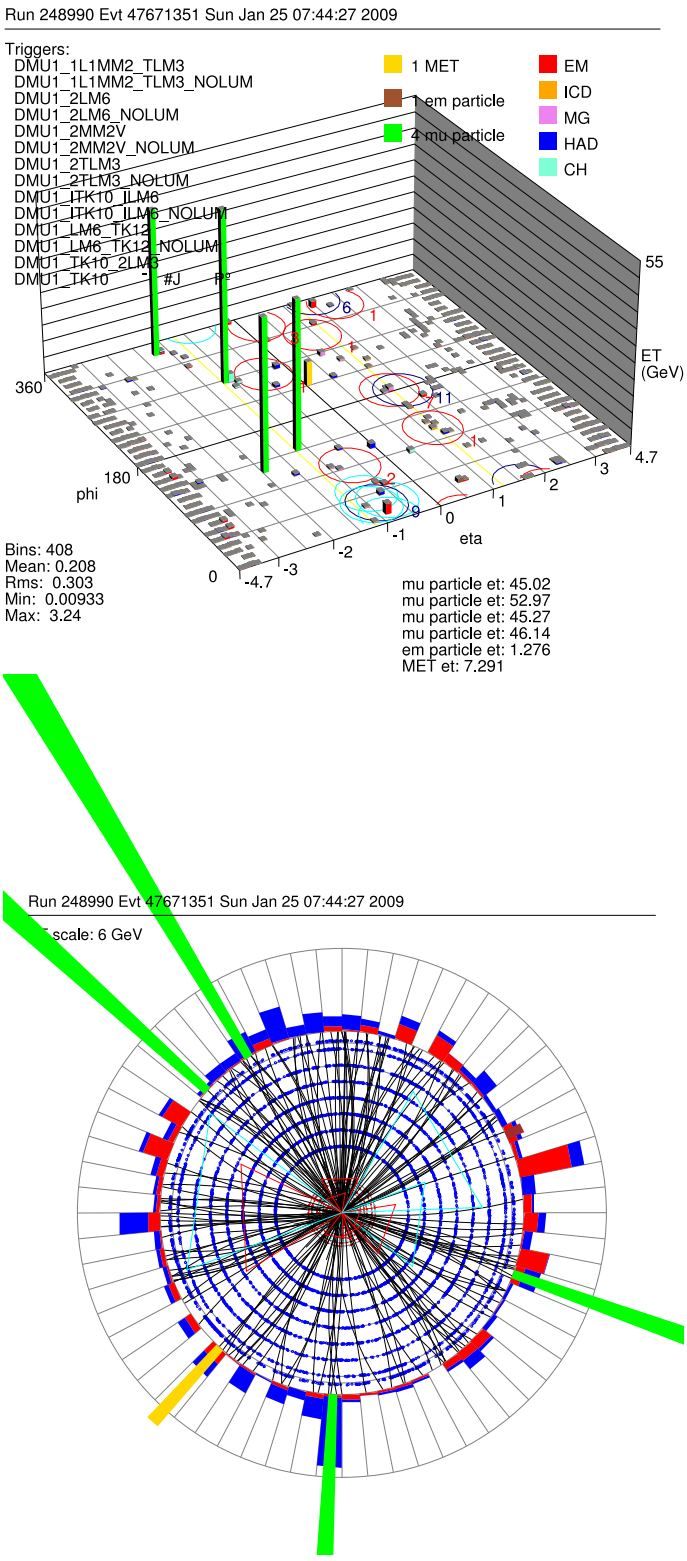

Figure D.8: $\mu\mu\mu\mu$ candidate event display for the Run 248990. (Four lepton invariant mass 201.9 GeV) (This event does not pass normal DQ)

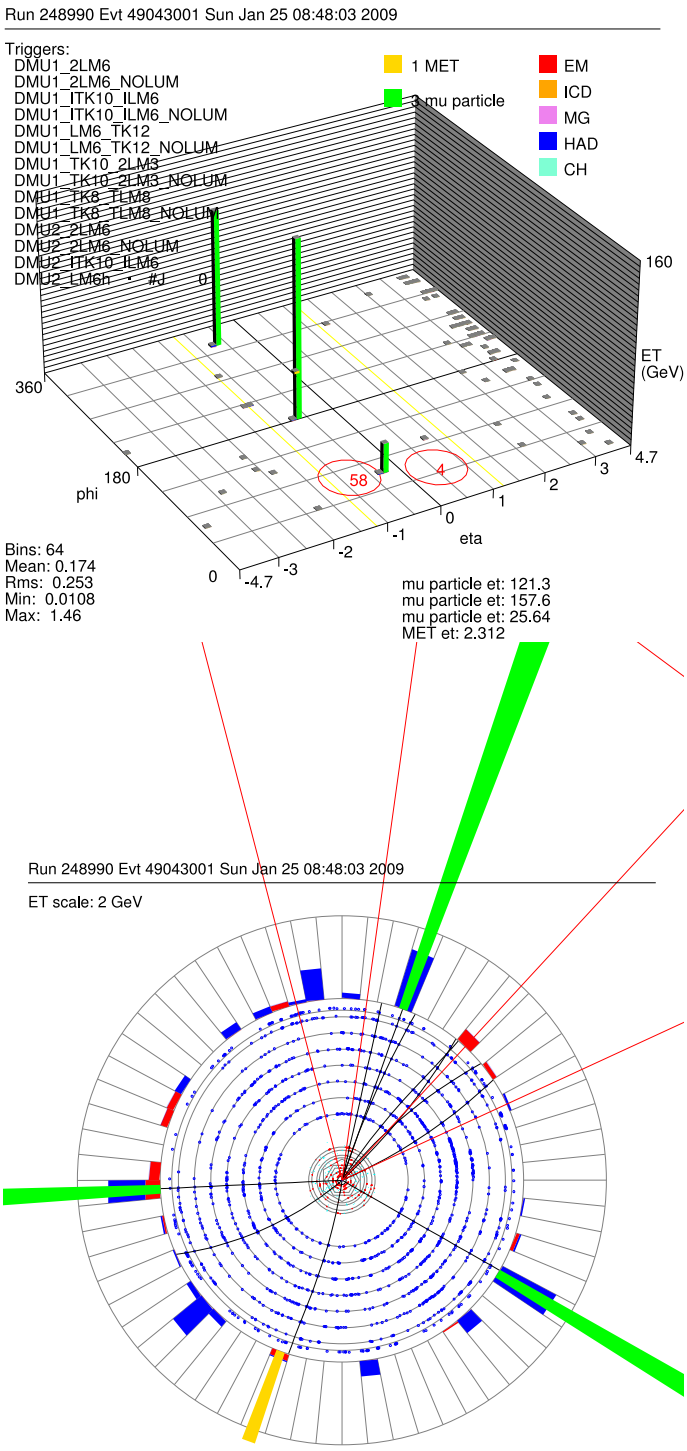

Figure D.9: $\mu\mu\mu\mu$ candidate event display for the Run 248990. (Four lepton invariant mass 339.5 GeV) (This event does not pass normal DQ)

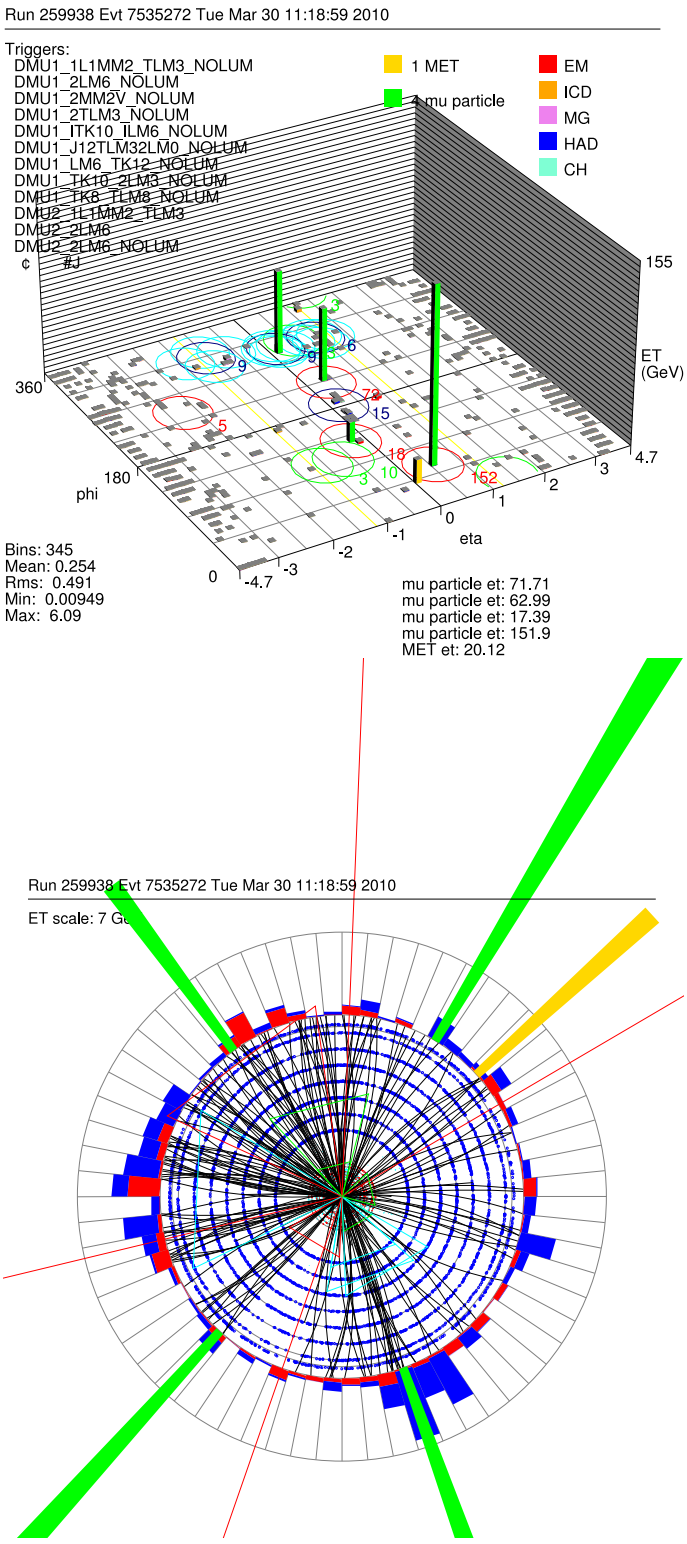

Figure D.10: $\mu\mu\mu\mu$ candidate event display for the Run 259938. (Four lepton invariant mass 308.8 GeV)

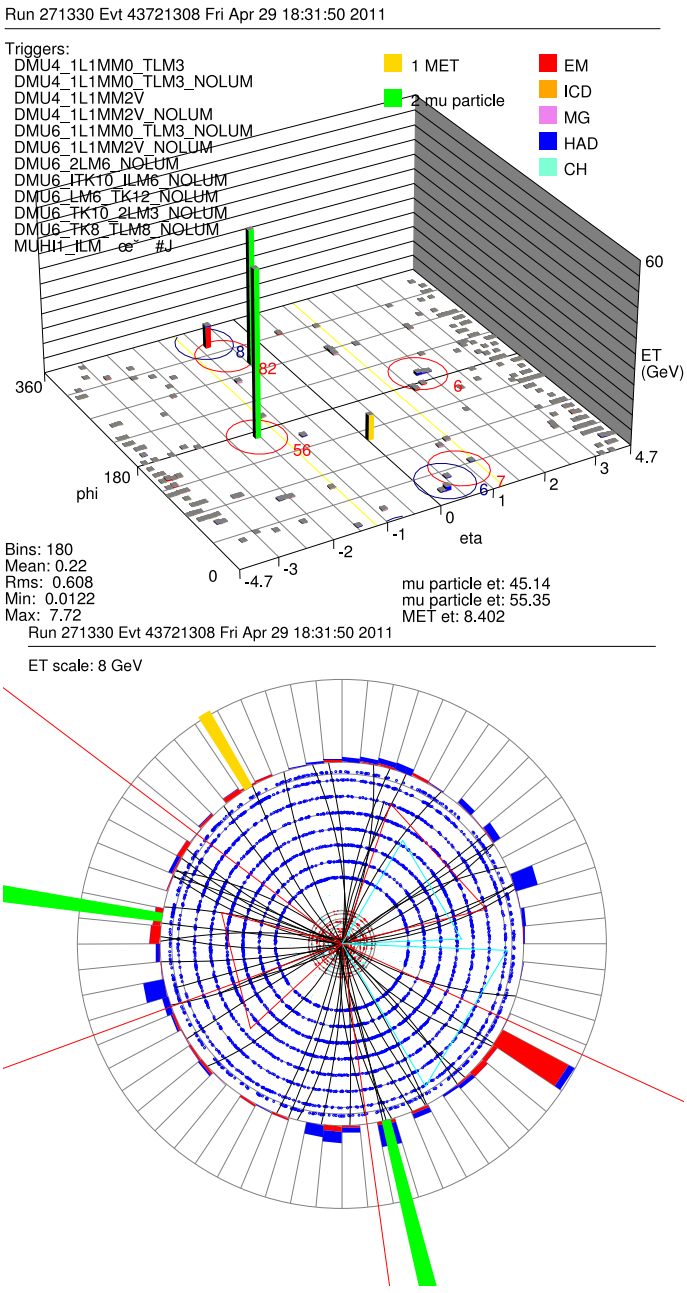

Figure D.11: $\mu\mu\mu\mu$ candidate event display for the Run 271330. (Four lepton invariant mass 274.9 GeV)

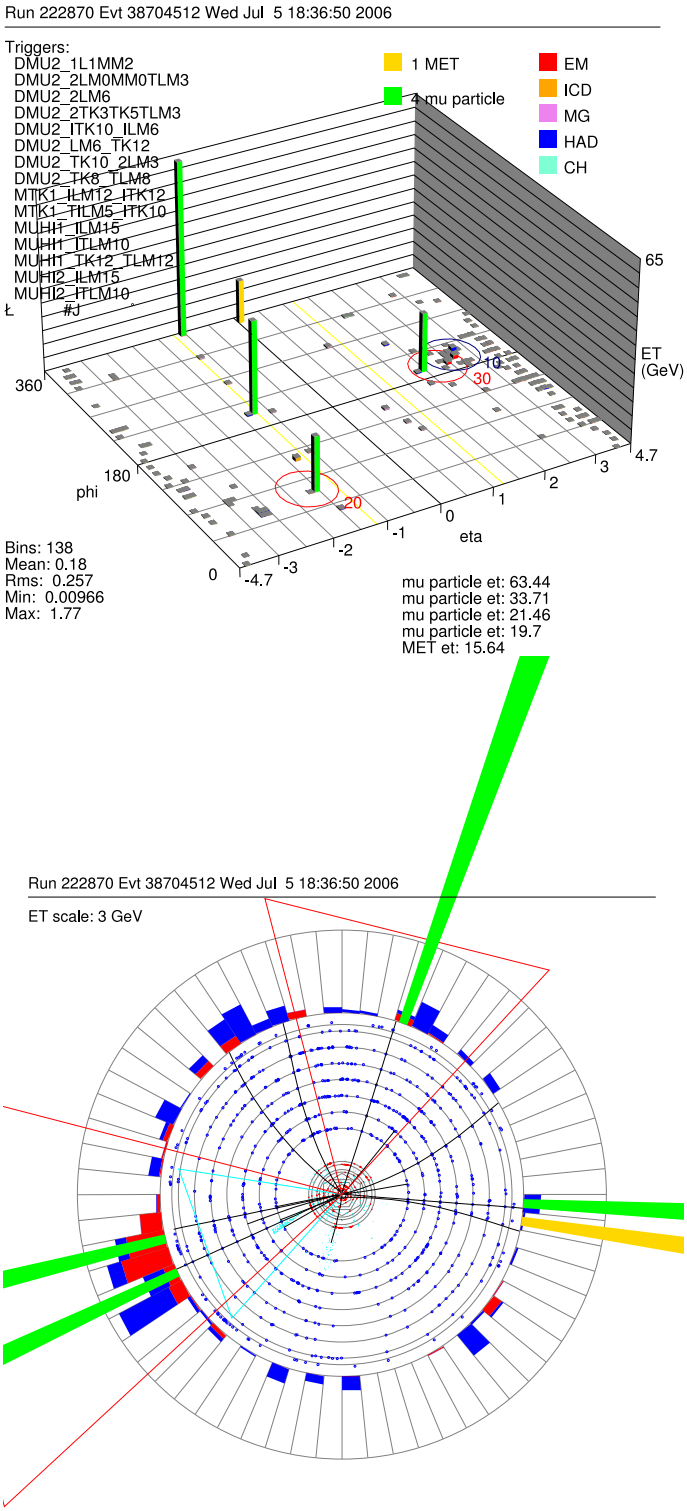

Figure D.12: $\mu\mu\mu\mu$ candidate event display for the Run 222870. (Four lepton invariant mass 270.1 GeV) (This event does not pass normal DQ)

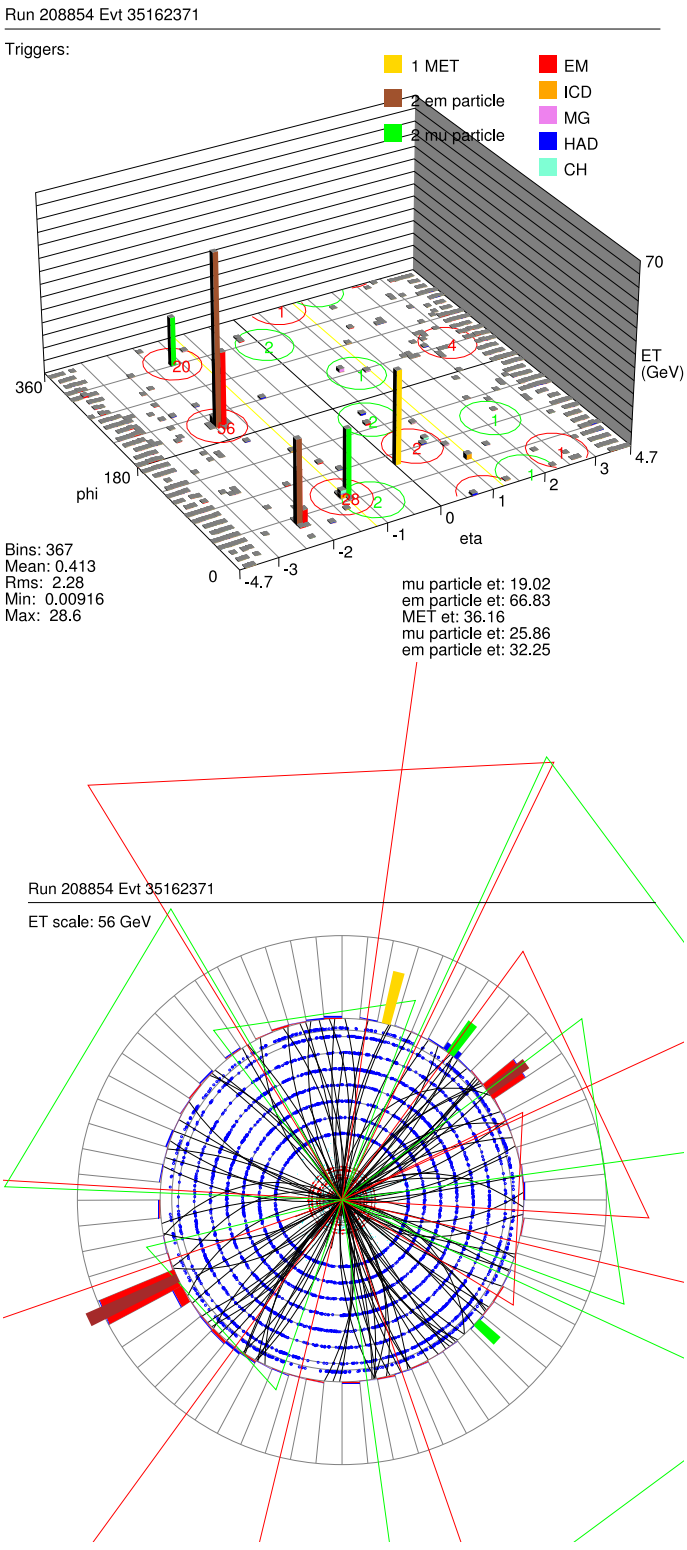

Figure D.13: $ee\mu\mu$ candidate event display for the Run 208854. (Four lepton invariant mass 151.5 GeV)

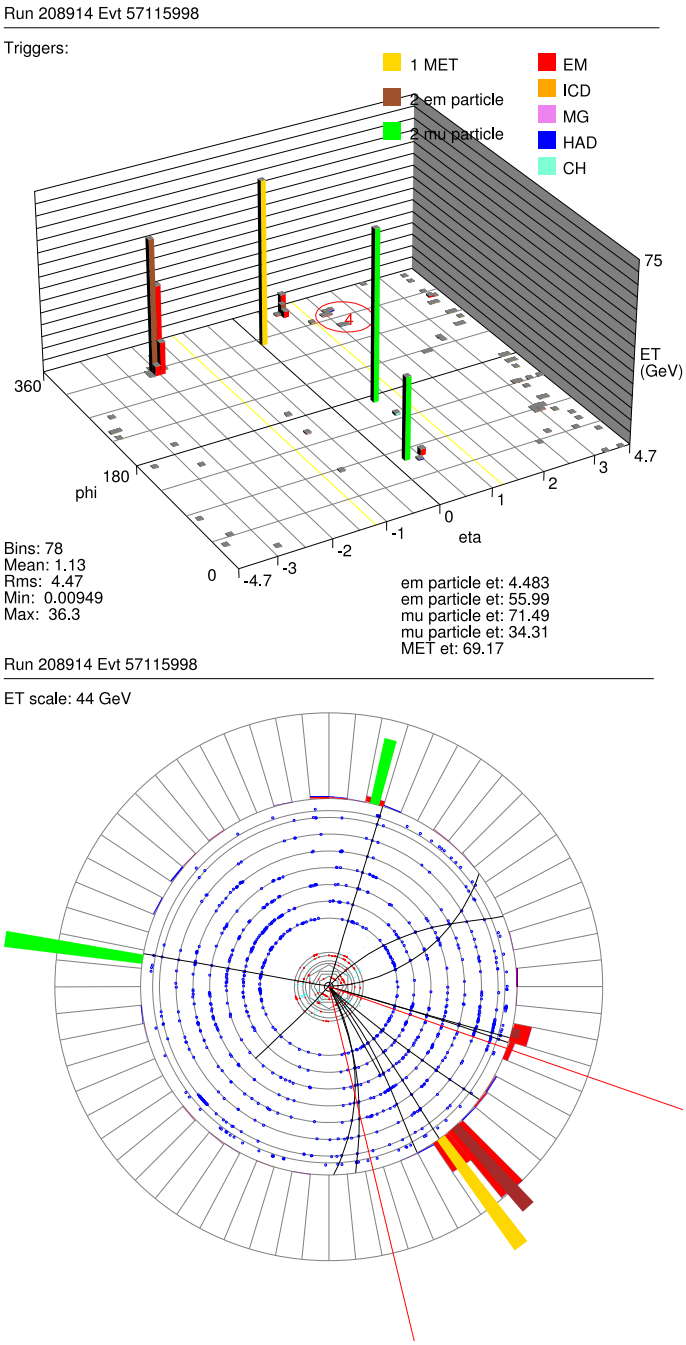

Figure D.14: $ee\mu\mu$ candidate event display for the Run 208914. (Four lepton invariant mass 359.1 GeV)

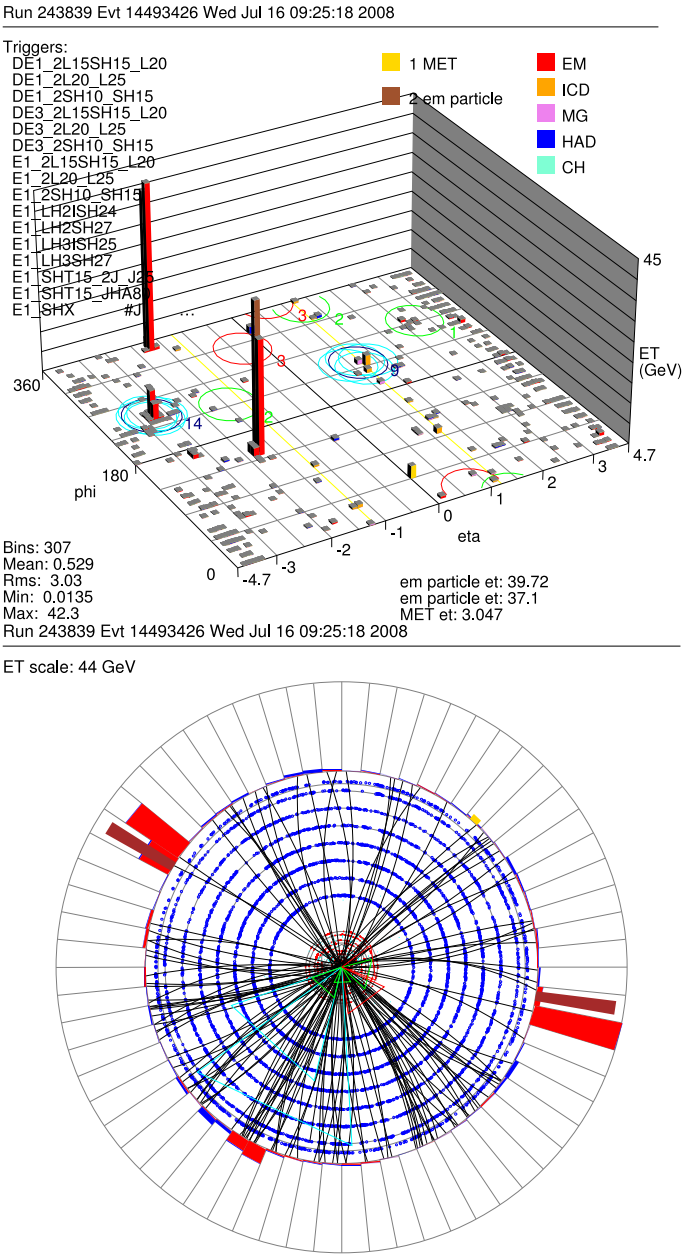

Figure D.15: $ee\mu\mu$ candidate event display for the Run 243839. (Four lepton invariant mass 277.3 GeV)

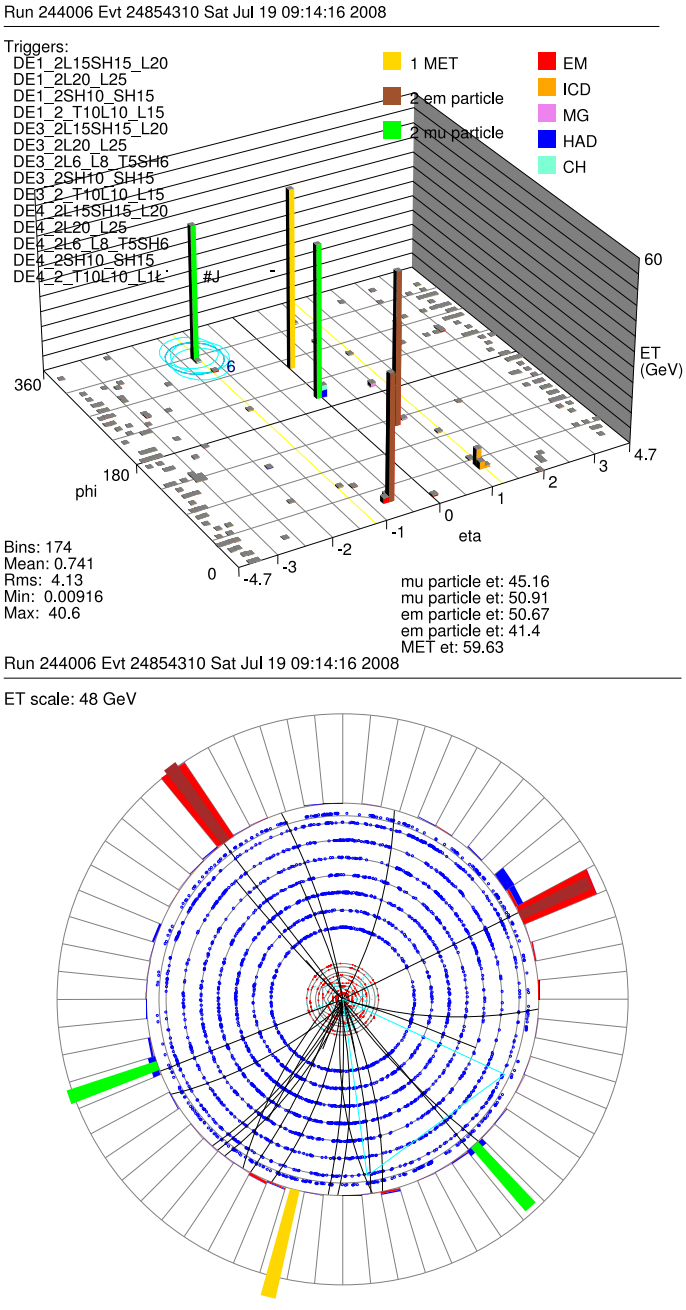

Figure D.16: $ee\mu\mu$ candidate event display for the Run 244006. (Four lepton invariant mass 235.5 GeV)

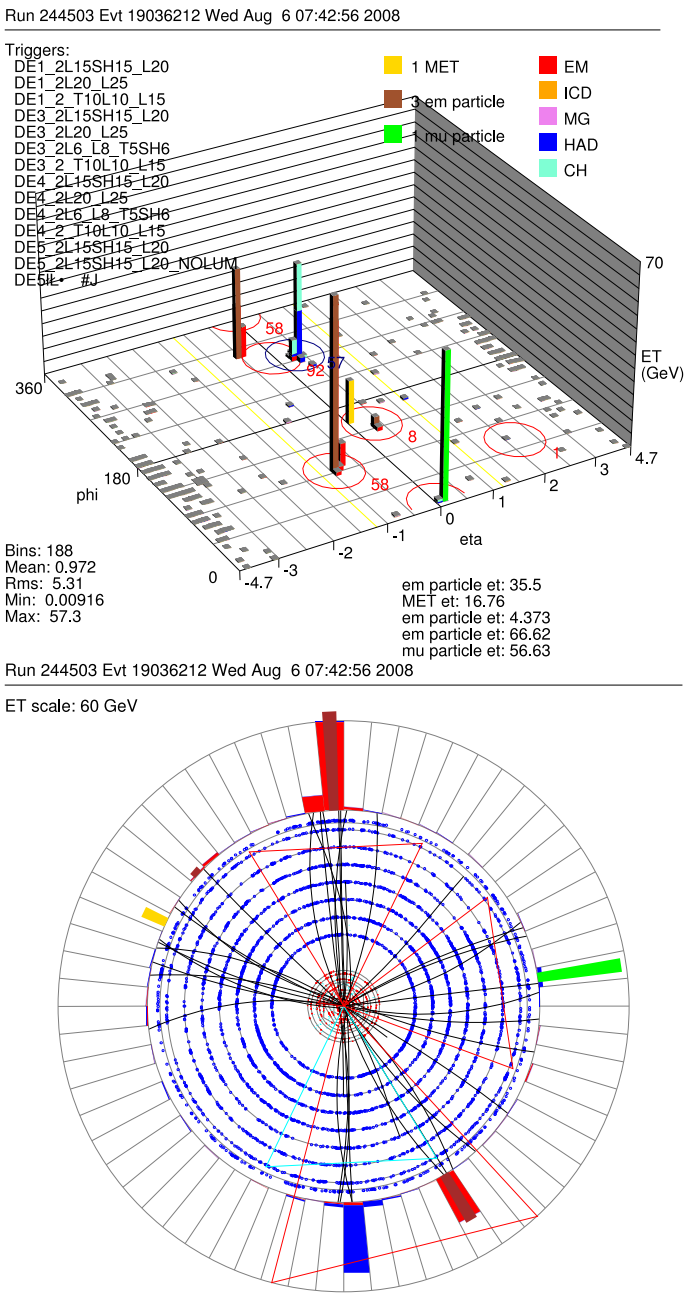

Figure D.17: $ee\mu\mu$ candidate event display for the Run 244503. (Four lepton invariant mass 237.8 GeV) (This event does not pass normal DQ)

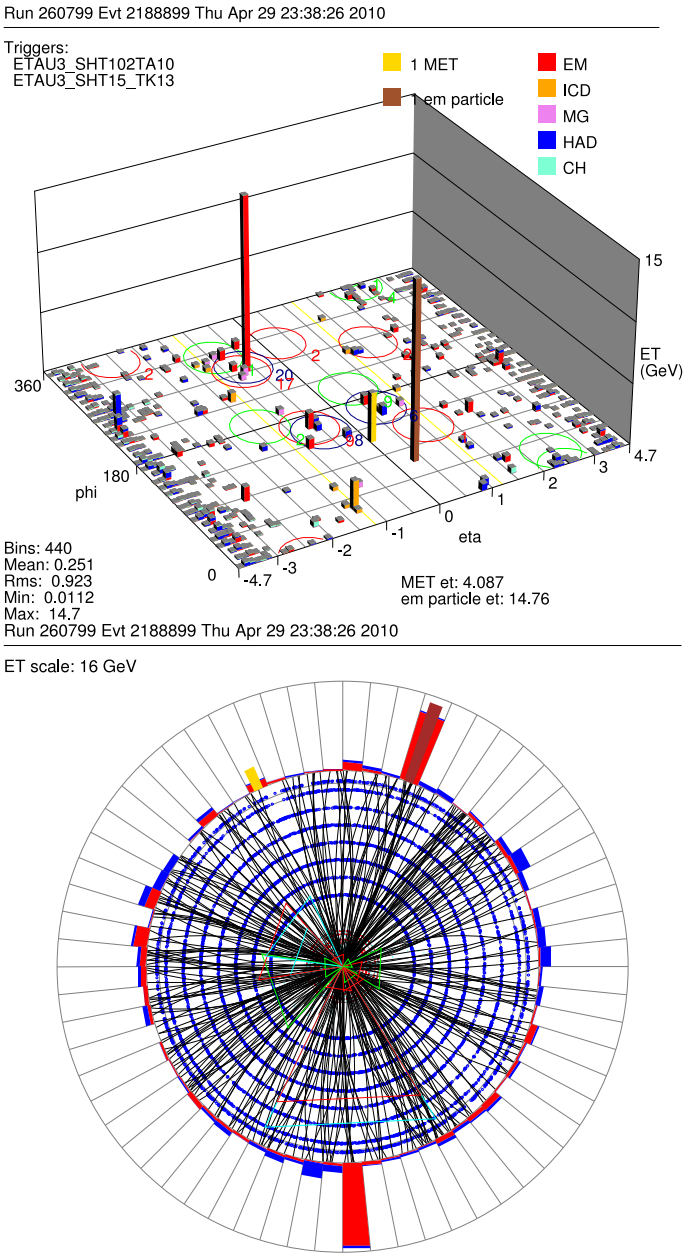

Figure D.18: $ee\mu\mu$ candidate event display for the Run 260799. (Four lepton invariant mass 136.8 GeV)